

# Observations of Active Galactic Nuclei with the MAGIC Telescope



Igor Oya Vallejo

Departamento de Física Atómica, Molecular y Nuclear  
Universidad Complutense de Madrid

Thesis advisors:

Dr. José Luis Contreras González

Dra. María Victoria Fonseca González

A thesis submitted for the degree of

*Doctor of Philosophy*

June 2010, Madrid

*I dedicate this thesis to  
my partner María Jesús,  
my parents Pili and Salus,  
and my sister Lorea.*

## Acknowledgements

I would like to express my gratitude to my supervisor José Luis Contreras for his help, advice, understanding, patience and friendship during these hard years. I thank my supervisor María Victoria Fonseca for the opportunity she gave me to join the GAE group of the UCM, and I much appreciate her help, guidance, care and financial support during my work in the group.

I acknowledge those MAGIC collaboration colleagues that helped me during these years. I will miss the good mood existing inside this great team. Particularly, I would like to thank Stefan Rügamer, Abelardo Moralejo, Juan Cortina, Florian Goebel, Daniel Mazin, Robert Wagner, Thomas Bretz, Daniela Dorner, Antonio Stamerra, David Paneque, Emiliano Carmona, Fabrizio Tavecchio, Pratik Majumdar, Masaaki Hamayashida, Rudy Bock, Eckart Lorenz, Razmick Mizoryan, Elvira Leonardo, Dario Hrupec and Diego Tescaro for their valuable help.

I would like to thank my friends Íñigo Cruz, Héctor Enríquez, Lucas Lamata, Carlos Hidalgo, Pedro Antoranz, Miguel Cámara and Emmanuel Aller for the friendship they exhibited to me these hard years.

A very special thanks goes to my friends in the Madrid MAGIC/GAE group for their support and for the good time we spent together: Fabrizio Lucarelli, Mariano Asensio, Pablo Casatella, Silvia Balestra, Debanjan Bose, Jose Miguel Miranda, Emma de Oña, Silvia Pardo, Rubén García, Adolfo Vázquez, Marcos López, Luis Padilla, Luis Ángel Tejedor, and José Luis Lemus. I found help from them whenever I needed it. I specially thank Raquel de los Reyes for her great help during the first years of my thesis work, Daniel Nieto for his help during the writing of this thesis, and Nestor Mirabal and Juan Abel Barrio for their advice, that helped me to cheer up during the last stages of my PhD work.

I also want to acknowledge that little monster that Yoda is, for the funny and lovely moments that has given to me, teaching me why the dog is considered to be man's best friend.

Of course I want to thank my family for all the support and love given to me during my whole life. Among my big family I acknowledge my parents Pili and Salus, my grandparents Eufrasio, Juan, Dolores and Ángeles, my sister Lorea, my aunt and uncles Juan Carlos, Rocío, Loli, Ana, Amaya, José Manuel, José Antonio and José Luis: All of them have proven me many times that I can count on them.

My most sincere appreciation goes to my “other” family: Manolo, María Jesús, Imma, Carmen, and José María have become an important part in my life.

Last, but not least, I want to acknowledge María Jesús her full, strong and reliable support, that has been the best help I had during this enterprise, together with a prove of what I can expect during my whole life from her.

# Contents

|          |  |          |
|----------|--|----------|
| <b>1</b> | <b>Introduction</b>                                      | <b>1</b> |
| <b>2</b> | <b>High energy gamma-ray astronomy</b>                   | <b>4</b> |
| 2.1      | Introduction . . . . .                                   | 4        |
| 2.2      | The origin of cosmic rays . . . . .                      | 5        |
| 2.2.1    | Galactic cosmic rays . . . . .                           | 5        |
| 2.2.2    | Extragalactic cosmic rays . . . . .                      | 6        |
| 2.3      | Gamma-ray production and absorption mechanisms . . . . . | 6        |
| 2.3.1    | Electron bremsstrahlung . . . . .                        | 8        |
| 2.3.2    | Matter-antimatter annihilation . . . . .                 | 8        |
| 2.3.3    | Gamma rays from $\pi^0$ -decay . . . . .                 | 9        |
| 2.3.4    | Nuclear $\gamma$ -ray emission lines . . . . .           | 10       |
| 2.3.5    | Inverse Compton scattering . . . . .                     | 10       |
| 2.3.6    | Synchrotron radiation . . . . .                          | 11       |
| 2.3.7    | Curvature radiation . . . . .                            | 12       |
| 2.3.8    | Black body emission and thermal bremsstrahlung . . . . . | 13       |
| 2.3.9    | Pair production . . . . .                                | 14       |
| 2.4      | Gamma-ray attenuation due to EBL . . . . .               | 15       |
| 2.5      | VHE gamma-ray sources . . . . .                          | 18       |
| 2.5.1    | Active galactic nuclei . . . . .                         | 18       |
| 2.5.2    | Gamma-ray burst . . . . .                                | 19       |
| 2.5.3    | Pulsars . . . . .  | 21       |
| 2.5.4    | Supernova remnants . . . . .                             | 23       |
| 2.5.5    | The Galactic Center . . . . .                            | 23       |
| 2.5.6    | $\gamma$ -ray binary systems . . . . .                   | 25       |
| 2.5.7    | Other sources . . . . .                                  | 27       |
| 2.6      | Detectors . . . . .                                      | 28       |
| 2.6.1    | Satellites and balloons . . . . .                        | 28       |
| 2.6.2    | Ground based detectors . . . . .                         | 31       |
| 2.6.2.1  | Particle and secondary photon detectors . . . . .        | 31       |
| 2.6.2.2  | Atmospheric Cherenkov detectors . . . . .                | 31       |

## CONTENTS

---

|  |           |
|--|-----------|
| <b>3 Active galactic nuclei</b>                      | <b>34</b> |
| 3.1 Introduction . . . . .                           | 34        |
| 3.2 Classification of AGN . . . . .                  | 36        |
| 3.2.1 Radio loud AGN . . . . .                       | 39        |
| 3.2.1.1 GPS/CSS . . . . .                            | 39        |
| 3.2.1.2 AGN with developed jets . . . . .            | 39        |
| 3.2.2 Radio quiet AGN . . . . .                      | 41        |
| 3.3 Blazars . . . . .                                | 42        |
| 3.4 Blazar models . . . . .                          | 42        |
| 3.4.1 Leptonic models . . . . .                      | 44        |
| 3.4.1.1 Synchrotron self-Compton . . . . .           | 44        |
| 3.4.1.2 External Compton . . . . .                   | 45        |
| 3.4.2 Hadronic models . . . . .                      | 45        |
| 3.5 The blazar sequence . . . . .                    | 46        |
| <b>4 The imaging air Cherenkov technique</b>         | <b>49</b> |
| 4.1 Introduction . . . . .                           | 49        |
| 4.2 Electromagnetic showers . . . . .                | 49        |
| 4.3 Hadronic showers . . . . .                       | 52        |
| 4.4 The Cherenkov effect . . . . .                   | 54        |
| 4.4.1 Cherenkov light in the atmosphere . . . . .    | 55        |
| 4.5 The Cherenkov imaging technique . . . . .        | 57        |
| <b>5 The MAGIC experiment</b>                        | <b>60</b> |
| 5.1 Introduction . . . . .                           | 60        |
| 5.2 Structure and mirrors . . . . .                  | 60        |
| 5.3 Drive . . . . .                                  | 62        |
| 5.4 Camera . . . . .                                 | 62        |
| 5.5 Readout . . . . .                                | 62        |
| 5.6 Trigger system . . . . .                         | 64        |
| 5.7 Calibration . . . . .                            | 66        |
| 5.8 MAGIC observation modes and file types . . . . . | 66        |
| <b>6 The MAGIC analysis method</b>                   | <b>69</b> |
| 6.1 Introduction . . . . .                           | 69        |
| 6.2 MARS . . . . .                                   | 69        |
| 6.2.1 Analysis scheme . . . . .                      | 70        |
| 6.3 The Crab Nebula . . . . .                        | 71        |
| 6.4 Monte Carlo simulated $\gamma$ -rays . . . . .   | 71        |
| 6.5 Data selection . . . . .                         | 72        |
| 6.6 Signal extraction and calibration . . . . .      | 73        |
| 6.6.1 Signal extraction . . . . .                    | 73        |

## CONTENTS

---

|          |   |           |
|----------|---|-----------|
| 6.6.2    | Calibration . . . . .   | 75        |
| 6.7      | Image cleaning and parametrization . . . . .                          | 75        |
| 6.7.1    | Image cleaning . . . . .  | 77        |
| 6.7.2    | Image parameters . . . . .  | 77        |
| 6.8      | Estimation of the characteristics of the primary particle . . . . .   | 80        |
| 6.8.1    | Rejection of the hadronic background . . . . .                        | 80        |
| 6.8.2    | Energy reconstruction . . . . .                                       | 82        |
| 6.8.3    | Arrival direction reconstruction . . . . .                            | 85        |
| 6.8.3.1  | Disp parametrization . . . . .  | 85        |
| 6.8.3.2  | Disp from RF . . . . .  | 85        |
| 6.8.4    | Event based quality cuts . . . . .                                    | 85        |
| 6.9      | Determination of excess events and statistical significance . . . . . | 86        |
| 6.9.1    | Sensitivity . . . . .   | 89        |
| 6.9.2    | Cut determination . . . . .   | 89        |
| 6.9.3    | Sky Map . . . . .   | 90        |
| 6.10     | Spectrum and light curve . . . . .                                    | 92        |
| 6.10.1   | Effective collection area . . . . .                                   | 92        |
| 6.10.2   | Effective on time . . . . .   | 92        |
| 6.10.3   | Unfolding . . . . .   | 93        |
| 6.10.4   | Light curve . . . . .   | 95        |
| 6.11     | Upper limit calculation . . . . .                                     | 96        |
| 6.12     | Systematic errors . . . . .   | 97        |
| <b>7</b> | <b>Data quality check software</b>                                    | <b>98</b> |
| 7.1      | Introduction . . . . .  | 98        |
| 7.2      | MARS and MAGICDC . . . . .  | 98        |
| 7.3      | MAGICDC: Telescope data quality check . . . . .                       | 99        |
| 7.3.1    | Steering scripts . . . . .  | 101       |
| 7.3.2    | Subsystems data quality check . . . . .                               | 103       |
| 7.3.2.1  | Overview . . . . .  | 103       |
| 7.3.2.2  | Program . . . . .   | 103       |
| 7.3.2.3  | Checked subsystems . . . . .  | 104       |
| 7.3.3    | Data acquisition quality check . . . . .                              | 108       |
| 7.3.3.1  | Overview . . . . .  | 109       |
| 7.3.3.2  | Program . . . . .   | 109       |
| 7.3.3.3  | Checks performed . . . . .  | 110       |
| 7.3.3.4  | MAGIC-II update . . . . .   | 114       |
| 7.3.4    | Calibration data check . . . . .                                      | 115       |
| 7.3.4.1  | The calibration system . . . . .                                      | 115       |
| 7.3.4.2  | Program . . . . .   | 115       |
| 7.3.4.3  | Calibration quality checks . . . . .                                  | 117       |
| 7.3.4.4  | PC-rubidium clock time plots . . . . .                                | 120       |

## CONTENTS

---

|          |   |            |
|----------|---|------------|
| 7.3.4.5  | Arrival time distributions for all events . . . . .             | 120        |
| 7.3.4.6  | MAGICDC update for MAGIC-II . . . . .                           | 120        |
| 7.3.5    | Analysis data check . . . . .                                   | 120        |
| 7.3.5.1  | Program . . . . .   | 121        |
| 7.3.5.2  | Analysis quality checks . . . . .                               | 121        |
| 7.3.6    | Automatic data check . . . . .                                  | 121        |
| 7.3.6.1  | Program . . . . .   | 121        |
| 7.4      | Conclusions and outlook . . . . .                               | 122        |
| <b>8</b> | <b>Quick on-site analysis software</b>                          | <b>125</b> |
| 8.1      | Introduction . . . . .  | 125        |
| 8.2      | La Palma computing and network . . . . .                        | 126        |
| 8.3      | Program description . . . . .                                   | 128        |
| 8.3.1    | Program control scripts . . . . .                               | 128        |
| 8.3.2    | <i>Sequencer</i> tasks . . . . .                                | 130        |
| 8.3.3    | <i>Littlesequence</i> tasks . . . . .                           | 132        |
| 8.3.3.1  | Calibration . . . . .   | 132        |
| 8.3.3.2  | Image cleaning and parametrization . . . . .                    | 133        |
| 8.3.3.3  | File copy and verification . . . . .                            | 134        |
| 8.3.4    | Other tasks . . . . .   | 134        |
| 8.4      | MAGIC-II update . . . . .                                       | 135        |
| 8.5      | Conclusion . . . . .  | 135        |
| <b>9</b> | <b>Mrk 421 2006 multiwavelength campaigns</b>                   | <b>137</b> |
| 9.1      | Introduction . . . . .  | 137        |
| 9.2      | MAGIC observations and data analysis . . . . .                  | 138        |
| 9.3      | Results . . . . .   | 141        |
| 9.3.1    | Results for 2006 April 22 – 30 . . . . .                        | 141        |
| 9.3.1.1  | Observations at other wavelengths . . . . .                     | 146        |
| 9.3.1.2  | Cross-band correlations . . . . .                               | 146        |
| 9.3.2    | Results for 2006 June 14 . . . . .                              | 148        |
| 9.4      | MWL campaign during April 29-30, 2006 and May 7, 2008 . . . . . | 149        |
| 9.4.1    | XMM-Newton observations . . . . .                               | 149        |
| 9.4.2    | Whipple observations (2006) . . . . .                           | 150        |
| 9.4.3    | VERITAS observations (2008) . . . . .                           | 150        |
| 9.4.4    | Results of the campaign . . . . .                               | 151        |
| 9.4.4.1  | Spectral energy distribution and modeling . . . . .             | 151        |
| 9.4.4.2  | Cross-band correlation . . . . .                                | 152        |
| 9.4.4.3  | Spectral hysteresis . . . . .                                   | 157        |
| 9.5      | Comparison with MAGIC published results . . . . .               | 157        |
| 9.6      | Discussion . . . . .  | 157        |
| 9.6.1    | Spectral shape . . . . .  | 157        |

## CONTENTS

---

|                   |   |            |
|-------------------|---|------------|
| 9.6.2             | Correlations between energy bands . . . . .                   | 162        |
| 9.7               | Summary . . . . .   | 165        |
| <b>10</b>         | <b>Observations of 1ES 1426+428 during 2008 MWL campaigns</b> | <b>169</b> |
| 10.1              | Introduction . . . . .  | 169        |
| 10.2              | MAGIC observations and data analysis . . . . .                | 170        |
| 10.3              | Observations at other wavelengths . . . . .                   | 174        |
| 10.3.1            | X-ray observations . . . . .                                  | 174        |
| 10.3.2            | Optical and UV observations . . . . .                         | 174        |
| 10.4              | Cross-band correlation . . . . .                              | 176        |
| 10.5              | Spectral energy distribution and modeling . . . . .           | 179        |
| 10.6              | Discussion . . . . .  | 179        |
| 10.7              | Summary . . . . .   | 182        |
| <b>11</b>         | <b>Observations of Mrk 421 and Mrk 501 during 2009</b>        | <b>184</b> |
| 11.1              | Introduction . . . . .  | 184        |
| 11.2              | MAGIC observations and data analysis . . . . .                | 185        |
| 11.3              | Results . . . . .   | 189        |
| 11.3.1            | Mrk 421 . . . . .   | 189        |
| 11.3.2            | Mrk 501 . . . . .   | 190        |
| 11.3.3            | Cross-band correlations . . . . .                             | 192        |
| 11.4              | Discussion . . . . .  | 194        |
| 11.5              | Summary . . . . .   | 197        |
| <b>12</b>         | <b>Concluding Remarks</b>                                     | <b>201</b> |
| 12.1              | Software work . . . . .                                       | 201        |
| 12.2              | Analysis of blazars . . . . .                                 | 202        |
| 12.3              | Outlook . . . . .   | 205        |
| <b>A</b>          | <b>Data quality check plots</b>                               | <b>208</b> |
| A.1               | Subsystems data check . . . . .                               | 208        |
| A.2               | Data acquisition system quality check . . . . .               | 218        |
| A.3               | Calibration data quality check . . . . .                      | 223        |
| A.4               | Hillas parameter plots . . . . .                              | 232        |
| <b>B</b>          | <b>Example of a sequence</b>                                  | <b>236</b> |
| <b>C</b>          | <b>List of acronyms and abbreviations</b>                     | <b>237</b> |
| C.1               | Acronyms used in the dissertation . . . . .                   | 237        |
| C.2               | Acronyms used in the bibliography . . . . .                   | 240        |
| <b>References</b> |   | <b>263</b> |

# List of Figures

|      |   |    |
|------|---|----|
| 2.1  | Bremsstrahlung . . . . .  | 7  |
| 2.2  | Electron positron annihilation . . . . .  | 7  |
| 2.3  | Proton anti-proton annihilation. . . . .  | 7  |
| 2.4  | Hadronic collision . . . . .  | 7  |
| 2.5  | Radioactive emission . . . . .  | 7  |
| 2.6  | Inverse Compton scattering . . . . .  | 7  |
| 2.7  | Synchrotron emission . . . . .  | 7  |
| 2.8  | Curvature radiation . . . . .   | 7  |
| 2.9  | Hot plasma . . . . .  | 7  |
| 2.10 | Simplified scheme of an electron-photon cascade . . . . .                                   | 14 |
| 2.11 | EBL attenuation coefficient vs. photon energy . . . . .                                     | 15 |
| 2.12 | $\gamma$ -ray horizon . . . . .   | 16 |
| 2.13 | Some models for EBL . . . . .   | 17 |
| 2.14 | Paradigm of radio loud AGN . . . . .  | 19 |
| 2.15 | Possible $\gamma$ -ray emitting regions of a pulsar . . . . .                               | 22 |
| 2.16 | Composite image from the SR IC 443 . . . . .  | 24 |
| 2.17 | VHE $\gamma$ -ray emission from the direction of the GC, as measured by MAGIC . . . . .     | 25 |
| 2.18 | VHE $\gamma$ -ray emission from the region around the GC, as measured by H.E.S.S. . . . . . | 26 |
| 2.19 | The sky as seen by EGRET . . . . .  | 29 |
| 2.20 | The sky as seen by <i>Fermi</i> . . . . .   | 30 |
| 2.21 | The geographical location of VHE ground detectors . . . . .                                 | 33 |
| 3.1  | Scheme of AGN according to unification model . . . . .                                      | 37 |
| 3.2  | AGN classification scheme . . . . .   | 38 |
| 3.3  | Main components of an AGN . . . . .   | 38 |
| 3.4  | Chandra image of Centaurus A . . . . .  | 40 |
| 3.5  | Example of a HBL SED . . . . .  | 43 |
| 4.1  | Schematic figure of an EM shower development in the atmosphere . . . . .                    | 50 |
| 4.2  | Longitudinal development of a $\gamma$ -ray originated shower . . . . .                     | 52 |

---

## LIST OF FIGURES

---

|      |   |     |
|------|---|-----|
| 4.3  | Scheme of an hadronic shower developed in the atmosphere . . . . .      | 53  |
| 4.4  | The Cherenkov effect . . . . .  | 54  |
| 4.5  | A simplified view of the formation of a shock wave front . . . . .      | 55  |
| 4.6  | Lateral Cherenkov photon density distribution. . . . .                  | 57  |
| 4.7  | Cherenkov photon density from different types of primary particles      | 57  |
| 4.8  | Basic idea of the “Imaging Cherenkov Technique” . . . . .               | 58  |
| 5.1  | MAGIC array photograph . . . . .  | 61  |
| 5.2  | Camera of MAGIC-I . . . . .   | 63  |
| 5.3  | Standard trigger configuration of MAGIC-I . . . . .                     | 64  |
| 5.4  | Scheme of MAGIC-II camera . . . . .                                     | 65  |
| 5.5  | The sum trigger configuration . . . . .                                 | 66  |
| 6.1  | Rate after image cleaning of selected sub-runs . . . . .                | 73  |
| 6.2  | Illustrative event images . . . . .                                     | 76  |
| 6.3  | Parametrization of a shower image with Hillas parameters . . . . .      | 79  |
| 6.4  | Importance of the RF input parameters . . . . .                         | 81  |
| 6.5  | Distribution of hadronness for a sample of $\gamma$ -ray MC and hadrons | 82  |
| 6.6  | Resolution of the energy reconstruction for some energy bins . . .      | 83  |
| 6.7  | Resolution and bias of the energy reconstruction . . . . .              | 84  |
| 6.8  | The migration matrix . . . . .  | 84  |
| 6.9  | <i>Alpha</i> distribution . . . . .                                     | 87  |
| 6.10 | $\theta^2$ distribution . . . . .                                       | 88  |
| 6.11 | Maps of excess events and significance . . . . .                        | 91  |
| 6.12 | Effective collection area . . . . .                                     | 93  |
| 6.13 | Crab Nebula differential spectrum . . . . .                             | 95  |
| 6.14 | Crab Nebula light curve . . . . .                                       | 96  |
| 7.1  | MAGICDC and on-site analysis programs scheme . . . . .                  | 100 |
| 7.2  | Scheme of the central control of MAGIC . . . . .                        | 104 |
| 7.3  | Cooling system . . . . .  | 106 |
| 7.4  | Starguider . . . . .  | 107 |
| 7.5  | GPS-rubidium clock . . . . .  | 108 |
| 7.6  | Receivers temperature . . . . .   | 109 |
| 7.7  | DAQ: Arrival time camera displays . . . . .                             | 111 |
| 7.8  | DAQ: Charge evolution plots . . . . .                                   | 112 |
| 7.9  | DAQ: Arrival time check . . . . .                                       | 114 |
| 7.10 | Calibration: Pedestal from calibration . . . . .                        | 117 |
| 7.11 | Calibration: Faulty pixels . . . . .                                    | 119 |
| 7.12 | Homogeneity plots . . . . .   | 122 |
| 8.1  | On-site analysis program scheme. . . . .                                | 127 |
| 8.2  | Scheme of directories relevant for the on-site analysis. . . . .        | 129 |

## LIST OF FIGURES

---

|       |  |     |
|-------|--|-----|
| 9.1   | Historical VHE light curve of Mrk 421 since it's first detection . . . . .                                       | 139 |
| 9.2   | Light curve for April 2006 Mrk 421 observations. . . . .   | 142 |
| 9.3   | Intra-night VHE light curve for the Mrk 421 observations in April 2006 . . . . .                                 | 143 |
| 9.4   | Differential energy spectrum of Mkn 421 for April 2006 . . . . .   | 144 |
| 9.5   | Differential energy spectra for Mkn 421 for individual nights in April 2006 . . . . .                            | 145 |
| 9.6   | Differential photon spectrum for Mrk 421 for June 14, 2006 . . . . .   | 149 |
| 9.7   | VHE spectra as measured with the VHE $\gamma$ -ray detectors on the two ToO <i>XMM-Newton</i> campaigns. . . . . | 151 |
| 9.8   | Spectral energy distribution with a SSC model for 2006 and 2008 <i>XMM-Newton</i> MWL campaigns . . . . .        | 152 |
| 9.9   | UV, X-ray and VHE light curves for April 29-30, 2006 and May 7, 2008 observations . . . . .                      | 154 |
| 9.10  | Simultaneous <i>XMM-Newton</i> EPN (0.5 - 10 keV) and VHE data . . . . .   | 155 |
| 9.11  | Simultaneous <i>XMM-Newton</i> EPN (0.5 - 10 keV) and OM (UVM2 band) data . . . . .                              | 156 |
| 9.12  | Hardness ratio vs intensity plots to study spectral hysteresis . . . . .   | 158 |
| 9.13  | Comparison of the spectra obtained with the two independent analysis . . . . .                                   | 159 |
| 9.14  | Spectral index vs. flux . . . . .  | 160 |
| 9.15  | Derived peak position using the log-P apex fit versus flux at 1 TeV  | 161 |
| 9.16  | EBL de-absorbed historical spectra of Mrk 421 . . . . .  | 164 |
| 10.1  | Light curve of the optical flux of 1ES 1426+428 as measured by the KVA telescope. . . . .                        | 175 |
| 10.2  | Light curve of the optical–UV flux of 1ES 1426+428 as measured by the Swift UVOT detector . . . . .              | 175 |
| 10.3  | Light curve of the X-ray flux of 1ES 1426+428 as measured by the Swift XRT detector . . . . .                    | 175 |
| 10.4  | V band (Swift UVOT) versus X-ray (Swift XRT) correlation . . . . .   | 177 |
| 10.5  | B band (Swift UVOT) versus X-ray (Swift XRT) correlation . . . . .   | 177 |
| 10.6  | U band (Swift UVOT) versus X-ray (Swift XRT) correlation . . . . .   | 177 |
| 10.7  | UVW1 band (Swift UVOT) versus X-ray (Swift XRT) correlation . . . . .  | 178 |
| 10.8  | UVM2 band (Swift UVOT) versus X-ray (Swift XRT) correlation . . . . .  | 178 |
| 10.9  | UVW2 band (Swift UVOT) versus X-ray (Swift XRT) correlation . . . . .  | 178 |
| 10.10 | Spectral energy distribution with a one-zone SSC model for the 2008 1ES 1426+428 MWL campaign . . . . .          | 180 |
| 11.1  | Historical VHE light curve of Mrk 501 since it's first detection . . . . .                                       | 186 |
| 11.2  | Light curve for April 2006 Mrk 421 observations. . . . .   | 190 |
| 11.3  | VHE differential energy spectrum for Mrk 421 during the 2009 MWL campaign . . . . .                              | 191 |

## LIST OF FIGURES

---

|       |   |     |
|-------|---|-----|
| 11.4  | Light curve during 2009 Mrk 501 MWL observations . . . . .  | 192 |
| 11.5  | VHE differential energy spectrum for Mrk 501 during the 2009<br>MWL campaign . . . . .                                | 193 |
| 11.6  | Differential energy spectrum in the (0.1-5000) GeV energy range<br>for Mrk 421 during the 2009 MWL campaign . . . . . | 194 |
| 11.7  | EBL de-absorbed historical spectra of Mrk 421 . . . . .   | 195 |
| 11.8  | Derived peak position of Mrk 421 in different epochs using the<br>log-P fit versus flux at 1 TeV . . . . .            | 195 |
| 11.9  | Differential energy spectrum in the (0.1-5000) GeV energy range<br>for Mrk 501 . . . . .                              | 197 |
| 11.10 | Measured historical spectra of Mrk 501 . . . . .  | 198 |
| 11.11 | SED of Mrk 421 averaged over the 2009 MWL campaign . . . . .  | 198 |
| A.1   | Drive system . . . . .  | 208 |
| A.2   | Camera status . . . . .   | 209 |
| A.3   | Power supplies . . . . .  | 209 |
| A.4   | HV settings . . . . .   | 210 |
| A.5   | DC report . . . . .   | 210 |
| A.6   | DT settings . . . . .   | 211 |
| A.7   | Active loads . . . . .  | 211 |
| A.8   | Low voltage . . . . .   | 212 |
| A.9   | Cooling system . . . . .  | 212 |
| A.10  | Trigger report . . . . .  | 213 |
| A.11  | Individual Pixel Rate . . . . .   | 213 |
| A.12  | Individual Pixel Rate distributions . . . . .   | 214 |
| A.13  | Starguider . . . . .  | 214 |
| A.14  | Starguider: correlated stars and sky brightness . . . . .   | 215 |
| A.15  | Weather station . . . . .   | 215 |
| A.16  | GPS-rubidium clock . . . . .  | 216 |
| A.17  | Receivers temperature . . . . .   | 216 |
| A.18  | Trigger delays . . . . .  | 217 |
| A.19  | DAQ: Charge camera displays . . . . .   | 218 |
| A.20  | DAQ: Arrival time camera displays . . . . .   | 219 |
| A.21  | DAQ: Pedestal camera displays . . . . .   | 219 |
| A.22  | DAQ: Charge evolution plots . . . . .   | 220 |
| A.23  | DAQ: Arrival time evolution plots . . . . .   | 220 |
| A.24  | DAQ: Npe, c. factor and hit fraction evolution plots . . . . .  | 221 |
| A.25  | DAQ: Difference of arrival times . . . . .  | 221 |
| A.26  | DAQ: Arrival time check . . . . .   | 222 |
| A.27  | DAQ: Arrival times distributions . . . . .  | 222 |
| A.28  | DAQ: Bad pixels . . . . .   | 223 |
| A.29  | Calibration: Noise peak position . . . . .  | 223 |

## LIST OF FIGURES

---

|  |     |
|--|-----|
| A.30 Calibration: Pedestals . . . . .  | 224 |
| A.31 Calibration: Pedestal from calibration . . . . .                                  | 224 |
| A.32 Calibration: Arrival time . . . . .   | 225 |
| A.33 Calibration: Signal charge . . . . .  | 225 |
| A.34 Calibration: Fitted charge . . . . .  | 226 |
| A.35 Calibration: Conversion factors . . . . .   | 226 |
| A.36 Calibration: Arrival time distributions . . . . .                                 | 227 |
| A.37 Calibration: Faulty pixels . . . . .  | 227 |
| A.38 Calibration: Relative arrival time . . . . .                                      | 228 |
| A.39 Distribution of PC-rubidium clock time differences . . . . .                      | 228 |
| A.40 Evolution of PC-rubidium clock time differences . . . . .                         | 229 |
| A.41 Size dependant distributions of calibration pulses for calibration runs . . . . . | 229 |
| A.42 Size dependant distributions of interleaved calibration pulses . . . . .          | 230 |
| A.43 Size dependant distributions of level 1 trigger events . . . . .                  | 230 |
| A.44 Size dependant distributions of level sum trigger events . . . . .                | 231 |
| A.45 Size dependant distributions for all events but calibration . . . . .             | 231 |
| A.46 Hillas parameters . . . . .   | 232 |
| A.47 Extended image parameters . . . . .   | 233 |
| A.48 Source-dependent image parameters . . . . .                                       | 233 |
| A.49 Homogeneity plots . . . . .   | 234 |
| A.50 Image parameters I . . . . .  | 234 |
| A.51 Image parameters II . . . . .   | 235 |

# Chapter 1

## Introduction

The era of very high energy (VHE,  $E > 30$  GeV)  $\gamma$ -ray astronomy started with the detection of VHE emission from the Crab Nebula in 1989 by the Whipple Imaging Atmospheric Cherenkov Telescope (IACT). More than one hundred sources had been established as VHE  $\gamma$ -ray emitters at the time of writing this thesis, comprising a population of galactic and extragalactic sources. The galactic sources are: supernova remnants, binary systems, the Galactic Center, pulsars, pulsar wind nebulae and those of unknown origin. The extragalactic sources are different type of radio loud active galactic nuclei (AGN) and starbursts galaxies.

MAGIC is one of the most sensitive detectors among the existing ground based VHE  $\gamma$ -ray ones. The MAGIC experiment is an array composed by two Imaging Atmospheric Cherenkov Telescopes (IACT), located at the Canary Island La Palma. MAGIC telescopes achieve the lowest energy threshold among all the currently existing IACTs. The work presented in this thesis can be divided in two branches: one is the technical work developed for MAGIC, consisting in the design, implementation and maintenance of the data quality and on-site reduction software, and the other one the study of VHE  $\gamma$ -ray emission from blazars in a multi-frequency context.

The data quality check and the quick on-site analysis programs of the MAGIC experiment, developed and maintained during several years by a team composed by the author and other UCM MAGIC group members, allowed to constantly monitor the performance of the different systems of the MAGIC experiment. The results obtained from the data quality check software permit a quick reaction to hardware malfunctions, consequently reducing the time lost due to technical problems, while keeping a constant monitor of the main parameters of the detector. The quick on-site analysis software of the MAGIC experiment has the goal of reducing the huge data volume recorded with MAGIC every night, allowing a fast transfer of processed data files to the MAGIC data-center, located in Barcelona. A few hours after the data taking finishes, analyzers have the possibility to download the mentioned reduced data, being able to quickly perform detailed analysis

---

before next data-taking starts. This allows to decide if it is convenient to follow with the observations of a certain source in the next observation night, for example if that source is showing a high state of activity.

Blazars are a rare type of radio loud AGN, powered by super massive black holes of masses of  $10^6 M_\odot - 10^{10} M_\odot$ . Even if the complex dynamics that happen in the region close to the compact object, located in the center of radio-loud AGN, are still not well understood, it is assumed that part of the mass falling into the black hole is ejected in the form of two ultra-relativistic jets. In the case of blazars one of the jets points to a direction close to the line of sight of the observer, while for other types of radio-loud AGN the angle is larger. Charged particles moving at relativistic speeds are able to produce non-thermal radiation in a broad energy range, including VHE  $\gamma$ -rays. Blazars exhibit a complicated behavior, showing unpredictable flux level changes in all timescales, from few minutes to years. Nevertheless, some characteristics have been identified to be often present in different blazars allowing to build several different theoretical models. Of particular interest for checking these models are simultaneous multifrequency studies, that allow to build a global picture of these systems. These kind of studies have usually been performed in epochs of high state of activity of the sources, and very often without true simultaneous multifrequency coverage, what means that the actual knowledge of VHE blazars is still biased and relatively poor. Results from four campaigns in which MAGIC participated together with detectors at other energy band are discussed in this thesis. These results include truly simultaneous measurements of blazars in different states of activity.

This thesis is structured as follows:

- Chapter 2 is an introduction to the field of  $\gamma$ -ray astronomy, including the description of the most relevant processes in  $\gamma$ -ray astronomy, known and candidate VHE sources, and the different types of instruments designed for the detection of  $\gamma$ -ray emission.
- An overview of AGN characteristics, focusing on those candidates to be VHE radiation emitters, is given in Chapter 3.
- Chapter 4 describes the imaging atmospheric Cherenkov technique, as used in detectors like MAGIC.
- A description of the main characteristics and components of the MAGIC experiment is given in Chapter 5.
- The analysis software of the MAGIC experiment, used in this thesis, is described in Chapter 6.
- The data quality check software is described in Chapter 7, where details of the goals of this software, as well as its output are detailed.

- 
- The quick on-site analysis software, that deals with the huge data volume gathered by MAGIC every data taking night, is the object of Chapter 8.
  - Chapter 9 reports on the results from a multiwavelength campaign of the blazar Mrk 421 performed in April–June 2006, including truly simultaneous measurements in the X-ray band with the *XMM-Newton* satellite and the TeV detectors MAGIC and Whipple. The results of this campaign are discussed together with those of another campaign of Mrk 421 with *XMM-Newton* and VERITAS in 2008.
  - Results from MAGIC observations of the blazar 1ES1426+428, performed together with optical, ultraviolet and X-ray observations in May–June 2008 are discussed in Chapter 10.
  - Chapter 11 describes results from MAGIC measurements of the blazars Mrk 421 and Mrk 501, performed during intense multiwavelength campaigns that took place in the first half of 2009, including data from the *Fermi* Large Area Telescope  $\gamma$ -ray detector.
  - Finally, Chapter 12 summarizes the work and some concluding remarks are exposed.

# Chapter 2

## High energy gamma-ray astronomy

### 2.1 Introduction

In the same way as it happens with the rest of the electromagnetic spectrum,  $\gamma$ -ray radiation allows to obtain information from the Cosmos and its evolution. Historically, astronomy begun as a discipline that studied the visible light of the celestial objects. It took a lot of time until the measurements extended to other energy bands of the electromagnetic spectrum. Due to the opacity of the atmosphere to different wavelength radiation, satellites and indirect observation techniques that take advantage of the atmospheric absorption have been developed in order to allow measurements through almost the entire electromagnetic range. From the astrophysical point of view, the field of the  $\gamma$ -ray astronomy above several MeV can be considered as the study of the non-thermal Universe. The history of  $\gamma$ -ray astronomy is very recent: both satellite and ground based techniques have been developed after the second half of the XX century.

Observational  $\gamma$ -ray astronomy is commonly divided in six energy ranges: *low* (LE: below 30 MeV), *high* (HE: 30 MeV - 30 GeV) *very high* (VHE: 30 GeV - 30 TeV), *ultra high energy* (UHE: 30 TeV - 30 PeV), and *extremely high* (EHE: above 30 PeV). In the low and high energy ranges the observations are carried out by detectors on satellite or balloons. Due to their small collection areas and the low  $\gamma$ -ray flux, the sensitivity of these detectors above 10 GeV is limited by low statistics. In order to explore higher energies, it is needed to use ground based detectors, which posses collection areas orders of magnitude larger. The astronomical objects that are studied in VHE  $\gamma$ -ray astronomy are, among others: Active galactic nuclei, galaxies, gamma-ray bursts (GRB), supernova remnants (SNR), pulsars, the Galactic Center, unidentified sources from HE detectors on satellites as EGRET CGRO and LAT in *Fermi*, and other sources of interest for

## 2.2 The origin of cosmic rays

---

cosmological and fundamental physics. Apart from the previous source types, objects of unknown origin have been detected in the VHE band.

The high and very high energy  $\gamma$ -ray astronomy can presently claim to be astronomical disciplines by their own right, fulfilling the following three conditions:

- An important population of objects with an intense production of  $\gamma$ -rays, caused by the acceleration of charged particles, and their interaction with the surrounding medium.
- Free propagation through the space with no deflection due to the galactic and extragalactic magnetic fields.
- Numerous detections confirmed in both satellites and ground based detectors.

## 2.2 The origin of cosmic rays

Cosmic rays (CR) are particles coming from outer space that hit Earth's atmosphere. Their discovery is normally attributed to Victor Hess by the beginning of the XXth century [Hes12]. Their basic composition is around 90% protons, 10% helium nuclei, and slightly under 1% are heavier elements and electrons. The word *ray*, used for historical reasons, may be confusing: the cosmic rays are individual particles that arrive to our atmosphere. The assumed origin of the cosmic rays depends on their energy, and spans from energetic processes in the Sun to the most energetic unknown processes in the Universe. The individual energy of a cosmic ray can exceed the  $10^{20}$  eV, that is far greater than the energy achievable by the most modern particle accelerators.

CR have different origins: either produced in the Galaxy (*galactic* CR) or outside the Galaxy (*extragalactic* CR).

### 2.2.1 Galactic cosmic rays

It is commonly believed that  $\gamma$ -rays may play an important role in the determination of the origin of the galactic cosmic rays. The idea is that due to the nature of some likely emission processes, the detected  $\gamma$ -ray sources show the location of potential CR emitters. The diffuse galactic  $\gamma$ -rays will provide information, arising from the interaction from CR with interstellar medium (ISM), about the propagation of CR through the Galaxy.

The generally accepted hypothesis for the generation of the cosmic rays up to  $10^{15}$  eV assumes that they originate in SNR, and therefore these sources are one important target for VHE observations. When this thesis was written 9 SNR had been detected in the VHE regime. The problem gets complicated as other galactic

## 2.3 Gamma-ray production and absorption mechanisms

---

source populations, like pulsars and micro-quasars can contribute substantially to the observed cosmic ray flux.

### 2.2.2 Extragalactic cosmic rays

Even if it is commonly accepted that the ultra-high energy cosmic rays (UHECRs), with energies  $E > 10^{19}$  eV are produced outside the Galaxy, their production mechanisms remain unknown. A diverse group of possible sources has been considered as the place where CR originate: blazars, radio galaxies, clusters of galaxies and the GRBs. All these objects are known or potential VHE  $\gamma$ -ray emitters.

Possibly the most intriguing suggestion of an association between UHECRs and AGN was put forward by the *Pierre Auger* collaboration [Abr04], that found a possible correlation between the arrival direction of 27 events with the position of nearby AGN [Abr07]. This correlation remained, but slightly weakened after the inclusion of additional UHECR events [Abr09]. On the other hand, a cross correlation study showed no evidence that UHECRs are associated with *Fermi* HE sources [MO10].

## 2.3 Gamma-ray production and absorption mechanisms

The origin of the  $\gamma$ -rays must be due to non-thermal processes. Except for hypothetical scenarios where extremely high temperatures may be present like in GRBs, it is not possible to reach the required minimum temperature to produce  $\gamma$ -rays by thermal processes. For example, to produce one MeV  $\gamma$ -ray, a temperature of the order of  $10^9$  K would be needed.

There is a rather wide variety of non-thermal phenomena as the origin of energy  $\gamma$ -rays of different energies. The following section describes the most relevant ones. More detailed descriptions can be found in, e.g. [RW93, Aha04a, Lon92, Wee03].

## 2.3 Gamma-ray production and absorption mechanisms

---

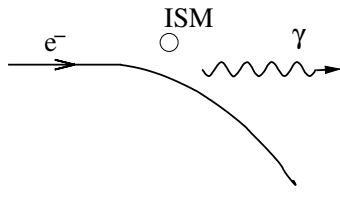


Figure 2.1: *Electron bremsstrahlung.*

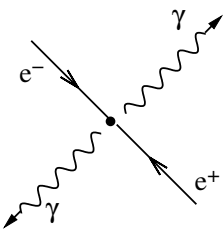


Figure 2.2: *Electron-positron annihilation.*

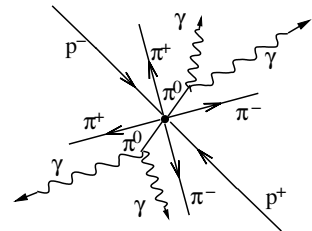


Figure 2.3: *Proton-antiproton annihilation.*

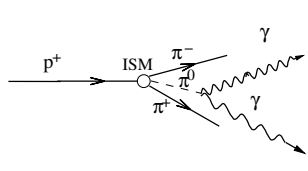


Figure 2.4: *Hadronic collision.*

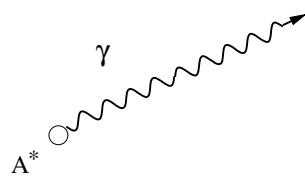


Figure 2.5: *Radioactive emission.*

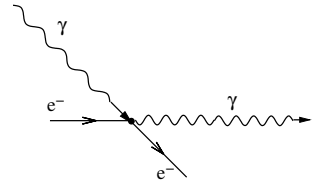


Figure 2.6: *Inverse Compton scattering.*

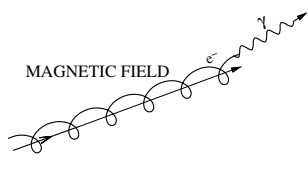


Figure 2.7: *Synchrotron emission.*

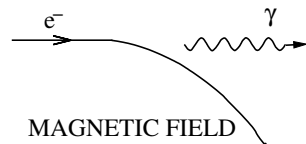


Figure 2.8: *Curvature radiation.*



Figure 2.9: *Hot plasma.*

*Summary of  $\gamma$ -ray production mechanisms.*  $A^*$  represents an excited nucleus, and ISM the interstellar medium.

## 2.3 Gamma-ray production and absorption mechanisms

---

### 2.3.1 Electron bremsstrahlung

This process happens when a charged particle interacts with an ion or a nucleus (see Figure 2.1). The trajectory of the incident electron is changed by the electric field of the nucleus, and a photon is emitted. The relevant scenario happens when the incident electrons moves at relativistic speeds, as for the low speeds the efficiency of the bremsstrahlung is overrun by ionization losses.

Both classical and quantum mechanical treatments of this effect give *average* cross section for many bremsstrahlung interactions of the same order:  $\sigma_b \simeq 4(1/137)(e^2/m_0c^2)Z^2 = 0.58$  millibarns/nucleus. It was shown [Ste75] that  $\gamma$ -rays resulting from bremsstrahlung from electrons in a gas have energies of the same order of the incident electrons, what means that if the electron population is characterized by a certain spectral index, the  $\gamma$ -ray spectrum will show approximately the same one.

Protons can, in principle, emit bremsstrahlung radiation in the same way as electrons do. However, their mass to charge ratio makes this mechanism rather inefficient. In certain situations these non-relativistic electron and proton bremsstrahlung processes may play an important role (e.g. generation of non thermal X-rays in solar flares) due to ionization loses, but in general these are very inefficient radiation mechanisms.

### 2.3.2 Matter-antimatter annihilation

Electron and positrons annihilate by the known process (see Figure 2.2):

$$e^+ e^- \rightarrow 2\gamma \quad (2.1)$$

Where, if  $e^+$  and  $e^-$  are at rest, both photons have energy of  $m_e c^2 = 0.511$  MeV. This sharp energy should be detected as a line, and this is what can be observed in the direction of the Galactic Center. However, thermalized positrons can interact with cold thermal electrons of the ambient gas or plasma, producing a 3-photon positronium continuum in the MeV range.

If the positrons are injected in the region with relativistic energies, a significant fraction of them annihilate in flight before they cool down to the temperature of the background gas. The spectrum of the annihilation radiation is steeper than the one of the parent positrons, but it reproduces the shape of the primary spectrum of positrons. For energies  $< 15$  MeV, the annihilation continuum starts to dominate over the bremsstrahlung spectrum.

Protons can annihilate with anti-protons producing pions (see Figure 2.3), that will decay in two  $\gamma$ -rays (see below). Anti-protons can be generated by interaction of energetic protons with matter, but this process is a very inefficient mechanism and actually it is more likely that pions are created directly in the interaction of protons with matter. On the other hand, in case that anti-matter

## 2.3 Gamma-ray production and absorption mechanisms

---

exists in significant quantities in the Universe, this process could contribute to  $\pi^0$  generation and therefore  $\gamma$ -ray production.

### 2.3.3 Gamma rays from $\pi^0$ -decay

The  $\pi^0$ -decay is the most relevant channel by which  $\gamma$ -rays are produced in hadronic interactions. Relativistic protons and nuclei interact in inelastic collision with matter and produce pions, kaons and hyperons. These secondary particles decay and emit high energy  $\gamma$ -rays (see Figure 2.4). In general only the pion component is taken into account in the models, ignoring the kaons and hyperons due to their modest presence.

If the original hadron's kinetic energy exceeds a minimum energy  $E_{th} = 2m_\pi c^2(1 + m_\pi/4m_p) \simeq 280$  MeV, being  $m_\pi = 134.97$  MeV the mass of the neutral pion, it may produce one  $\pi^0$  through the  $p + p \rightarrow \pi^0$  channel. The  $\pi^0$ -meson provides the main channel of conversion of the kinetic energy of protons to high energy  $\gamma$ -rays:

$$\pi^0 \rightarrow 2\gamma \quad (\text{Prob} = 0.99) \quad (2.2)$$

$$\pi^0 \rightarrow e^+e^-\gamma \quad (\text{Prob} = 0.01) \quad (2.3)$$

The neutral pions have much shorter lifetime ( $8.4 \cdot 10^{-17}$  s) than charged  $\pi$ -mesons ( $2.6 \cdot 10^{-8}$  s). The produced high energy  $\gamma$ -ray spectrum essentially reproduces the spectrum of the parent protons. Assuming that the electrons and protons are accelerated with the same power-law spectrum in an hydrogen medium, and assuming an electron to proton ratio  $r \geq 10$ , the contribution of  $\gamma$ -rays from  $\pi^0$  decays dominates the one from electron bremsstrahlung. At very high energies, the effect of the inverse Compton and synchrotron losses make the contribution from electron bremsstrahlung negligible [Aha04a].

Given that the CR spectrum follows power-law spectral distribution with a spectral index  $\Gamma_P$ , at high energies the observed  $\gamma$ -ray spectrum will also have a power law-spectrum with an index  $\Gamma_\gamma = 4/3(\Gamma_P - 1/2)$  [Aha04a].

At high energies, all three types of pions are produced with comparable probabilities. The decay of charged pions produces neutrinos. The neutrino spectrum would be similar to the  $\gamma$ -ray spectrum from  $\pi^0$ -decay. However, at high energies, due to their long life-time, the charged pions will interact with other hadrons before decaying, which results in a smaller neutrino flux with respect to  $\gamma$ -rays. The discovery of neutrino and  $\gamma$ -ray correlated spectra would be the strongest indications of the presence of hadronic acceleration mechanisms.

## 2.3 Gamma-ray production and absorption mechanisms

---

### 2.3.4 Nuclear $\gamma$ -ray emission lines

Even if protons with kinetic energy below 300 MeV cannot produce pions, they still can play a role in the  $\gamma$ -ray emission mechanisms. These protons can excite the medium nuclei. When these nuclei de-excite they produce  $\gamma$ -ray lines whose energy range spans from several hundred keV to several MeV (see Figure 2.5). Other type of nuclei can also be projectiles.

$\gamma$ -ray emission is formed by the contribution of both projectile and target nuclei, and the line of both components is Doppler broadened. The broadening of the target comes from its recoil momentum, and depends on the lifetime of the excited nucleus and on the density and temperature of the medium. The line of the projectile is even broader, due to the typical higher velocities (0.1c or more). Some of the most important lines are:  $^{16}\text{O}$ ; (6.1 MeV),  $^{12}\text{C}$ ; (2.3 and 5.1 MeV),  $^{14}\text{N}$ ; (2.7 and 6.9 MeV);  $^{56}\text{Fe}$ ; (0.85 MeV);  $\alpha - \alpha$ ; (0.45 MeV).

One important case happens when the nuclei move at relativistic motion toward the observer. In this case, the emitted  $\gamma$ -rays may be boosted to high energies.

### 2.3.5 Inverse Compton scattering

When a relativistic electron (or positron) moves with a Lorentz factor  $\gamma$  towards a photon of energy  $E$ , in the rest system of the relativistic particle the photon is seen with energy  $\gamma E$ . After the collision (see Figure 2.6), the scattered photon will have energy  $\leq \gamma E$  in the rest system, but when transformed to the laboratory reference frame, it becomes  $\sim \gamma^2 E$ . The energy of the boosted photon will be:

$$E_\gamma \approx E\gamma^2 \quad \text{if } \gamma E \ll m_e c^2 \quad (2.4)$$

and

$$E_\gamma \sim E_e \quad \text{if } \gamma E \gg m_e c^2 \quad (2.5)$$

This process, called inverse Compton (IC) scattering, becomes relevant when the ambient photon density is high. The IC scattering is a very efficient method to increase the energy of the photons to very high energies. The cross section of both regimes can be described, respectively, by the following formulae:

$$\sigma_T = \sigma_t \left( 1 - \frac{2\gamma E}{m_e c^2} \right) \quad \text{if } \gamma \ll m_e c^2 \quad (2.6)$$

and

$$\sigma_e = \frac{3}{8} \left( \sigma_T \frac{m_e c^2}{\gamma E} \right) \left[ \ln \left( \frac{2\gamma E}{m_e c^2} \right) - \frac{1}{2} \right] \quad \text{if } \gamma \gg m_e c^2 \quad (2.7)$$

## 2.3 Gamma-ray production and absorption mechanisms

---

Being  $\sigma_T = 8\pi r_e^2/3 \simeq 6.65 \cdot 10^{-25} \text{ cm}^2$  the Thomson cross section. The regime described by equation 2.4 is named Thomson regime. It is commonly experienced in connection with the interaction of electron with the 2.7 K CMR (Cosmic Microwave Radiation). In this case, the energy of the photons is  $\langle E_\gamma \rangle \simeq 6 \times 10^{-4}$  eV. The condition will be therefore fulfilled if  $\gamma \leq 10^9$ , corresponding to energies  $E_e \leq 10^{14}$  eV. In this case, the electron and photon energies can be related with the following equation:

$$\langle E_\gamma \rangle = \frac{4}{3} \gamma^2 \langle E_e \rangle \quad (2.8)$$

Equation 2.7 describes the Klein-Nishina regime, where the maximum energy that photons can gain is:

$$E_{max} \sim 4\gamma E_e \quad (2.9)$$

In the Thomson regime, the emitted photons follow the spectral shape of the seed photons. In the Klein-Nishina regime, given that the electron's spectrum follows a power law of index  $\Gamma_e$ , the resulting  $\gamma$ -ray spectrum will follow a power law of  $(\Gamma_e + 1)/2$  up to a certain energy, where a sharp cut-off exists which is determined by the maximum energy of the incident electrons.

It is believed that the hadronic processes previously described (the decay of neutral pion) and the IC scattering are the most important sources of VHE  $\gamma$ -rays. However, there is not a consensus in the community about which of these two processes is the dominant one. In case that the  $\pi^0$  decay would be the dominant, it would point to the existence of hadronic accelerators and this would solve a part of the unknown of the origin of CR. In case that the inverse Compton process would be the dominant one, the leptonic acceleration processes would be favored, and this would mean that the origin of CR stays as an open issue.

### 2.3.6 Synchrotron radiation

When a charged particle moves through a transverse magnetic field, it generates photons. A non relativistic electron moving on a magnetic field will follow an helical path along the field lines (see Figure 2.7). The motion consists of two components, one being parallel to the field lines and the other being the rotation around the field line, that can be described by the angular frequency of the Larmor precession:

$$\omega_L = eB/m_e v \quad (2.10)$$

## 2.3 Gamma-ray production and absorption mechanisms

---

$B$  being the intensity of the magnetic field normal to the velocity vector  $v$  of the electron. The radiation emitted is equivalent to the one of a dipole with frequency  $\omega_L$ .

The relativistic scenario is a more complex one as the radiation gets beamed into a cone of angle  $\theta \simeq m_e c^2 / E$ . Now the emission will not happen in a single frequency but as a continuum spectrum where the maximum would be:

$$\omega_c = (3/2) (eB/m_e c) \gamma^2 \sin\phi \quad (2.11)$$

$\phi$  being the pitch angle between the direction of the magnetic field and the velocity vector of the electron. The emitted power distribution in the relativistic case is:

$$P(\omega/\omega_c) = 0.256 (\omega/\omega_c)^{1/3} \quad \text{for } \omega < \omega_c \quad (2.12)$$

$$P(\omega/\omega_c) = 1/16 (\pi \omega/\omega_c)^{1/2} e^{-2\omega/3\omega_c} \quad \text{for } \omega > \omega_c \quad (2.13)$$

### 2.3.7 Curvature radiation

The magnetic field in the magnetosphere of a pulsar is so huge that the electrons and positrons are constrained to move parallel to the magnetic field lines with almost zero pitch angle. As the field lines are curved the particles will radiate photons in the direction of their movement (see Figure 2.8), following the expression:

$$E_\gamma(eV) \approx \frac{3}{2} \frac{\hbar c \gamma^3}{\rho_c} = \frac{2.96 \times 10^{-5} \gamma^3}{\rho_c(cm)} \quad (2.14)$$

In the previous formula,  $\rho_c$  is the radius of curvature of the magnetic field line,  $\hbar = h/2\pi$  and  $\gamma = E_e/m_e c^2$ . This process is important in the environment of a pulsar for very high energy electrons and positron. As an example, a  $10^{13}$  eV electron moving along a field line with a curvature of  $10^8$  cm, typical for a pulsar, emits photons of energy  $\approx 1.5$  GeV.

In principle, the protons would also emit curvature radiation. But, as it happens with their bremsstrahlung  $\gamma$ -ray emission, the efficiency of this mechanism is very low due to the mass to charge ratio of the protons.

## 2.3 Gamma-ray production and absorption mechanisms

---

### 2.3.8 Black body emission and thermal bremsstrahlung

An optically thick body emits thermal radiation as a function of its temperature according to the well known Planck formula (see Figure 2.9):

$$I_{BB}(\nu)d\nu = \frac{2\pi h\nu^3}{c^2} \left[ \frac{1}{e^{(h\nu/kT)-1}} \right] \quad (2.15)$$

Where  $T$  is the temperature in Kelvin,  $h$  is the Planck constant, and  $k$  is Boltzmann constant. The photon number spectrum, i.e., the number of photons emitted per unit area of the source per unit time and per energy interval can be described by the following formula [RW93]:

$$N(E_\gamma) = 9.89 \times 10^{40} E_\gamma^2 \left[ \frac{1}{e^{1.16 \times 10^{10} E_\gamma/T} - 1} \right] \text{ ph cm}^{-2} \text{ s}^{-1} \text{ MeV}^{-1} \quad (2.16)$$

$E_\gamma$  is the energy of the  $\gamma$ -ray in MeV. One can determine, according to Wien's law, the energy corresponding to the maximum in the wavelength distribution. This would be the characteristic black body energy:

$$E_w(\text{MeV}) = 4.7 \times 10^{-10} T(K) \quad (2.17)$$

$T$  being the temperature in K. The average photon energy would be:

$$\langle E \rangle (\text{MeV}) = 2.7kT = 1.3 \times 10^{-10} T(K) \quad (2.18)$$

According to previous formulae, in order to have photons of energy higher than 1 MeV with an appreciable flux, temperatures of the order of  $10^{10}$  K are needed. These temperatures can only be achieved in the very early Universe and in explosive phenomena like GRB. With respect to the early Universe, however, it has to be noted that the cosmological red-shift will displace the photons energies to remarkably lower values.

The formulae 2.15 and 2.16 refer to a black body emission, that is an optically thick medium. For an optically thin medium, these equation have to be modified to take into account the absorption coefficient of photons in a hot plasma. The resulting spectrum of thermal bremsstrahlung can be approximate by:

$$N(E_\gamma) \propto \frac{n_e^2}{T^{1/2}} \frac{1}{E_\gamma} \exp(-E_\gamma/kT) \quad (2.19)$$

$n_e$  being the electron density in the plasma and  $T$  the temperature in K.

## 2.3 Gamma-ray production and absorption mechanisms

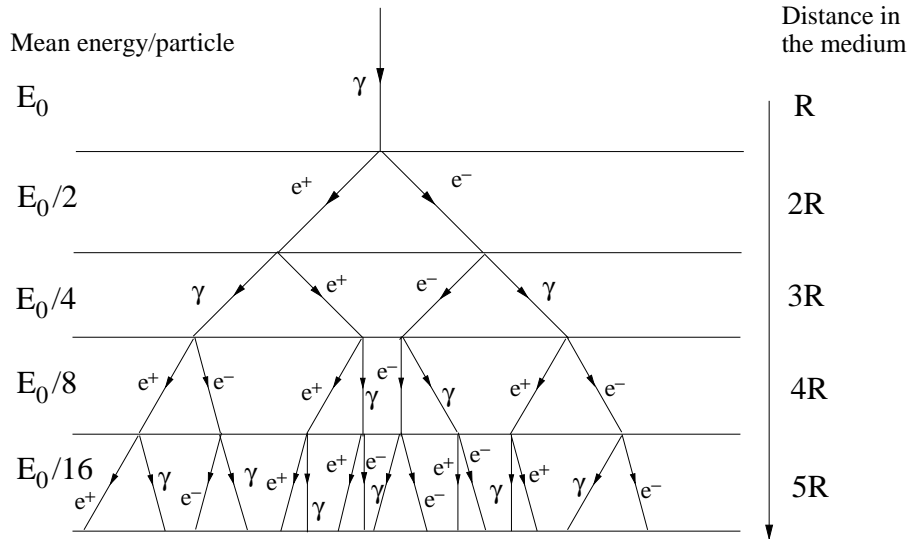


Figure 2.10: *Simplified scheme of an electron-photon cascade.*

### 2.3.9 Pair production

This mechanism plays a very important role in the energy loss processes for HE and VHE  $\gamma$ -rays. If a photon has energy higher than  $2m_e c^2$ , it may produce an electron-positron pair in the vicinity of a nucleus. The need of a nearby nucleus comes from the requirement of the conservation of the energy and momentum. In optically thick environments the pair production can create a shower development. A cascade or shower can be originated from a single photon, which originates an  $e^+ - e^-$  pair in the vicinity of a nucleus. These electrons and positrons emit later on a photon through a bremsstrahlung process, then this photon can originate another  $e^+ - e^-$  pair, and so on. When the electrons reach a certain energy, the cascade will stop growing, and the particles will lose their energy by ionization processes (see Figure 2.10).

The cross section for pair production rises with the photon energy, and becomes dominant above energies of  $\simeq 30$  MeV, after which reaches an asymptotic value, with a cross section of:

$$\sigma_{pp} = \sigma_0 Z^2 [(28/9) \ln(183/Z^{1/3}) - 2/27] \quad (2.20)$$

Where  $\sigma_0 = (1/137)(e^4/m_e c^4) = 0.58$  millibarn.

The pair production mechanism is used to detect  $\gamma$ -rays in HE pair-production telescopes (e.g. EGRET, *Fermi*).

## 2.4 Gamma-ray attenuation due to EBL

---

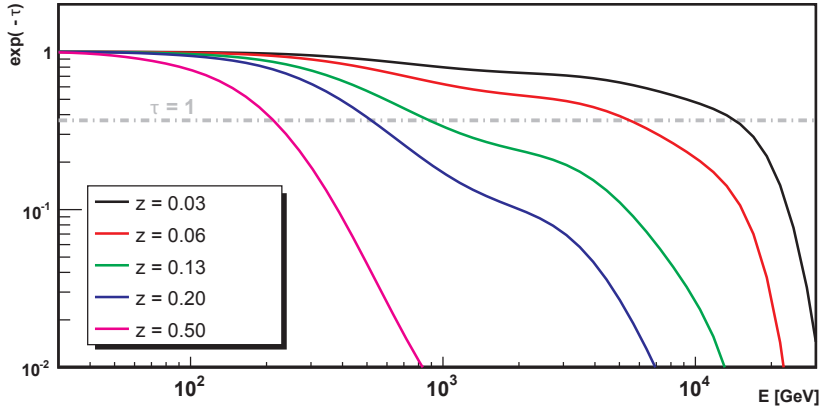


Figure 2.11: Representation of the attenuation coefficient as a function of the photon energy, for some values of  $z$ , according to the “lower limit” model of EBL density described in [KD08]. Relevant for this thesis are the curve of  $z=0.03$ , that represents approximately the attenuation for photons coming from the blazars Mrk 421 and Mrk 501 ( $z=0.030$  and  $z=0.034$ , respectively), and the curve of  $z=0.13$ , that represent the attenuation for photons coming from the blazar 1ES 1426+428 ( $z=0.129$ ). The horizontal dashed line represents the optical depth of  $\tau=1$ : for energies above the point where the attenuation curve crosses this line the Universe can be considered as opaque.

## 2.4 Gamma-ray attenuation due to EBL

The extragalactic background light (EBL) is a diffuse radiation field composed by low energy photons. This light has been created and integrated during the star and galaxy formation history of the Universe.

The EBL has three main components, the cosmic microwave background (CMB) radiation, the cosmic infrared background (CIB), and the cosmic optical background (COB). The radiation of the first component peaks at a wavelength of  $\simeq 1.9$  mm and it is a relic of the hot *Big Bang* fireball. The radiation of the second component peaks at  $\simeq 100$   $\mu\text{m}$ , and it is believed to be due to dust inside galaxies, that emits radiation after it has absorbed stellar light. The radiation of the third component peaks at  $\simeq 1$   $\mu\text{m}$ , and it is believed to be originated directly at stars.

When a VHE photon travels through the intergalactic medium, it may interact with an EBL photon through a pair-production process:

$$\gamma_{VHE} + \gamma_{EBL} \rightarrow e^+ e^- \quad \text{if} \quad E_{\gamma_{VHE}} E_{\gamma_{EBL}} > 2(m_e c^2)^2 \quad (2.21)$$

The relevant EBL wavelength range for the absorption of VHE  $\gamma$ -rays spans from UV light ( $0.1 \mu\text{m}$ ) to far-infrared (a few  $100 \mu\text{m}$ ).

It is possible to define an optical depth  $\tau_{\gamma\gamma}$  for VHE  $\gamma$ -rays, as a function of the redshift  $z$  and the energy of the  $\gamma$ -ray (see [DK05]). The  $\gamma$ -ray flux would be

## 2.4 Gamma-ray attenuation due to EBL

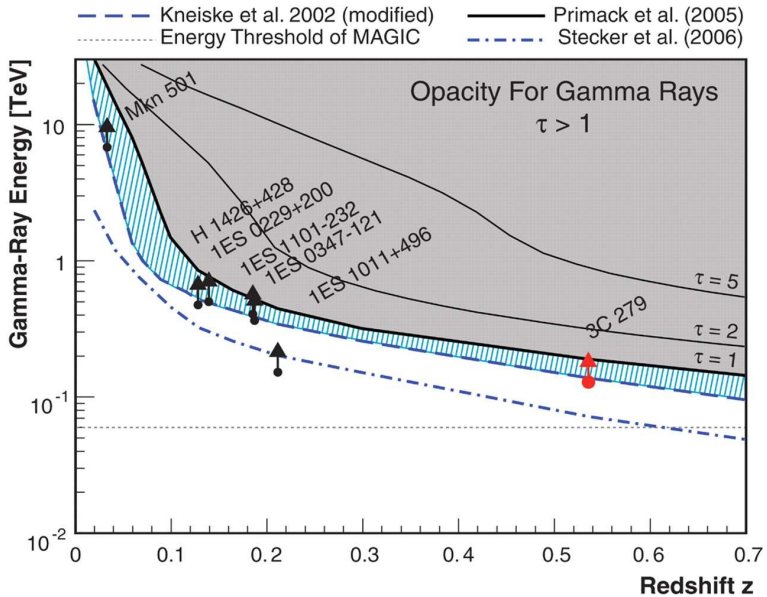


Figure 2.12:  $\gamma$ -ray horizon limits, according to upper limits from IACTs measurements, and lower limits from galaxy counts, from [Col08]. The narrow blue band describes the allowed region for the EBL. The lower EBL (solid black line) is given by [PBS05], that is nearly coincident with galaxy counts. The maximum EBL is given by a tuned model of [KMH02] based on the 3C 279 measurements [Col08], that assumes a limit on the spectral index of  $\geq 1.5$ , represented by the red arrow.

attenuated as the following:

$$F(E) = F_0(E) e^{-\tau_{\gamma\gamma}(E,z)} \quad (2.22)$$

$F(E)$  being the measured flux and  $F_0(E)$  the intrinsic flux. Figure 2.11 shows the representation of the attenuation factor  $\exp(-\tau_{\gamma\gamma}(E, z))$  for different values of  $z$ , according to the “lower limit” model described at [KD08]. From this figure it is evident that the attenuation plays an important role for sources with relative low  $z$ . For distant blazars, a low energy threshold for the VHE detector becomes of capital importance.

Different methods have been proposed to describe the EBL density. Models like the one by Primack et al. [PBS05, PGS08], calculate the EBL density and its redshift dependence assuming parametrizations of the evolution of the stellar populations and the resulting emission spectra of galaxies. In this model, the predicted luminosity function for different galaxy types is in agreement with the observed luminosities. On the other hand, other models like the one from Stecker et al. [SMS06] and Franceschini et al. [FRV08] use the opposite approach, that consists in the measuring of the actual galaxy distributions and the derivation of a backwards evolution, in order to determine the EBL density. Finally, models like

## 2.4 Gamma-ray attenuation due to EBL

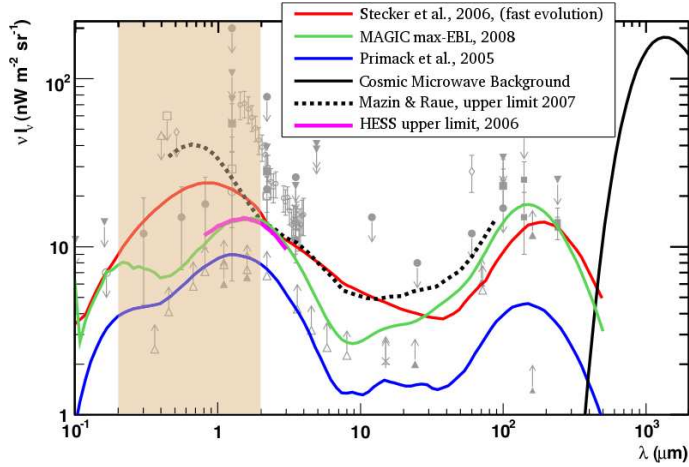


Figure 2.13: Some models for EBL, for  $z=0$ , together with measurements and limits of direct observation, in various wavelengths. The red line represents the model [SMS06], the green line is from [Col08] based in the model by [KMH02], the blue line represents the model by [PBS05]. The dotted line is derived from the combined analysis of 13 blazars ([MR07]). The pink line represents the upper limit from the measurement of H.E.S.S. of 1ES 1101-232 and H 2356-309 [AAB06]. The shaded vertical band indicates the range of frequencies where MAGIC is most sensitive.

the previously mentioned model by Kneiske et al. [KMH02, KBM04, KD08], make use of the existing cosmological data (galaxy counts, redshift distributions and luminosity functions), together with a backwards evolution model.

The EBL affects the VHE  $\gamma$ -rays observations of distant sources, but, in the other hand, these VHE observations can be useful to derive constraints of the EBL density. The differential spectrum of blazars are often well described by a simple power law in the form of:

$$dF/dE = F_0(E/r)^{-\Gamma} \quad (2.23)$$

where  $r$  is the normalization energy,  $F_0$  is the flux at the normalization point, and  $\Gamma$  is the spectral index.

The idea to limit the EBL density relies in the theoretical prediction from leptonic models that the intrinsic spectral index  $\Gamma$  cannot be harder than 1.5 (see [Aha01a] for details). The observational facts support the previous assumption: none of the EGRET measurements (not affected by the EBL) of blazars, or the VHE observations of the nearby blazars like Mrk 421 or Mrk 501 (modestly absorbed) have never shown an index harder than 1.5. This assumption was used in [Col08] to constrain the magnitude of the  $\gamma$ -ray horizon (see Figure 2.12), defined as the source redshift for which the optical depth is  $\tau(E, z)=1$ . In the mentioned article an upper limit on the density of the EBL also derived (see Figure 2.13).

## 2.5 VHE gamma-ray sources

---

It has been argued, however, that the assumed limit on the spectral index  $\Gamma$  for the source 3C279 could be too strict. Being a Flat Spectrum Radio Quasar (FSRQ), it shows intense optical emission lines (from the broad line regions, see later), and suggest a possible internal absorption of the intrinsic emission, what means that a harder value of  $\Gamma$  cannot be discarded (see [Maz08] and references therein for further details). In addition, some authors [KGTe06] have described a scenario where a narrow distribution of relativistic electrons, that causes the VHE emission due to IC scattering, is able to produce an intrinsic spectral index as hard as  $\Gamma = 0.7$ . These arguments suggest that the real limits on the density of the EBL and  $\gamma$ -ray horizon could be different from the ones calculated in [Col08].

## 2.5 VHE gamma-ray sources

With more than 100 sources of different origin firmly detected, the VHE sky is a more complex and rich scenario than it was originally thought. In this section, the most important *a priori* targets for ground based Cherenkov telescopes will be described.

### 2.5.1 Active galactic nuclei

AGN are compact extragalactic objects that emit very luminous electromagnetic radiation. They are divided in two types: those that have intense radio emission and those that don't have it. The radio-loud AGN are the ones that also emit VHE  $\gamma$ -rays. For both types, the assumed paradigm considers that a central massive black hole (MBH) is the power engine of the whole system. Gas from the galaxy's interstellar medium, from a cannibalized galaxy, or from a star that stays too close, falls onto the MBH. The gravitational attraction of the MBH forms an accretion disk. In the case of radio loud AGN, two jets are formed of particles moving with ultra-relativistic speeds, perpendicular to the plane of the accretion disk, emitting huge amounts of light across the electromagnetic spectrum. The source population consists of several different type of galaxies with substantially observational different characteristics, but the main concept of the AGN assumes that the differences on these types depends basically on the random pointing direction of the object with respect to the observer and not on intrinsic physical properties [UP95]. One popular sketch of the physical structure and the type of AGN depending on the line of sight is shown in Figure 2.14. The sources whose jet is pointing close to the line of sight to the observer are the so-called blazars, one of the best known and frequent VHE  $\gamma$ -ray emitters. Also radio galaxies, whose jet is not pointing to us can be VHE emitters when they are close enough like M 87 and Centaurus A (see e.g. [The09b]). AGN will be further described in Chapter 3.

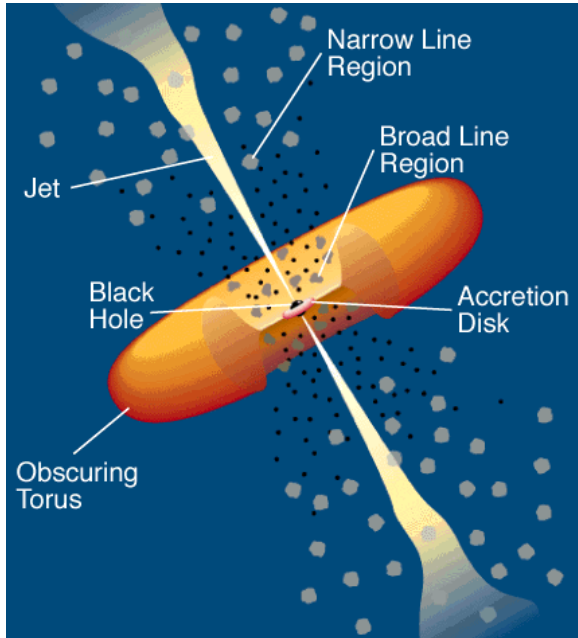


Figure 2.14: Schematic illustration of the current paradigm of radio loud AGN. In the center of the system there is a super-massive black hole of  $10^6$ – $10^{10} M_\odot$  whose gravitational potential energy powers the whole system. This energy can be released as non-thermal emission of ultra-relativistic jets or by thermal emission of the accretion disk. The jet extends well beyond the host galaxy. The accelerated particles interact with the ambient photons and magnetic fields, what produces non-thermal emission of electromagnetic radiation. Broad emission lines are produced in clouds orbiting around the accretion disk. The accretion disk and the broad-line region are surrounded by a thick dusty torus. Narrow emission lines are produced in clouds that are located much farther away from the central engine. Adapted from [UP95].

### 2.5.2 Gamma-ray burst

Gamma-ray bursts are brief events, extremely luminous in  $\gamma$ -rays. When a GRB occurs it outshines any other  $\gamma$ -ray source, including the Sun. These events occur at a rate of about one per day and it is believed that they are the most concentrated and brightest explosions in the Universe.

GRBs were first detected in 1967 by the Vela satellites [KSO73], during their routine search of  $\gamma$ -ray emission from nuclear weapon explosions that could violate the *Nuclear Test Ban Treaty*. For long time, they were undetected at any wavelengths other than  $\gamma$ -rays, which provided poor directional information and hence no direct clues about their site of origin. The Beppo-SAX satellite succeeded in detecting them in X-rays in 1997 [Cos97], which allowed to find accurate positions for large ground-based telescope follow-up observations on optical and other wavelengths. This allowed the possibility to measure the redshift distances,

## 2.5 VHE gamma-ray sources

---

the identification of candidate host galaxies, and the confirmation that they were indeed at cosmological distances. Their extragalactic origin was confirmed by further multi-wavelength observations.

GRBs are very distant sources, as distant as the most distant known quasars (up to Gigaparsecs), but even at these extreme distances, when they occur, for the brief time they exist, they outshine galaxies and quasars by a very large factor. This obviously means that their energies must be huge. In case of isotropic emission, their electromagnetic energy output during tens of seconds is estimated to be from  $\sim 5 \times 10^{51}$  erg to  $\sim 3 \times 10^{54}$  erg, comparable to the energy of the Sun over the approximate age of the Universe, or to the energy of our entire Galaxy over a few years. GRBs are thought to be highly focused explosions: Taking this effect into account, their energy release would be comparable to the energy released in a supernova ( $\sim 10^{51}$  erg).

The current interpretation of how GRBs are able to produce and release such prodigious energy is that a correspondingly large amount of gravitational energy (equivalent roughly to a solar rest mass) is released in a very short time (seconds or less) in a very small region (about tens of kilometers) by a cataclysmic stellar event (the collapse of the core of a massive star, or the merging of two remnant compact cores). Most of the energy would escape in the first few seconds as thermal neutrinos, while another substantial fraction might be emitted as gravitational waves. This sudden energy liberation would result in a very high temperature fireball ( $kT \geq$  MeV) consisting of  $e^\pm$ ,  $\gamma$ -rays (emitted through the processes explained in section 2.3.8) and baryons, moving at highly relativistic speeds. The fireball is transparent to the gravitational waves, and after several interaction lengths, also to neutrinos. This leads to the prompt emission (on timescales of a few seconds) of roughly comparable energy amounts (several times  $10^{53}$  ergs) of thermal  $\nu_e \bar{\nu}_e$  with typical energies 10–30 MeV, and of gravitational waves mainly near  $10^2 - 10^3$  Hz. These last two energy forms would be by far the dominant ones, but they have not been detected yet.

The above described fireball would later develop into a blast wave as it decelerates against the external medium, producing an afterglow which gets progressively weaker. The resulting electromagnetic energy emitted appears to be of the order of a percent or less of the total energy output, but even this photon output (in  $\gamma$ -rays) is comparable to the total kinetic energy output leading to optical photons by a supernova over weeks. For further details on the theoretical models of GRBs see, e.g., the review article by [Mes06]. The remarkable thing about this theoretical scenario is that it is able to successfully predict many of the observed properties of the bursts. This fireball shock scenario have been extensively tested against observations, and has become the leading paradigm for the current understanding of GRB.

The HE  $\gamma$ -ray emission of GRB was first detected by EGRET CGRO [Som94]. Emission above 100 MeV was detected for a few of distinct cases (see, e.g.,

## 2.5 VHE gamma-ray sources

---

[Som94]). The Large Area Telescope (LAT) on the *Fermi* Gamma-ray Space Telescope observatory, working together with the the Gamma-ray Burst Monitor (GBM), that is the other instrument on-board the mission, has provided recent observations of GRBs in the HE regime (see, e.g. [Bou08] for a brief summary).

Any hypothetical GRB emission in the TeV range should be restricted to rare, close-by events, due to the attenuation of VHE  $\gamma$ -rays by the EBL. VHE emission of GRBs has only been reported by weak evidences like the  $3\sigma$  level for GRB970417a, reported with the water Cherenkov detector *Milagrito* [Atk00]. Another possible TeV detection of GRB971110 has been reported with the GRAND array, at the  $2.7\sigma$  level [Poi03]. Stacking of data from the TIBET array for a large number of GRB time windows has led to an estimate of a  $7\sigma$  composite detection significance [Ama02]. The observations of nine different GRBs (among others: GRB0507013a, 40 s after the burst original time, and GRB050904, 160 s after the burst original time) by the MAGIC telescope only allowed to derive upper limits to their emission [Alb07b].

### 2.5.3 Pulsars

Pulsars are believed to be neutron stars that have a very intense magnetic field, and emit pulsed electromagnetic radiation. The first pulsar detected, PSR 1919+21, was discovered in 1967 by a radio detection. Pulsars may emit in the whole electromagnetic radiation spectrum, even if not all pulsars have been detected to emit in all energy wavelengths. The best known pulsar, and of capital importance for the VHE  $\gamma$ -ray astronomy, is the one located in the first object of the Messier catalog (M1), and better known as the Crab Nebula.

The emission of the pulsar below the GeV energies is explained by the magnetohydrodynamic model from [RG74], and is believed to come from the rotational energy of the pulsar. This model was further developed in [KC84a, KC84b]. It is believed that HE  $\gamma$ -ray emission of a pulsar may come from three different regions. These three regions are the pulsar magnetosphere, the unshocked relativistic wind, and the synchrotron nebula (see Figure 2.15).

The pulsar provides a continuous flow of charged particles moving at ultra-relativistic speeds (Lorentz factors from  $10^6$  to  $10^7$ ), called pulsar wind. A stable shock front is created where the wind pressure is balanced to the total pressure of the surrounding pulsar wind nebula (PWN) or *plerion*. The particles in the wind are accelerated to ultra-relativistic speeds, to energies up to 100 TeV. The particles loose their energy by synchrotron emission. This emission takes place up to an energy of few hundred MeV. Above 1 GeV, it is believed that the dominant source of  $\gamma$ -ray emission is the IC scattering of synchrotron photons by electrons (the same ones that produce the synchrotron radiation in the shocked wind region, for details see, e.g. [dH92]). To explain the observed VHE  $\gamma$ -ray spectrum, some extra seed photon are believed to contribute to the inverse Compton scattering.

## 2.5 VHE gamma-ray sources

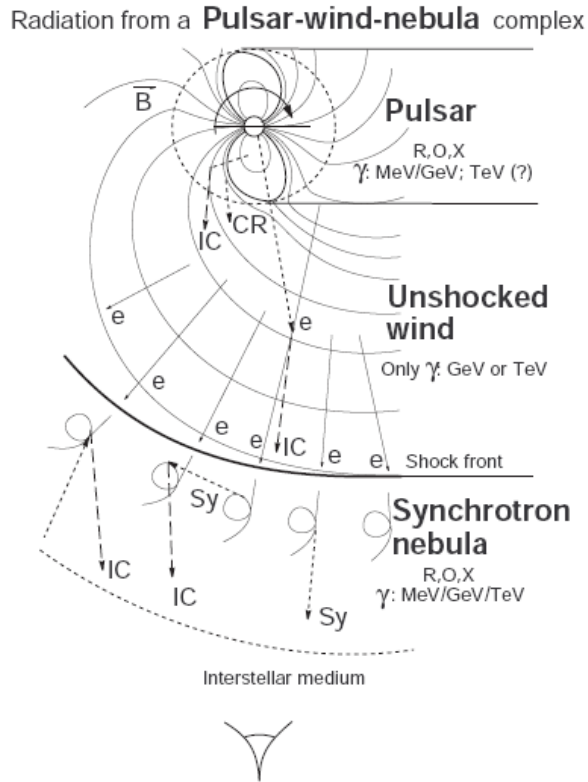


Figure 2.15: *Schematic illustration of the three regions that may emit non-thermal HE and VHE  $\gamma$ -rays in the proximity of a pulsar (from [AB03]). Pulsar: The closest region to the central neutron star, where magnetospheric pulsed radiation of all wavelengths (from radio to  $\gamma$ -rays) is produced, mainly from synchrotron and curvature radiation. Unshocked wind region: The part of the wind of cold relativistic plasma, close to the previous region, which effectively emits GeV and TeV  $\gamma$ -rays through the IC mechanism. Synchrotron Nebula: The surrounding synchrotron nebula, called plerion, which emits broad-band electromagnetic radiation from radio to TeV through the synchrotron and IC processes.*

The seed photons could be far-infrared excess, the cosmic microwave background, and millimeter-photons (see, e.g., [Aha04b]). The first detected VHE source was the Crab Nebula, a PWN [Wee89].

The VHE pulsed emission is reasonably well described by the IC scenario, but it is possible that other processes may contribute to this emission. Processes in the wind that produce hadronic showers and subsequent  $\gamma$ -ray emission from the  $\pi^0$  decays (see section 2.3.3), would modify significantly the VHE spectrum (see, e.g., [BB03]). Other possibilities to explain the fluxes at GeV energies are an *amplified* bremsstrahlung flux from electrons that are trapped, at least partially, in a high density gas of dense filaments (see, e.g., [AA96]) and the presence of IC scattering by relativistic electrons in the unshocked pulsar wind [BA00].

## 2.5 VHE gamma-ray sources

---

The origin of the high energy radiation from the pulsar magnetosphere is believed to be synchrotron (see section 2.3.6) and curvature radiation (see section 2.3.7) from charged particles accelerated by the pulsar. It is not yet clear if the emission occurs close to the neutron star (polar cap model, see, e.g., [RS76]) or farther in the magnetosphere (slot-gap [AS79] and outer gap models [CHR86]). The detection of pulsed emission from the Crab Nebula up to 60 GeV by the MAGIC experiment [Ali08] favours the slot-gap and outer-gap models, as well as recent *Fermi* [Tt10] measurements do.

### 2.5.4 Supernova remnants

Supernova remnants can be classified into two broad categories: *plerionic* (that are the PWN explained in previous section) and *shell-like*. Here the latter type of SNR will be discussed. In *shell-like* SNR, the shock wave from the supernova explosion plows through space, heating any interstellar material it encounters, thus producing a big shell of hot material. There is not a hard distinction between these two types, and therefore a *composite* type exists, in which both a shell and a plerion are present. For example SNR G 0.9+0.1 shows a bright compact core surrounded by a shell [Aha05c].

It is believed that diffusive shock processes that are originated during supernova explosions are the source for the major population of galactic CRs (see, e.g., [Dur83]). The VHE emission from SNRs is often explained as coming from inelastic collisions of the CRs with the ambient matter of the shell, producing  $\gamma$ -ray and neutrinos through hadronic showers and  $\pi^0$  decay (see section 2.3.3).

VHE  $\gamma$ -ray flux coming from eight *shell-like* remnants was known when this thesis was written. The location of some of these sources in space positions of high density environments, like large molecular clouds and OH maser emissions e.g., SR IC443, see Figure 2.16, first detected in VHE by MAGIC [Alb07a] and the SNR detected by H.E.S.S.: HESS J1834-087 and HESS J1813-178 [Aha06a] (also detected by MAGIC), support the hadronic hypothesis for the origin of  $\gamma$ -rays. Other mechanisms like IC scattering of ambient photons by accelerated electrons (see section 2.3.5) may contribute significantly to the observed VHE flux as well.

### 2.5.5 The Galactic Center

The region of the Galactic Center (GC) contains an important quantity of objects which are candidates to be  $\gamma$ -ray emitters (see [AN05]). Among others, the compact radio source *SgrA\**, which is believed to be a super-massive black hole that acts as the dynamical center of the Galaxy, is located there.

The GC has been observed in VHE  $\gamma$ -rays by all the contemporaneous IACT experiments: VERITAS [Kos04], CANGAROO [Tsu04], H.E.S.S. [Aha04c] (see

## 2.5 VHE gamma-ray sources

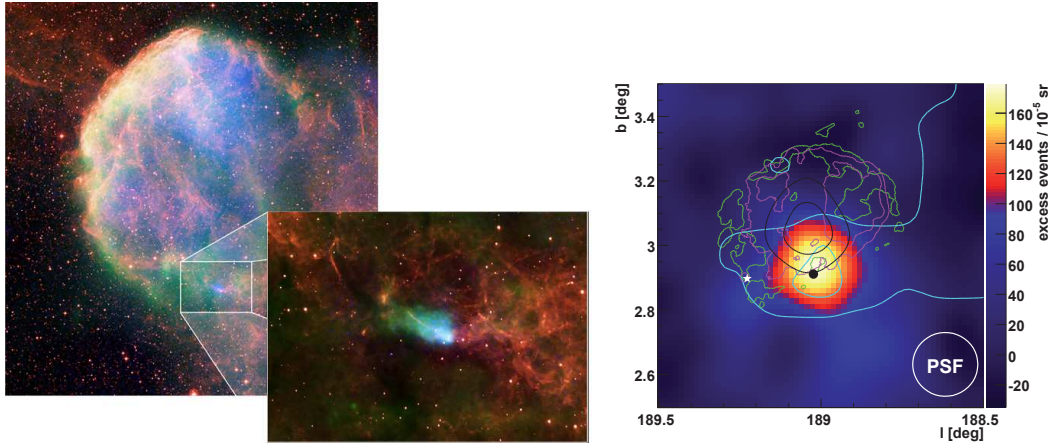


Figure 2.16: *Left:* Composite image from the SR IC 443, from Chandra X-ray observatory webpage (<http://chandra.harvard.edu/>). The wide field image is composed by X-ray observations (in blue) by ROSAT and Chandra, radio (in green) from the Very Large Array, and optical (in red) from the Digitized Sky Survey. The image of the zoomed region (a composite with a Chandra x-ray close-up) shows how the neutron star is expelling HE particles. (Credit: Chandra X-ray: NASA/CXC/B.Gaensler et al; ROSAT X-ray: NASA/ROSAT/Asaoka & Aschenbach; Radio Wide: NRC/DRAO/D.Leahy; Radio Detail: NRAO/VLA; Optical: DSS). *Right:* Sky map of VHE  $\gamma$ -ray candidate events (background subtracted) in the direction of MAGIC J0616+225 for an energy threshold of about 150 GeV (galactic coordinates), from [Alb07a]. Overlayed are  $^{12}\text{CO}$  emission contours (cyan), contours of 20 cm VLA radio data (green), X-ray contours from ROSAT (purple) and  $\gamma$ -ray contours from EGRET (black). The white star denotes the position of the pulsar CXOU J061705.3+222127. The black dot shows the position of the 1720 MHz OH maser. The white circle shows the MAGIC PSF of = 0.1°.

Figure 2.18), and MAGIC [Alb06a] (see Figure 2.17). The observed flux, of the level of 15% of the Crab Nebula, is rather steady in a time scale of years.

It is not yet clear what is the origin of these VHE  $\gamma$ -rays. The most likely source would be  $\text{Sgr A}^*$ , that could be producing a jet similar to those that are produced by blazars [FMB93]. However, the unfavourable orientation of this hypothetical jet would produce a VHE  $\gamma$ -ray flux relatively low compared to the observed one, and on the other hand, variable in short-term scales. Among other possibilities considered, electrons may accelerate to high energies at the end shock produced due to the accretion flow into the super-massive black hole [AD04].

Apart from the possible emission mechanism caused by  $\text{Sgr A}^*$ , the long list of possible candidates to emit  $\gamma$ -rays are young SNRs like Sgr A East, massive stellar clusters (composed by dozens of OB type stars surrounded by dense gas), and non-thermal radio arcs.

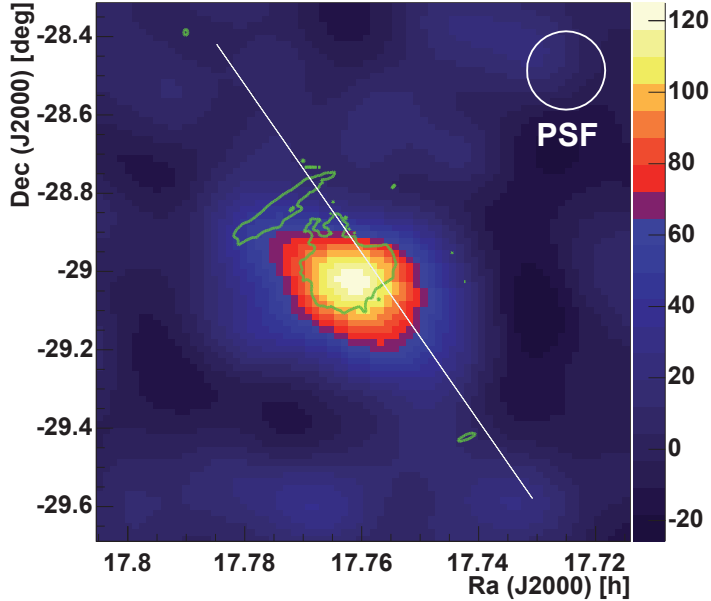


Figure 2.17: Smoothed sky map of VHE  $\gamma$ -ray candidates (background subtracted) in the direction of the Galactic Center, from [Alb06a]. Overlayed are green contours of radio data. The white line shows the Galactic Plane. The MAGIC  $\gamma$ -ray PSF ( $0.1^\circ$ ) is also shown.

### 2.5.6 $\gamma$ -ray binary systems

$\gamma$ -ray binary systems have two objects of several solar masses gravitationally bound, where one compact object accretes matter from a massive star. These objects are often called X-ray binary systems, as they are among the brightest X-ray sources in the Galaxy. X-rays are emitted when matter falls from the star to the compact object. The accreting object is either a neutron star or a black hole of few solar masses. Four of these sources have been firmly detected in the VHE range: LS 5039, detected by H.E.S.S [Aha05b], PSR B1259-63, also detected by H.E.S.S. [Aha05a], LS I+61 303, detected by MAGIC [Alb06b], and Cygnus X-1, also detected by MAGIC [Alb07f].

In these systems particles could be accelerated up to very high energies. There are two scenarios that predict VHE  $\gamma$ -ray emission from these sources. One model assumes that these systems may behave as AGN's do, but in a much smaller scale. Here, it is believed that the accretion disks and jets are created in the same way as they are created in the compact object in the center of the host galaxies of AGN. In the same way as it happens in blazars, these objects would emit VHE  $\gamma$ -rays. These objects are so called *micro-quasars* (see [Bos06] for more details). In the other scenario, the emission is produced in a system composed of a pulsar

## 2.5 VHE gamma-ray sources

---

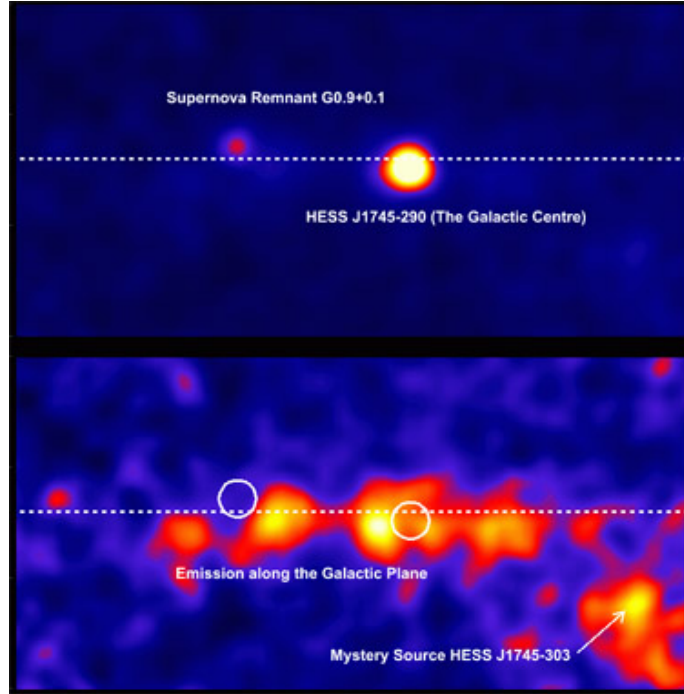


Figure 2.18: *VHE  $\gamma$ -ray emission from the region around the GC, as measured by the H.E.S.S. experiment [Aha06b].* The top panel shows the  $\gamma$ -ray image of the GC region. Two bright sources dominate the view: HESS J1745-290, what corresponds to the location of the hypothetical super-massive black hole that acts as the dynamical center of the Galaxy; about 1 degree away, the gamma-ray supernova remnant G 0.9+0.1. The lower panel shows the same image with the bright sources subtracted, where a band of  $\gamma$ -ray emission emerges, tracing the Galactic Plane. Below the Plane, the additional source HESS J1745-303 is visible.

and massive star, where the  $\gamma$ -rays are generated in the shock due to the pulsar wind interacting with the massive companion [MT81].

As an example of this kind of sources, LS I +61 303, has been well studied by MAGIC (see [Alb06b], [Alb09] and [And09a]), and by VERITAS [Acc08]. *Fermi* has also observed this source [Abd09a], finding a cutoff on the emission at  $6.3 \pm 1.1(\text{stat}) \pm 0.4(\text{syst})$  GeV. Moreover, the orbital phase of maximum emission in the HE range is close to periastron, what hints at inverse Compton scattering as the main radiation mechanism. However, previous VHE  $\gamma$ -ray observations by MAGIC show peak emission close to apastron, as well as VERITAS observations do. This together with the energy cutoff seen with *Fermi* suggest the link between HE and VHE  $\gamma$ -rays is a rather complicated one.

### 2.5.7 Other sources

Some other type of sources, apart from those listed above, are confirmed or candidates to be VHE radiation emitters.

Starburst galaxies are those that exhibit an enhanced and strongly localized supernova explosion rate, in regions called starburst regions. In these regions the gas and proton densities are very high. Therefore, due to the acceleration caused by the high density of expected SNRs, a high density of CRs is expected, and consequently,  $\gamma$ -ray emission due to  $\pi^0$  decay (see section 2.3.3). A VHE  $\gamma$ -ray detection of  $11\sigma$  confidence level from NGC 253 was claimed by the CANGAROO experiment ([Ito02]). Nevertheless the H.E.S.S. array, a detector with much better sensitivity, was able to detect this source with a much worse statistical significance ( $5.2\sigma$ ) after 119 hours of good quality data observation [Ace09]. A  $4.8\sigma$  detection of another starburst galaxy, M82, was reported recently by the VERITAS collaboration [The09a], confirming the starburst galaxies as VHE  $\gamma$ -ray emitters.

In the context of the search for non barionic dark matter (DM), one of the best candidates to observe are the Dwarf spheroidal galaxies (dSphs). These galaxies are found orbiting larger galaxies, and according to the dynamics of the stars they contain, it is believed they contain large DM halos with masses between  $10^5 M_\odot$  and  $10^8 M_\odot$ . The massive, weakly interacting particle predicted by Super-Symmetric (SUSY) theories beyond the Standard Model, as the *neutralino*, are one of the best candidates to be component of this hypothetical DM halo. The way to detect these particles is through the  $\gamma$ -rays produced after neutralino annihilation. The various observation in the VHE range by different experiments (MAGIC observed Draco [Alb08e] and Willman 1 [Ali09b], Whipple observed Draco and UMi [Woo08], and H.E.S.S. observed Sagittarius [Aha08]) have not given evidence of DM originated emission. However, these observations do not have enough sensitivity to rule out any SUSY parameter space region.

Clusters of galaxies are also good candidates for VHE  $\gamma$ -ray emission. These objects are the largest gravitational bound systems known in the Universe, having few Mpc radii and masses around  $10^{15} M_\odot$ . The cosmic rays accelerated in the clusters would be confined there during cosmological times, therefore improving the possibilities of inelastic proton-proton collisions that create  $\gamma$ -rays from  $\pi^0$  decays. On the other hand, large scale shocks associated with the formation of large scale structures in the Universe could be the cause of electron acceleration up to VHEs, and after interaction with the CMB photons by inverse Compton scattering to create VHE  $\gamma$ -rays. More details of these mechanisms can be found in [BGB07]. These objects could be also targets for VHE emission coming from DM annihilation. No emission has been yet detected in  $\gamma$ -rays from clusters of Galaxies. (see, e.g., the upper limits for the VHE emission from MAGIC

## 2.6 Detectors

---

observation [And10]). The results from MAGIC are compatible with cosmological cluster simulations for the cosmic ray induced  $\gamma$ -ray emission.

Finally, globular clusters are a receptacle of a large content of evolved objects like millisecond pulsars. Some models (e.g. [BS07]) predict VHE  $\gamma$ -ray emission due to this population of pulsars and the acceleration of leptons in their surroundings. These leptons would accelerate photons (from the CMB or from the thermal emission of dense clusters of stars) through inverse Compton scattering up to high energies. Globular clusters have been observed by Cherenkov telescopes: Whipple and MAGIC observed M13 ([Hal03] and [And06]) VERITAS observed M15 ([LeB03]), CANGAROO  $\omega$  Centauro [Kab07] and H.E.S.S. Tuc 47 ([Aha09a]). No significant VHE emission in any of these observations was found, meaning that either millisecond pulsars are fewer than expected or they accelerate leptons less efficiently than predicted. On the other hand, *Fermi* was able to detect HE emission from Tuc 47 [Gui09], confirming the globular clusters as HE  $\gamma$ -ray sources.

## 2.6 Detectors

Earth's atmosphere is opaque to  $\gamma$ -ray photons. Even at high mountains, the  $\gamma$ -ray rate is negligible. Therefore, the only way to directly detect primary  $\gamma$ -ray photons is at high altitudes, with satellites and balloons. On the other hand, ground detectors are able to take advantage of the  $\gamma$  absorption and reconstruct the primary  $\gamma$ -ray characteristics from the products of its interaction with the atmosphere.

### 2.6.1 Satellites and balloons

As it has been previously said, the only way to detect primary  $\gamma$ -rays is by detectors located in balloons or satellites. These detectors use techniques similar to those of particle physics.

The first  $\gamma$ -ray measurements from a satellite were obtained by OSO-3 in 1963 [CGK68]. It detected an emission of 100 MeV from the Galactic Plane, whose flux was close to the expected one from the interaction of cosmic rays with the galactic interstellar gas. The  $\gamma$ -ray instrument was composed of a multilayer scintillation detector and an energy detector containing several layers of NaI, “sandwiched” by layers of tungsten.

This discipline experimented a big advance in the decade of the 70s thanks to both the detection in 1971 of pulsed high energy  $\gamma$ -ray emission from the Crab Pulsar by a telescope in a balloon [BRW71] and to the results obtained by two new satellites: SAS-2 [Fic75] and COS-B [Big75]. These detectors used the following technique: When a photon impacts the detector, a positron-electron

## 2.6 Detectors

---

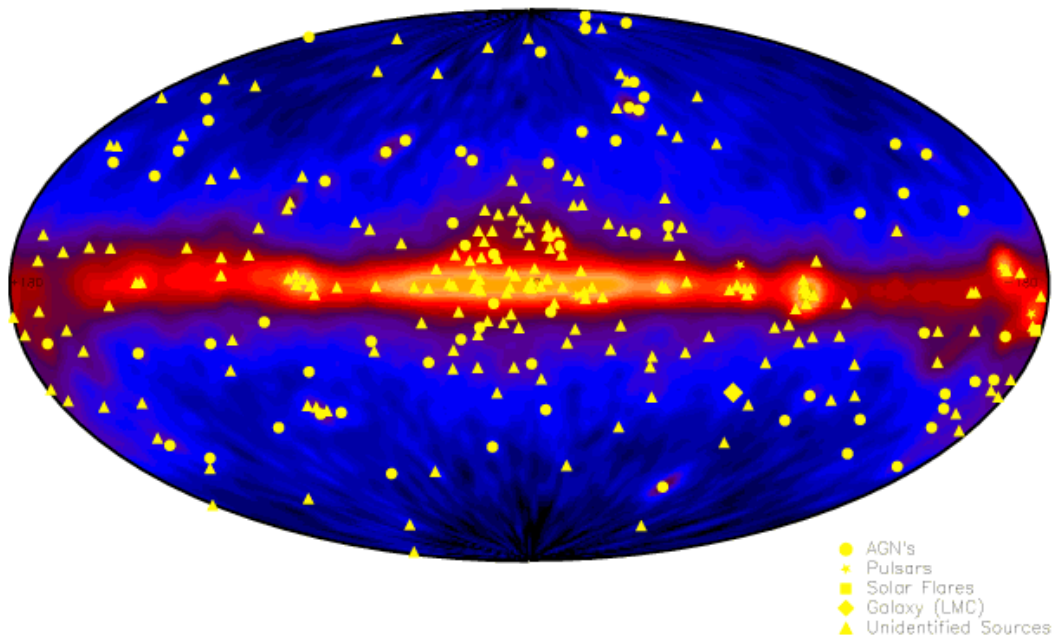


Figure 2.19: *The sky as seen by EGRET, shown in Galactic coordinates. In this false color image, the Galactic Center lies in the middle of the image. From <http://heasarc.gsfc.nasa.gov>.*

pair is created. The direction of the photon is determined by the trajectory of the generated positron electron pair. The energy is determined by total absorption calorimeters. A thin layer of scintillator material is used to suppress the charged particles background, working in anti-coincidence mode.

The Compton Gamma Ray Observatory (CGRO) was launched in April 1991 and was operative until June 2000. This observatory carried four detectors, each one with its own energy range (from 15 keV to 30 GeV). This satellite achieved many interesting results (see, e.g. [Sch01] for a review). The detector of higher energies carried by CGRO was EGRET, that used the same technique as SAS-2 and COS-B detectors, but with a much larger collection area ( $\simeq 1500 \text{ cm}^2$ ). It had a working energy range between 30 MeV and 30 GeV. This satellite made a detailed sky map, discovering 271 sources out of which 7 pulsars and 50 AGN (see [Tho08] for a detailed review of EGRET results).

## 2.6 Detectors

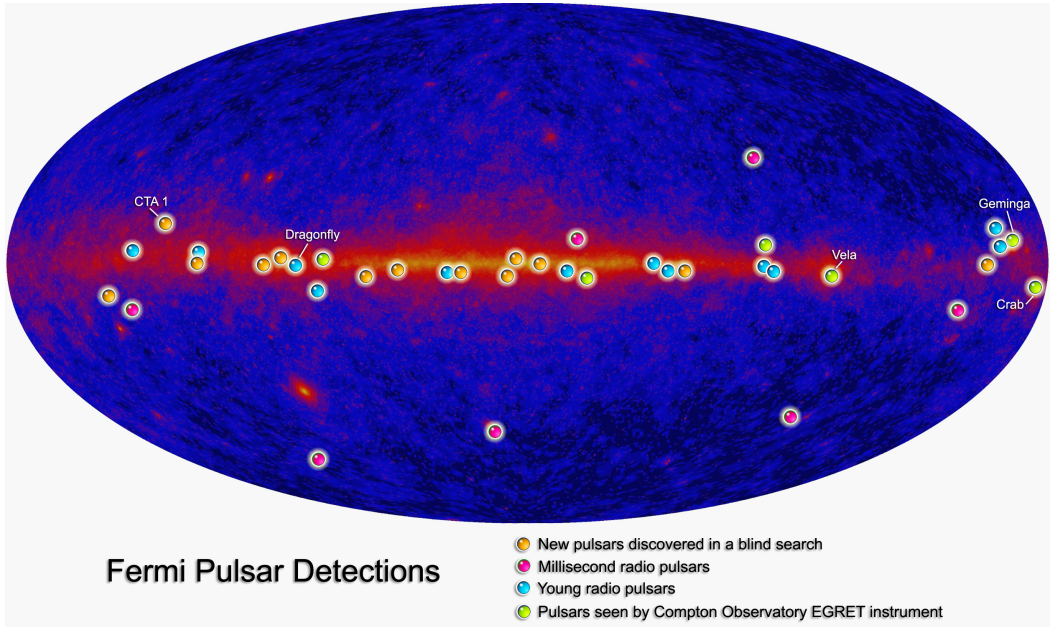


Figure 2.20: *Image on false colours of the sky as seen by Fermi Gamma-ray Space Telescope, were the detection of pulsars are highlighted. The image shows 12 previously unknown pulsars (orange), detected  $\gamma$ -ray emission from known radio pulsars (magenta, cyan) and from known or suspected  $\gamma$ -ray pulsars identified by CGRO.* Credit: NASA/Fermi/LAT Collaboration.

More recently, the INTEGRAL satellite was launched on 2002, and it is still active. This satellite works with LE  $\gamma$ -rays, from 15 keV to 10 MeV. Apart from the  $\gamma$ -rays, it is able to measure optical light, therefore it can help to identify the object emitting the  $\gamma$ -rays (for example, when there is correlated variability in both energy bands). It has two  $\gamma$ -ray instruments: IBIS and SPI. The IBIS detector uses two parallel planes of pixels located one on top of the other, one being able to detect lower energy  $\gamma$ -rays, and the other higher energy ones. The division into two layers allows to track the paths of the photons in 3D, as they scatter and interact with more than one element. It is complemented with the SPI (Spectrometer on INTEGRAL), that is able to make accurate  $\gamma$ -ray energies measurements. SPI uses 19 hexagonal high purity germanium detectors cooled down to a temperature of 85 K. An additional objective of this detector is to study GRBs.

The latest incorporation to the  $\gamma$ -ray satellites is *Fermi*. It was launched on June 2008, and started to take data on August 2008. Its main instrument is the LAT, a pair production detector that operates from 20 MeV to  $\simeq$  300 GeV [Atw09]. It has also a gamma ray burst monitor [Bou08]. First *Fermi* source catalogs have been recently published or are in preparation (e.g, pulsar catalog [Abd09b]). For the time being more than 1400 sources have been detected with *Fermi*. According to simulations, it is expected that it will detect several

## 2.6 Detectors

---

thousands of new sources during its lifetime. *Fermi* LAT detector uses the same technique as used by SAS-2, COS-B and EGRET.

### 2.6.2 Ground based detectors

Due to the very low  $\gamma$ -ray flux at VHE and the small collection areas at satellites ( $\leq 1 \text{ m}^2$ ), ground based detectors are the only ones capable to study emitters on this energy band (due to their large effective collection areas of  $\sim 10^5 \text{ m}^2$ ). Even if the atmospheric absorption prevents the gamma rays photons from reaching the detector, their interaction with the atoms of the atmosphere create a huge number of secondary particles, that allow to detect indirectly the primary incident photon. These secondary particles are named *extensive air showers* (EAS). The ground based detectors measure these EAS. The main problem of these detectors is the very large charged cosmic ray background. Cosmic rays also create EAS that are difficult to distinguish from the ones generated by  $\gamma$ -rays. The detection capability of these instruments improves when located at medium-high altitudes, where they can measure weak showers from the least energetic photons of the VHE range.

EAS can be identified in two ways: by detecting the shower particles ( $e^+$ ,  $e^-$ ,  $\gamma$ ) or the Cherenkov radiation produced by the shower. Therefore, there are two type of detectors: particle and Cherenkov detectors.

#### 2.6.2.1 Particle and secondary photon detectors

These types of detector are commonly named *air shower detectors* or *particle counter matrices*. They detect directly the EAS particles and secondary  $\gamma$ -rays, and there are two types:

- Dense sampling detectors, which sample a significant fraction of the EAS, like the water Cherenkov extensive air shower array MILAGRO [Col03] and the single layer of Resistive Plate Chambers detector ARGO-YBJ [DR07]. These detectors have relative low energy thresholds ( $\sim 250 \text{ GeV}$ ).
- Sparse sampling detectors composed by an array of scintillators counters like Tibet AS [Ame99], HEGRA scintillator array [AH98], CASA-MIA [Col97] and the HAGAR array. Contrary to dense sampling detectors, these have higher energy thresholds (about few TeV).

#### 2.6.2.2 Atmospheric Cherenkov detectors

The Cherenkov light detectors, also called atmospheric Cherenkov detectors, are of two types. The first type are the sampling Cherenkov devices like AIRO-BICC [AH98], BLANCA ([For99]) and the solar devices like STACEE [Han02] , CACTUS[Mar05] and GRAAL [Arq02].

## 2.6 Detectors

---

The second type of detector are the so called *Imaging Atmospheric Cherenkov Telescopes*. The current “Big three” detectors of this kind are MAGIC, H.E.S.S. and VERITAS (Figure 2.21 shows their geographical location). An excellent review of the goals achieved by the IACTs up to mid 2008 can be found in [Wee08].

IACT detectors have a single or multiple telescope reflectors with a *photomultiplier* (PMT) tubes composite cameras at the focal plane. Some future prototypes are planned with different light detectors like HPDs or gAPDs.

Despite of sharing some similarities, optical telescopes and IACTs have also some remarkable differences. The EASs are extensive phenomena, and therefore the IACTs need large fields of view. The signal is faint and also very fast (of the order of ns). The angular resolution is not as important as for the CCD cameras of the optical telescopes, but it is more important a good sensitivity to individual photons, and to have the best possible temporal resolution. A high temporal resolution is important to reduce the light from the light of nigh sky background (LONS). On the other hand, the quality of the mirrors is less important than in the case of optical telescopes, since the spatial fluctuations of EASs are much larger that the ones of the punctual objects like the stars.

IACTs can work individually or forming arrays. Experiments as MAGIC, CANGAROO, VERITAS and H.E.S.S. are arrays of IACT detectors, even if some of them (like MAGIC, worked as individual telescopes on the firsts phases of the experiment. The arrays of telescopes can determine the impact parameter, direction and energy of individual showers more accurately and have a better background rejection.

## 2.6 Detectors

---

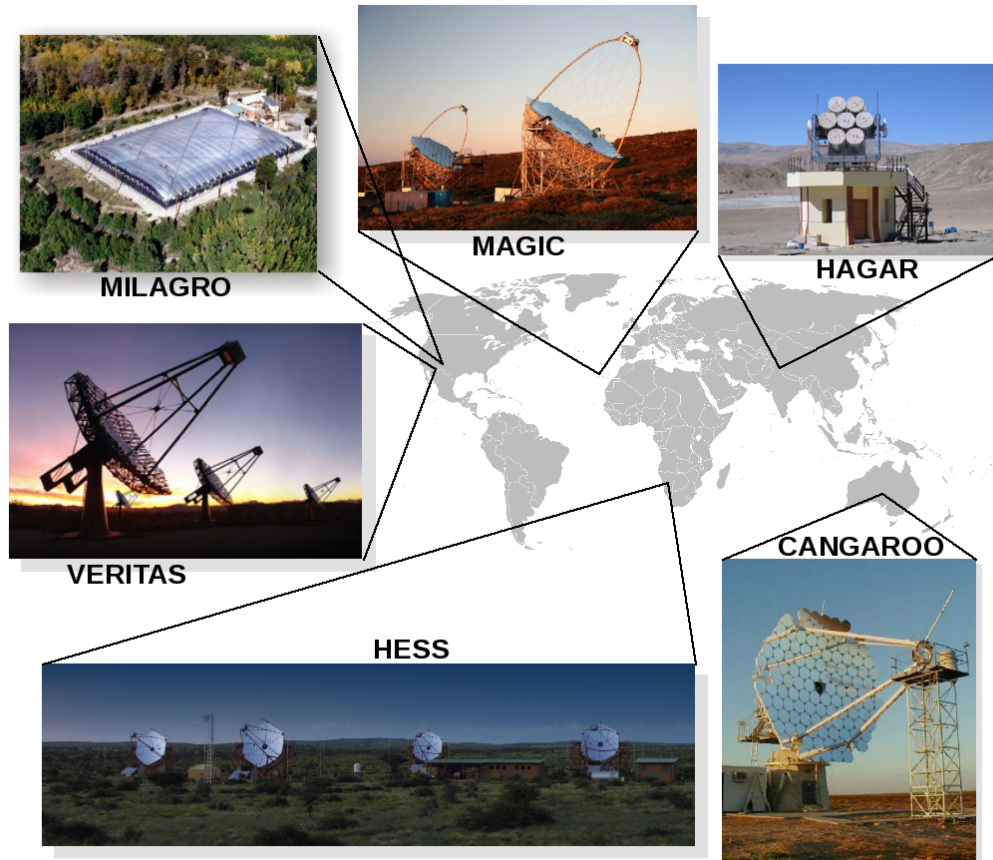


Figure 2.21: *The geographical location of the “big three” VHE ground detectors (MAGIC, H.E.S.S. and VERITAS), together with other relevant detectors.*

# Chapter 3

## Active galactic nuclei

### 3.1 Introduction

The studies of AGN started when E.A. Fath, in the Lick observatory in 1908, performed his study of the optical spectra of what in these times were called “spiral nebulae” (the concept of galaxies was not yet established). He found that most of these objects showed absorption lines in their spectra, that he understood as coming from the integrated light of a large number of stars present on these “nebulae”. Fath found, however, that the spectrum of the nucleus of one of these galaxies, NGC 1068, showed six emission lines (including the  $H_{\beta}$  line) characteristic of gaseous nebulae. The study of these nuclei was further developed by V.M. Slipher in 1917 and E. Hubble, who discovered two more objects (NGC 4051 and NGC 4151) that showed characteristics similar to the previously mentioned objects.

In 1943, C.K. Seyfert published a paper ([[Sey43](#)]) where he demonstrated that a very small fraction among the total galaxies showed spectra with many high-ionization emission lines. He also noted that these nuclei were specially luminous and that the emission lines were broader than the absorption lines present in the spectra of normal galaxies. In his honour, the AGN that show broad emission lines (that cover a wide range of ionization levels), coming out from a bright, small, and with quasi-stellar appearance nucleus, are nowadays known as *Seyfert* galaxies. These Seyfert galaxies constitute the most common type of AGN.

After Second World War there was a fast development of the radio-astronomy, that allowed to identify optically strong radio sources. One of the detected radio sources, Cygnus A was identified with a faint galaxy with a redshift  $z = 0.057$ , proving its extragalactic origin. After this discovery, other similar sources were quickly found, and were subsequently called radiogalaxies. The spectra of the compact, very luminous cores of these sources were quite often rich in emission lines considerably broader than the ones seen in normal galaxies, and very similar

### 3.1 Introduction

---

to those present in Seyfert galaxies. On the other hand, Seyfert galaxies are radio-quiet<sup>1</sup> objects. Radio galaxies exist in a considerably smaller proportion compared to the Seyfert galaxies.

A fraction of the previously detected radio sources were found to show remarkably different characteristics compared to those shown by radiogalaxies. It was not possible to find any sign of nebula or galaxy associated with these radio sources in their optical images. On the other hand their spectra were continuous, with no absorption lines, but with broad emission lines that were not possible to recognize. They were first understood to be a kind of star, perhaps white dwarfs with an unusually high abundance of heavy elements. Their extragalactic origin was understood in 1963, when Maarten Schmidt identified several well known nebular emission lines from the object 3C 273, which had this stellar appearance. It was found that the redshift of this source was very large (for those times standards):  $z = 0.158$ . After this discovery, it soon followed the one of 3C 48, with even a larger redshift:  $z = 0.367$ . The redshift of this last source meant that it was farther than any galaxy discovered at that time. It was therefore understood that these sources were not stars, but *quasi-stellar*, abbreviated as *quasar*, very luminous and distant radio sources. Presently it is known that are AGN, but they are so distant that it was not possible to detect their host galaxies with the technology of the '60s. With the advent of the CCD technology, it was possible to detect their host galaxies, and currently is it possible to isolate the nucleus of stellar appearance with high precision.

Another quasi-stellar appearance, high-luminous, but radio quiet objects were discovered soon after radio-loud quasars were discovered. They were also called then “quasi-stellar” objects, but, except for purists, are now considered inside the *quasar* definition, and it will therefore be distinguish between radio-loud and radio-quiet quasars.

The most important type of AGN for this thesis also had a confusing origin. Before radio-astronomy was well developed, a population of stars that showed very irregular changes in their luminosity was established. These “stars” were called *irregular variable stars*. In 1968, it came out that one of these variable stars, “BL Lacertae”, was connected with the strong radio source VRO 42.22.01. This source was showing many of the characteristics of quasars, but its optical spectrum showed just continuum emission, without the emission lines present in quasars. Finally, in 1974, signs of a host galaxy were found, what proved the extragalactic origin of this object. More objects like BL Lacertae were found later, and they are known now as “BL Lacertae” or just “BL Lac” objects.

Some of the detected radio-loud quasars were found to share many of the characteristics of BL Lac objects, but keeping the existence of emission lines. These objects were subdivided in groups: Optically Violently Variable (OVV)

---

<sup>1</sup>But not radio-silent.

### 3.2 Classification of AGN

---

quasars, Highly Polarized Quasars (HPQ), Core-Dominated Quasars (CDQ) or FSRQ. Later it was found that the distinction between these objects corresponded just to empirical differences, and it was understood that they were intrinsically the same type of object. To avoid confusions they will be referred as FSRQ in this thesis.

More details about the different AGN discoveries in an historical context can be found in [Ost89] and [Pet97].

## 3.2 Classification of AGN

AGN can be divided in two big groups, *radio loud* and *radio quiet* AGN. Inside of these groups, further sub-classifications exist. Figure 3.2 shows an schematic AGN classification, based in the morphology of the host galaxy, the luminosity and the inclination angle with respect to the observer.

The so called *unification models* (see for example [Ant93] and [UP95]) explain the main differences of the AGN according to a few characteristics. In the center there is a super massive black hole with a mass of  $10^6 M_\odot - 10^{10} M_\odot$ , that is the final engine of the system. This black hole accretes matter forming a disk of hot plasma. The gas close to the accretion disk gets ionized and constitutes the broad line region (BLR), named in this way because lines are Doppler-broadened due to the fast ( $\simeq 1000\text{-}5000$  km/s) motion caused by the proximity of this gas to the black hole. Farther from the central engine, other clouds with slower motion ( $\simeq 500$  km/s) constitute a region where both narrow emission and absorption lines (narrow line region, NLR) are observed. Finally, the previous regions are surrounded by a dusty torus in the equatorial plane that, depending on the viewing angle, obscures all the central region. In the case that the accretion rates are high enough, a pair of opposite jets of ultra-relativistic moving plasma will emerge from the polar regions of the system. As the jets move at relativistic speeds, any radiation produced inside is measured greatly modified due to Doppler effect. Sometimes large radio lobes are seen close to the outer end of the jet. The main differences observed in AGN could be explained according to these *unification models*, as due to the viewing angle of the objects, the matter accretion rate, and the mass of the central black hole.

Radio-loud AGN always show jets. According to the lengths of these jets, radio-loud AGN can be divided into the ones where the jet gets stuck in dense matter or the ones from where the jet is able to escape, developing typical jet lengths of  $>100$  kpc.

The spectra of the AGN are in general composed of two parts: the thermal and the non thermal part. The thermal part is also called *blue bump*, it has its maximum at optical-UV wavelengths, and is interpreted as radiation coming from the inner accretion disk. The origin of the low energy (from radio to soft x-ray

### 3.2 Classification of AGN

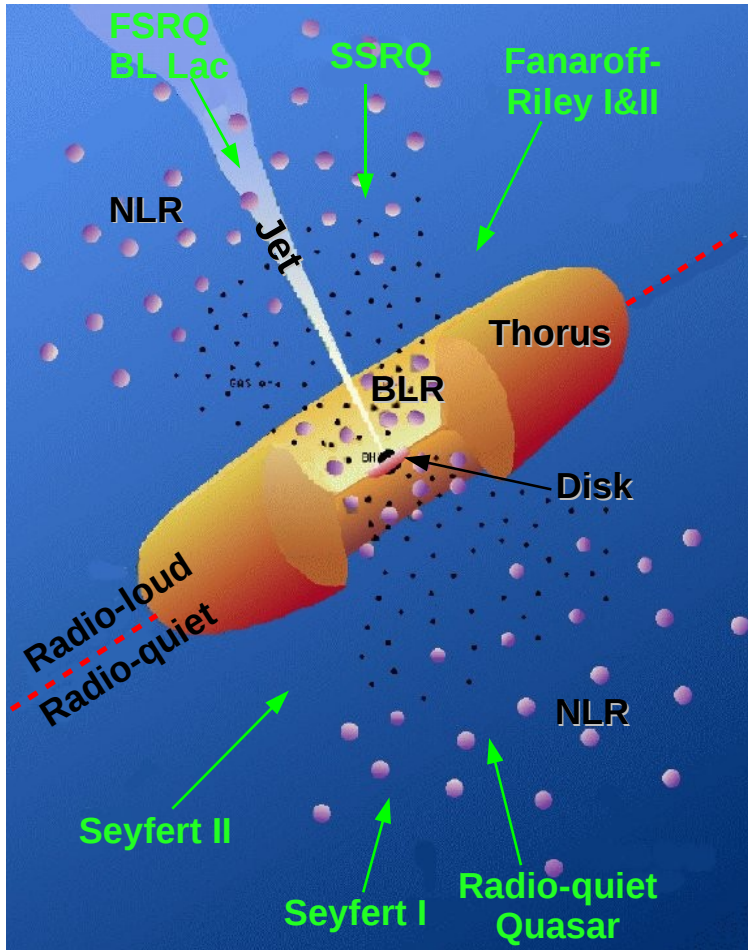


Figure 3.1: Schematic illustration of AGN according to unification model. The upper half corresponds to radio-loud AGN, while the lower half to radio quiet AGN. The main differences on AGN types inside these two families are more a matter of the random observing direction than of intrinsic physical properties. Adapted from [UP95].

wavelengths) non thermal component is understood as caused by synchrotron radiation from electrons (or positrons, see section 2.3.6). Some AGN also show a high energy non thermal component (at GeV-TeV energies), that is understood to be created by inverse Compton effect (see section 2.3.5) of the electrons of the jet over low energy photons (see section 3.4.1) or by hadronic showers originated in the jet (see section 3.4.2).

The thermal spectrum can show superimposed emission lines. These lines are classified as narrow or broad lines, and as explained before, they come from the slowly moving clouds of the narrow line region outside the torus, or from the fast moving clouds near the accretion disk. The broad lines can be hidden by the torus, depending on the angle of observation.

The radio emission is understood to come from the synchrotron emission of

### 3.2 Classification of AGN

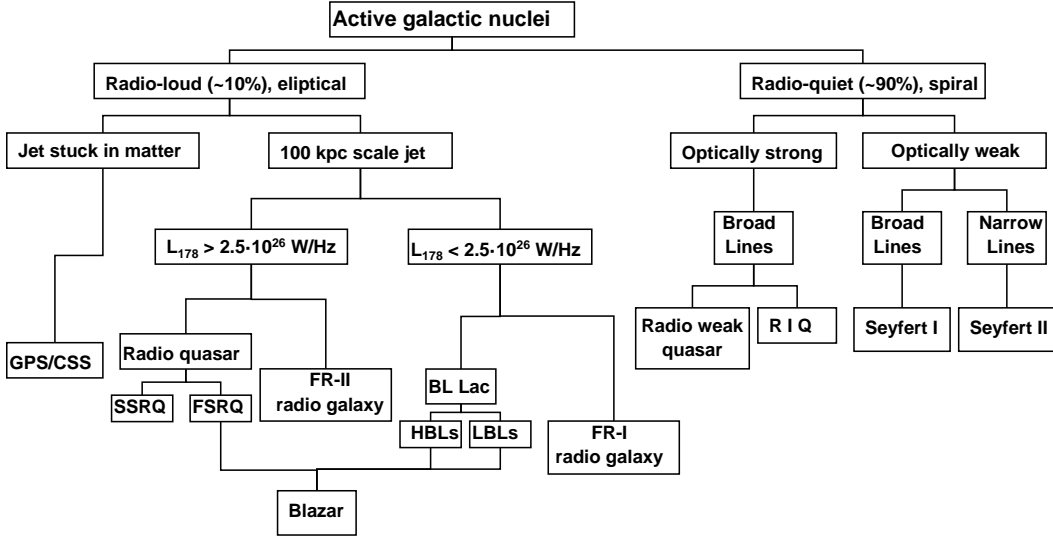


Figure 3.2: *AGN classification scheme, according to the morphology of the host galaxy, luminosity, and inclination angle. Adapted from [Ach06].*

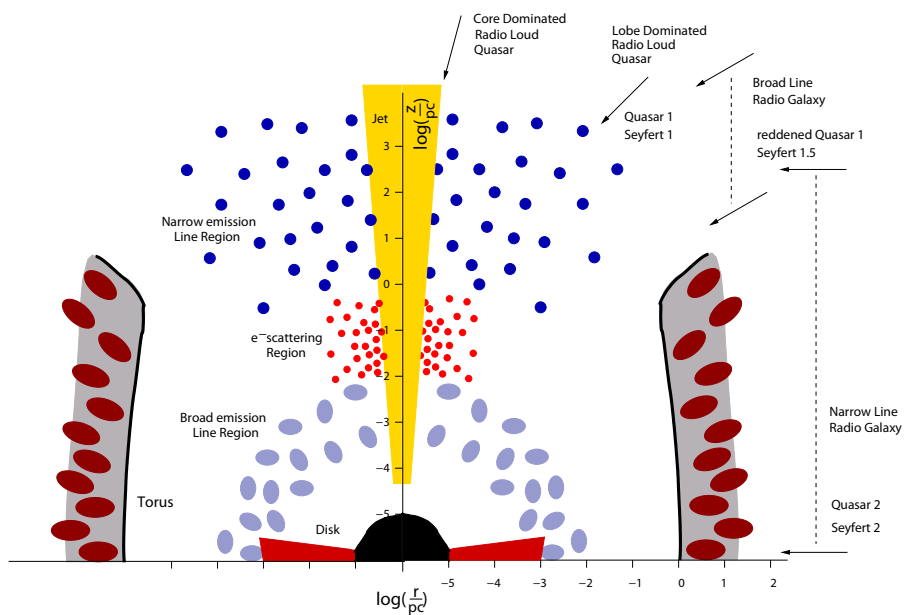


Figure 3.3: *Schematic view of the main components of an AGN, according to the unification models. The central MBH is not drawn to scale. From [Bie02].*

## 3.2 Classification of AGN

---

electrons moving in the relativistic jet. Sometimes it could be necessary to set a criterion to discriminate between radio-loud and radio-quiet AGN. A commonly used one is described at [Kel89], that considers the relative radio  $R_{r-o}$  and optical flux, for example, at 6 cm (5 GHz) and at 4400 Å: For the radio loud AGN,  $R_{r-o}$  is typically about 10-1000, while radio quiet ones are normally  $0.1 < R_{r-o} < 1$ . This consequently means that there will be some ambiguous cases close to the  $R_{r-o} > 10$  demarcation line. Radio-loud AGN are located in elliptical galaxies, while radio-quiet AGN are mostly in spirals, and very seldom in ellipticals.

### 3.2.1 Radio loud AGN

#### 3.2.1.1 GPS/CSS

Radio-loud AGN with evidences of short or absent jets show a very steep radio spectrum up to a certain turnover frequency. When this turnover is in the MHz range, the source is called Compact Steep Spectrum (CSS) source. When the turnover is in the GHz range, the source is called GHz Peaked Source (GPS). The size of these sources is smaller than the one of usual AGN: The GPS are about 1 kpc wide, while, the CSS are 1–15 kpc wide. These two types are understood as the same type of object that has continuous transition between both types, with decreasing turnover frequency with growing size. The highly energetic emission of these sources is understood to originate in a central engine as it happens in other AGN, while the explanation of their compactness is that the jet is stopped by dense matter in his path. Some authors [OBS91] suggest a connection between GPS/CSS and other radio-loud AGN in the sense that the first ones are young states of the second ones.

#### 3.2.1.2 AGN with developed jets

The radio-loud AGN that show developed jets can be further divided according to their luminosity, that is correlated to differences in the morphology of the jets [FR74]. The usual criterion to distinguish “high” and “low” luminosity sources is the radio luminosity at 178 MHz [FMB95]:

- **Objects with  $L_{178} > 2.5 \times 10^{26} \text{ W/Hz}$ .** These highly luminous AGN show strong jets that extend far outside the host galaxy. The jet luminosity is increased at the outer region, showing extended radio lobes and hot spots. These objects are further divided into FSRQ, Steep Spectrum Radio Quasars (SSRQ), and Fanaroff-Riley type II (FR-II) radio galaxy types.
- **Objects with  $L_{178} < 2.5 \times 10^{26} \text{ W/Hz}$ .** The jets on these AGN are fainter than in the previous, more luminous AGN. Also, the jet luminosity decreases at larger distances from the central engine. The jet does not show

### 3.2 Classification of AGN

---

hot spots. These objects are further divided in the Bl Lac objects and in Fanaroff-Riley type I (FR-I) radio galaxy types.

It is understood that the different types of AGN inside each of the luminosity groups mentioned above are intrinsically the same objects, but the inclination angle of the jet makes that the observed characteristics differ considerably. If the observation angle of the jet is large, the torus obscures the inner part of the AGN, and therefore the broad line region, as well as the thermal continuum radiation from the disk are shielded. In this case, the AGN is classified as a radio galaxy. Figure 3.4 shows a X-ray, radio and optical composite image of a radio galaxy where the jets can be clearly distinguished. For intermediate inclination angles, where the jet is not aligned, but the inner core is not shielded by the torus, the spectrum contains the broad emission lines and the *blue bump* from the accretion disk. These objects are the previously mentioned SSRQ and show a steep spectrum with a dominance of the lobes and have always been observed as high luminosity AGN.

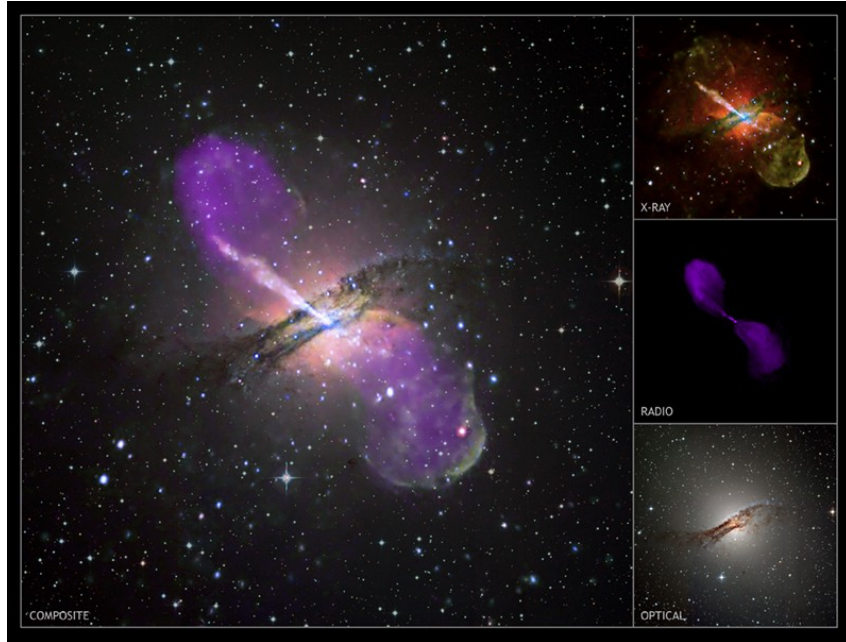


Figure 3.4: *A Chandra image composite with radio and optical data, of the nearby FR-I radio galaxy Centaurus A, providing a view of the two opposite jets coming from the central super massive black hole, extending to the outer reaches of the galaxy. At the end of each jet an extended radio lobe is present. This source has been confirmed as a VHE gamma-ray emitter by the H.E.S.S. array [He09]. (Credit: X-ray: NASA/CXC/CfA/R.Kraft et al; Radio: NSF/VLA/Univ.Hertfordshire/M.Hardcastle; Optical: ESO/WFI/M.Rejkuba et al.) from <http://chandra.harvard.edu/photo/2008/cena/more.html>*

## 3.2 Classification of AGN

---

For very small inclination angles ( $<12$  deg), the jet points towards the observer. Since the bulk motion of the jet is relativistic, with the effect of greatly increasing the luminosity from the jet radiation, the radiation from the AGN is dominated by the radiation from the jet. These AGN show a flat radio spectrum, with a highly variable flux, and polarized radiation, characteristics of a strong beamed emission. The AGN that fit well in the previous description are both the FSRQ and the BL Lac objects, that are commonly grouped in the term *blazars*<sup>1</sup>. The flat radio spectrum from blazars is explained by the dominance of the boosted spectrum over the non boosted steep spectrum from the radio lobes. The FSRQ are high luminous objects that show a FR-II type jet and strong emission lines, while the BL Lac objects are less luminous objects that show a FR-I type jet and almost no emission lines.

The BL Lac objects can be further divided into High-frequency BL Lac (HBL) and Low-frequency BL Lac (LBL). ‘High’ and ‘Low’ refer to the maximum of the synchrotron spectrum. The emission from blazars is often shown in Spectral Energy Distribution (SED) plots. The SED is generally plotted as  $\nu F_\nu$  against  $\nu$ , that is a measure of the power observed at each frequency. The multiwavelength measurements of blazars have shown that their SEDs have a two bump structure (see Figure 3.5), but, due to the lack of measurements in the energy region between hard X-rays and HE  $\gamma$ -rays, it cannot be discarded that there is a more complex structure between these two bumps. For most of the FSRQs and LBLs the peak of the low energy bump is located between the sub-millimeter to optical wavelengths, while for the HBLs, the peak is between the UV and the X-rays. An intermediate class of BL Lacs can be further defined, called Intermediate-frequency BL Lac (IBL), referring to the objects whose low energy peak frequency is between the ones of the HBL and LBLs. The high energy peak of the SED of blazars is normally located at the MeV–GeV range.

### 3.2.2 Radio quiet AGN

Radio-quiet AGN are classified according to their optical luminosity. The intrinsically most luminous objects are both the radio quiet quasars and the Radio Intermediate Quasars (RIC). It is understood that both are intrinsically the same objects, but radio-quiet quasars are observed with moderate inclinations (20–60 deg), while RICs are observed with low inclinations. The RICs show relativistic beamed radio emission, in a similar way as the blazars do. The intrinsically weaker radio-quiet sources are both types of Seyfert galaxies. The Seyfert I galaxies show both narrow and broad lines, while the Seyfert II galaxies only show narrow lines, and therefore it is understood that the observation inclination

---

<sup>1</sup>The first time that this term was used to group together the FSRQ and BL Lac object was by E. Spiegel during a banquet at the Pittsburgh Conference on BL Lac objects in April 1978 [Pet97].

### 3.3 Blazars

---

makes that the broad line region is obscured by the torus. The Seyfert galaxies do not show beamed emission.

## 3.3 Blazars

The main characteristic that distinguishes blazars from the other AGN types is their non-thermal beamed continuum emission, that is attributed to plasma moving at relativistic speeds, along directions close to the line of sight of observation. As stated before, the term blazar is applied to both FSRQ and BL Lac objects because they share this main characteristic.

Blazars are compact sources, and strong radio emitters. The radio emission from the core dominates the total radio emission. They are also strong millimeter emitters, showing a flat/inverted radio spectrum. Blazar are bright in all wavelengths. Their optical emission also dominates the one of the host galaxy. Blazars also exhibit strong flux variabilities (from minutes to years time scales) in any observed energy band. The optical emission is strongly polarized ( $P > 3\%$ ), and it is also variable, as well as happens with the radio emission ( $P > 1\text{--}2\%$ ). Many blazars are strong  $\gamma$ -ray emitters, also in the VHE band. From the total of the 38 extragalactic sources firmly detected so far in the VHE energies, 30 are blazars (M 87 and Centaurus A are radiogalaxies, while MAGIC J0223+430 and VER J0521+211 are candidates to be radiogalaxies too; NGC 253 and M 82 are starburst galaxies; the nature of VER J0521+211 and RGB 0648+152 is not yet clear). Most of the BL Lac type AGN detected in the VHE energies are HBLs. All the VHE extragalactic sources detected so far are listed in Table 3.1.

As it was said in section 3.2.1.2, blazars show a two bump structure in their SED, that is understood to originate by emission from the electrons from the jet, spiraling at relativistic velocities in the magnetic field lines of the jet. The low energy component of the SED is attributed to electron synchrotron emission (see section 2.3.6). The high energy component origin is still debated, being the so-called *leptonic* and *hadronic* scenarios or models the two main feasible explanations present in the literature.

## 3.4 Blazar models

AGN show a lot of particularities that make them very uncommon objects. The presence of very high luminosities, fast and apparently random variability of flux level, together with their unusual emission spectra, among other characteristics, are evidences of their complex nature. The hints of the presence of a central super-massive black hole as the engine of the whole system, surrounded by an accretion disk, a dusty torus, both narrow and broad line emission regions, and finally the relativistic moving jet just underline this complexity.

### 3.4 Blazar models

---

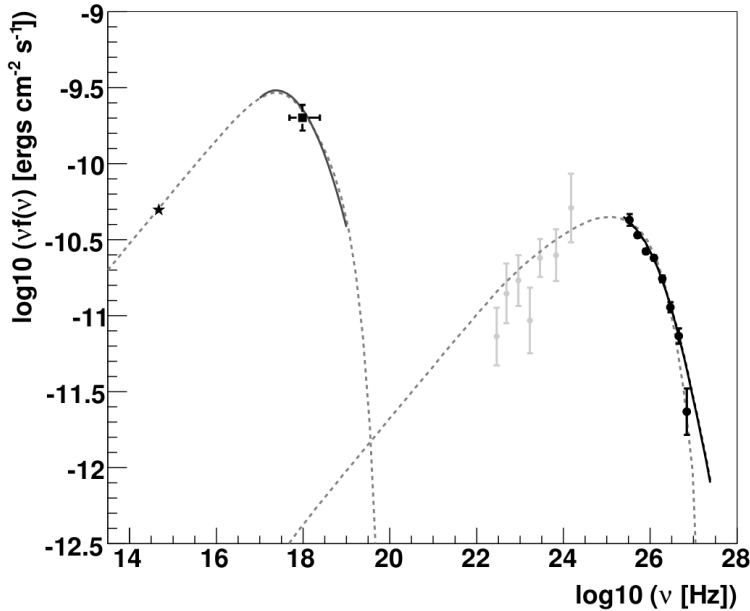


Figure 3.5: Example of the SED of Mrk 421, a VHE  $\gamma$ -ray emitter blazar, as measured in 2004-2005 by various instruments (see [Alb07c] for details): The optical measurements of the KVA telescope (star), X-rays from RXTE/ASM (full square) and MAGIC (full points). The archival EGRET measurements are shown in grey squares. The gray dashed line is a leptonic SSC model as in [Kra04].

Blazars have the particularity that they can be observed almost in the full electromagnetic spectrum, along about 20 decades of energy. Blazars are the most energetic types of AGN at high energies<sup>1</sup>, showing huge luminosities: Assuming an isotropic emission, their luminosity would be as high as  $L_\gamma \simeq 10^{49}$  ergs/s. A more realistic assumption of a beamed emission with a beaming factor of  $10^{-3}$  would still mean a very high luminosity of  $L_\gamma \simeq 10^{46}$  ergs/s, while the total power of the particles that emit this radiation would be even greater.

As stated before, the origin of the energy that powers the system is the central MBH. But it is not obvious how the energy can be extracted from the black hole, and in particular, why should it appear as a relativistic jet. The formation of a jet is a phenomenon often seen in astrophysics, for example, in stellar systems, but in these places the outflow, even if supersonic, is far from the speed of light.

Even if the main source of the energy of the AGN is the gravitational energy of the central super massive black hole, it is understood that the energy needed to create the beams is coming from the rotational energy of the black hole. This rotational energy would come either from a residual angular momentum from the original cloud of gas that created the black hole, by accretion of

<sup>1</sup>They are not, however, the most luminous AGN in terms of total isotropic luminosity: the most luminous AGN are radio quiet quasars.

## 3.4 Blazar models

---

extragalactic material, or from a merge of two black holes. Models that explain the jets involve thermal pressure of the accreting gas and the relativistic effects of a rotating black hole (magnetohydrodynamics models, see e.g. [MKU01]). Alternative models explain the origin of the jets caused by the effect of a rotating charged black hole [KM99].

One evidence of the relativistic nature of the jets comes from the observed synchrotron emission by relativistic electrons, that give origin to the low energy emission peak. Another evidences are the presence of highly variable polarization in both optical and radio emission, and the apparent super-luminal motion of knots in the jet. The HE and VHE observations are also strong and independent evidences of the presence of relativistic jets: The short term variability of the source points to its compactness, what would make the existence of the huge observed  $\gamma$ -ray luminosity for such a compact source without the attenuation caused by  $\gamma - \gamma$  pair production impossible, unless the relativistic beaming exists.

### 3.4.1 Leptonic models

Leptonic models are inverse Compton and synchrotron mechanisms based models. Electrons (or positrons) are accelerated beyond the velocity of the bulk Lorentz outflow. It is believed that this acceleration is achieved due to the collisions of shocks moving through the jet with inhomogeneities. Due to the presence of the magnetic field of the jet, electrons will move in spiral-type motion, and will radiate due to synchrotron effect (see section 2.3.6). This emission will produce the low energy peak of the SED, that is often called *synchrotron peak*, referring to the emission mechanism. The presence of the polarization is an argument to support this mechanism. The position of the peak is determined by the efficiency of the shock acceleration mechanisms and also by the cooling processes. Example of leptonic models can be found in the references [MGC92, Kra04, BC02, TMG98].

The second peak of the SED is explained by an inverse Compton scattering (see section 2.3.5) of optical to X-ray photons. There are two possible origins of these photons: either they are the same photons generated by the previously mentioned synchrotron process or they come from outside the jet.

#### 3.4.1.1 Synchrotron self-Compton

The synchrotron photons radiated by the electrons spiraling in the jet make a soft photon population of targets able to be boosted by the electrons (or positrons) due to inverse Compton effect. After this boost, the photons get almost all the energy of the electrons (see section 2.3.5). These models are called Synchrotron Self-Compton (SSC).

The simplest possible scenario are the so-called *one component* or *one zone* models. These models assume that both synchrotron and inverse Compton effects

### 3.4 Blazar models

---

take place in the same homogeneous region. More realistic models assume multiple and/or inhomogeneous zones of emission. The VHE observations of BL Lac objects point to a better explanation of the observed SEDs by SSC mechanisms over the EC ones (see below), as correlations have been found between X-ray and VHE flux levels during large flares (e.g. [Kra01, Bl05]).

In the most simplistic SSC scenario, namely an homogeneous one-zone SSC, the  $\gamma$ -rays are produced in an accelerating region of spherical shape named “blob” that is parametrized by a radius  $R$  and that moves out along the jet at relativistic speed  $v/c = (1 - 1/\Gamma^2)^{1/2}$ , where  $\Gamma$  is the bulk Lorentz factor. The angle between the observer and where the jet is pointing is small.

The observed low energy (synchrotron) component spectral shape can be explained to originate in a diffusive shock acceleration mechanism and subsequent radiative cooling effects, so the electron spectrum is described by a broken power-law of the form  $dn/dE = n_0 E^{-n^i}$  with spectral indices  $n_1$  and  $n_2$ , below and above the break energy  $E_b$ . For energies above  $E_b$ , the radiative cooling becomes the dominant effect. The typical values of  $n_1$  and  $n_2$  are  $\simeq 2$  and  $\simeq 3$ , respectively. Three energies are also defined regarding this spectrum, that are the minimum ( $E_{min}$ ), break ( $E_{break}$ ) and maximum ( $E_{max}$ ) energy of the electron population. Finally, the three last ingredients are the magnetic field ( $B$ ), electron energy density ( $K$ ) and Doppler beaming factor ( $\delta$ ).

#### 3.4.1.2 External Compton

It may happen in certain scenarios that the population of seed photons for the inverse Compton scattering is not mainly coming from synchrotron photons but it has an external origin. The presence of sources of soft radiation was deduced from observations of non-blazar AGN: additional thermal bumps in the UV, infrared and in x-rays, understood to come from the accretion disk, the hot torus, and the disk corona, respectively, were observed in these sources.

The inverse Compton scattering of the seed photons, that are produced outside the jet, and have been re-processed in the broad line region or scattered off the thermal plasma, is modeled by the *External Compton* (EC) models [DS93]. These models have been able to reproduce better than the SSC models the observed features of the FSRQ SEDs (see, e.g., [Col08]). The presence of intense broad lines in this type of quasar is understood to be an evidence of a high density of photons outside the jet.

#### 3.4.2 Hadronic models

In the same way as leptonic models do, hadronic models explain the low energy component of the SED as originated by synchrotron radiation of the electrons, but the explanation for the high energy component is different. Some hadronic

### 3.5 The blazar sequence

---

models explain the emission of the higher energy bump as generated by proton (or other nuclei) initiated cascades. In these models, the protons are accelerated in the jet up to  $10^{18}$  GeV. The protons interact either with soft photons [MB92], matter [Bed93], both [MP01], or magnetic fields [Aha00], producing mesons. The HE component is consequently explained by the decay of neutral pion, while the charged pions are the source of the electrons and positrons for the synchrotron radiation of the low energy component, and in principle the models can explain the SED features. Other hadronic models, called *synchrotron proton blazar* explain the  $\gamma$ -ray emission as synchrotron radiation of protons accelerated up to  $10^{20}$  eV [MP01].

The hadronic models also give an explanation for the origin of the extragalactic cosmic ray radiation, solving one of the important unknowns about their origin. Also, according to these models, the decay of charged pions will produce a large amount of high energy neutrinos, that might be detectable with the next generation neutrino detectors. The detection of such a flux of neutrinos will both help in understanding the AGN  $\gamma$ -ray emission mechanisms and the origin of extragalactic cosmic rays.

It has to be said, however, that the observations seem to prefer the leptonic models over the hadronic ones, as for example it is difficult to explain the often observed X-ray and  $\gamma$ -ray correlation in the latter models. On the other hand, it could be that both leptonic and hadronic phenomena are affecting the blazar emission in different degree.

## 3.5 The blazar sequence

The existence of a “blazar-sequence” was proposed in 1998 in two papers [Fos98, Ghi98]. The authors found an anti-correlation of the position of the synchrotron peak with the flux of the source: the most powerful sources had the peak in the lowest frequencies, and vice-versa. They also found that the frequency of the peak of the high energy bump was correlated with the peak frequency of the low energy one, and that the luminosity ratio between the high energy and the low energy components was scaling with the bolometric luminosity.

The main virtue of this model was that it could explain the different shapes of the SEDs of blazars, and therefore their behaviour, by the energy density of the sources, that is proportional to the observed bolometric luminosity.

It was recently explained [Pad07] that the previously mentioned anti-correlation between  $\nu$ -peak and source luminosity could be explained by selection effects, and that after these effects are taken into account, the anti-correlation disappears. In addition there are some experimental facts that contradict the prediction of the blazar sequence: contrary to predictions, the LBL are the most numerous BL Lac subclass ( $\simeq 90\%$ ). The “missing” FSRQ class that shows its synchrotron

### 3.5 The blazar sequence

---

peak at frequencies comparable to those of LBLs has been observed. The authors of [NVT08] contributed with more arguments against the existence of a blazar sequence: they have suggested that the blazar sequence is just an artifact of variable Doppler boosting across the peak frequency range (see [NVT08]).

### 3.5 The blazar sequence

---

Table 3.1: The 38 extragalactic VHE sources detected so far.

| Redshift        | Source                   | Type             |
|-----------------|--------------------------|------------------|
| 0.0007          | M82                      | Starburst Galaxy |
| 0.0008          | NGC 253                  | Starburst Galaxy |
| 0.00183*        | Centaurus A<br>(3.8 Mpc) | FR I RG          |
| 0.0044          | M87                      | FR I RG          |
| 0.0215?         | MAGIC J0223+430          | FR-I RG?         |
| 0.019           | RBS 0413                 | HBL              |
| 0.019           | IC 310                   | “head-tail RG”   |
| 0.02            | PKS 0447-439             | HBL              |
| 0.029           | 1ES 0414+009             | HBL              |
| 0.030           | Mrk 421                  | HBL              |
| 0.034           | Mrk 501                  | HBL              |
| 0.034           | 1ES 0502+675             | HBL              |
| 0.044           | 1ES 2344+514             | HBL              |
| 0.045           | Mkn 180                  | HBL              |
| 0.047           | 1ES 1959+650             | HBL              |
| 0.069           | BL Lacertae              | LBL              |
| 0.069           | PKS 0548-322             | LBL              |
| 0.071           | PKS 2005-489             | HBL              |
| 0.080           | RGB J0152+017            | HBL              |
| 0.101           | W Comae                  | IBL              |
| 0.116           | PKS 2155-304             | HBL              |
| 0.129           | 1H 1426+428              | HBL              |
| 0.125           | PKS RGB J0710+591        | HBL              |
| 0.138           | 1ES 0806+524             | HBL              |
| 0.140           | 1ES 0229+200             | HBL              |
| 0.165           | H 2356-309               | HBL              |
| 0.182           | 1ES 1218+304             | HBL              |
| 0.185           | 1ES 0347-121             | HBL              |
| 0.186           | 1ES 1101-232             | HBL              |
| 0.212           | 1ES 1011+496             | HBL              |
| 0.31            | S5 0716+71               | IBL              |
| 0.36            | PKS 1510-089             | FSRQ             |
| 0.444           | 3C 66A                   | IBL              |
| 0.536           | 3C 279                   | FSRQ             |
| 0.06 < z < 0.66 | PKS 1424+240             | IBL              |
| 0.09 < z < 0.80 | PG 1553+113              | HBL              |
| ?               | VER J0521+211            | RG?              |
| ?               | RGB 0648+152             | ?                |

The sources are HBLs (22), IBLs (4), LBLs (2), radio galaxies (3–5), starburst galaxies (2), FSRQ (2), and of unknown origin (1). The distance to Cen A is given also in Mpc: due to its proper motion, the calculated  $z$  value differs significantly from the distance determined by other means. See <http://magic.mppmu.mpg.de/~rwagner/sources/> for references of the detection of the sources and further information.

# Chapter 4

## The imaging air Cherenkov technique

### 4.1 Introduction

When a high energy cosmic ray or  $\gamma$ -ray enters in Earth's atmosphere, it interacts with its atoms initiating a shower. The mean radiation length for high energy  $\gamma$ -rays is  $\approx 36 \text{ g/cm}^2$ . Particles created in the shower move with higher velocities than the speed of light in the medium, producing Cherenkov light. Even if the electrons and photons of the cascade are absorbed by the atmosphere, the Cherenkov light passes through and it is able to reach detectors at ground level. The Cherenkov light flash is very short ( $T \approx 2.5 \text{ ns}$ ). For a 300 GeV  $\gamma$ -ray originated shower, a few million of photons spread over a lateral distance of several hundred meters are created, as it happens with a proton originated shower. The total Cherenkov photon light is proportion to the original  $\gamma$ -ray energy at first order of approximation. This feature, together with the possibility of reconstructing the directions of the incoming particles according to geometry of the recorded images, enables ground detectors as MAGIC to use the Cherenkov light to reconstruct the characteristics of the original VHE particles.

### 4.2 Electromagnetic showers

When a  $\gamma$ -ray of energy above 20 MeV hits Earth's atmosphere, it interacts with one of the atmospheric nuclei by an electron-positron pair. The first pair of particles will loose energy mainly by producing high energy photons due to bremsstrahlung if the energy is high enough (the critical energy  $E_c \geq 83 \text{ MeV}$ , below which the main energy loss is due to ionization). The typical bremsstrahlung spectrum is:

## 4.2 Electromagnetic showers

---

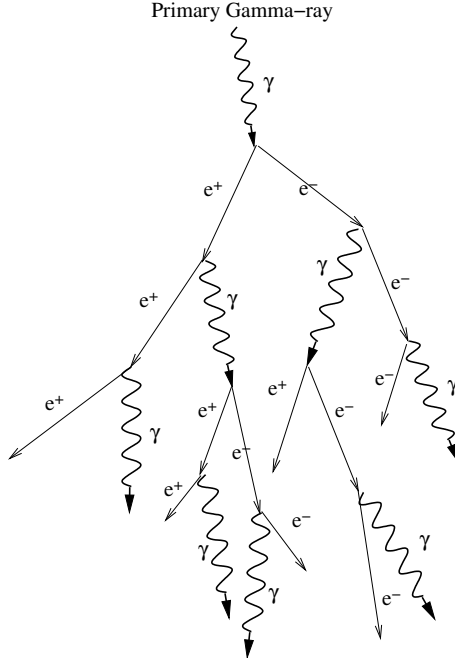


Figure 4.1: *Schematic figure of an EM shower development in the atmosphere.*

$$dN_{photon}/dE_{photon} \propto \frac{1}{E_{photon}} \quad (4.1)$$

and it produces a reasonable quantity of hard photons. Following this process, subsequent electron-positron pairs will be produced from the generated HE photons, while more low energy photons will be produced by bremsstrahlung processes of the charged particles. An electromagnetic (EM) shower will be produced (see Figure 4.1), and will grow until the ionization processes start to be dominant. At the shower maximum, the energy of the electron/positrons is  $\approx 300$  MeV. The shower slowly dies out after the maximum .

The maximum distance a shower can penetrate in the atmosphere increases with the energy of the primary  $\gamma$ -ray. Primary particles from 30 GeV to 30 TeV generate showers that develop well above the altitude of MAGIC (2200 m above sea level).

A simple model will be used in order to quantify some characteristics of electromagnetic showers [RG41, Gai90]. In this model, it is assumed that the number of particles is duplicated after each radiation length. The so-called shower age is defined as:

$$s = \frac{3T}{T + 2\ln\left(\frac{E_\gamma}{E_c}\right)} \quad (4.2)$$

## 4.2 Electromagnetic showers

---

$E_\gamma$  being the energy of the primary  $\gamma$ -ray,  $E_C = 83$  MeV the critical energy in air, and  $T$  the shower depth.  $s = 0$  marks the starting point of the shower,  $s = 1$  is the shower maximum, and the shower dies when  $s = 2$ . The atmospheric depth  $T$  can be described in unit of radiation lengths as:

$$T = T_0 e^{(-\frac{H}{H_0})} \quad (4.3)$$

where an isothermal atmosphere has been assumed.  $H$  is the height above sea level,  $H_0=8400$  m is the scale-height, and  $T_0$  is:

$$T_0 = \frac{X_{air}}{X_0 \lambda \cos\theta} \quad (4.4)$$

with  $X_{air} \approx 1013$  g/cm<sup>2</sup> being the column height of air at sea level,  $X_0$  the mean free path of electrons in air (37.2 g/cm<sup>2</sup>), and  $\theta$  the incident angle of the air shower. The total number of electrons above the critical energy  $E_C$  can be described according to this model by:

$$N_e(s) = \frac{0.31}{\sqrt{\ln(E/E_0)}} e^{T(-1.5 \ln(s))} \quad (4.5)$$

Figure 4.2 shows the shower size in  $N_e$  as a function of the shower depth and age. The lateral shower distribution in the region  $0.5 \leq s \leq 1.5$  (only valid strictly for  $1 \leq s \leq 1.4$ ) can be described by the Nishimura-Kamata-Greisen formula (see [Gai90])

$$f(r) = \frac{\Gamma(4.5 - s)}{2\pi\Gamma(s)\Gamma(4.5 - 2s)} \left(\frac{r}{r_M}\right)^{s-2} \left(1 + \frac{r}{r_M}\right)^{s-4.5} \quad (4.6)$$

Where  $r_M$  is the Moliere radius  $r_m \approx 21.2$  MeV  $\cdot (X_0/E_c)$  ( $\sim 78$  m at sea level) and  $\Gamma$  is the Gamma function. Anyway, the lateral distribution is widen by the effect of the multiple scattering processes and by the effect of the geomagnetic field. The EM showers are more compact than hadronic showers (see below).

The density of electrons in the shower can be described therefore as a function of  $r$ ,  $E$  and  $T$ :

$$\rho_N(r, E, T) = \frac{N_e(E, T)}{r_M^2} f(r) \quad (4.7)$$

### 4.3 Hadronic showers

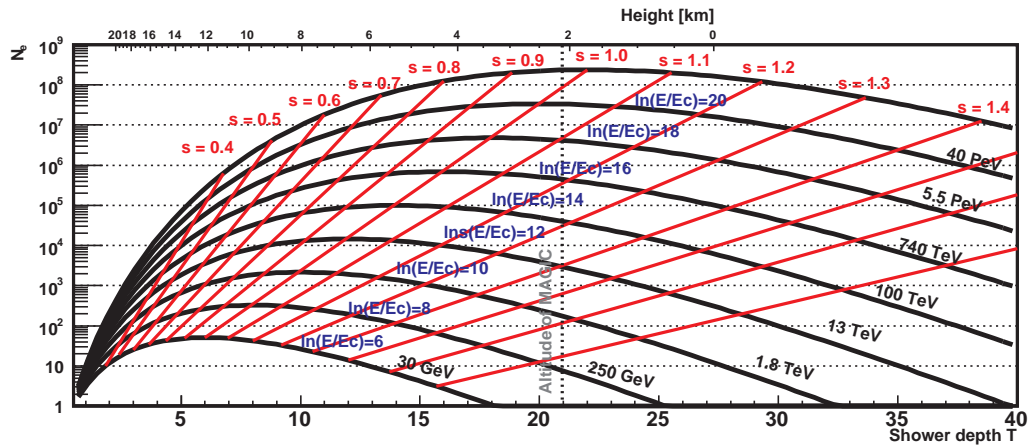


Figure 4.2: *Longitudinal development of a  $\gamma$ -ray shower. The shower size  $N_e$  is plotted versus the radiation length  $T$ . The red lines indicate the shower development according to the shower age  $s$ . The dotted black line shows MAGIC altitude, for vertical incidence.*

## 4.3 Hadronic showers

When a charged cosmic ray impacts Earth's atmosphere, it also creates a shower of particles (see Figure 4.3). The charged particle will interact (through strong interaction) with a nucleus of the atmosphere. The products of this interaction are mainly pions and kaons (about 90% and 10%, respectively), but also light baryons (proton, neutrons and their antiparticles). Also other particles may be created, with much smaller probability. The produced pions and kaons may interact again with the nuclei in the atmosphere, or decay. The part of the shower that continues to interact hadronically with the atmosphere constitutes the so-called hadronic core of the shower, and will continue suffering hadronic interactions until the energy per nucleon is smaller than the pion production threshold ( $\simeq 1 \text{ GeV}$ ). Charged pions decay in muons and neutrinos with high probability ( $\pi^+ \rightarrow \mu^+ \nu_{\mu} \bar{\nu}_{\mu} \quad P = 0.99\%$ ,  $\pi^- \rightarrow \mu^- \bar{\nu}_{\mu} \nu_{\mu} \quad P = 0.99\%$ ), while charged kaons may decay to muons, neutrinos, pions, electrons (or positrons).

Neutral pions decay mainly in two photons almost as soon as they are generated and it is not likely that they will interact with the nuclei of the atmosphere (see section 2.3.3 for more details). The neutral kaon decay is a more complicated process.  $K^0$ 's carry strangeness and therefore cannot be their own antiparticle. There are two  $K^0$ 's, the so called  $K_L^0$  (K-long, and  $K_s^0$  (K-short), with very different lifetimes.

The long life of the muon, together with his small bremsstrahlung cross-section implies that it will only interact in ionization processes with the atmosphere, and will very rarely decay before reach ground. Neutrinos will not interact with the atmosphere due to their low cross-section. On the other hand,  $\gamma$ -s from neutral pion decays will initiate electromagnetic sub-showers.

### 4.3 Hadronic showers

---

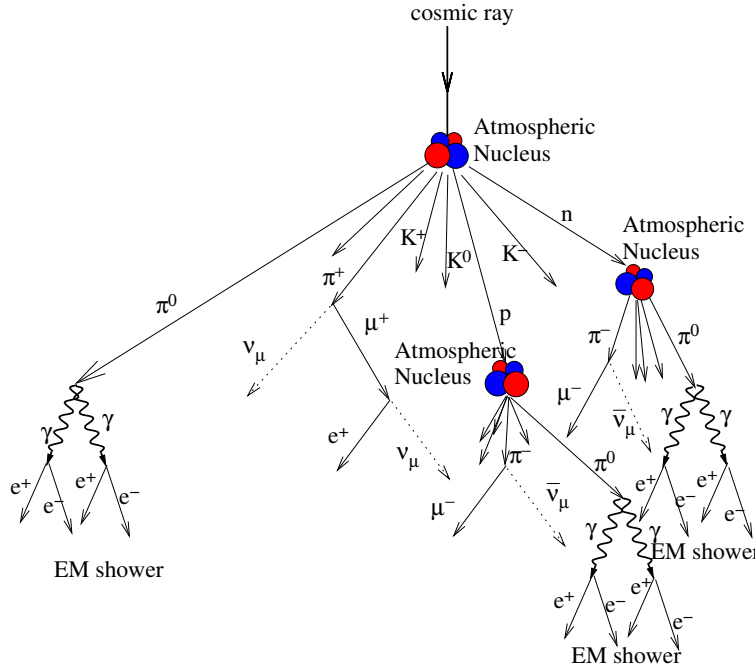


Figure 4.3: Schematic figure of an hadronic shower developed in the atmosphere. The superposition of the  $\gamma$ -ray sub-showers originated after the  $\pi^0$  decays creates the irregular shape of the hadronic showers.

The hadronic absorption length in air  $\lambda_h \approx 90 \text{ g/cm}^2$  is more than twice the one for  $\gamma$ -rays, what means that hadronic showers reach and develop their maximum deeper in the atmosphere, compared to an electromagnetic shower created by a primary  $\gamma$ -ray of similar energy.

One important characteristic of hadronic showers is that hadrons are able to transfer significant transverse momenta to the products generated during the decay, making their transverse evolution wider than the one of EM showers. The development of hadronic showers also shows large fluctuations, what makes them more irregular than EM showers.

The last important characteristic for Cherenkov telescopes about hadronic showers is that, contrary to  $\gamma$ -rays, the origin of these hadrons is not the pointed source, but the whole sky and therefore their arrival directions are isotropic. This characteristic, together with morphological and timing differences, are the key features used for the signal/background discrimination in Cherenkov telescopes.

## 4.4 The Cherenkov effect

---

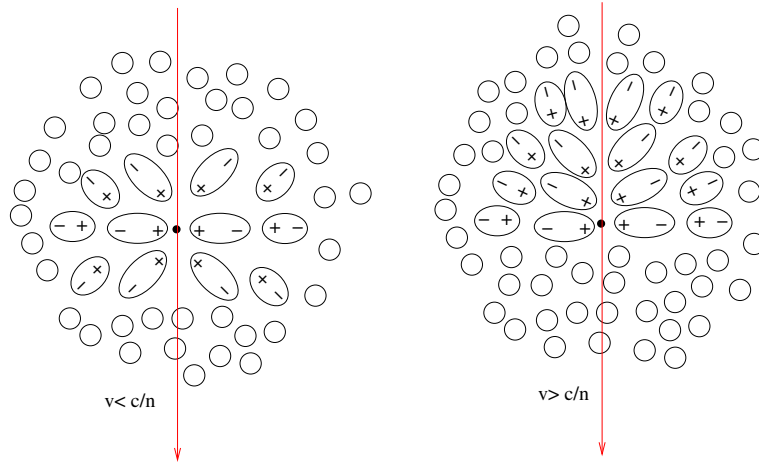


Figure 4.4: When a charged particle moves through a transparent medium, it instantaneously polarizes the medium. As long as the speed is  $v < c/n$ , the net field is zero (left). But if the speed exceeds the one of the light in the medium, then the dipoles get arranged asymmetrically, and a field is generated (right).

## 4.4 The Cherenkov effect

When a charged particle moves at superluminal speed in a transparent medium Cherenkov light is created. This condition can be achieved in any medium with refraction index  $n > 1$ . When the charged particle moves through the medium, it instantaneously polarizes it. As long as the speed is  $v < c/n$ , the induced polarization is symmetric. But if the speed exceeds the one of the light in the medium, then the generated dipoles get arranged asymmetrically, and an electric field is generated (see Figure 4.4). In this last situation, a shock wave is created, which is analogous to the supersonic shock front phenomenon (see Figure 4.5). The Cherenkov light can be used to develop detection techniques in different high energy physics disciplines, like in neutrino detectors in both ice and water, in water Cherenkov tanks, as well in atmospheric Cherenkov detectors like MAGIC.

Cherenkov light is emitted in a cone, with a characteristic angle  $\theta$ , in first order of:

$$\cos(\theta) = \frac{1}{n\beta} \quad (4.8)$$

$\beta$  being the speed in units of the speed of light. The previous formula is just the Huygens principle. A more detailed calculation, which can be performed by taking into account the recoil due to the emitted Cherenkov photons is:

## 4.4 The Cherenkov effect

---

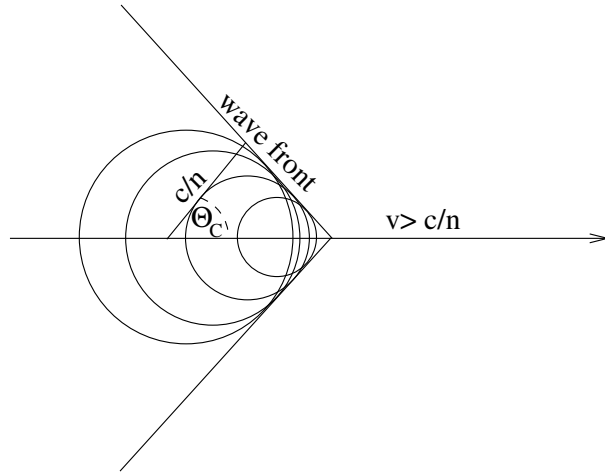


Figure 4.5: A simplified view of the formation of a shock wave front.

$$\cos\theta = \frac{1}{n\beta} + \frac{\hbar k}{2p} \left(1 - \frac{1}{n^2}\right) \quad (4.9)$$

But the second term of previous equation can be neglected due to the fact that the momentum of the Cherenkov photon ( $k$ ) is much smaller than the one of the charged particle ( $p$ ). From equation 4.8 it is possible to determine the particle minimum speed ( $\beta = n^{-1}$ ), and the maximum angle that would be achieved (with  $\beta = 1$ ). If  $m_0$  is rest mass of the charged article, the minimum energy of a particle moving in a medium to emit Cherenkov radiation is thus given by:

$$E_c^{thr} = \frac{m_0 c^2}{\sqrt{1 - \beta_{min}^2}} = \frac{m_0 c^2}{\sqrt{1 - (1/n)^2}} \quad (4.10)$$

The number of photons produced per *track length* can be described by [Yao06]:

$$\frac{d^2N}{dx d\lambda} = \frac{2\pi\alpha}{\lambda^2} \left(1 - \frac{1}{\beta^2 n^2(\lambda)}\right) \quad (4.11)$$

$$(4.12)$$

$\lambda$  being the wavelength,  $\alpha$  the fine-structure constant. In an EM shower, about 500 photons are created per GeV of primary  $\gamma$ -ray energy, taking  $\beta \approx 1$ .

### 4.4.1 Cherenkov light in the atmosphere

The energy of Cherenkov photons spans from infrared to ultraviolet, being more intense at higher frequencies. But on the other hand, there are also important

## 4.4 The Cherenkov effect

---

absorption processes, that displace the maximum number of photons that reach the ground to the blue region  $\lambda \simeq 330\text{ nm}$ . The most relevant attenuation processes for the Cherenkov light are the following ones:

- Absorption caused by the ozone layer ( $O_3 + \gamma \rightarrow O_2 + O$ ), it is important mainly in the stratosphere where almost all photons with wavelength lower than 290 nm are absorbed through this process.
- Rayleigh scattering produced by air molecules, that happens when the wavelength of the Cherenkov photon is bigger than the size of the molecules, and is proportional to  $\lambda^{-4}$ . During good atmospheric conditions, this is the process which causes the main attenuation of the Cherenkov light.
- Mie scattering by aerosol particles, water droplets and dust present in the atmosphere. The attenuation produced is especially important when atmospheric conditions are not optimal, i.e., if there is dust, pollution, clouds, fog, etc. The Mie scattering of Cherenkov photons has a strong dependence in the wavelength ( $\propto \lambda^{-1} - \lambda^{-1.5}$ ).
- Infrared absorption caused by  $H_2O$  and  $CO_2$  molecules, that occurs for Cherenkov photons whose wavelengths are above 800 nm.

One important feature of the EASs is that the total Cherenkov light of a shower is proportional, in first order, to the energy of the primary particle. This allows to use the atmosphere as a calorimeter for  $\gamma$ -ray initiated showers.

The refraction index in the atmosphere is not constant but changes due to the dependence of the density, pressure and temperature with the altitude. A simple model that assumes an isotherm atmosphere predicts a height dependence of the refraction index. In effect, the density of this model is given by the barometric formula [Hal86]:

$$\rho(h) = \rho_0 e^{-h/h_0}; \quad \rho_0 = 1.35 \text{ kg m}^{-3}, \quad h_0 = 7250 \text{ m} \quad (4.13)$$

$\rho$  being the density of the air, and  $h$  the height above the sea level. With this approximation, the refraction index becomes:

$$n(h) = 1 + n_0 e^{-h/h_0} \quad (4.14)$$

where  $n_0 = 0.00029$ . With this variable refraction index, and according to equation 4.8, the Cherenkov angle will increase with decreasing height. This dependence of the angle on height causes that the light emitted by the shower electrons and positrons at a range of different heights reaches the ground at

## 4.5 The Cherenkov imaging technique

---

approximately the same distance from the axis of the shower. This effect produces an enhancement of the Cherenkov light density, creating a sort of a ring, called hump. It typically occurs for a radius between 100 and 130 m from the center of the Cherenkov light pool. In the case of a shower, the Cherenkov light at the ground is the superposition of all the light emitted in cones integrated over the whole shower longitudinal path. It must be also taken into account that in an EAS, due to multiple scattering the trajectories of secondary electrons and positron are slightly deviated from the track of the incoming primary  $\gamma$ -ray, and consequently, the ideal shape of the previous ring gets smeared. The lateral Cherenkov photon distribution at 2200 m above sea level from a  $\gamma$ -ray initiated shower is shown in Figure 4.6. The photon density inside the Cherenkov light pool as a function of the energy of the primary particle is shown in Figure 4.7.

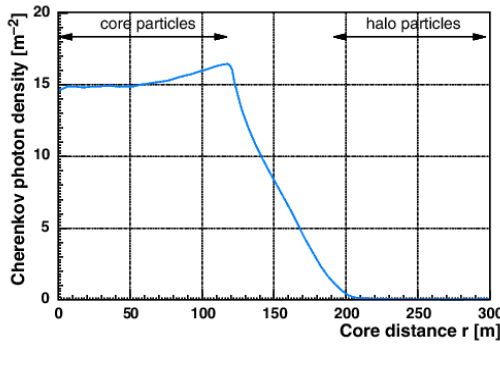


Figure 4.6: *Lateral Cherenkov photon density distribution development as observed at MAGIC altitude (2200 m. a.s.l.) from a vertical incident 100 GeV  $\gamma$ -ray originated shower. From [Wag06].*

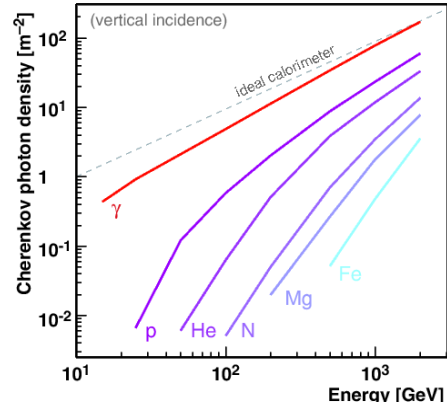


Figure 4.7: *Average Cherenkov photon density for vertical inciding showers, within 125 m of the core, generated due to different type of primary particles. The  $\gamma$ -ray initiated showers behave close to an ideal calorimeter. From [Wag06].*

## 4.5 The Cherenkov imaging technique

The basic idea behind of the Cherenkov imaging technique is shown in an schematic way in Figure 4.8. The mirror surface of the telescope collects a fraction of the Cherenkov light generated by the charged particles of the showers, and a camera composed of pixels (that are photo-detectors) located at the focal plane transforms the Cherenkov photons into electric pulses, what allows to record the image of the EAS.

## 4.5 The Cherenkov imaging technique

---

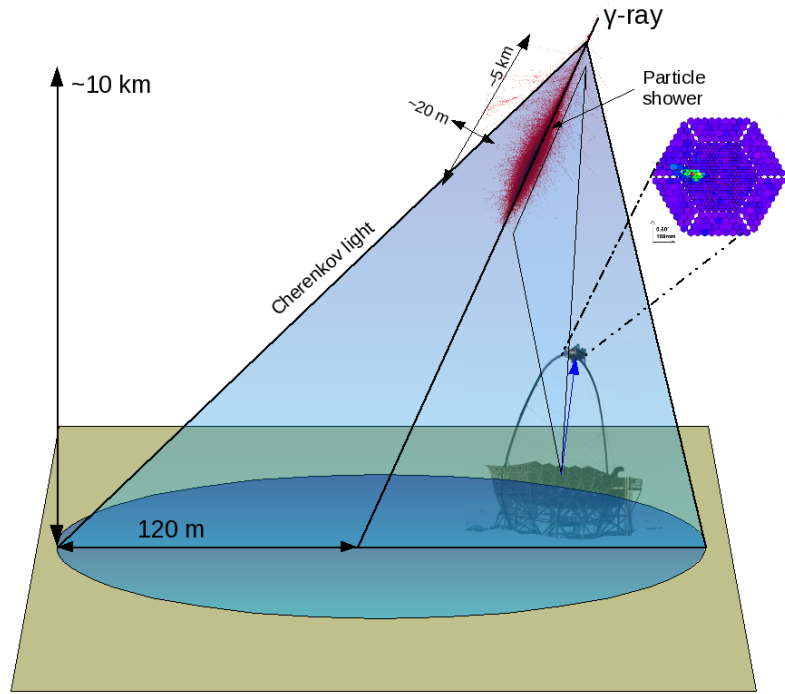


Figure 4.8: *Scheme of the basic idea of the imaging Cherenkov technique.*

One important task of this technique is to discriminate the EAS light from the fluctuations of the LONS, that is composed of light of stars, diffuse light from the Galactic Plane, zodiacal light, air-glow, diffuse Cherenkov light, polar light and artificial light, and is very dependent on the sky region (increases in the Galactic Plane), zenithal angle, and moon phase. In order to achieve this discrimination, IACTs use short exposure times ( $\approx 10$  ns) and trigger designs that make use of the spatial and temporal characteristics of the EAS.

The images recorded in the photo-detectors allow to derive the characteristics of the primary particle that originated the EAS. The recorded light is proportional to the total number of secondary particles generated in the cascade, and therefore also proportional to the original energy of the particle. In the case that the energy of the primary particle is  $> 1$  TeV, or when the impact parameter is larger than 120 m, a good knowledge of the lateral distribution (from detailed Monte Carlo simulations, for example) is also needed for a proper reconstruction of the original energy. The differences on the shower development between EM and hadronic showers get reflected in morphological differences on their recorded images, what permits to reject hadronic background events. The arrival time information in each individual photo-detector allows to further discriminate EM events from

## 4.5 The Cherenkov imaging technique

---

the hadronic ones, according to the differences in the temporal development of both showers. Additionally, the morphology of the recorded images allows to determine the arrival direction of the primary particles, allowing a further  $\gamma$ -hadron separation. (See Chapter 6 for a detailed description of analysis technique used in the MAGIC Collaboration).

# Chapter 5

## The MAGIC experiment

### 5.1 Introduction

MAGIC (Major Atmospheric Gamma Imaging Cherenkov)<sup>1</sup> is a system composed of two 17 m diameter IACTs located at El Roque de los Muchachos Observatory in the Canary island La Palma ( $28.8^{\circ}\text{N}$ ,  $17.9^{\circ}\text{W}$ ). It was designed to have a high sensitivity for low energies (above 25 GeV) and a fast response to variable phenomena. Both telescopes are able to quickly reposition themselves to any sky position for fast reaction to GRB alerts from X-ray or  $\gamma$ -ray satellites. The MAGIC telescopes are the biggest detectors of their kind working presently. The telescopes were renamed MAGIC *Florian Goebel* Telescopes in memory of the project manager of MAGIC-II, who died shortly before completing the second telescope in 2008.

The MAGIC telescopes acquire images of the fast flashes of Cherenkov light originated by atmospheric showers. The current energy threshold of MAGIC I telescope is around 25 GeV with the so-called sum trigger setup [Ali08] (used for pulsar studies), and 50–60 GeV with the standard setup [MP07]. The commissioning phase of MAGIC-II had recently finished when this thesis was written, and the system of two detectors had started to operate in stereo mode.

In the following sections the most relevant characteristics of the MAGIC telescopes will be briefly described.

### 5.2 Structure and mirrors

The dish of both telescopes has a 17 m diameter, with an active mirror surface of  $239 \text{ m}^2$ , in the case of MAGIC-I composed of square elements of  $0.5 \text{ m} \times 0.5 \text{ m}$ , and in the case of MAGIC-II, square elements of  $1 \text{ m} \times 1 \text{ m}$ . The mirrors

---

<sup>1</sup><http://magic.mppmu.mpg.de>

## 5.2 Structure and mirrors

---



Figure 5.1: *Photograph of the MAGIC array: MAGIC-I is the telescope on the left side, and MAGIC-II is the one on right side. From <http://magic.mppmu.mpg.de>.*

had an original reflectivity around 85%, that slowly degrades with the time. The actual reflectivity of M-I mirrors is estimated to be still above 80%. The focal distance to diameter relation ( $f/D$ ) is  $\simeq 1$ . The mirror dishes form parabolic shapes in order to achieve the minimum possible time spread of the Cherenkov light reflected into the camera, allowing to reduce the time window to extract the signal, granting a smaller noise integration, and thus a better signal to noise ratio. Another benefit from this design is the enhancement of the discrimination between hadronic and electromagnetic showers by making use of their different temporal characteristics (as hadronic shower development take longer than EM showers).

The structure of each telescope is built with carbon fiber together with epoxy resin in order to make it as light as possible, with the previously mentioned aim of being able to react fast to GRB alerts. The total weight of each telescope including the motors is about 60 tons. The weight of the telescopes makes the structure to slightly deform, what creates a degradation of the optical performance of the telescope, depending on the pointing position. To compensate for this effect, each mirror panel can be re-adjusted during the telescope operation by the Active Mirror Control (AMC) [Gar06].

## 5.3 Drive

The drive systems of the MAGIC telescopes exhibit a high degree of accuracy together with a fast repositioning time, despite of the dimensions of the structures. Each telescope has two azimuthal motors and one single motor for the elevation axis. The repositioning time is about 20 s for a 180° separation in azimuth.

A system named *starguider* monitors the pointing quality of the telescope, and allows a latter offline correction of any possible mispointing present in the data. The *starguider* consist of a charge-coupled device (CCD) camera located close to center of the dish, pointing to the MAGIC camera, with 4.6° of FoV, that measures the light from bright stars close to the FoV of the PMT camera. The PMT camera has some LEDs in its border that allow the *starguider* to recognize it. The actual telescope pointing is then determined with accuracy by comparing the position of the bright stars on the FoV with their known exact position in a catalog.

## 5.4 Camera

When the Cherenkov light hits the reflector of a Cherenkov telescope, it is reflected in the mirrors and focused into the camera. The camera is a key element of an IACT: the type and distribution of the used photo-sensors will influence the sensitivity, energy threshold and signal/background discrimination capacity.

The cameras of both MAGIC telescopes have 1.5 m diameter. The pixel region of MAGIC-I camera is hexagonal shaped (see Figure 5.2), and has an internal part composed by 397 PMTs of 30 mm (0.1°) diameter, with a total FoV of about 2.2°. This internal part is surrounded by 180, 60 mm diameter PMTs, with a total of ~3.6° FoV. All these PMTS have a maximum quantum efficiency (QE) peak of 25–30%. The pixel region of MAGIC-II camera is circular shaped (see Figure 5.4), and it is composed of 1039 PMTs of 25 mm diameter and 35% QE peak.

Each PMT is surrounded by a *Winston Cone*. These are hexagonal shaped light concentrators that compensate the dead space between the PMTs, that are round shaped. The hemispherical upper window of the PMTs is coated with a milky lacquer doped with a wavelength shifter. These add-ons result in the increase of the effective quantum efficiency of the PMTs of about 20% compared to flat window PMTs [Pan04].

## 5.5 Readout

The MAGIC electronic readout is situated in a building nearby the telescopes, called *Counting House*. Both MAGIC telescopes have their readout systems inside

## 5.5 Readout

---



Figure 5.2: *Photograph of the MAGIC-I camera. The hexagonal shaped pixel region is divided in two areas: inner one with smaller pixels and outer one with bigger pixels. The two camera lids are only open during night observation, except for maintenance works. From <http://magic.mppmu.mpg.de>.*

this building. To take the readout outside the cameras allows to substantially reduce their weight and eases the space constraints for the electronic devices, while making easier their maintenance. The telescope's control systems are also located the *Counting House*.

The electrical signal measured at each PMT is transformed into an optical one. Then, along the distance of about 160 m to the *Counting House*, the fast analog signals are transmitted over optical fibers, driven by Vertical Cavity Surface Emitting Laser Drivers (VCSELs). The use of optical fibers reduces the cable weight and allows electrical decoupling, noise immunity, as well as signal transmission with only weak attenuation and pulse deformation. In the *Counting House*, the optical signal is received and converted back into an electrical one with a fast Gallium Arsenide (GaAs) PiN photo-diode. At this point, the signal is divided in two branches. One of the branches goes to the trigger system, that will govern whether the acquisition system records a measurements. The other branch of the signal is digitized, presently with 2 GSample/s digitization systems.

The Cherenkov pulses from  $\gamma$ -ray showers are very short (1–3 ns). The parabolic shape of the reflector of the MAGIC telescopes preserves the time structure of these pulses. A fast signal chain allows to minimize the integration time and thus reduce the influence of the background from the LONS. In addition, a precise measurement of the time structure of the images can help to reduce the background due to hadronic events. In order to get the information from the Cherenkov pulse, its arrival time and amplitude are determined. This is achieved in MAGIC-I by using ultra-fast FADCs (flash analog to digital converters). The

## 5.6 Trigger system

---

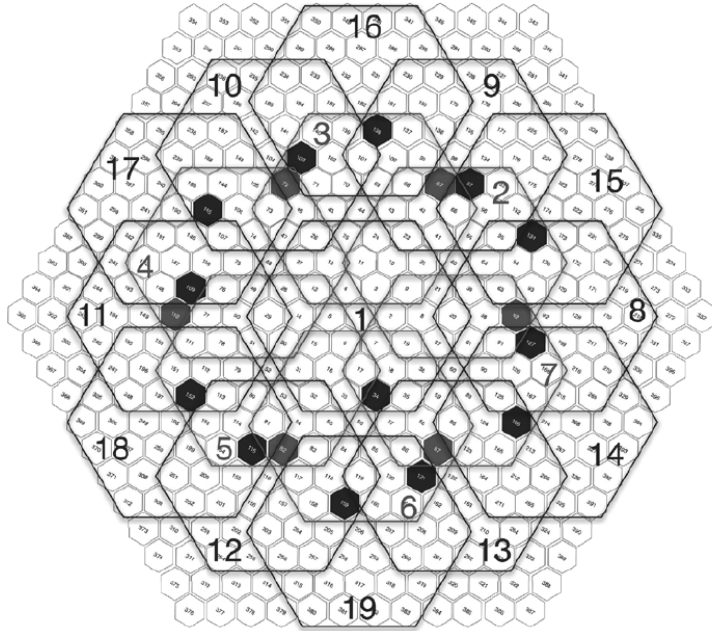


Figure 5.3: Standard trigger configuration of M1. The trigger area is restricted to the inner camera. The trigger cells are mutually overlapping to ensure an efficient coverage of all logic combinations of next neighbor pixels. From [MP07].

first phase of the MAGIC-I telescope (until February 2007) used a 300 MSample/s, 30 slice, 8 bit readout. The actual second phase of the MAGIC-I telescope has a low power fast analog sampler, with 2 GSsample/s, 80 slices and 10 bit readout. In the case of MAGIC-II, a low power analog sampler called *Domino Ring Sampler* coupled to a slower ADC is used. The system has a a 2 GSsample/s sampling frequency, with 12 bit resolution and 70 usable ADC channels [CGS09]. The ADCs continuously write the digitized amplitude information into a ring buffer. In case there is a trigger, the digitization process is stopped and the information contained in the ADCs is stored to a disk.

The system is set so the arrival times of the pulses are always located in the same ADC slice. The small differences on the arrival times between signals from different pixels are later corrected at calibration stage (see Chapter 6).

## 5.6 Trigger system

There are four trigger levels in the MAGIC system:

- **Level 0:** Also called discriminator threshold (DT). If the analog signal of one camera pixel exceeds a certain threshold, which can remotely be controlled and tuned by the central control software at the *Counting House*, a comparator gives an approximately 6 ns long logic output signal.

## 5.6 Trigger system

---

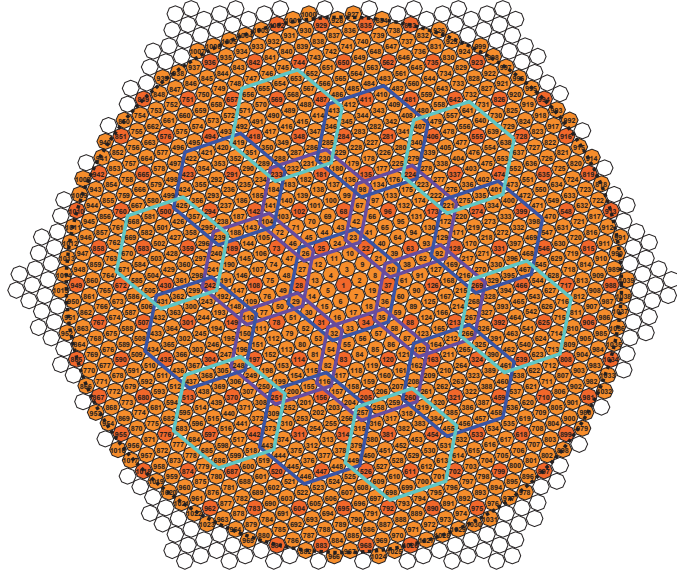


Figure 5.4: Scheme of MAGIC-II camera. Only colored pixels in a round configuration are equipped. The hexagonal shapes constitute the trigger region, which is almost twice as large as the trigger region of the first telescope. From [CGS09].

- **Level 1:** This trigger level requires that a minimum signal is present in at least four next neighbour pixels (4NN), inside a maximum allowed time range. If the trigger condition is fulfilled, the charge in all the pixels is recorded. The trigger area is centered inside each camera. For MAGIC-I it is about  $2^\circ$  wide and it is composed by 325 pixels and for MAGIC-II it is  $2.5^\circ$  wide and it is composed of 559 pixels. The 4NN configuration can be changed by setting different L1 trigger tables (2NN, 3NN, 5NN).
- **Level 2:** This trigger would allow a further online discrimination based on the shape of an event that already passed level 1. Up to now, the level 2 has not been implemented in the usual data taking modes of MAGIC.
- **Level 3:** With the new stereo operation mode a trigger mode has been set that only records events that exhibit time coincidence at the two telescopes. This is the standard mode of operation of the MAGIC system since MAGIC-II started to fully operate.

Another available trigger logic is the *analogue sum trigger*, that consists in the linear sum of the signals of large patches of pixels. The trigger area is doughnut shaped, surrounding the center of the camera. It comprises 24 different patches consisting of 18 pixels each, with four different shapes repeated 6 times (rotated in  $60^\circ$  angle steps, see Figure 5.5). The objective of this trigger setting is to reach to a lower threshold in energies, what is crucial to look for VHE emission from pulsars.

## 5.7 Calibration

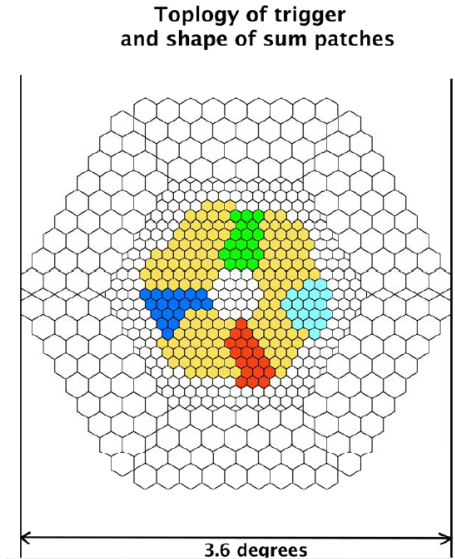


Figure 5.5: *The sum trigger configuration. The trigger topology (shape and size of patches), the pulse width (2.5–3.0 ns), the clipping threshold and the sum threshold have been optimized for a 10–20 GeV point-like  $\gamma$  source. Cherenkov light from low-energy showers illuminate the doughnut area around the camera center due to the small Cherenkov emission angle of typically  $0.3^\circ$ – $0.7^\circ$ . From [Ali08].*

## 5.7 Calibration

The goal of the calibration is to find the response of the whole light detection and amplification chain to get the correspondence between the incident photons from the Cherenkov light and the digitized information (see [Gau06] for details). For MAGIC-I different ultra-fast LEDs (frequencies of 370 nm, 460 nm and 520 nm) are used, that illuminate uniformly the camera with fast pulses of adjustable intensities. These pulses trigger the data acquisition, and are recorded in dedicated calibration runs and as interleaved events in the data runs, so gain variations during the data taking are corrected. For the case of MAGIC-II, the LEDs have been replaced by a frequency tripled passively Q-Switched Nd-YAG laser, operating at the third harmonic at 355 nm. The pulse width at 355 nm is 700 ps [CGS09].

## 5.8 MAGIC observation modes and file types

MAGIC observations are performed in two modes: *on-off* and *wobble* modes.

- During *on-off* observations the telescope points to the source position. In order to be able to subtract the background from the signal without any bias, observations of *off* regions are required: these *off* regions are those

## 5.8 MAGIC observation modes and file types

---

without any known source in their FoV but with the same characteristics (zenithal angle, galactic or extragalactic region).

- During *wobble* observations [Dau97], two opposite sky directions, each one  $0.4^\circ$  off the source, are tracked alternatingly for 20 minutes each. The *on*-source data are defined by calculating image parameters with respect to the source position, whereas background control (*off*) data are obtained from the same data set, but with image parameters calculated with respect to the corresponding position on the opposite side of the camera, the *anti-source* position. More *anti-source* positions can be defined, for example at the positions at  $90^\circ$  and  $270^\circ$  in the camera. The simultaneous measurement of signal and background makes additional dedicated *off* data unnecessary. In order to avoid an unwanted contribution from  $\gamma$ -events in the *off* sample, and to guarantee the statistical independence between the *on* and the *off* samples in the signal region, events included in the signal region of the *on* sample are excluded from the *off* sample and *vice-versa*. The disadvantage of the *wobble* mode is that it has a slightly lower efficiency than at the *on-off* mode.

The events are gathered and recorded in *runs*, identified by an unique *run number*. Before MAGIC-II was installed, each *run* was recorded in the *raid* system as a single file. The maximum number of events in each data run was limited by a maximum file size (1 GByte), containing events recorded during several minutes.

After the installation of MAGIC-II, the run numbering was changed. Run numbers are common for both telescopes when observing in stereo mode. Each run is recorded in the disk distributed in several files called *sub-runs*, these being defined according to a maximum size of 2 GBytes of disk usage. The concept of *run* has therefore changed, and now it is defined according to a pre-defined maximum elapsed time.

During the regular operation of the MAGIC system, three type of *runs* are recorded:

- **Pedestal runs:** These are taken at the beginning of the observation of each source and also after each full hour of observation time. They contain randomly triggered events, with the signature of the noise due to the LONS and the readout chain.
- **Calibration runs:** These are taken right after each pedestal run. They contain camera images of pulses from the calibration LEDs or the laser. They are used to determine the calibration constants.
- **Data runs:** These contain the triggered images from shower candidates. Additionally, interleaved calibration events are taken at a 25 Hz rate, in

## 5.8 MAGIC observation modes and file types

---

order to account for the evolution of the calibration constants (caused, e.g. by changes of the ambient temperature). Interleaved pedestals are also obtained from fractions of the images free of recorded showers.

There are other types of runs, used for technical and test purposes, that are not discussed here.

Some minutes after the MAGIC data start to be stored, an *on-site* analysis initiates the reduction of these data using the computing machines at the *Counting house*. This *on-site* analysis is described in Chapter 8. When the files are properly reduced, they are transferred by Internet to the MAGIC data center PIC<sup>1</sup> (Port d'Informació Científica) [Rei09]. The raw files are taped and will usually arrive to the data center by airmail several days after they are recorded.

---

<sup>1</sup><http://magic.pic.es>

# Chapter 6

## The MAGIC analysis method

### 6.1 Introduction

The opaqueness of the atmosphere to  $\gamma$ -rays prevents the direct measurement of VHE sources. On the other hand, it makes possible to develop detectors that make use of the secondary products from the original tiny VHE photon flux. As it was described in Chapter 4, IACTs record images of Cherenkov light from atmospheric showers originated by  $\gamma$ -rays, allowing to reconstruct the direction and energy of the original particle.

In this chapter the analysis technique used in MAGIC will be described in detail.

### 6.2 MARS

The scientific results presented in this thesis, as well as the main part of the MAGIC results have been obtained using the *MAGIC Standard Analysis Software* (MARS) [BW03, Alb08f].

MARS is a collection of programs for the analysis of the MAGIC data. It is written in C++, in the framework of the ROOT data analysis object-oriented software maintained at CERN<sup>1</sup>. The repository of the MARS code and the MAGIC data center are both located at PIC in Barcelona.

Another independent MAGIC analysis software exists, named *MARS Cheobs Edition* [BD09], used mainly by the MAGIC Würzburg group.

---

<sup>1</sup>Find details about ROOT at <http://root.cern.ch/>

## 6.2 MARS

---

### 6.2.1 Analysis scheme

The main tasks performed during a standard data reduction with MARS can be summarized by the following steps:

1. **First data quality selection**, according to electronic runbook information and data quality check plots.
2. **Signal extraction**. Determination of the charge content and arrival time of the Cherenkov pulses in FADC counts and FADC slices, respectively, for each PMT of the camera.
3. **Calibration** is done after subtraction of the pedestal signal, and consists in the conversion of each pixel's charge from counts to photo-electrons, and correction of the arrival times of individual pixels from individual cable length differences.
4. **Image Cleaning** of the calibrated images according to light content of pixels and arrival time distributions.
5. **Image parametrization** of cleaned images, according to *Hillas parameters*.
6. **Second data quality selection**, according to individual (sub)run qualities, quantified by parameters like event rate before and after image cleaning, cloudiness and humidity.
7. **Event classification** as a “ $\gamma$ -ray coming from the source”, or event of hadronic background origin.
8. **Energy estimation** of individual events.
9. **Determination of the direction** of the original particle.
10. **Determination of excess events** coming for the source, and the statistical significance of this excess, and optionally, creation of a *sky map* of the position of the excess events.
11. **Differential and integral flux, and light curve** determination in case of significant signal detection, or determination of **upper limits to the flux** if no significant signal was present.

## 6.3 The Crab Nebula

The Crab Nebula is an stable and bright VHE emitter, that is used as the *standard candle* for MAGIC and the other detectors of its kind. Being a very well studied source, it is used as *test bench* of the analysis chain as well as for cross calibration between different detectors. Along the description of the analysis in this chapter, a data reduction of some MAGIC Crab Nebula measurements performed by the author will be used to exemplify the different steps.

The Crab Nebula is the remnant of the famous supernova explosion that occurred in AD 1054 and that was documented by Chinese, Korean, and Native American witnesses [May39, CCM99]. The Nebula is located at  $\simeq 2$  kpc distance. This object emits radiation in almost all energy bands, and it is the best studied non-thermal astronomical object. It is widely accepted that the engine of the system is a pulsar located inside the nebula. The signature of the pulsar has also been detected in most of the energy bands, from radio to GeV energies, as well as recently measured by MAGIC [Ali08].

This source was the first one to be detected in the VHE band, by the Whipple telescope, in 1989 [Wee89]. It is the strongest steady galactic emitter on this energy band, and has been extensively studied in the 100 GeV to 80 TeV energy range. A detailed description of Crab Nebula VHE observation and interpretation can be found in [Alb08f] and references therein.

The data analyzed here as an example of the data reduction procedure were taken by MAGIC-I during the nights of 2009 January 22, 24 and March 17. The data were taken in *wobble-mode* and with standard trigger settings, under good weather conditions. In total, the observation time was 7.4 h.

## 6.4 Monte Carlo simulated $\gamma$ -rays

The reconstruction of  $\gamma$ -ray initiated air shower characteristics requires detailed Monte Carlo (MC) simulations of the shower development and of the response of the telescope. In particular, when using the atmosphere as a calorimeter in the way IACT experiments do, it is not possible to perform a direct calibration of the system as for calorimeters like the ones on satellite detectors.

The MC simulation program of MAGIC uses the software CORSIKA 6.019 [HKC98].  $\gamma$ -ray initiated showers are simulated, under the US standard atmosphere, and the output Cherenkov photons that arrive to ground level are recorded. In a second step, the so-called *reflector* program first computes the Cherenkov light attenuation due to both Rayleigh and Mie scatterings. Then the reflexion of the photons on the dish mirrors is simulated, in order to determine their distribution, incoming direction and arrival time on the camera plane. At next step, the *camera* program simulates the response of the telescope's PMTs

## 6.5 Data selection

---

and both trigger and DAQ systems. *Camera* also performs a smearing of the arrival directions according to the optical point spread function (PSF) of the telescope. After this point, the simulated events are ready to be used in the MAGIC analysis chain. Details on *reflector* and *camera* programs can be found in [Maj05].

## 6.5 Data selection

Data quality selection is usually performed in two steps, corresponding to steps 1 and 6 of the scheme shown in section 6.2.1.

At step 1, the information from the *electronic runbook* and the data-quality check reports from different sub-systems will allow to discard measurements if either the atmospheric conditions or the performance of the detector are not good enough. The quality check reports are part of the work presented in this thesis, and are described in Chapter 7.

This preliminary study of the data will allow to perform dedicated non-standard data reductions that compensate adverse conditions, as happened with the analysis described at Chapter 9 where due to hardware problems, the data calibration required a dedicated procedure. In a similar way, moon or twilight observations require a more severe image cleaning.

At step 6, more detailed methods can be used to reject bad quality data. This is performed in run or sub-run basis. The main parameter that is used is the *event rate*, that can be studied before or after image cleaning. The DTs of the telescopes (see section 5.5) are adjusted in such way that an stable rate (dependent on the zenithal angle) is achieved. The rate is influenced with almost any possible hardware or atmospheric condition: high clouds may cause drops in the rate, while technical problem during observation may manifest as fluctuations in the rate. The light from a passing car will be shown as a sudden increase of the rate.

Parameters like the estimation of the cloudiness in the camera FoV obtained from a pyrometer installed in the MAGIC-I telescope, the humidity as measured in the site weather station, and the DT settings allow to make additional data rejection.

For the case of the Crab Nebula test data sample, the rate after cleaning was used as main indicator of the quality of the data, as shown in Figure 6.1. After this criterion, the DT and cloudiness parameters were checked, but it was found that they were inside the safe limits. From the total of 7.4 h of observation time, 6.2 h survived for further analysis.

## 6.6 Signal extraction and calibration

---

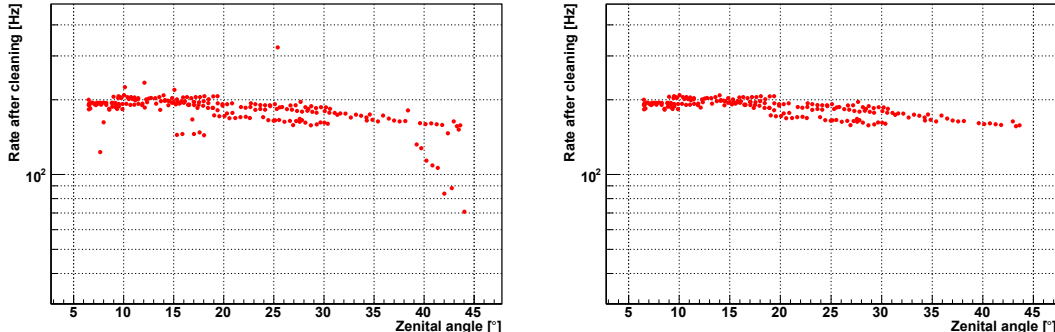


Figure 6.1: *Left:* Event rate after image cleaning of the analyzed Crab Nebula sample, where some outliers can be perfectly identified. *Right:* Event rate after image cleaning of the selected runs of the Crab Nebula sample.

## 6.6 Signal extraction and calibration

When an event is triggered, the light recorded in all PMTs of the camera is read. The Cherenkov pulses last few ns, depending on their particle origin. In the actual MAGIC I settings, a time window of 40 ns is opened where the light collected by the PMT is digitized at this stage in units of counts, in function of the arrival time, quantified in FADC slices. The FADC have 80 slices, corresponding each one to a 0.5 ns time window.

The signal stored at each PMT is extracted, and later transformed from counts to photo-electrons. These two tasks are performed by a MARS executable named *callisto*.

### 6.6.1 Signal extraction

In order to extract the signal from the measured information at the PMTs, the first task that is performed is the determination and subtraction of the pedestal flux coming from the LONS and photons of sources close to the telescope, together with the noise of the readout chain. For that, special *pedestal* runs are taken, as explained at section 5.8. Any change of the pedestal signal along the observations is corrected by using the region without expected signal in the FADC window from the data runs.

There are several methods implemented in order to extract the signal from the FADC samples. Here, the most relevant four ones will be described (see [Alb08c] for further details):

- **Cubic Spline:** This extractor interpolates the pedestal-subtracted charges in the FADC slices using a cubic spline algorithm. After the position of

## 6.6 Signal extraction and calibration

---

the spline maximum is determined, there are two ways to determine the charge: by the amplitude of the spline maximum or the integration of the spline in a fixed size window. The pulse arrival time can be determined in two ways: by the position of the spline maximum or by the position of the half maximum at the rising edge of the pulse.

- **Digital Filter:** This extractor determines the charge as the weighted sum of  $n$  consecutive FADC slices. The weights are used to give more importance to the slices where most part of the signal is contained, in order to reduce the noise contamination on the extracted signal. These weights are determined by the expected shapes of the signals, obtained from MC simulation and are different for cosmic, MC and calibration pulses.
- **Fixed Window:** This extractor adds the pedestal-subtracted FADC slice charges of a given number of consecutive slices at a fixed position. The window has to be chosen large enough to cover the complete pulse, and therefore adds up more noise than the other extractors. On the other hand, the reconstructed signals do not have any bias. Finally, no arrival time is determined with this extractor.
- **Sliding Window:** This extractor searches for the maximum integral charge of a given quantity of consecutive pedestal-subtracted FADC slices. The arrival time is determined as:

$$t = \frac{\sum_{i=i_0}^{i_0+ws-1} s_i t_i}{\sum_{i=i_0}^{i_0+ws-1} s_i} \quad (6.1)$$

$i$  being the FADC slice index, starting from slice  $i_0$  and running over a window of size  $ws$ . The  $s_i$  are the pedestal-subtracted FADC slice contents at slice position  $i$ .

Both the digital filter and spline extractor are based in the selection of the highest FADC sample, and therefore they will be biased towards mistaken LONS fluctuations with small signals. On the other hand, they are preferred over unbiased extractors like the fixes window, that would sum up higher number of FADC samples, picking in the process much more LONS. In general, the digital filter is a faster process when compared to the cubic spline. On the other hand, the spline allows to treated correctly those signals that arrive too early or too late in the FADC digitization window. In the different analysis performed in this thesis the cubic spline algorithm was used.

## 6.7 Image cleaning and parametrization

---

### 6.6.2 Calibration

The main purpose of the calibration is to determine the *conversion factors* from FADC counts to photoelectrons. Another task performed consists in the correction of the raw arrival times as calculated by the signal extractor from the different cable lengths, in order to assign physical meaning to these arrival times.

The conversion factors are determined from the collected light from calibration pulses, stored in calibration and data runs (see section 5.8). There are different techniques to obtain these conversion factors, the one used in MAGIC is the so-called *F factor*, also known as excess noise factor method [GB05].

This method assumes a Poisson's variance of the number of incoming photons, an uniform photo-electron detection efficiency, and that the excess noise introduced by the readout chain does not depend on the signal amplitude. The following formula is used to determine the number of photo-electrons [ML97]:

$$\langle N_{phe} \rangle = \frac{F^2 \cdot Q^2}{\sigma_Q^2 - \sigma_P^2} \quad (6.2)$$

Where  $\sigma_P$  is the resolution of the signal extractor (coming mainly from the noise of the LONS), and measured as the standard deviation of the pedestal,  $\sigma_Q$  is the standard deviation of the measured charge and  $Q$  is mean reconstructed (and pedestal-subtracted) charge.  $F$  stands for the excess noise factor, previously measured in the laboratory, and has been measured as  $F^2 = 1.15$  for MAGIC-I telescope, and  $F^2 \simeq 1.10$  from MAGIC-II. The conversion factor for each pixel will be :

$$C = N_{phe}/Q \quad (6.3)$$

The arrival times are corrected by using a certain pixel (*n.<sup>o</sup> 2*) as reference, so all the arrival times are relative to this pixel and therefore comparable. Further details on MAGIC calibration can be obtained in [Gau06].

After the data is calibrated the information from some key subsystems is added to the data, like the reports from the drive system (that will be used to know the pointing of the telescope), the reports from the *starguider* system (that will allow to minimize the effect of any present mispointing) and the information from the MAGIC weather station (so quality cuts can be performed).

## 6.7 Image cleaning and parametrization

Image cleaning and parametrization of calibrated images is performed by the *star* program. The mispointing correction by using *starguider* camera information is usually applied here, but can also be done later in the analysis.

## 6.7 Image cleaning and parametrization

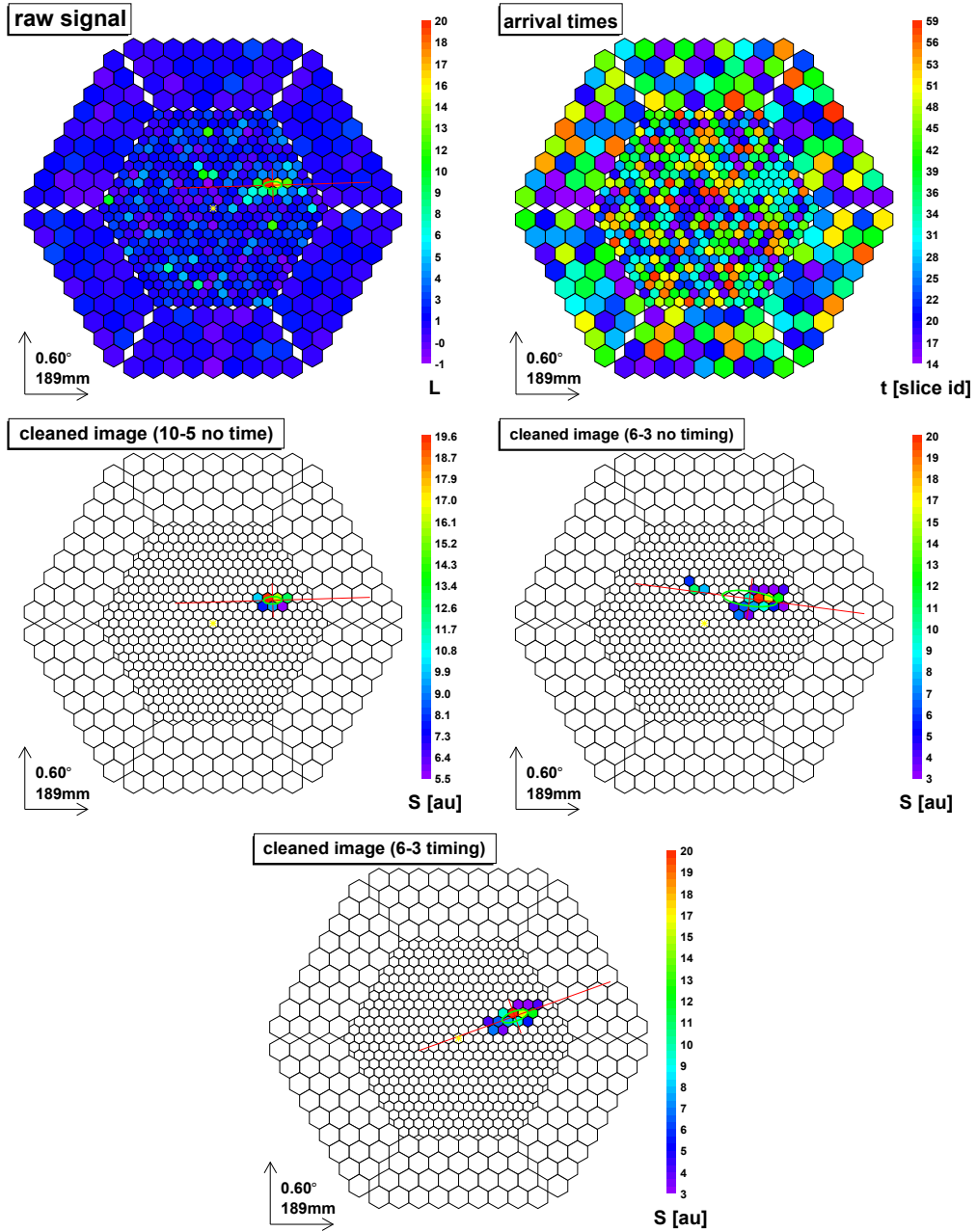


Figure 6.2: Illustrative event images of a Monte Carlo simulated  $\gamma$ -ray shower. First row: display of raw recorded data (left) and arrival times information (right). Second row: comparison of standard absolute image cleaning with 10-5 phe minimum levels (left) and 6-3 phe minimum levels (right). Bottom: image obtained with the time image cleaning (6-3 phe minimum levels and 4.5 ns and 1.5 ns as time constrains). The simulated  $\gamma$ -ray source, located in the center of the camera is identified by a yellow star. From [Ali09a]

### 6.7.1 Image cleaning

The aim of the image cleaning is to remove the pixels that only contain noise and to keep those that have signal from the atmospheric shower. The image cleaning is also called sometimes *tail cut*.

The introduction of high accuracy FACD system at 2007 allowed to make use of the arrival times of the pixels to further improve the image cleaning [Ali09a].

Different image cleaning procedures are available in MARS. The commonly used one is called *absolute* image cleaning. This cleaning is performed in two steps: First, groups of at least two pixels with a phe content higher than a minimum value  $q_1$  are identified. The grouped pixels conform the *core(s)* of the image, and the pixels of the layer surrounding it, called *boundary* pixels, can be added to the cleaned image in a second step if they exceed a signal  $q_2$ , that is lower than the one required for *core* pixels. It is also required that a *boundary* pixel has at least another boundary pixel exceeding  $q_2$ . In the case of MAGIC-I, the different size of inner and outer pixels require that the charge threshold is scaled accordingly. In the next step, the mean arrival time of all *core* pixels defined before is calculated. The individual *core* pixels with arrival time outside an interval  $\Delta t_1$  with respect to the mean arrival time are excluded. For the boundary pixels, it is required that the arrival time difference between each boundary pixel and its neighbor *core* pixels is smaller than a fixed value  $\Delta t_2$ .

The usual image cleaning setting used in MAGIC analysis is an *absolute* one with  $q_1 = 6$  phe,  $q_2 = 3$  phe,  $\Delta t_1 = 4.5$  ns and  $\Delta t_2 = 1.5$  ns. When arrival time information is not used, a harder image cleaning is applied(e.g. the (*absolute*  $q_1 = 10$ phe and  $q_2 = 5$ phe configuration). Figure 6.2 shows the effect of different image cleanings on a raw image. Special data sets, like the ones measured during moonlight or twilight, require a stricter image cleaning. Timing analysis of pulsars, on the other hand, may benefit from softer image cleanings.

The Crab Nebula test sample was cleaned with the default configuration mentioned before: Absolute 6–3 phe image cleaning with 4.5–1.5 ns time constrains.

### 6.7.2 Image parameters

The cleaned images can be characterized by the so-called *Hillas Parameters* [Hil85], that are related to the statistical moments up to third order of the images. Some other parameter are also determined at this step, that will be used later for the estimation of the characteristics of the original particle. In what follows, a brief description of some of these parameters will be exposed (see Figure 6.3 for a graphical representation). The following parameters are independent of the position of the source in the camera field:

## 6.7 Image cleaning and parametrization

---

- **Length:** The RMS spread of the light along the major axis of the shower, which is a measure of its longitudinal development. This parameter is usually larger for hadron-induced showers than for  $\gamma$ -induced ones.
- **Width:** The RMS spread of the light along the minor axis of the shower, which is a measure of its lateral spread. The broader lateral development of hadronic showers make this parameter larger for hadron-induced showers than for  $\gamma$ -induced ones, and therefore can be a good indicator for background rejection.
- **Size:** Total charge contained on the cleaned image pixels, measured in *phe*. This parameter is roughly proportional to the energy of the primary particle (for impact parameters smaller than 120 m), and it is therefore used as the main indicator to estimate the energy of the primary  $\gamma$ -ray that initiated the air shower.
- **M3Long (Third longitudinal moment):** Third moment of the image along its major axis, that indicates the shower direction. This parameter is used to determine which side of the image is closer to the direction of the incident particle, and can be useful for background rejection. For small images this parameter is not well defined due to statistical fluctuations and its background rejection power drops dramatically.
- **Conc(N):** Fraction of the light content contained in the N brightest pixels with respect to the total light content of the image. It is used to estimate the compactness of the shower image, which tends to be larger in  $\gamma$ -induced showers than in hadronic origin ones, and therefore can be used for  $\gamma$ -hadron separation. In the standard analysis chain, the concentration of the two brightest pixels (*Conc (2)*) is normally used, and it is abbreviated as *Conc*.
- **Time RMS:** It is the RMS of the arrival times of all pixels that survived the image cleaning, and measures the time spread of the arrival times regardless of the pixel position in the camera. As  $\gamma$ -ray and hadron originated showers have a different time development, this parameter is good for  $\gamma$ -hadron discrimination.
- **Leakage:** This parameter gives the ratio of the content of the pixels in the outermost ring of the camera to the total content of the cleaned pixels of the event *size*. It is used as indicator of events with an important fraction of their image contained outside the camera, what is more likely to happen in the case of higher energy events. When an important fraction of an event is not contained in the camera, it is not possible to determine reliable Hillas

## 6.7 Image cleaning and parametrization

---

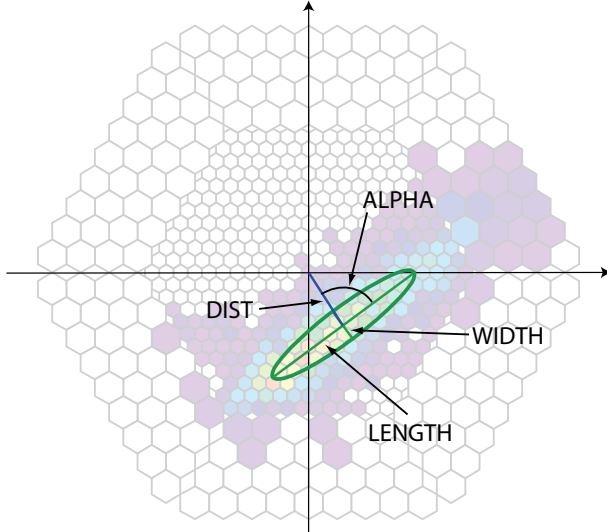


Figure 6.3: *Parametrization of a shower image with Hillas parameters, from [Alb08f].*

parameters. Therefore, the events with a high leakage (minimum value from 0.1 to 0.3) are discarded.

- **Asym:** It is the distance from the pixel with highest content to the center of the ellipse, projected onto the major axis. It is used to estimate the asymmetry of the light distribution along the major axis, what helps to determine the shower's head and tail.

The following image parameters are dependent on the position of the source in the camera field.

- **Alpha:** It is the angle between the major axis of the shower ellipse and the connection line from the source position to the center of gravity of the image. Images from  $\gamma$ -ray showers from the source will point to the source position in the camera, and therefore will have small *alpha* values. On the other hand, hadronic showers are isotropically distributed and their *alpha* distribution tends to be flat, what makes it the most powerful discrimination parameter.
- **Dist:** It is the angular distance between the center of gravity of the shower image and the expected source position in the camera. It is used as an estimator of the impact parameter of the shower, improving the accuracy of the energy estimation
- **Time Gradient:** This parameter is obtained from a linear fit of the arrival time versus the space coordinate along the major axis. The slope of the previous fit is called *time gradient* of the image, and the sign of this

## 6.8 Estimation of the characteristics of the primary particle

---

parameter is defined as positive if the arrival time increases when moving away from the location of the source in the camera, and negative otherwise. In order to determine this parameter, the position of the source has to be assumed. As it happens with the *Time RMS* parameter, it is possible to use the *Time Gradient* parameter to take advantage of the differences on the temporal development between the hadronic and  $\gamma$ -ray originated showers.

## 6.8 Estimation of the characteristics of the primary particle

The steps 7, 8 and 9 summarized in section 6.2.1 have the goal of estimating the main characteristics of the primary particle that originated the air shower, by using the information of the previously determined image parameters. The characteristics to be determined are three: the nature of the particle, its energy, and its direction.

These tasks are performed by two MARS programs *osteria* and *melibea*, re-laying on the *Random Forest* regression method (RF) [Bre01] (see [Alb08b] for its implementation for the MAGIC analysis). The RF method is used for background suppression, energy estimation, and arrival time direction estimation. This last characteristic can be also determined by a parametrization.

### 6.8.1 Rejection of the hadronic background

The previously described image parameters (see section 6.7.2) can be used to discriminate images from  $\gamma$  showers from the much more abundant images of hadronic origin, as well as those from isolated muons and fluctuations of the LONS. Methods like static, dynamical, or scaled cuts on image parameters have been developed and commonly used for the  $\gamma$ /hadron separation. On the other hand, most of MAGIC analysis make use of the previously mentioned *Random Forest* method for this task. The different MAGIC data analysis discussed in this thesis also uses RF for  $\gamma$ /hadron separation. Other methods for hadron suppression in IACTs also exist (e.g. model analysis method of H.E.S.S experiment [dR09]).

The RF method uses a *forest* of decision *trees* to classify each event. The decision *trees* are created (trained) from MC simulated  $\gamma$ -ray events and real events from hadron events from unfiltered data samples. When available, *off* data samples are used for the hadron training. On the other hand, often happens that it is not possible to find an adequate off data sample. In these cases, it is justified to use an *on* data sample as background estimator, since even for sources as bright as the Crab Nebula, less of 1% the stored events have  $\gamma$ -ray origin.

## 6.8 Estimation of the characteristics of the primary particle

---

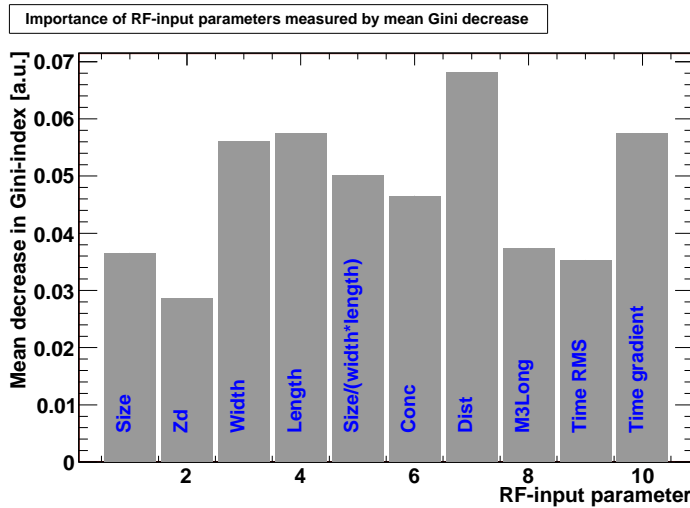


Figure 6.4: *Relative importance of the RF input parameters, characterized by the mean decrease in Gini index, for the performed Crab Nebula analysis.*

The individual *trees* are grown by using a list of image parameters with a proven discrimination power and finding adequate cuts on these parameters over the training sample. From the training sample, a binary decision tree can be constructed, subdividing the parameter space first in two parts depending on one of the parameters, and subsequently repeating the process again and again.

For event classification, events will be characterized by a vector  $v$  in the selected image parameter space. Each event will pass through all decision *trees*. At the first node of each *tree* the event will take one of the paths (called the “left” or “right” path here), by comparing the image parameter value of  $v$  and the reference value previously decided in the training. At next levels, the event will further proceed left or right according to components on  $v$  and reference values on the nodes, until it reaches a terminal node. The event  $v$  will then get the  $l$  value of the terminal node. When all *trees* have assigned a  $l$  value to  $v$ , a parameter called *hadronness* ( $h$ ) is calculated:

$$h = \frac{\sum_{i=i_0}^{n_{trees}} l_i(v)}{n_{trees}} \in [0, 1] \quad (6.4)$$

When  $h$  is closer to 0, it means that the event is more  $\gamma$ -like, and when  $h$  is closer to 1, it means that the event is hadron-like. This allows to use the *hadronness* as main background rejection parameter (together with the angular parameter, see section 6.9).

In order to grow the trees and train the *hadronness* parameter, two type of image parameters are used. The fist type is composed by those parameters that

## 6.8 Estimation of the characteristics of the primary particle

---

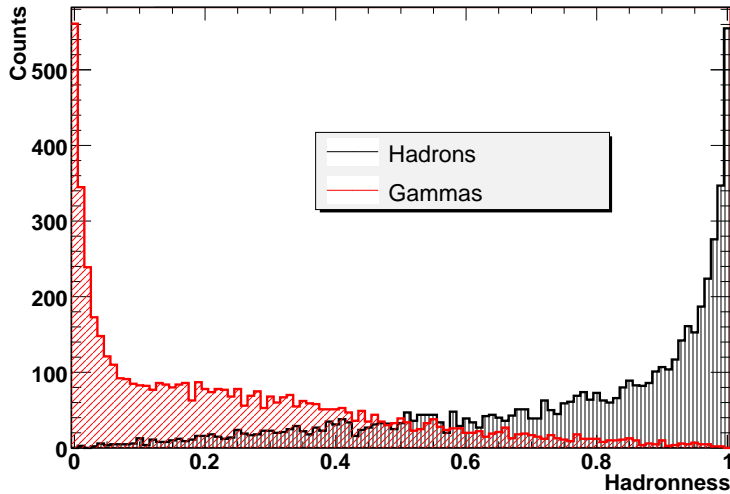


Figure 6.5: Distribution of hadronness for a sample of  $\gamma$ -rays MC (red) and hadrons (black).

have proven good separation capacities. They can be source position dependent or independent. The standard parameters used in MAGIC are *width*, *length*, *conc*, *time RMS*, *dist*, *M3Long* and *time Gradient*, being the latter three source dependent<sup>1</sup>. The other type of parameters are the ones used for correlation purposes: It is known that the separation power of some parameters strongly depends on *size* and *zenith distance (ZD)* parameters. By including these two parameters, the background rejection cuts will scale dynamically with variation on the *size* and *ZD*.

The discrimination power of individual parameters can be identified by the decrease of the Gini index (see Figure 6.4).

### 6.8.2 Energy reconstruction

As it was mentioned before, the *size* of those events with impact parameter below 120 m is in first order proportional to their energy. The energy also has a dependence in other parameters like the ZD, impact parameter, and atmospheric extinction.

The energy of the  $\gamma$ -ray events is also reconstructed by the *Random Forest* method, with training MC  $\gamma$ -ray samples. A MC simulated  $\gamma$ -ray sample with known primary  $\gamma$ -ray energy is filled in bins of logarithmic energy. The classifier will be trained to accommodate each event in a particular energy bin. After training, each tree will assign a specific energy range to each event, that will be

---

<sup>1</sup> *M3Long* and *time Gradient* are source independent parameters but for the RF train their sign is set with respect to the nominal source position and therefore become source dependent.

## 6.8 Estimation of the characteristics of the primary particle

---

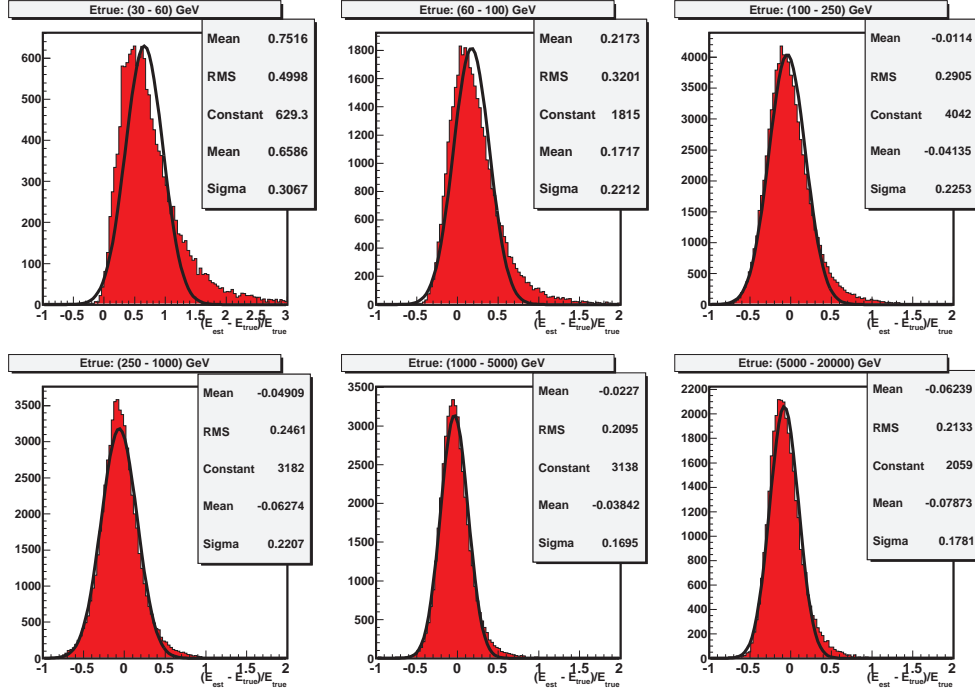


Figure 6.6: Resolution of the energy reconstruction for some energy bins, tested with a MC sample. Note that for lower energies the Gaussian function does not describe the distributions as well as it does for higher energies.

analogous to the previously described *hadronness* parameter (noted as  $H_i$ ). The estimated energy of the event will be:

$$E_{est} = \frac{\sum_{i=i_0}^{n_{trees}} E_i H_i}{\sum_{i=i_0}^{n_{trees}} H_i} \quad (6.5)$$

The parameters used normally are *width*, *length*, *size*,  $\log(\text{size}/(\text{width} \times \text{length}))$  *conc*, *leakage*, *ZD*, *dist* and *time gradient*, being the last two source position dependent. The obtained energy resolution is about 20 % for energies from 100 GeV to 10 TeV, increasing at lower energies and decreasing for higher ones (see Figure 6.6). The energy of the  $\gamma$ -rays is usually overestimated at low energies ( $< 100$  GeV) and underestimated at higher energies ( $> 10$  TeV) as can be seen in Figure 6.7). The finite resolution and bias require that the energy estimation is later corrected by the spectrum unfolding, using a migration matrix (see Figure 6.8).

## 6.8 Estimation of the characteristics of the primary particle

---

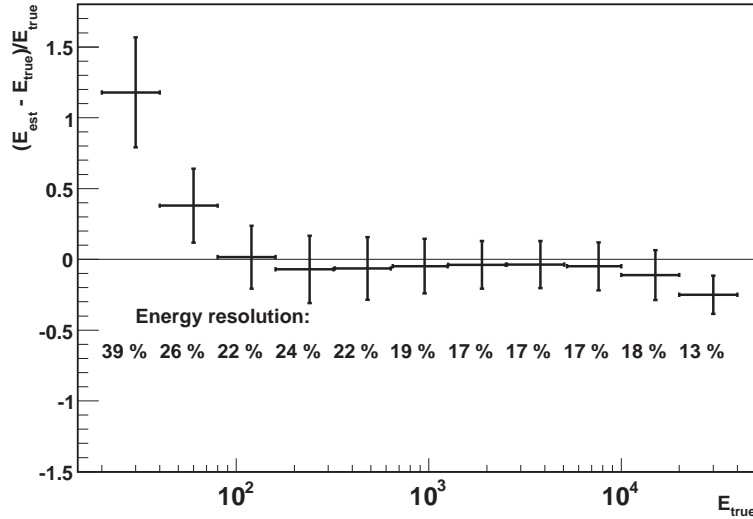


Figure 6.7: *Resolution and bias of the energy reconstruction, as a function of the energy. The numbers below the data points display the energy resolution, obtained from Gaussian fits as it is shown in the previous figure.*

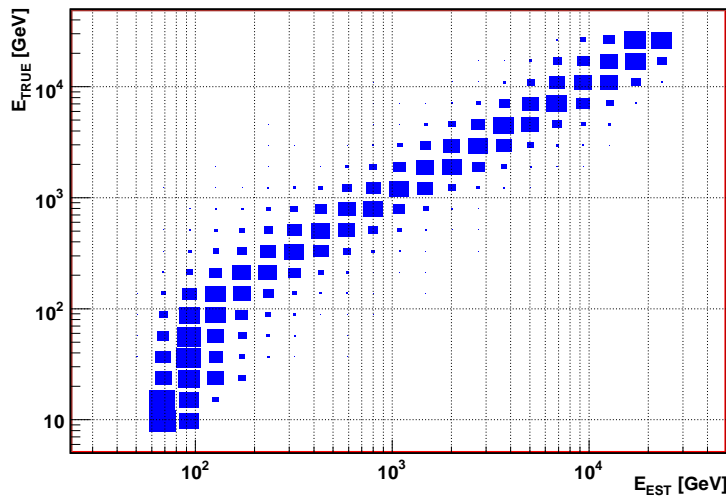


Figure 6.8: *The migration matrix describes the migration of events from bins of true energy to bins of estimated energy. It is determined from a MC sample, independent from the one used for the RF training. During the unfolding procedure, this matrix is used to convert the excess event distributions in estimated energy into distributions in true energy. Note the degeneracy towards low energies in the 100 GeV region.*

## 6.8 Estimation of the characteristics of the primary particle

---

### 6.8.3 Arrival direction reconstruction

The angular parameter *alpha* assumes a well known position of the source. It is trivial to determine the position of the source in *on-off* mode of observation of point-like sources, as it is just in the center of the camera. But in the observation of extended sources, or when the source position is not in the center of the camera like in *wobble mode*, source dependent parameters (*alpha* and *dist*, for example) have to be recalculated in terms of other reference points.

A method that does not require to assume a source position relies on a parameter named *disp*, that is defined as the angular distance between the source direction and the center of the image along the major axis of the image [Fom94, Dom05]. The *disp* parameter can be determined in two ways in MARS: by a parametrization or by again using a *Random Forest* method.

#### 6.8.3.1 Disp parametrization

*Disp* is parametrized in MARS by the following formula:

$$disp = A(size) + b(size) \frac{width}{length + C(size) \cdot leakage} \quad (6.6)$$

*A*, *B*, and *C* are determined by a MC  $\gamma$ -ray sample, in which *disp*  $\equiv$  *dist*. Once *disp* is calculated there are two possible solutions in the source position determination, corresponding each one to the *head* and the *tail* of the image, on opposite sides of the COG. The correct solution is obtained by the *M3long* parameter, that will allow to select the source position as the closest to the *head* of the image. This last step is often called *ghost-busting*.

#### 6.8.3.2 Disp from RF

Another method exists in MARS that allows to reconstruct the *disp* parameter using a RF method [SS09], in a similar way as it is done for the Energy reconstruction. The default parameter are *width*, *length*, *size*, *length/width leakage*, *ZD*, and *asym*. It has been found that by using this method the sensitivity slightly improves.

### 6.8.4 Event based quality cuts

At *melibea* stage some event basis quality checks are performed, with the aim of rejecting unphysical events as well as those without a possible reconstruction. The typical cuts are:

## 6.9 Determination of excess events and statistical significance

---

- **Spark cut:** This cut is performed to get rid of some unphysical events, named *sparks*. These are produced by discharges between the PMTs shielding and some other metallic elements. A fast flash of light may be partially reflected towards the PMTs by the plexiglass window and illuminate the pixels around the sparky one. These events are characterized by very concentrated charges, and can be recognized using a logarithmic *size* vs. *conc* graph.
- **Size cut:** For a normal analysis, a lower *size* cut of  $\sim 80$  *phe* is performed to get rid of events which have not a chance to be reconstructed reliably, what also speeds up the analysis process.
- **Filter cuts:** Events that will be difficult to reconstruct will be filtered here. Typical values for rejection are *leakage* ( $>0.2$ ), *number of core pixels*  $<3$  and *number of islands*  $>3$ .
- **Dist Cut:** When there is no *off* data available, a *size* dependent *dist* cut is sometimes applied to flatten the *alpha* distribution in order to allow the extrapolation of the background level into the signal region. An absolute *dist* cut can be also useful to remove very distant showers for which the energy reconstruction does not work so well.

## 6.9 Determination of excess events and statistical significance

The events candidates to be coming from the source are identified performing the so-called  *$\gamma$ -hadron separation*. This separation is performed by a cut in the *hadronness* parameter and defining a signal region in the *angular parameter*, that can be the previously defined *alpha* parameter or another one, called  $\theta^2$ , that will be described later.

The distribution of the angular parameter *alpha* is expected to peak at  $0^\circ$  for events from a point-like  $\gamma$ -ray source, while it is expected to be flat for events of an *off* source (or the *off* positions in *wobble* mode). A signal region corresponding to low values of *alpha* parameter is chosen after performing the *hadronness* cut and scaling the *off* sample to the *on* level, to determine the number of events coming from the source. As *alpha* can have positive or negative sign, it is the absolute value of this parameter what is usually plotted (see Figure 6.9).

The angular parameter  $\theta$  is the angular distance between the source position and the estimated shower arrival direction of an event. Here, the source position is estimated by the *disp* parameter. Events from the source will have small  $\theta$  value. It is better to use the square of  $\theta$ , because by doing that the distribution

## 6.9 Determination of excess events and statistical significance

---

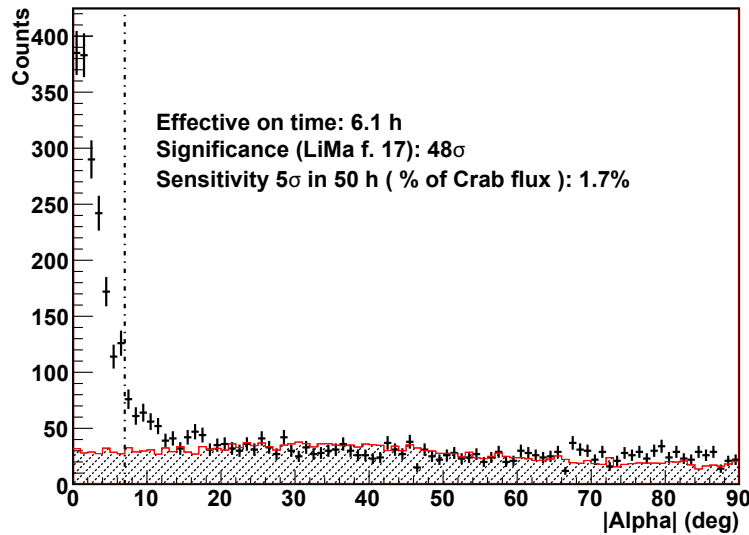


Figure 6.9: *Distributions of the alpha parameter for on and off observations (after normalization) from the Crab Nebula test sample, after applying detection cuts. The off sample was determined from 3 off regions in the camera. The  $\gamma$ -ray excesses from the source are expected in the low alpha region, and are calculated as the difference between the number of on and off events in this region.*

of background events is flat<sup>1</sup> while the  $\gamma$ -ray signal is expected to show an exponential shape peaking at zero. In consequence, it is possible to use this parameter to define a signal region and determine the events coming from the source as it is done with *alpha*. Figure 6.10 shows a  $\theta^2$  plot obtained from the Crab Nebula data sample.

If  $N_{on}$  is defined as the number of events from the *on* sample in the angular parameter signal region as defined before, and  $N_{off}$  the number of events from the *off* sample in the same region, we can obtain the number of events from the source, also named *excess events*, as:

$$N_{exc} = N_{on} - \beta N_{off} \quad (6.7)$$

$\beta$  being the on/off normalization factor.

The statistical significance of the measured excess events is evaluated by a test where the null hypothesis is such that all the observed excess events are coming from with background fluctuations [LM83]. The significance level is determined by this expression:

$$S = \sqrt{2} \left( N_{on} \ln \left[ \frac{1 + \beta}{\beta} \left( \frac{N_{on}}{N_{on} - N_{off}} \right) \right] + N_{off} \ln \left[ (1 + \beta) \left( \frac{N_{off}}{N_{on} - N_{off}} \right) \right] \right)^{1/2} \quad (6.8)$$

---

<sup>1</sup>When using source-independent parameters in the *hadronness* estimation.

## 6.9 Determination of excess events and statistical significance

---

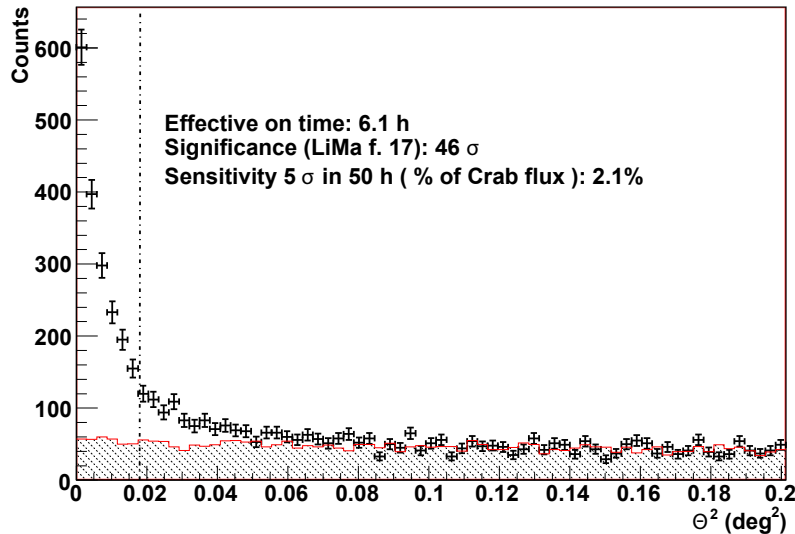


Figure 6.10:  $\theta^2$  distribution of on and off events (after normalization) after detection cuts from the Crab Nebula test sample. In the same way as with the alpha analysis, the off sample was determined from 3 off regions in the camera. The  $\gamma$ -ray excess from the source are expected in the low  $\theta^2$  region, and are calculated as the difference between the on and off events in this region. The  $\theta^2$  analysis was performed with source independent image parameters and it is slightly less sensitive than the alpha one.

As for an stable  $\gamma$ -ray source the significance scales with the square root of time, the detecting power of an IACT or of one of its analysis methods is sometimes quantified as  $\sigma/\sqrt{t}$ , where  $t$  is time in hours, from an analysis of the Crab Nebula.

A signal from a source is accepted as a detection when the statistical significance level is  $5\sigma$  (as it has been established in the VHE astronomy community). The “ $5-\sigma$ “ detection of a new source should be claimed if it was obtained with *a priori* selected cuts (see below), otherwise it will have to be corrected by the number of trials performed. Indeed, given a probability  $P$ , the corrected probability  $P_{\text{corrected}}$  after  $n$  trials given by  $P_{\text{corrected}} \simeq 1 - (1 - P)^n \simeq nP$  for small probabilities. As described in [LM83], the probability of detecting at  $n \sigma$  detection level when there is not a real detection follows a normal distribution, and therefore the probability calculated by:

$$P = \text{errf}(\sigma/\sqrt{2}) \quad (6.9)$$

Being  $\text{errf}$  the error function. The post trial significance will therefore be:

$$P_{\text{corrected}} = \text{errf}^{-1}(P^n)\sqrt{2} \quad (6.10)$$

## 6.9 Determination of excess events and statistical significance

---

### 6.9.1 Sensitivity

Apart from the  $\sigma/\sqrt{t}$  from the Crab Nebula, another parameter more frequently used to describe the detecting capacity of an analysis is the *sensitivity*. Assuming a Gaussian approximation of eq. 6.8, the sensitivity after an observation time  $t$  is calculated by the following expression:

$$S(t) = \frac{N_{exc}}{\sqrt{N_{off}}} \sqrt{\frac{t}{T}} \quad (6.11)$$

where  $T$  is the time for which  $N_{exc}$  and  $N_{off}$  were measured. This parameter is usually given in relative flux level of a source with respect to Crab Nebula flux, after 50 hr of observation:

$$S_{5\sigma, 50h}(t) = 5 \frac{N_{off}}{\sqrt{N_{exc}}} \sqrt{\frac{T}{t}} \quad (6.12)$$

The previous expression will tell the minimum flux (so, the faintest possible source) in *Crab units* that will be possible to detect with a  $5\sigma$  significance level after 50 hr of observation. The sensitivity obtained in the *alpha* analysis of the test sample was “1.7%”: A source with a flux 1.7% of the Crab Nebula will be detected on a  $5\sigma$  level after 50 h of observation. The  $\theta^2$  analysis is slightly less sensitive (2.1%), as expected due to the fact that source dependent parameters were not used on it.

### 6.9.2 Cut determination

In general, two types of cuts are used in the  $\gamma$ /hadron separation process, namely *detection* and *loose* cuts. The *detection* cuts are the cuts that look for the best source detecting power, while *loose* ones are applied after detection, and they sacrifice detecting power in exchange of being able to gather more statistics (more excess and background events). *Loose* cuts also allow to have a larger collection area, and minimize the systematic errors. They are used for spectrum determination.

Two possible ways to determine what *detection* cuts apply to a data set are:

- **Optimize sensitivity or significance from Crab Nebula data:** Being a stable and strong source, the Crab Nebula is used as standard candle, and therefore adequate for cut optimization. An scan on *hadronness* and signal region is performed for different *size* bins, and the parameters that give higher significance or sensitivity are used (usually both are maximum for similar parameters). It is important to choose a Crab sample with similar

## 6.9 Determination of excess events and statistical significance

---

Table 6.1: *Set of cuts used to estimate the significance of the  $\gamma$ -ray signal from the Crab Nebula.*

| Type      | <i>hadronness</i> | <i>alpha</i>            | combined acceptance |
|-----------|-------------------|-------------------------|---------------------|
| Detection | $\leq 0.05$ (41%) | $\leq 7.5^\circ$ (87 %) | 36%                 |
| Loose     | dynamical (90%)   | dynamical (80%)         | 72%                 |

characteristics to the ones of the data to be analyzed: data should be of the same epoch to ensure a similar telescope performance and the *ZD* range should be similar. It should be also taken into account that the expected spectrum of the analyzed source should be similar to the reference source, because a different shape would have an effect on the optimal cuts. Table 6.1 shows the cuts determined from the Crab Nebula test sample significance optimization, together with the used *loose* cuts.

- **Quality Factor:** This method seeks for the best relation between the background reduction with the number of surviving  $\gamma$  events. The required input events are from MC test samples and *off* data, independent from the training sample. The efficiency (acceptance) of a certain value of *hadronness* and signal region cuts would be:

$$\epsilon_\gamma = \frac{N_\gamma(\text{after cuts})}{N_\gamma^{\text{total}}} \quad (6.13)$$

The quality factor or *Q-factor* to maximize will be:

$$Q = \frac{\epsilon_\gamma}{\sqrt{\epsilon_{\text{had}}}} \quad (6.14)$$

$\epsilon_{\text{had}}$  being the efficiency for the hadrons, calculated in the same way as  $\epsilon_\gamma$ . A minimum  $\epsilon_\gamma$  can be imposed to ensure that a minimum number of  $\gamma$ -s survive the selection.

### 6.9.3 Sky Map

The *disp* method, together with an adequate camera acceptance description allows to build an *sky map* of the arrival directions of  $\gamma$ -ray events. The background estimation is the main problem to solve when producing an sky map, because the camera acceptance for  $\gamma$ -rays is not homogeneous, and other factors like stars, malfunctioning pixels, trigger inefficiencies and zenith angle dependence have an important effect on the sky plot. One benefit of *wobble* observations is that the background estimation can be done with the same data set, an thus, minimizing some of the previous problems.

## 6.9 Determination of excess events and statistical significance

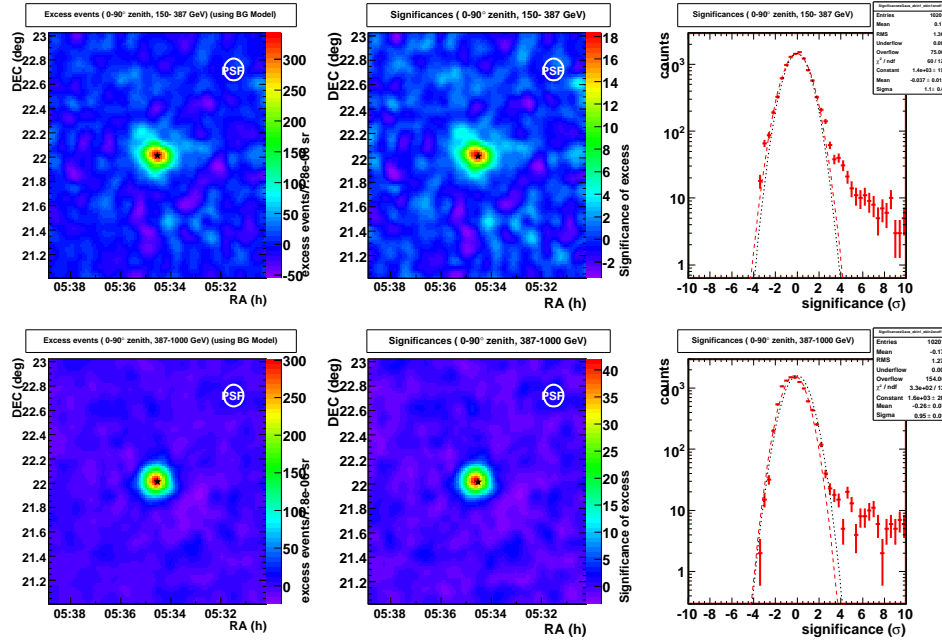


Figure 6.11: *Maps of excess events (left) and significance (center), together with the significance distribution (right), for the Crab Nebula test data sample. A black star indicates the catalog position of the Crab Nebula. Upper plots correspond to low energy region  $\simeq 150-400$  GeV while lower ones to the intermediate energy region  $\simeq 400-1000$  GeV.*

Sky plots are produced in MARS by a program called *celestina*. It produces sky plots with three background estimation methods, depending on the observation mode, there are methods for *on-off* and *wobble*, and the *model* method, suitable for both observation methods.

The *on-off* method uses the *off* data to build the background, assuming a flat distribution in the arrival directions before camera acceptance. The *wobble* method is based on the projection of the events with a reconstructed incident direction located in the half of the camera where the *anti-source* is located into the other half of the camera, where the *wobble* position is located. The *model* method creates a model of the camera that resembles its behavior [Del09].

After the background is built, a map of excess events is generated by subtracting to the  $\gamma$ -ray candidates the distribution of background events. The excess map is smoothed using a gaussian PSF with  $\sigma = 0.1^\circ$ , corresponding to the  $\gamma$ -ray PSF of the telescope<sup>1</sup>. Figure 6.11 shows the sky map obtained for the Crab Nebula.

<sup>1</sup>The  $\gamma$ -ray PSF, also known as the angular resolution, can be determined as the  $\sigma$  of a Gaussian fit to the  $\theta^2$  distribution of the MC simulated  $\gamma$ -rays.

## 6.10 Spectrum and light curve

The differential energy spectrum of a source is defined as the number of  $\gamma$ -rays arriving to Earth, per unit of energy, time and area:

$$\frac{dF}{dE} = \frac{dN_\gamma(E)}{dt dA(E) dE} \quad (6.15)$$

Following the previous formula,  $dA(E)$  and  $dE$ , the *effective collection area* of the detector and the *effective on time* of the observation, respectively, will have to be determined.

To derive a differential spectrum of a detected source, the previously mentioned *loose* cuts are applied. These *loose* cuts have the benefit of increasing the number of excess events while enlarging the effective area.

### 6.10.1 Effective collection area

The effective collection area is defined as the area in which  $\gamma$ -rays can be observed by the detector, folded with the detector efficiency  $\epsilon(E, \theta, \phi, b)$ , after all analysis cuts:

$$A_{eff}(E, \theta) = \int_0^{2\pi} \int_0^\infty \epsilon(E, \theta, \phi, b) b db d\phi. \quad (6.16)$$

Here  $E$  is the energy of the primary  $\gamma$ -ray,  $\theta$  is the zenith angle,  $\phi$  is the azimuth angle, and  $b$  is the impact parameter. The efficiency  $\epsilon(E, \theta, \phi, b)$  is obtained from MC simulated events, by computing the ratio between the events surviving the analysis cuts and the total simulated events:

$$\epsilon(E, \theta, \phi, b) = \epsilon(E, \theta, \phi, b)_{trigger} \epsilon(E, \theta, \phi, b)_{cuts} \quad (6.17)$$

$$= \frac{dN_{\gamma, cuts}(E, \theta, \phi, b) \epsilon(E, \theta, \phi, b)}{dN_{\gamma, total}(E, \theta, \phi, b) \epsilon(E, \theta, \phi, b)} \quad (6.18)$$

The effective area increases with the zenithal angle, moderately for low angles but significantly for higher ones ( $\gtrsim 45^\circ$ ) .

### 6.10.2 Effective on time

The effective on time of an observation is defined as the time within which the telescope was effectively recording events. Non-ideal detectors have a dead time when they are not able to record data. This dead time is caused because, while the detector is processing one event, another one may occur and this last one will

## 6.10 Spectrum and light curve

---

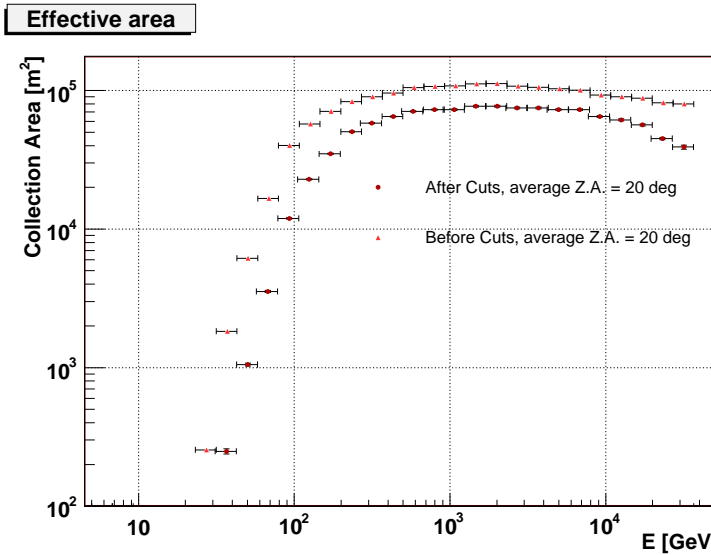


Figure 6.12: *Effective collection area, before and after loose cuts, obtained from the MC test sample.*

not be recorded. This dead time has to be subtracted from the observation time. The effective on time is given by:

$$t_{eff} = \frac{N}{r} \quad (6.19)$$

$N$  being the total number of recorded events and  $r$  the event rate if the detector was ideal. Assuming that a number of events in a time range is given by a Poisson distribution, the distribution of time differences between consecutive events is exponential. The “ideal detector” event rate is therefore obtained by a fit to an exponential function of the time differences of two consecutive events:

$$\frac{dN}{dt} \propto \frac{N}{\sigma} \quad (6.20)$$

The dead time of MAGIC is of the order of 1%. Apart from the dead time correction, all the time when the telescope is not recording data, for example when changing from *wobble* position, will have to be taking into account in the calculation of the  $t_{eff}$ .

### 6.10.3 Unfolding

Due to the finite resolution of the detector and the bias introduced in the energy estimation, the measured spectra get distorted. The unfolding procedure intro-

## 6.10 Spectrum and light curve

---

duced in MARS (described in detail in [Alb07d]) tries to correct this distortion. Mathematically the distortion can be described as:

$$Y_i = \sum_{j=1}^{nb} M_{ij} S_j \quad (i = 1, \dots, na) \quad (6.21)$$

Here  $Y_i$  is the number of measured events in the estimated energy bin  $i$ ,  $S_j$  is the number of events in the true energy bin  $j$ ,  $M$  is the migration matrix,  $na$  is the total number of estimated energy bins and  $nb$  is the number of true energy bins.

The aim of the unfolding procedure is to invert the relation 6.21, to recover the true energy distribution  $S$  from the measured distribution  $Y$ . The apparently simplest approach would be to invert the matrix  $M$ , but it has two inconveniences: first, there are large correlations between adjacent bins, and second,  $M$  is usually not invertible. A better method, called *forward unfolding* uses an *a priori* parametrization of the true energy distribution  $S$  that for the  $\gamma$  ray spectrum of many sources it typically a power law. The solution obtained by the *forward unfolding* method is the best fit to the true energy distribution of events with their errors, but it is not able to provide the actual values of the individual data points.

More elaborated methods, that are able to provide the unfolded data points, are available in MARS. They are the *Tikhonov*, *Bertero* and *Schmelling* methods, described in detail in [Alb07d]. There is a certain degree of arbitrariness as to which unfolding result should be considered representative and final. In MAGIC a selected unfolding result is considered representative if all other unfolding methods yield results, which are also acceptable and statistically consistent with the selected result. In addition, it is required that also the previously described *forward unfolding*, using a reasonable parametrization of  $S$ , gives a consistent result. An uncertainty due to the unfolding procedure can be determined from the spread of the  $S_j$ , obtained from the different unfolding methods.

In Figure 6.13, the spectrum of the Crab Nebula test sample unfolded using the *Bertero* method for the 1 off *alpha* analysis is shown. The resulting spectrum is fitted to a log-logarithmic power law [Mas04], and gives a differential flux of:

$$\frac{dF}{dE} = (5.14 \pm 0.20) \cdot 10^{-10} \left(\frac{E}{r}\right)^{-2.16 \pm 0.07 - (0.16 \pm 0.07) \cdot \log(E/r)} \text{ TeV}^{-1} \text{s}^{-1} \text{cm}^{-2} \quad (6.22)$$

with  $r = 0.3$  TeV. The uncertainties shown in eqn. 6.22 are statistical only. See later for a brief comment on systematic uncertainties.

## 6.10 Spectrum and light curve

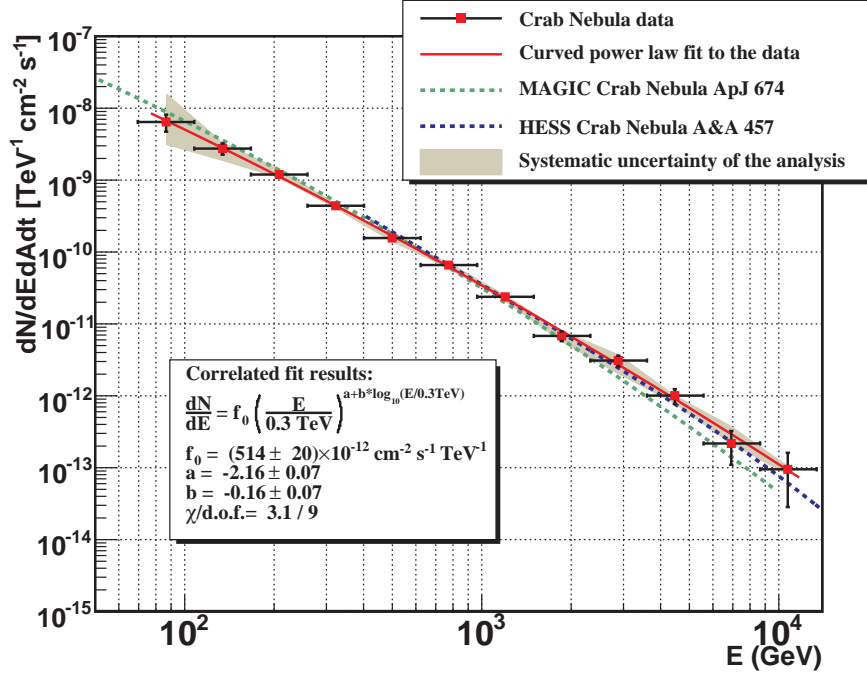


Figure 6.13: *Measured Crab Nebula differential spectrum from the test data set. Vertical error bars denote  $1\sigma$  statistical uncertainties, while the shaded region is the estimation of the systematic uncertainty from the analysis, obtained comparing different analysis methods ( $\text{Alpha}$ ,  $\theta^2$ , both with one and three off regions) and different unfolding methods. A log-logarithmic curved power law was fit to the data between 80 GeV and 10.5 TeV. For comparison, the published parametrization from MAGIC (green dashed line) and H.E.S.S. (blue dashed line) are shown.*

### 6.10.4 Light curve

In the context of MAGIC analysis, a *light curve* is defined as the time evolution of the integral flux above a certain energy. In the same way as in the spectrum calculation, *loose cuts* are used for the light curve determination.

The measured Crab Nebula light curve is shown in Figure 6.14. A fit to a constant flux resulted in a reduced  $\chi^2 = 44.5/38$  ( $P = 22\%$ ), that indicates the stability of the flux. The average integral flux above 200 GeV, obtained from the previous fit is:

$$F(E > 200 \text{ GeV}) = (2.26 \pm 0.08) \times 10^{-10} \text{ cm}^{-2} \text{s}^{-1} \quad (6.23)$$

Here the uncertainties are statistical. These results are compatible with previous  $\gamma$ -ray measurements of the Crab Nebula in the VHE band.

## 6.11 Upper limit calculation

---

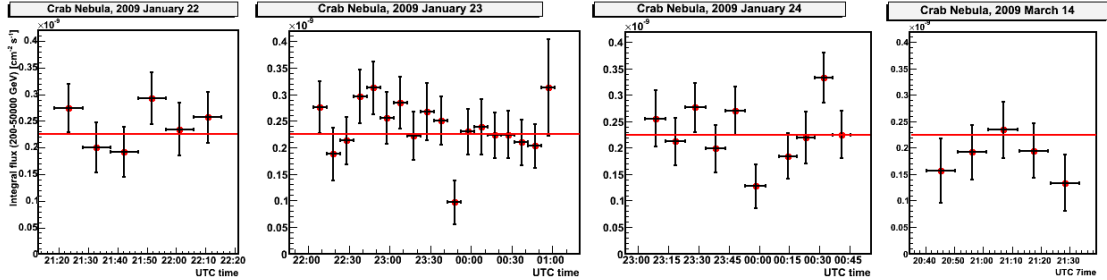


Figure 6.14: Combined 10 m light curve of the four selected nights of the Crab Nebula test sample. The dashed line indicates the measured mean flux, obtained by a constant fit to the whole data sample

## 6.11 Upper limit calculation

Whenever no significant  $\gamma$ -ray signal is detected from some observations, it is possible to calculate an upper limit to the emission of the source. The method used in MAGIC is based in the prescriptions of Rolke et al. [Rol05]. The method used here (Rolle model “3”) computes confidence intervals for the number of excess events assuming a Poisson distribution of *on* events, in the presence of background approximated as Gaussian. The uses a fully frequentist treatment of the uncertainties in the efficiency and background estimate using the profile likelihood method. This method is able to provide a correct coverage by construction.

If it is assumed that the  $\gamma$ -ray spectrum is a general function of the energy, the differential flux measured can be written as [ND09]:

$$\frac{dF}{dE} = \phi(E) = K_0 S(E) \quad (6.24)$$

Being  $K_0$  a normalization constant. This constant can be expressed as:

$$K_0^{ul} = \frac{N_{exc}^{ul}}{t_{eff}} \frac{1}{\int_0^{\infty} A_{eff}(E) S^{res}(E) dE} \quad (6.25)$$

Where  $S^{res}(E)$  is the energy spectrum smeared with the energy resolution. The integral flux upper limit for a certain confidence level will be:

$$\phi^{ul}(E > E_0, c.l.) = K_0^{ul} \int_{E_0}^{\infty} S(E) dE \quad (6.26)$$

In is possible to derive differential upper limits by assuming that locally around energy  $E_0$ ,  $S(E)$  follows a power-law in a small energy region. If we

## 6.12 Systematic errors

---

cut in the reconstructed energy as  $E_1 < E < E_2$  then the mean  $\gamma$ -ray energy will be:

$$E_0 = \frac{\int_0^\infty E S(E) A_{eff}(E, E_1, E_2) dE}{\int_0^\infty S(E) A_{eff}(E, E_1, E_2) dE} \quad (6.27)$$

and therefore obtaining an upper limit of:

$$K = \frac{N_{ul}}{\int_0^\infty S(E) A_{eff}(E, E_1, E_2) dE} \quad (6.28)$$

## 6.12 Systematic errors

In addition to statistical uncertainties, the reconstructed  $\gamma$ -ray flux is also affected by systematic uncertainties. As an IACT cannot be directly calibrated, the energy determination and detector efficiencies have to be estimated from MC simulations. In addition, Earth's Atmosphere shows short and long term fluctuations in its characteristics. The telescope itself is built from elements which may change over time (for example mirrors loose reflectivity while PMTs degrade). Even if the performance of the telescope is regularly monitored (see Chapter 7) and the MC simulations adjusted accordingly, some systematic errors will still be present. As described in [Alb08f], systematic errors affect both the energy and flux level determination.

The energy estimation can be affected by changing atmospheric transmission, reflectivity uncertainty of the mirrors, uncertainty of the PMT's quantum efficiency and their F-Factor, among other influences. The biggest contribution comes from the uncertainty of the photo-detection efficiency, which includes the transmission through the plexiglass in front of the camera, dust in the Winston cones and the PMT's quantum efficiency. In total, the uncertainty in the energy scale is estimated to be  $\simeq 16\%$  [Alb08f].

The flux level uncertainty is caused among other reasons, by dead channels, and trigger inefficiencies. This uncertainty is estimated to be  $\simeq 11\%$  [Alb08f]. In the case of “Crab-like” power law spectrum, the systematic error has been estimated to be  $\pm 0.2$  in the spectral slope [Alb08f].

# Chapter 7

## Data quality check software

### 7.1 Introduction

This chapter is an overview of the MAGIC data quality check program. This program carries out a continuous check on the telescope performance and the quality of the data taken. This code was developed in collaboration by R. de los Reyes [De 08] and the author of this thesis.

The MAGICDC (MAGIC Data Check) program is launched everyday at 9:00 UT, after the telescopes are switched off. It checks all the data recorded during the night by all the subsystems of the telescope, in order to detect problems and solve them as soon as possible. Its last step is the evaluation of the most relevant quality parameters, that is done by the automatic daily-check task.

The MAGICDC software is run at the computing system of the MAGIC site, in the *muxana* machine (see section 8.2 of next chapter for a description of the system). The results can be accessed at the MAGICDC web page at La Palma<sup>1</sup> and also at the MAGIC data center at Port d'Informació Científica<sup>2</sup> (PIC), where all plots are mirrored and stored.

In the coming sections a detailed description of the software will be exposed.

### 7.2 MARS and MAGICDC

The data quality check software uses the standard analysis software for the MAGIC experiment, MARS, that is described in Chapter 6. Apart from the MARS macros (displayed inside diamonds in Figure 7.1), some MARS executables are used:

---

<sup>1</sup>[www.magic.iac.es](http://www.magic.iac.es)

<sup>2</sup><http://magic.pic.es/>

### 7.3 MAGICDC: Telescope data quality check

---

- *Merpp*: converts the “raw” and ASCII format of the report output of MAGIC subsystems to ROOT package format. The output files have the “.root” extension that will be inherited by the following analysis products.
- *Callisto*: calibrates the data. The calibrated files can be recognized by the “\_Y\_” characters in their name. Besides the standard “.root” files, it is also able to directly calibrate the “raw” files.
- *Star* calculates the Hillas parameters. The executable output files can be recognized by the “\_I\_” characters, and are called star files.
- *Showplot*: displays graphical information of the output summary files, and allows to convert this graphical information as Postscript file format (“.ps”), as well as other formats like “.pdf”, “.png”, etc.

*Callisto* and *star*, as well as other executables from MARS not used in the data quality check software, use input cards to modify the analysis parameters. The input cards files usually have the default name of the executable name followed by the “.rc” extension. This is the case of “callisto.rc” and “star.rc”.

The analysis executables, *callisto* and *star*, run based on “sequences”. A sequence is a plain text file that lists the basic information of a data sample to analyze. To find an example of a sequence, see Appendix B.

The MAGICDC program only uses the latest official MARS release versions. Therefore, the data check program is, together with the on-site analysis program (see Chapter 8), the first one to test the latest changes on the MARS software itself, what frequently requires software debugging.

## 7.3 MAGICDC: Telescope data quality check

Each MAGIC telescope consists of several telescope elements, called subsystems, which perform specific tasks within the normal data taking. The quality of the data depends on the good functioning of the telescope and therefore the performance of these subsystems. The program MAGICDC has been developed to check these subsystems behavior and functionality. It is executed automatically each morning after data taking ends and extracts all the useful information about the telescope status. For final stage, this information is evaluated by a component of the MAGICDC software called Automatic Data Check (see section 7.3.6).

The MAGICDC program consists on a set of subprograms (see Figure 7.1) which carry out four main tasks: the first one is to check the data reported for each telescope subsystem and compiled at .rep files, the second one is to check the Data Acquisition (DAQ) statistics file, the third one is to check the output of the calibration files, and the last one to evaluate the telescope performance.

### 7.3 MAGICDC: Telescope data quality check

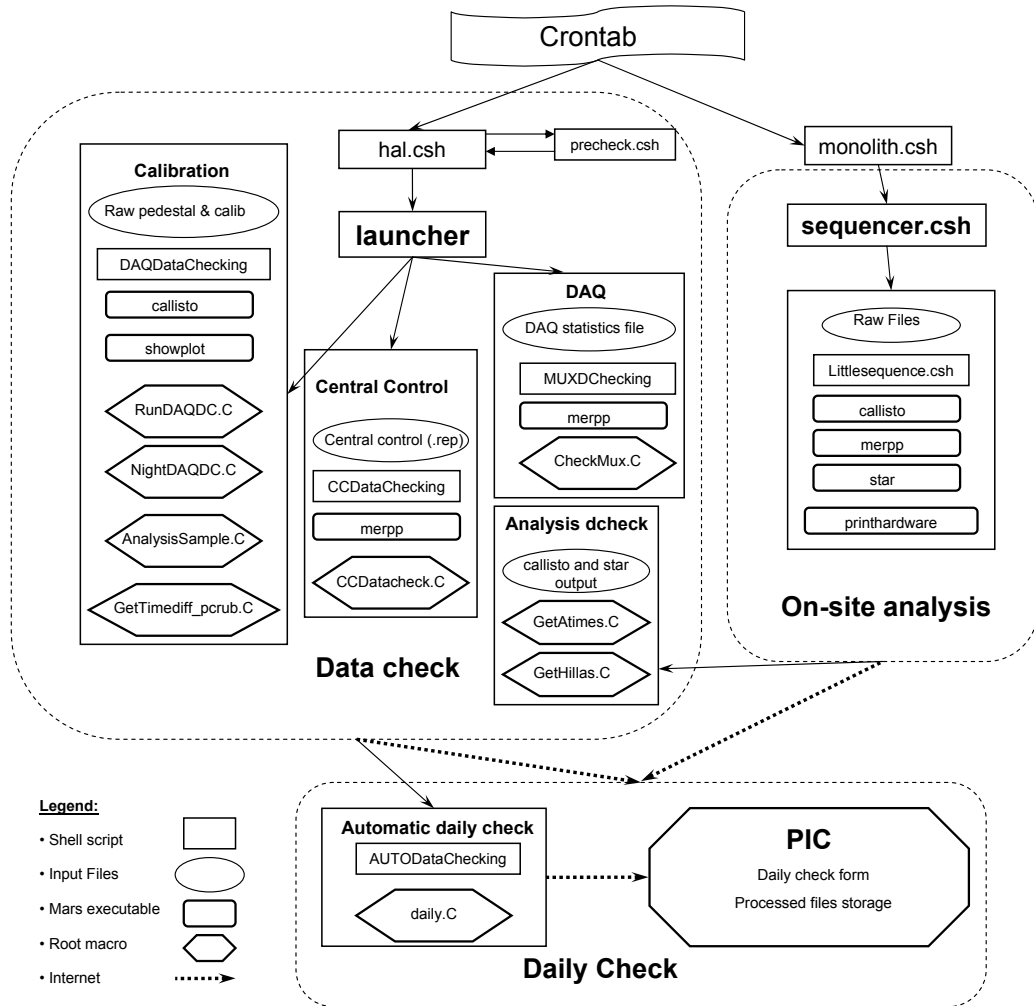


Figure 7.1: *MAGICDC and on-site analysis programs scheme.* After the scripts “*hal.csh*” and “*precheck.csh*” have confirmed that the computing system is ready, the script launcher will govern the execution of all processes of the different data check sections. Some of the output files generated by the on-site analysis (*calib.root*, *signal.root* and *star.root*) are used as input by the data check program.

## 7.3 MAGICDC: Telescope data quality check

---

This software produces more than 200 plots every night. For simplicity, only few examples of plots will be shown in this chapter. The whole set is shown in the Appendix A.

### 7.3.1 Steering scripts

The telescope data check program runs in the *muxana* computer, but can be also run in *muxana{2-9}* machines if needed, and belongs to the local user *analysis*. The program is located at *muxana* in the *analysis* user home directory at *\$MAGICDC* directory (see Table 7.1 for the full path).

All the results and log files of the programs are presently saved at the NFS system named *raid2*, in the directory *\$results* (see Table 7.1), under different sub-directories, depending on the running job.

The MAGICDC program is managed through the Linux *cron daemon* at *muxana* using the *crontab* file from user *analysis*, which launches the MAGICDC program.

The crontab files of the *analysis* user launch two different jobs (C-shell scripts) (Figure 7.1):

- *hal.csh*: This job is launched daily every 20 minutes from 9:00 a.m to 20:00 p.m (UTC) to look for unfinished MAGICDC jobs.
- *monolith.csh*: Takes care of the on-site analysis of the previous days, checking if it has finished properly. Details on the on-site analysis can be obtained in Chapter 8.

The cron job *hal.csh* is launched giving as third parameter a specific date in the format “<year>-<month>-<day>” (all numerical digits), that in normal operation is the current date.

In a first step the *hal.csh* job calls to the *precheck.csh* script which performs the following checks: computers are switched on, */local* directory at *muxana* is available, all the subsystem data are available and which kind of data checks should be done. This last check depends on the subsystem data available and whether any of the data check jobs has been already done and finished properly.

The result of the *precheck.csh* script is always an exit code. In case of the first checks, or if all the data check jobs have finished properly, the program *hal.csh* exits with an error message (different for each exit code) referring to the last task unable to accomplish. In case of missing data check jobs, the *hal.csh* is launched with the adequate configuration.

Depending on the exit code of the *precheck.csh* script, *hal.csh* calls the *launcher* script with different options:

1. Type of data check: cc, cal, cmux and prof (not mutually exclusive).

## 7.3 MAGICDC: Telescope data quality check

---

2. Mode: auto, manual, plot or webpage (exclusive).
3. Day: “<year>\_<month>\_<day>”

The *launcher* script is the main script which runs the check jobs for the different kinds of data (1.):

- I. Subsystems (Central control) data (cc option): *CCDataChecking* script (sec. 7.3.2).
- II. DAQ data (cmux option): *CheckMUX* program (sec. 7.3.3).
- III. Calibration data (cal option): *DAQDataChecking* script (sec. 7.3.4).
- IV. Automatic data check (prof option): *prof* (see sec. 7.3.6).

The *launcher* script can call any of the jobs mentioned above in one mode from the following list:

- **auto**: corresponds to the process automatically launched by the “cron” daemon everyday at 9:00 UTC. This process activates *hal.csh*, which launches consequently the *launcher* script with the **auto** option.
- **manual**: launches the data check of any day (the “Day” has to be specified in (“3.”) option).
- **webpage**: transfers the portable document format (“.pdf”) files with the result plots to the web page.
- **op**: allows the operator user to launch the MAGICDC scripts at any time. This is specially useful to test how are the systems behaving after hardware updates, without waiting to the end of the night shift.

As example of how the launcher could be called is:

```
$MAGICDC/bin/launcher daqccalc muxprof manual 2010_01_09
```

This command launches the whole datacheck and analysis programs for 2010 January 9th.

While running each job all the log files are written at the directory called *\$logsr*. When each check job is finished, the *launcher* script moves the logs files into the job working directory, it sends (by e-mail) a notification to the MAGICDC program developers ([gae-dc@gae.ucm.es](mailto:gae-dc@gae.ucm.es)) and copies all the output Portable Document Format (“.pdf”) files into the MAGIC web page at La Palma (see sec. 8.2). Its log file (*launcher.out*) is written into the \$MAGICDC/bin subdirectory.

## 7.3 MAGICDC: Telescope data quality check

---

All the information shown by the MAGICDC program is checked by the MAGIC *professional daily-checkers*, coordinated by the Udine group of MAGIC collaboration, who have to fill a daily report about the MAGIC telescope status and, in case of problems, solutions should be sought and be carried out by the experts and the shifters to solve the problems for the next data taking day.

### 7.3.2 Subsystems data quality check

The inspection of the subsystems data, gathered by the Central Control (CC), is the first task done in MAGICDC. This job checks the performance of all the MAGIC telescope subsystems involved in the data taking, and provides, together with the DAQ data check (see sec. 7.3.3) a first estimation of the night's data quality.

#### 7.3.2.1 Overview

All the subsystems in the MAGIC site are run and controlled independently by their own programs but they allow the access to most of their functionalities and report all the useful information, through the central control software of the MAGIC telescope (Figure 7.2), called SuperArehucas. This software also controls all the subsystems of the MAGIC-I and MAGIC-II telescopes, which constitute the second phase of the MAGIC experiment.

This program stores, at a rate of 1 kHz, all the subsystems reports in two different kind of ASCII files, both with the extension “.rep”. One kind contains the subsystems reports for one subrun, and therefore there is one of these reports for each subrun, and its name starts with the date of the night. The second kind of file starts with the “CC” characters and keeps all the reports of the subsystems for the whole night. In addition to these reports, specifically sent to the CC, each subsystem could have its own report, log and data check files.

#### 7.3.2.2 Program

The part of the MAGICDC program which checks the subsystems reports is called by the script *CCDataChecking*. This script joins all the night .rep files (*CC.rep*, see Table 7.1), merpps the joined .rep file, calls a ROOT macro, *CCDataCheck.C*, to read the generated “.root” file and displays the corresponding subsystems report plots. These plots are classified depending on the subsystem: drive, camera and cooling, trigger, *starguider*, weather station and time.

The check plots of this part display the information in two different representations: *variable versus time*, to check the variable stability during the night of the subsystem, and *variable versus some other variable* to check previously known correlations between them.

## 7.3 MAGICDC: Telescope data quality check

---

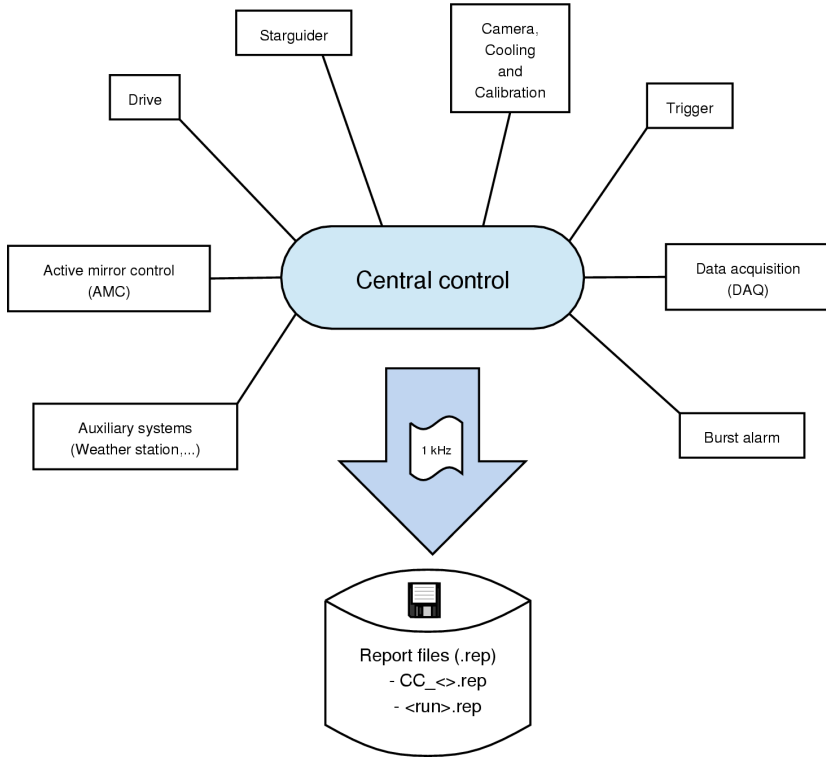


Figure 7.2: Scheme of the central control of MAGIC for the normal data taking. From [De 08].

The log file of *CCDataChecking* job (*CC.out*, see Table 7.1) is copied, together with the CC results, into the directory `$CCresults`.

### 7.3.2.3 Checked subsystems

**Drive** Reports plots of the zenithal angle, status of the motors, and telescope's position in both axes according by the shaft encoder. If the plots show that there is a deviation higher than 1.3 arc-minutes this means that the drive is not working properly.

**Camera** The MAGIC-I camera is fed with HV (high voltage) by two external power supplies which divide the camera in two halves (A = sectors 1,2,6 and B = sectors 3,4,5). The camera and calibration control program (*La Guagua*) evaluates the status of every controlled subsystem (LV, cooling, lid, calibration, etc.) from their regular reports with a given frequency. A program within the *SuperArehucas* program called *Sentinel* protects the camera against dangerous situations and does not allow certain camera and calibration systems operations [Fli06].

Several plots related to the camera subsystem are produced:

- The status of several monitored elements (PMT high voltages, camera lids, cooling system, PMT direct currents (DC) and camera sentinel) versus time.

### 7.3 MAGICDC: Telescope data quality check

---

- The high voltage power supplies and applied direct current as a function of time.
- The camera mean high voltage, direct current, and DT settings as a function of time. The DT settings can be changed along the night by the operators due to different astronomical constrains (moon, twilight) or automatically by the Individual Pixel Rate (IPR) control.
- The applied low voltage and the relative humidity in the LV box as well as their general status and the status of the power supply request, as a function of time.
- The high voltage and current of the 360 V active loads and the 175 V power supply of the 5th and 6th PMT dynodes versus time.
- The time average of the HV and threshold settings versus the pixel number.

Another part of the camera report to the CC concerns the cooling of the camera. To check the cooling system, these plots show the temperature at the center and the walls of the camera, the temperature of the optical links and the water deposit, as well as the relative humidity at the camera center and walls as a function of time. The distribution of the optical links temperature is also displayed but only during the data taking time (see Figure 7.3). The red dashed lines define the range in which the temperature at the center of the camera should lie during the data taking. A temperature outside these limits or with a non stable behavior will have an important effect on the amplification at the optical links. If the temperatures at the optical links and at the camera center differ by more than 2 degrees it means that there is a problem with the fan inside the camera, and therefore that the temperature is not homogeneous. A non homogeneous temperature will cause a different response among the pixels, affecting the camera homogeneity.

**Trigger** Checks of the first and second level trigger rate versus time, the second level trigger rate versus zenith angle and the night-mean (and RMS) of the IPR per pixel are performed. Apart from these checks, further information the IPR is displayed: the integral and differential distribution of the rate over the number of pixels. If more than 50 pixels have a rate lower than 60 kHz, or more than 10 pixels a rate above 5 MHz, this may indicate that the DTs have been set incorrectly or that the ambient light is too strong. Additionally, if a large number of pixels show too low or too high IPR, it may also be that the HVs have been set incorrectly or that the IPR is not working properly.

### 7.3 MAGICDC: Telescope data quality check

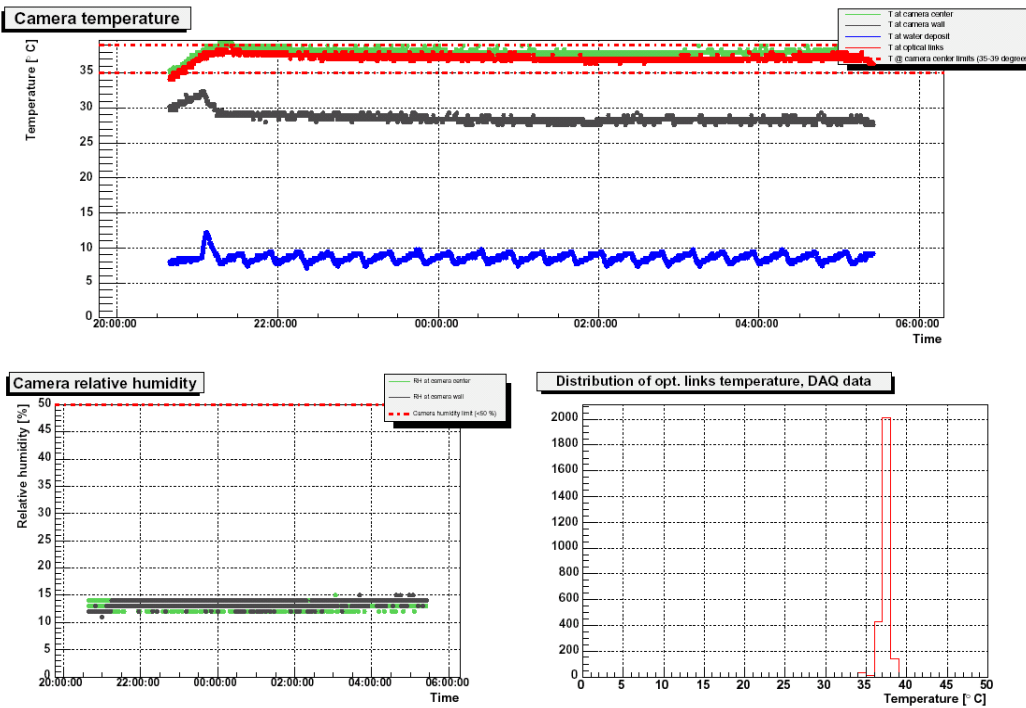


Figure 7.3: *Cooling system report plots. Top display: temperature versus time of the camera center (green), wall (grey), water deposit (blue) and optical links (red). Bottom left: humidity of the camera at its center (green) and walls (grey). Bottom right: distribution of the optical links temperature during the data taking.*

**Starguider** This subsystem improves the pointing accuracy of the telescope. Its reports indicate whether the telescope is pointing properly and will be important in the data analysis. The mispointing is determined by a comparison of the position of bright stars in a region of sky around the telescope pointing position and using reference LEDs on the camera.

To check the telescope pointing stability, the zenithal and azimuthal mispointings are displayed, together with the X and Y coordinates of the pixel in the CCD where the camera center is found versus time (see Figure 7.4). The number of correlated stars and the sky brightness is also measured with the CCD camera versus time. A low number of recognized stars reduces the precision of the mispointing measurement.

**Weather station** The MAGIC telescope has its own weather station, located in the vicinity of the Counting House. The values registered by the station are read out every 40 seconds and sent to a graphical display over the web, in different time scales. This web page can be accessed publicly<sup>1</sup>. As the other subsystems, the weather station also sends a report to the CC with all the gathered information.

<sup>1</sup><http://www.magic.iac.es/site/weather/>

### 7.3 MAGICDC: Telescope data quality check

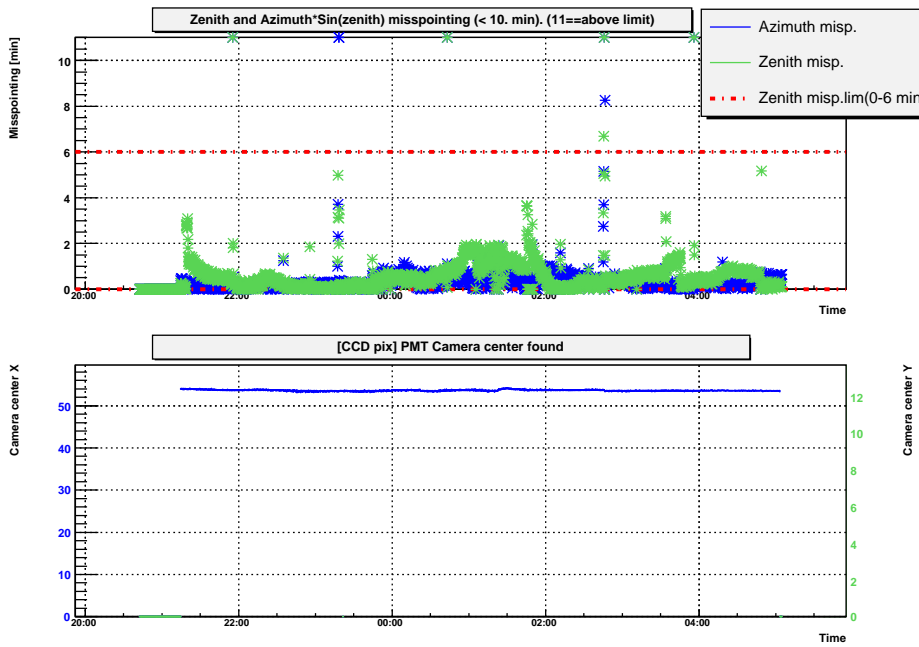


Figure 7.4: *Starguider report plots. Top: Absolute value of the zenith and azimuth misspointing (arc-min.) versus time. Bottom: The X and Y position in the CCD camera of the PMT camera center versus time. The red-dotted line corresponds to a misspointing within 1 camera pixel.*

The weather could affect the data quality but also to the telescope own integrity, since MAGIC is not protected by any dome. To check the weather conditions outside, the telescope data check program plots the humidity, the temperature and wind speed against time, together with their corresponding safety limits of operation.

**Time** The date and time information of a triggered event is determined on an absolute time scale (UTC) and added to the data in the DAQ readout process. The time accuracy is achieved with a calibrated atomic clock (Rubidium clock), a MAGIC specific module called TIC (Time Interval Counter), a HM8125 GPS Time/Frequency Standard and sub-sec NIM modules. The Rub-clock is extremely stable at short time scales of minutes to days but drifts at longer time scales. In order to keep the atomic clock accurate, the drift is corrected by a reference time that remains accurate over periods of months and years. This is achieved by a radio receiver that synchronizes the rubidium time to GPS time. The time difference must be always within  $\leq 2.00 \mu\text{s}$ . In case of a larger difference the GPS-Rubclock must be synchronized manually. A time difference higher than the limits may indicate that there is a problem with the GPS receiver, in the rubidium clock, or at the electronics that take care of the synchronization. As an example, Figure 7.5 shows the evolution of this difference during one night.

### 7.3 MAGICDC: Telescope data quality check

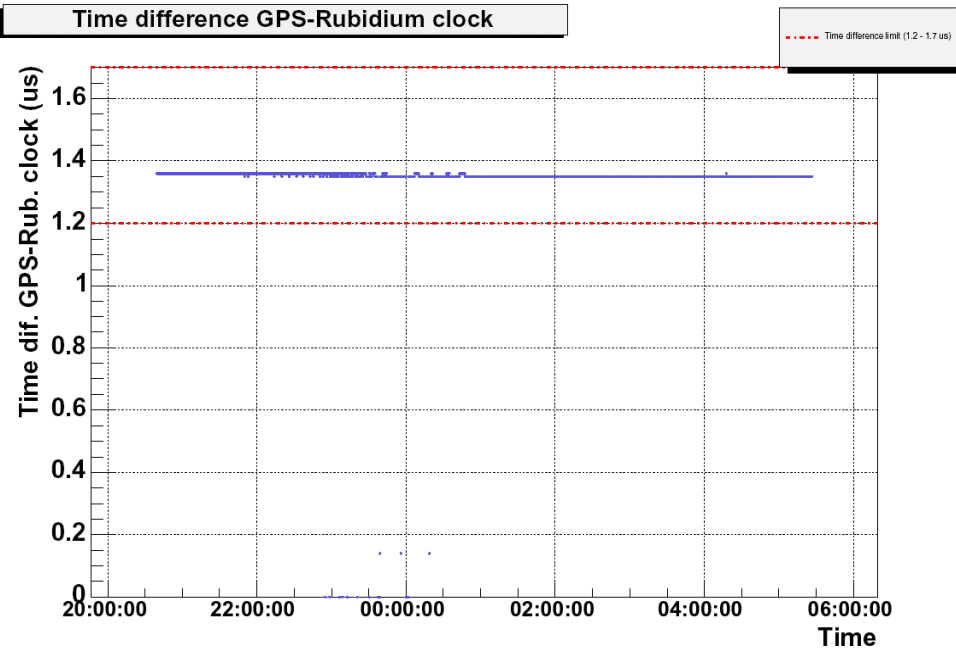


Figure 7.5: *Time report plot. Time difference ( $\mu\text{s}$ ) between GPS and rubidium clock. The red dotted lines are upper and lower limits.*

**Receivers temperature** Too high temperature at the receivers rack may affect the telescope performance. Moreover, fast changes of their temperature can provoke fast changes of the pedestal, calibration charges and signal charges. Figure 7.6 shows the evolution of the median of all receiver temperatures along the night.

**Trigger delays** The function of the trigger delays is to compensate both the slightly different length of the optical cables and the transit time differences in the different PMTs due to construction and operation voltage differences. The trigger delays settings, fixed by experts, are saved to non-volatile memories in the receiver boards. It may happen that these memories get deleted, for example, after a power cut. The mean parameter value is checked as time evolution plot and individual pixel's delays are checked as camera displays.

#### 7.3.3 Data acquisition quality check

The DAQ quality check program processes the DAQ system statistics files of MAGIC-I. This program gives an overview on the status of the performance of the DAQ over the whole data taking night.

### 7.3 MAGICDC: Telescope data quality check

---

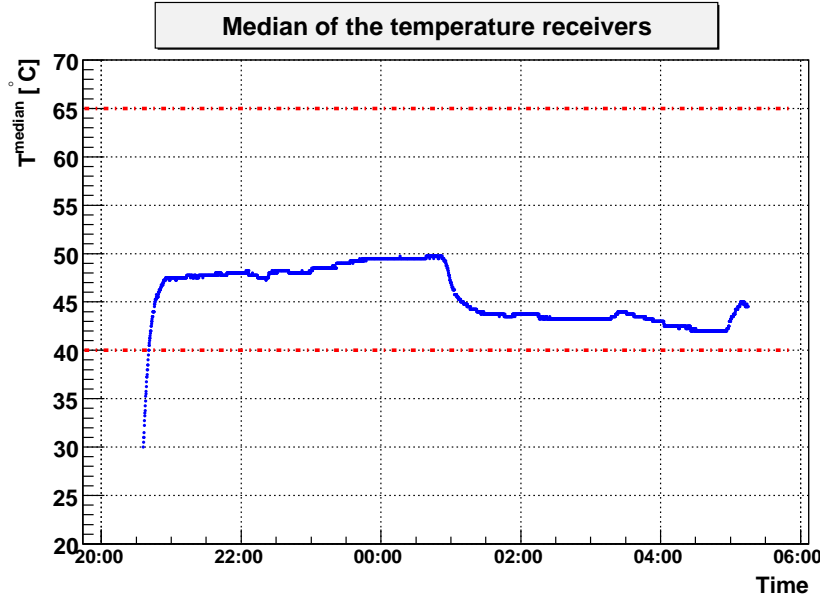


Figure 7.6: *Receiver temperature evolution along the night. The red dashed lines represent the safety limits.*

#### 7.3.3.1 Overview

During the telescope data taking, the DAQ subsystem performs a simple analysis of the recorded events. This analysis determines an average pedestal, signal charge and arrival time for each event and pixel. The so called “cosmics events” are the ones that have given trigger. From these cosmic events, a pulse is defined as “signal” if it exceeds a certain FADC count value. Therefore, the collection of pixels whose charges exceed this threshold for a certain event constitute a cosmic “signal” event. For each data file, the threshold is defined in the DAQ statistics file, being 8000 FADC counts the default value for MAGIC-I.

The average sub-run results obtained from the previously described analysis are written to an ASCII file (`$muxin/MuxDatacheck.txt`) at the end of each sub-run [Goe04]. The format of the input file is described in [Lie05].

#### 7.3.3.2 Program

The part of the MAGICDC program which checks the DAQ is called by the script *MUXDCChecking*. This script joins all the night DAQ statistics files and merges the joint (*Mux.root* file, see Table 7.1). Finally, it calls a ROOT macro, *Check-Mux.C*, to read the previously created “.root” files and display the corresponding subsystems report plots.

The check plots of this part are of two kinds: *camera display views* and *variable versus run*. They show the overall behavior of the camera for different parameters, and the evolution of these parameters during the night.

## 7.3 MAGICDC: Telescope data quality check

---

The log file of *MUXDCChecking* job (*Mux.log*) is copied, together with the results of the process, into the directory *\$MUXresults*.

An additional task made by the DAQ job is to launch the script *MUXDC-CheckingMonth*, that works in the same way as *MUXDCChecking* but using as input all the information gathered during the month of study. The results are stored into the directory *\$MUXresultsM*.

### 7.3.3.3 Checks performed

**Pixel charge** The mean charge in FADC counts of each pixel along the data taking night is studied in these checks. Different type of events are studied separately: calibration events from dedicated calibration runs, interleaved calibration events<sup>1</sup>, cosmic events and cosmic “signal” events.

The calibration pulser is sensitive to the external temperature so the calibration charge will always show some degree of instability (of the order of 60 counts). A mean charge well below the safety limits indicates that there was something wrong with the calibration pulser (it may have not been switched on correctly) or that the PMTs have not reached their nominal HV.

When individual pixels show too low charge values they most likely have hardware problems. In general less than 10 pixels should be in this situation. A higher number may point to a more general problem: e.g. some HV regulator master card or some FADC module is broken.

The hit fraction of cosmics “signal” events (in percentage) is also plotted in these checks. A pixel hit fraction is the fraction of the total number of events for which this pixel is part of a Cherenkov shower, and it is not related with the calibration. In general this number is 0.005 - 0.009. The hit fraction should be symmetric in the camera. If a certain part of the camera exhibits a low hit fraction it could be that the response of the pixels is low, or that some trigger macrocell in the area is faulty (malfunctioning or triggering too early or too late).

**Pixel arrival time** The arrival time for both calibration and signal events should be contained inside the safe ranges on individual pixels to prevent the pulses from being truncated. If a pixel shows too low or high arrival time value this may point to a hardware problem. The distribution of the arrival times is checked through camera display view, containing the mean pixel value and RMS of this parameter for signal cosmic events and calibration pulses for the whole night. Again, calibration events from calibration runs and interleaved calibration events from data runs have been processed and displayed independently. Figure 7.7 is an example of this kind of plot.

---

<sup>1</sup>As they showed discrepancies in the past, pulses from dedicated calibration runs and calibration pulses stored as interleaved events are treated separately.

### 7.3 MAGICDC: Telescope data quality check

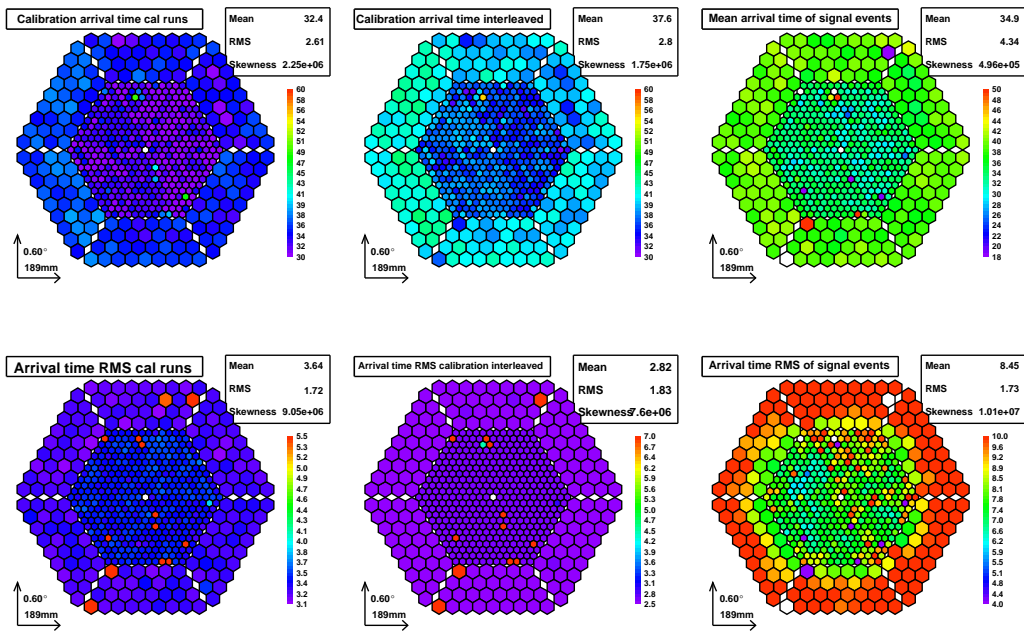


Figure 7.7: Top left: Mean arrival time from calibration events of calibration runs. Top center: Mean arrival time from calibration interleaved events. Top right: cosmic signal events. Bottom left: The arrival time RMS from events of calibration runs. Bottom center: Arrival time RMS from calibration interleaved events. Bottom right: Arrival time RMS from cosmic signal events.

**Pixel pedestal** The distribution of pedestals over the camera is checked in camera display views containing the mean pixel value and RMS of the pedestal in FADC counts for both pedestal and data runs for the whole night. The value of pedestal RMS is obtained as RMS from the number of slices of the pedestal extractor window divided by the number of slices.

Too low a pedestal RMS may point to too low HV (decreased by mistake), or problems with the data acquisition. The pedestal RMS increases noticeably during moon observations, in particular when we take data close to full moon.

The number of photo-electrons and the conversion factor from FADC counts to photo-electrons are also checked. Too low or high values may mean that the PMTs are not in their standard settings, or that there are problems with the calibration box. To calculate the number of photo-electrons at the PMT photocathode, the excess noise factor was used (see section 5.7), through the formula:

$$N_{pe} = F^2 \frac{\langle Q_{cal} \rangle^2}{\sigma_{calQ}^2 - \sigma_{ped}^2}, \quad \text{with } F^2 = (1.15)^2 \quad (7.1)$$

To apply the previous formula, it has to be taken into account that in the input DAQ statistics file the pedestal RMS is obtained for a certain pedestal extractor window size, different from the signal extractor window size. In the actual MAGIC-I configuration, 50 slices for the pedestal extractor and 10 slices

### 7.3 MAGICDC: Telescope data quality check

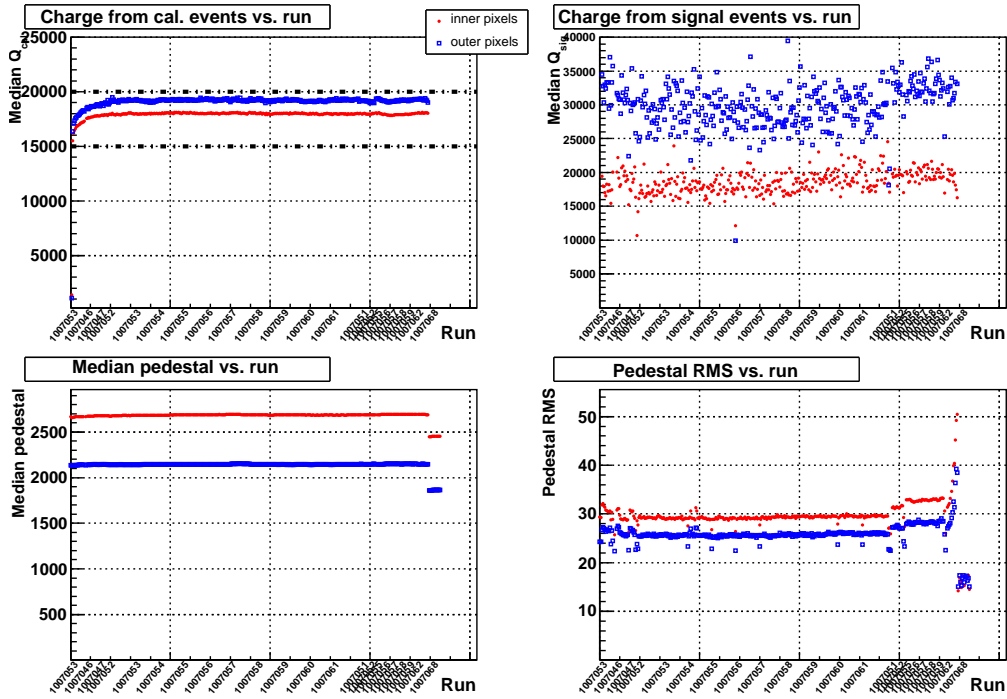


Figure 7.8: Top: Evolution of the median charge for calibration (left) and cosmic signal events (right) versus run number, for both inner and outer pixels. Bottom: Average pedestal and its RMS for inner and outer pixels.

for the signal extractor are used, whereas 40 and 7 slices respectively are used for the MAGIC-II configuration. For MAGIC-II  $F$  was not yet calculated when this thesis was written, but was estimated to be  $F^2 \leq 1.1$ <sup>1</sup>.

**Charge and pedestal evolution** The stability along the night of the charges is checked by evolution displays of the median value of the charge for calibration and cosmic signal events. Having different PMTs with different sizes, inner and outer camera sections are treated separately. The stability may be affected by changes in the temperature (especially in the optical links) or the HV that is supplied to the PMTs.

The stability of the pedestal and its RMS, independently studied for inner and outer camera, are checked in night evolution plots. The pedestal RMS is correlated to the square root of the DC, so it is possible to check if both parameters change coherently. Figure 7.8 exemplifies this kind of plots.

**Arrival times evolution** The evolution/stability along the night of the median and RMS value of the arrival time, in units of FADC slices, is studied for calibration and cosmic signal events. Inner and outer pixels are treated separately. The calibration arrival time is sensitive to the ambient temperature and

<sup>1</sup>M. Gaug, private communication.

### 7.3 MAGICDC: Telescope data quality check

---

the signal arrival time to the temperature in the electronics room. For some parts of the year it may be necessary to adjust the time window in the FADCs so that the pulses do not break the safety limits.

**Calibration factors evolution** This check studies the evolution over the night of four different parameters:

- The evolution of the number of Npe calculated according to formula 7.1, for inner and outer pixels.
- The average conversion factor from charge to Npe for both types of pixels.
- The evolution of the hit fraction of events in percentage of cosmic signal events over the total cosmic events.
- The last plot shows the evolution of the ratio of average charge in cosmic events to the pedestal RMS for both inner and outer pixels.

**Arrival time differences** Further checks of the arrival times are performed.

- The maximum difference of the average arrival time in FADC slices of any two pixels, for different type of events, in terms of the data run, calculated separately for inner and outer pixels.
- The evolution of the averaged difference between arrival times of calibration and signal events, obtained as the difference between the median arrival time of calibration events and the median arrival time of cosmic “signal” events.
- The difference of arrival times for calibration and cosmic “signal” events between two particular pixels: 173 and 197. The positions of these two pixels in the camera are located approximately at half distance between the camera center and the camera edge, symmetrically with respect to the camera center.

**Arrival time check** The arrival times at the FADC should be correctly set in order to be sure that the pulses are never truncated. It was imposed that most of the distribution of arrival times is inside certain limits. This is expressed as the following quality criterion<sup>1</sup>:

$$\bar{T}_{cal} - 2\bar{\sigma}_{T_{cal}} > \text{Lower limit} \quad (7.2)$$

---

<sup>1</sup>J. Cortina and A. Moralejo, private communication.

### 7.3 MAGICDC: Telescope data quality check

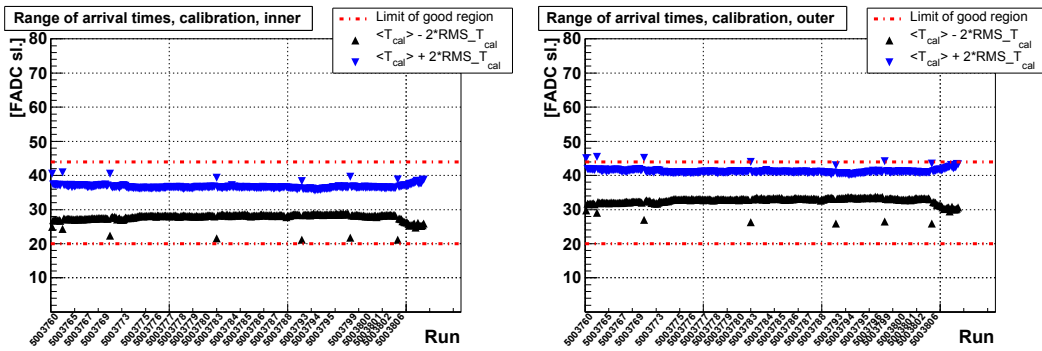


Figure 7.9: *Evolution of arrival time quality check for calibration pulses along the night.*

$$\bar{T}_{cal} + 2\bar{\sigma}_{T_{cal}} < \text{Upper limit} \quad (7.3)$$

The ideal limits would be 10 slices away from both lower and upper limits of the DAQ window, with additional 10 more slices in the upper limit to take into account the physical time evolution of the showers. The corresponding limits for MAGIC-I have to be modified to consider that from the total of 80 slices, the first 15 and last 15 are affected by switching noise. For MAGIC-II, from the total of 70 slices, the first 20 are used to extract the pedestal baseline. In summary, this means that the lower limits are 20 for both telescopes, and the upper limits are 44 and 49 for first and second telescope, respectively.

Figure 7.9 shows the evolution of the check of the arrival times for MAGIC-I telescope, for both inner and outer pixels.

Another check performed is one that shows the evolution during the night of the number of bad pixels present in the camera. The list of the used criteria is detailed in [Oya09a]. Following the established criteria, it is normal to have around 20-30 bad pixels in the camera.

**Arrival time distributions** With the aim of checking if all the pulses are arriving inside the ADC window, and with the approximate same position, the distributions of arrival times for calibration pulses and cosmic signals is checked. The histogram include the statistics for the whole night. For each run, the mean of the arrival time of each pixel is used to fill the histogram. The correct window for MAGIC-I is from slice 15 to slice 65, whereas from MAGIC-II it is from slice 20 to slice 60.

#### 7.3.3.4 MAGIC-II update

In order to check the quality of the data taken during the commissioning phase of MAGIC-II, a modification of the macro *CheckMUX.C*, named *CheckDomino.C* was created. It makes the same set of plots of the MAGIC-I macro, but with the

## 7.3 MAGICDC: Telescope data quality check

---

information gathered by the MAGIC-II DAQ statistics files. The format of the input file is the same as the one of MAGIC-I. For the time being the safety limits of the parameters have not been established yet and therefore this data check step is in a preliminary state. The final version of the MAGIC-II DAQ check will be defined in the following months (Spring 2010).

### 7.3.4 Calibration data check

The calibration data check step performs a full determination of the calibration parameters using the previously mentioned standard collaboration software, MARS. At this step, the response of the whole light detection and amplification chain is checked. More information about the calibration process can be found in section 6.6 and in reference [Gau06].

#### 7.3.4.1 The calibration system

The MAGIC-I telescope requires a precise and regular calibration system of the camera and the readout chain over a large dynamic range of amplitudes. This is achieved with the help of a number of powerful ultra-fast LED pulsers located inside a pulser box. A pulsating mode (pulser box) is used to calibrate the detector response to Cherenkov light with 2 ns pulses, while a continuous mode is used to calibrate the response of the DC readout to background light (star and moonlight). The absolute light flux is calibrated using three blind pixels hosted at the camera and a calibrated PIN diode located at 1.1 m distance from the pulser box [Gau06].

For the calibration process two kind of runs are taken consecutively: the first one is a pedestal run, which consists of 1000 events triggered by a random signal sent by the calibration box to L2T. These events should contain nearly no Cerenkov pulses. The second one is a calibration run, which contains 4096 events of light pulses data sent by the calibration box following a number of actions predefined by a calibration script. The number of photo-electrons is determined from the light pulser using the previously mentioned F-Factor method. The default signal reconstruction algorithm is the cubic spline extractor, described in section 6.6.1.

#### 7.3.4.2 Program

The script which carries out the calibration data check is named *DAQDataChecking* (Figure 7.1) and is called through option “cal” on *launcher* main script. It consists of three logical parts:

### 7.3 MAGICDC: Telescope data quality check

---

- I. **Running *callisto* over individual sequences.** The first task of the script is to define the callisto-sequences (sec. 7.2). To do this the script reads the CC .run files (joined in a single file) which contains a summary of the data taking of the night. Then a night summary file (*NightSummary.txt*, see Table 7.1) is created with the variables needed by the program. The run information is extracted from this night summary file to build the analysis sequences.

As it has been explained before, to extract and check the calibration constants it is necessary to have a pedestal-calibration pair of runs. With each of these pairs we define a sequence for the *callisto* MARS executable.

Then *callisto* is run on the sequence, it calculates the calibration parameters and saves them into a “calib<SequenceNumber>.root” file. This file is then read by the MARS executable *showplot* making the calibration data check plots (see next section for a description) and saving them as a PDF file.

Finally, for each sequence the *RunDAQDC.C* macro is run. It extracts the mean values of the calibration factors and bad pixel information of the sequence, and saves it into an ASCII file (*BadCalPixels.dat*).

- II. **Checks over the whole night sample.** The second step is to run a set of macros to perform several other checks over all the night calibration constants already calculated (calib.root files of all sequences):

- *NightDAQDC.C*: Plots the calibration parameters evolution versus time. It can be used to see the evolution of these values over the whole night [Oya06]. The plots are stored in the file *AllNightDataCheck.pdf*.
- *AnalysisSample.C*: Creates an ASCII file called “samples.txt” with all the information of the night sequences. It will be used in the analysis data check.
- *get\_timediff\_pcrub.C*: Calculates the time difference between the PC and the Rubidium clock for the first and last events of each calibration and pedestal run. The results are displayed in a Postscript file *TimeDiff.pdf* and also in an ASCII file.
- *GetAtimes.C*: Obtains the arrival time distributions of the calib.root and signal.root from the on-site analysis output, explained in Chapter 8. The macro is called by the on-site analysis script *sequencer.csh*. This script also converts the output file to “.pdf” format. Results are available at same directory of calibration data check results, in the file *Atimes\_MARS.pdf*.

### 7.3 MAGICDC: Telescope data quality check

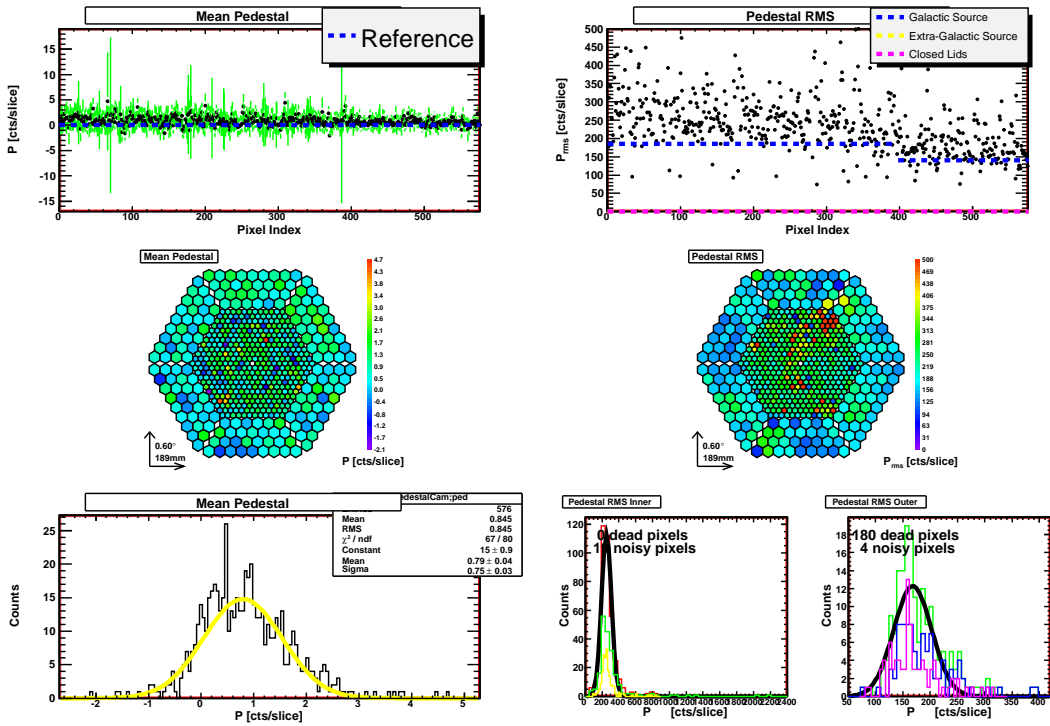


Figure 7.10: Pedestal mean and RMS (from calibration extracted run). From top to bottom: pedestal mean (left) and RMS (right) versus pixel index in profile and camera display views, and the mean and RMS distributions together with the gaussian fits. The reference lines correspond to the pedestal values when pointing to galactic (blue) and extragalactic (yellow) sources and with closed lids (pink).

**III. Manipulation of the ntuple.** The last set of macros (see Figure 7.1) corresponds to the manipulation of a ntuple which accumulates and stores relevant information about the calibration (*MakeTreeDAQ.C* macro) and then it is plotted (*ReadTreeDAQ.C* macro) into a Postscript file named “DAQCntuple.ps”. These last result plots are saved into the *\$Calresults* directory [Oya06].

All the mentioned Postscript files are converted to Portable Document Format (“.pdf”) files and saved all together at *\$Calresults*, where the job log file *Mux.log* is also stored.

#### 7.3.4.3 Calibration quality checks

**Switching noise peak position** The mean switching noise position for each pixel of the sequence is plotted as a camera display.

**Pedestals from pedestal run** The mean and RMS of the pedestal charge distribution is displayed for each pixel versus the pixel index as a profile and

### 7.3 MAGICDC: Telescope data quality check

---

as a camera display, and also their distributions. The mean and RMS camera distributions are fitted to gaussians, where pixels  $-4.5\sigma$  away from the distribution mean are called “dead” pixels and those at  $+25\sigma$  are called “noisy” pixels.

**Pedestal from signal extractor** The pedestal from signal extractor is plotted for each pixel versus the pixel index as a profile and as a camera display. Figure 7.10 display shows the mean and RMS of the pedestal charge distribution but from the calibration extracted signal, where the pedestal has already been subtracted. Therefore the mean pedestal is expected to be 0 (blue reference line) for all pixels and the camera pedestal distribution should be centered at 0. The default extractor is the spline extractor [Alb08a]. The extraction region is from the slice 15 to slice 65. The extracted pedestal is updated every 500 of these “pedestal events”.

**Arrival time** The distribution of mean arrival times (ADC sl.) of the calibration signal events, as well as their behaviour versus time is monitored. Checking is done separately for inner and outer pixels. The position of the half maximum at the rising edge of the pulse determines the arrival time.

**Calibration signal charge** Here the distribution of the calibration signal mean charge (in ADC counts) and its behaviour versus time (sec) for inner and outer pixels are checked.

**Fitted charge** The mean (in ADC counts) and RMS of the fitted signal charge versus camera pixel number is checked as a profile and as a camera display. Additionally, the distribution of the fitted mean allows to quantify the number of outlier pixels (too low or too high charge) and the flat-field precision. Finally, the charge RMS and Npe RMS distributions are shown (for inner and outer pixels) with the number of dead and noisy pixels. The pixels suffering from too low or too high amplification, as well as the dead and noisy pixels are determined from the integral of the distributions, being those beyond  $\pm 4\sigma$  of the fitted distributions. The flat-field precision is defined as the  $\sigma$  of the gaussian fit of the charge divided by the mean from the same fit, and multiplied by a factor 100. The number of photo-electrons is computed by the F-factor method.

**Absolute times** The mean and RMS values of the arrival ADC slice are checked for calibration events versus pixel number, in a profile and camera display views. The distribution of the RMS for inner and outer pixels is used to determine the corresponding number of outliers: “early” and “late” pixels (pixels at  $\pm 4\sigma$  of the fitted mean of the mean arrival time per pixel), “too stable” and

### 7.3 MAGICDC: Telescope data quality check

“jittering” pixels (at  $\pm 4\sigma$  of the average of the mean arrival time rms). Here the pulse peak position is used to determine the arrival time position.

**Faulty pixels** Figure 7.11 shows the defective pixels found in a given calibration process. A legend is shown with the criteria (in different colors) to classify the pixels into “non suited” and “non reliable” pixels [Gau06]. They are shown with the same color criteria in a camera display.

The pixels marked as “non suited” are not used in the further analysis to build the images, while the “non reliable” pixels will be replaced in the image cleaning analysis process by the mean signal of their surrounding neighbors.

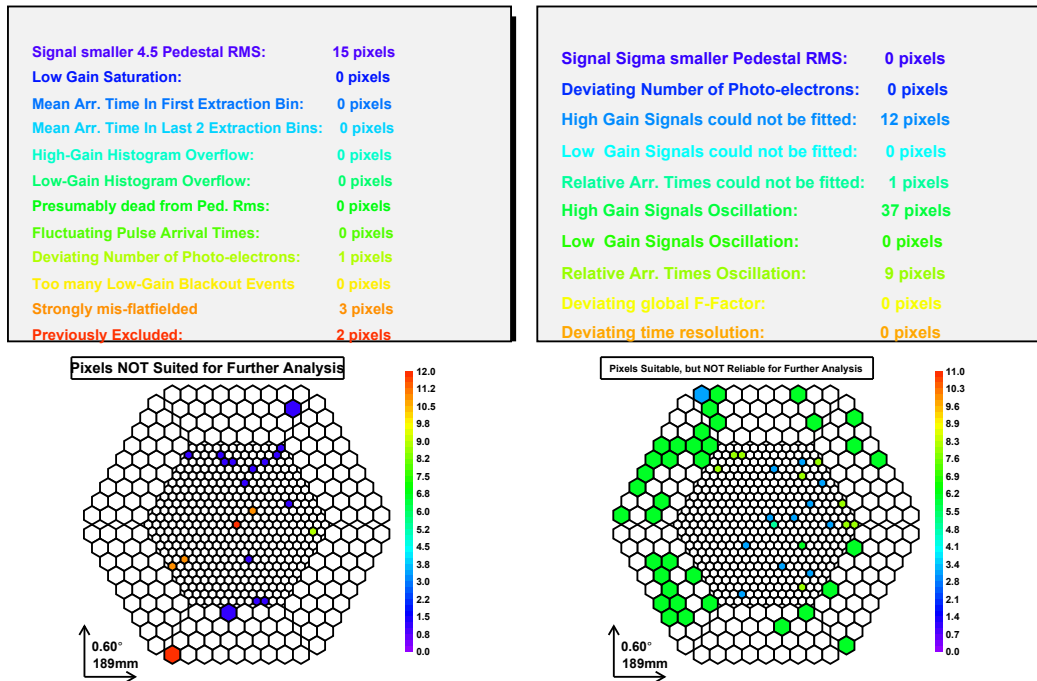


Figure 7.11: *Faulty pixels*. Legend with information about the calibrated defective pixels and a camera display showing the corresponding pixels, with colors indicating the kind of defect. On the left the “non suited pixels” and on the right the “non reliable” pixels.

**Relative times** The mean time delay (FADC slice) and its RMS per pixel in a profile and camera display are checked. The relative arrival times are calculated with regard to pixel number 1 (hardware number = 2). The distribution of the camera mean and RMS for inner and outer pixels is also checked allowing to identify the number of early, late, “too stable” and “jittering” pixels.

## 7.3 MAGICDC: Telescope data quality check

---

### 7.3.4.4 PC-rubidium clock time plots

The synchronization between GPS and Rubidium clock is only performed for sub-second time scales. It may be that there is a mismatch of exactly 1 second multiples between them. In order to detect super-second mismatches, the distribution of time differences between PC and the rubidium clock, with two entries per run is checked. It is obtained comparing the run start time (from the PC, synchronized over Internet) with the time of the first event (time from the rubidium clock), as well as comparing the run stop time and the time of the last event. A difference of less than 1 second means that the system is synchronized. The evolution along the night, in terms of the run number of this time difference is also displayed.

### 7.3.4.5 Arrival time distributions for all events

In order to check that no events (both calibration and cosmic ones) are truncated, distributions of the arrival times obtained from the whole sample of events are produced. The distributions are obtained using the arrival times obtained directly from the pixels of individual events, but in order to speed up the process but to have a significant sample of data, a 10% of all the events of the data taking night are used, selected randomly and according to the type of event: calibration, trigger level 1 or sum trigger event. The calibration pulses are not yet calibrated: for these the number of photo-electrons is estimated as signal charge, multiplied with a global estimation of the conversion factor.

### 7.3.4.6 MAGICDC update for MAGIC-II

In order to check the quality of the data taken during the commissioning phase of MAGIC-II, a modification of the script *DAQDataChecking* was created. It makes the same set of plots of the MAGIC-I procedure, but with the information gathered by the MAGIC-II telescope calibration.

## 7.3.5 Analysis data check

The image parameters of the Cherenkov showers can be used to give an additional estimation of the night data quality. Having available the on-site analysis products in the same computing cluster, it is possible to evaluate the image parameters for all the data taken during the night.

## 7.3 MAGICDC: Telescope data quality check

---

### 7.3.5.1 Program

The input files for this job are the Hillas image parameters [Hil85] and other similar ones, obtained in the regular star processes from the on-site analysis. As described in Chapter 8, the on-site analysis runs the *star* MARS executable over all data runs of the data taking night. Each time *star* runs, an output *star.root* file is generated. This output file contains all relevant parameters obtained from the images of the showers. The on-site analysis script *littlesequence.csh*, that takes care of processing each sequence, also launches the *GetHillas.C* ROOT macro. This ROOT macro gets the image parameters from the *star.root* files. The input and output files are copied at the directory *\$Hillasresults*. Finally, *littlesequence.csh* also copies the output “.pdf” files to the webpage at La Palma.

### 7.3.5.2 Analysis quality checks

The analysis data quality checks use the obtained image parameters after the image cleaning, performed with the so-called *absolute time image cleaning*, see section 6.7.1 for details. The configuration is the MARS default one: absolute 6/3 photo-electrons for core/boundary pixels, 4.5 ns maximum time difference between mean core pixels arrival times and single core pixels arrival times, and 1.5 ns maximum time difference between a boundary pixel arrival time and its core pixel neighbor arrival time. An independent set of plots is created from each different source, two sets per source if the observation has been carried out in wobble mode. Figure 7.12 shows an example of these kind of plots (center of gravity in different size bins).

### 7.3.6 Automatic data check

The automatic data check program evaluates a set of the most important plots in order to detect possible defective working subsystem. It then fills a form, later on completed by human supervision, only for the plots with suspected problems. The human supervision is performed by a team of person inside the MAGIC collaboration, called *professional daily checkers*, that are coordinated by the Udine group of the MAGIC collaboration.

After the human supervision a mail report is sent to the whole MAGIC collaboration while, if any important problem is spotted, experts are contacted by the person in charge of the daily check. A detailed explanation of the daily-checker duties can be obtained at reference [CO06].

### 7.3.6.1 Program

The part of the MAGICDC program which evaluates the previously obtained results is called by the script *AUTODATAChecking*. This script calls a ROOT

## 7.4 Conclusions and outlook

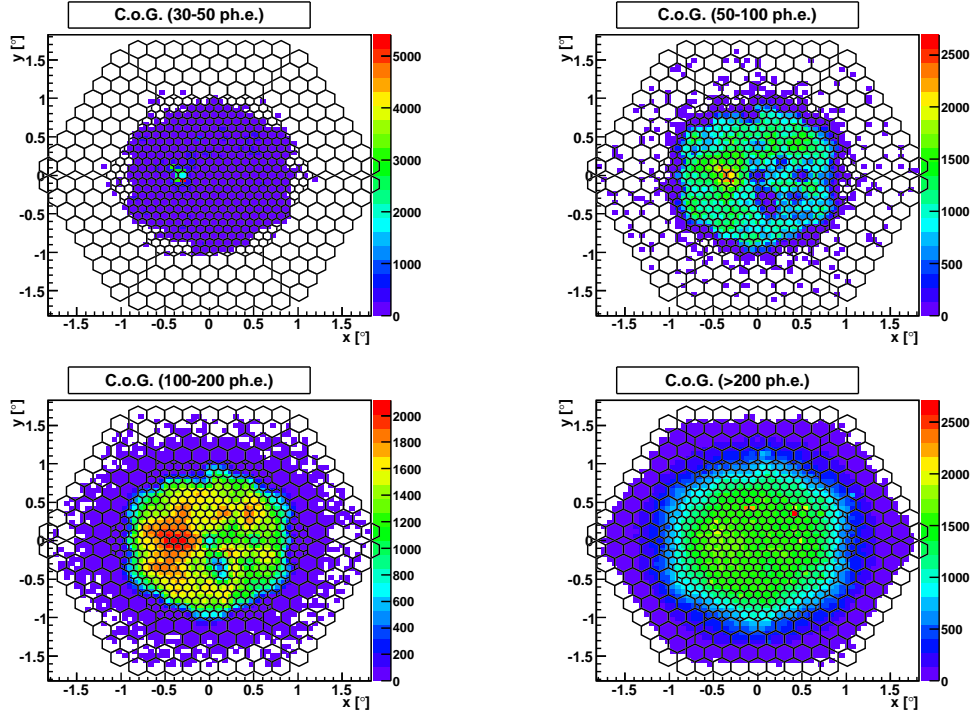


Figure 7.12: *Homogeneity plots. Center of gravity of the cleaned image (deg) for different size bins.*

macro, *daily.C*<sup>1</sup>, to read the previously created “.root” files at cc, daq and calibration jobs. The macro will evaluate the different parameters in the previously described plots and generate an ASCII file with the results of the evaluation (*autocheck.txt*)

The log file of *AUTODATAChecking* job (AUTODataChecking.out is copied, together with the program results, into the directory *\$Autoresults*

The daily check form is filled at PIC<sup>2</sup>. A copy of the questions are stored at the data check webpage at La Palma<sup>3</sup>.

## 7.4 Conclusions and outlook

The MAGICDC software, together with the on-site analysis (see Chapter 8), allows the experts from the MAGIC collaboration to know any system failure before 10:00 UTC, allowing a fast reaction to hardware malfunctions.

Since its installation in January 2004 [De 08], the MAGICDC program has kept growing with an increasing number of subsystems to check and therefore a

<sup>1</sup>This macro was developed by Nijil Mankuzyjil, Udine University.

<sup>2</sup>[www.magic.pic.es/priv/dailycheck/](http://www.magic.pic.es/priv/dailycheck/)

<sup>3</sup><http://www.magic.iac.es/operations/datacheck/WWW/dailycheck.txt>

## 7.4 Conclusions and outlook

---

larger number of plots. The increase has been due to the addition of new reports to the CC, improvements in the software and, most of all, the feedback from users and system responsibles about known/unknown new subsystem features. The results presented in this chapter have been publishes as a MAGIC internal document [Oya09a] and at the VIII meeting of the Spanish Astronomy Society [OR08].

In the coming future there are plans to perform more improvements for the optimization of the program itself:

- Finish the software update for MAGIC-II and the system of the two telescopes.
- Make a long term study of the telescope parameters.

These previous tasks will be performed by the Croatian Consortium members of the MAGIC collaboration, who have undertaken the data quality responsibilities since the beginning of 2010.

## 7.4 Conclusions and outlook

---

Table 7.1: Abbreviated name of relevant directories and files for the MAGICDC software as used in this chapter.

| Short Name            | Full path or name   |
|-----------------------|---|
| \$logs                | /remote/pc1/home/control/SuperArrehucas_CC/logbooks/              |
| \$MAGICDC             | /home/analysis/DataCheck/MAGICDC                                  |
| \$logsr               | \$MAGICDC/logs  |
| \$muxin               | /mnt/raid1/muxdata/   |
| \$results             | /mnt/raid2/analysis/DataCheck/Data                                |
| \$CCResults           | \$results/ccdata/<year>-<month>/<year>-<month>-<day>              |
| \$MUXresults          | \$results/analysis/<year>-<month>/CCDAQCHECK                      |
| \$MUXresultsM         | \$results/analysis/<year>-<month>/<year>-<month>-<day>/CCDAQCHECK |
| \$Calresults          | \$results/daqdata/<year>-<month>/<year>-<month>-<day>             |
| \$Hillasresults       | \$results/hillas/<year>-<month>/<year>-<month>-<day>              |
| \$Autoreresults       | \$results/auto/<year>-<month>/<year>-<month>-<day>                |
| CC.rep                | CC-<year>-<month>-<day>.rep                                       |
| MuxDatacheck.tex      | MuxDatacheckCC_-<year>-<month>-<day>.txt                          |
| CC.out                | CCDataChecking_-<year>-<month>-<day>.out                          |
| Mux.root              | MuxDataCheck_M1-<year>-<month>-<day>.root                         |
| Mux.log               | MUXDCChecking_-<year>-<month>-<day>.out                           |
| NightSummary.txt      | NightSummary_-<year>-<month>-<day>.txt                            |
| BadCalPixels.dat      | BadCalPixels <Source>-<PedestalRun>-<CalibrationRun>.dat          |
| AllNightDataCheck.pdf | AllNightDataCheck_-<year>-<month>-<day>.pdf                       |
| TimeDiff.pdf          | TimeDiff_-<year>-<month>-<day>.pdf                                |
| Atimes_MARS.pdf       | Atimes_MARS_-<year>-<month>-<day>.pdf                             |
| autocheck.txt         | <year>-<month>-<day>autocheckv2.txt                               |
| AUTODataChecking.out  | AUTODataChecking_-<year>-<month>-<day>.out                        |

# Chapter 8

## Quick on-site analysis software

### 8.1 Introduction

This chapter is an overview of the MAGIC experiment quick on-site analysis program (QOSA). Due to the data volume recorded with the MAGIC telescopes (see Table 8.1), it is still not possible to transfer the raw data by Internet. The software presented here performs a key role in the MAGIC experiment data pipeline, reducing the raw data at MAGIC site so reduced products can be delivered by Internet to the experiment data center at PIC [Rei09] with the needed promptness. The raw files are taped and will usually arrive to the data center by airmail several days later.

A different package called *Online Analysis* [ZMH08] is commonly used to detect high state activity of the sources and it is very useful to decide observation strategies. It is, on the other hand, not as sensitive as a full analysis. The observation strategies for weak sources benefit from the possibility of having a fast full analysis as the one delivered by the QOSA software.

| Phase | R[Hz] | P    | S  | D     | 1 hour | 1 day  | 1 year |
|-------|-------|------|----|-------|--------|--------|--------|
| 1     | 300   | 577  | 30 | 8     | 19 GB  | 150 GB | 36 TB  |
| 2     | 300   | 577  | 50 | 10    | 39 GB  | 300 GB | 72 TB  |
| 3     | 300   | 1616 | 50 | 10/12 | 110 GB | 875 GB | 210 TB |

Table 8.1: *Estimation of the data volume of different MAGIC experiment phases. R is the event rate P is the number of pixels, S is the number of samples recorded in the ADC window, D is the resolution. Phase 1 corresponds to old Siegen FADCs of MAGIC-I (2004-2007), phase 2 new MUX FADC for MAGIC-I (2007-2009), and phase 3 both MAGIC-I and MAGIC-II operating together (from 2009 on). During sum trigger observations the event rate is multiplied by a factor between 2 and 3, and therefore the real data volume will be higher than these estimations.*

## 8.2 La Palma computing and network

---

QOSA uses MARS software (see Chapter 6 and section 7.2) and it is run at the MAGIC computer cluster at La Palma, described at section 8.2. The QOSA program only uses the latest official checked MARS release unless during special situations that require temporal solutions, generally related to hardware or input files format changes. Except for very few cases, the files reduced with the on-site analysis are final products, and are not re-processed.

## 8.2 La Palma computing and network

The computing system at the MAGIC site is a cluster of computers linked by an internal network, connected to Internet through a firewall ([wwwint.magic.iac.es](http://wwwint.magic.iac.es)) [Coa06] and an external machine ([www.magic.iac.es](http://www.magic.iac.es)).

The internal network connects of the subsystems PCs and the on-site analysis computers. All the computers save their subsystem disks locally, sharing the data through NFS (local mount point in `/remote`). The subsystems computers (*PC1–PC7*) are software “clones” with OS Suse 7.2, connected to the internal network at 100 Mbytes, while the analysis computing (*muxana, muxana{2,3,4,5,6,7,8,9}*) are also “clones” among them but equipped with OS Red Hat 3.4. Another two machines are used as auxiliary processing machines, these are the two telescope DAQ computers: *muxdaq* for MAGIC-I, and *pc19* for MAGIC-II. The first one has OS Red Hat 3.4 installed while the second one uses OS CERN SLC 4.5. These latter two machines can only be used for analysis when the data taking is over. Some details of the analysis machines capacities are shown in Table 8.2.

The storage capacity of the cluster is provided by four RAID systems. Each partition of each raid system has 6.4 Tbytes capacity. RAIDs 1 and 2 have a single partition, RAID 3 has two partitions and RAID 4 has three partitions. In total, 45 Tbytes are available. The read/write speed of the system is between 250 and 300 MB/s.

The analysis machines are connected with the RAID system through a high speed Gigabit Ethernet connection. Further details on MAGIC site computing system can be found in reference [Car09].

The central control reports for both telescopes are stored during the data taking at `$logs` directory and after 7:30 UTC moved to the `$logsr` directory at raid2. Raw data from MAGIC-I are stored at the RAID system `/mnt/raid1/muxdata`. MAGIC-II raw files are stored at `/mnt/raid4_1/M2rawdata/` directory.

The processed files are copied to the MAGIC data center at PIC. The transference of calibrated files starts as soon as the full night is processed. On the other hand, image parameter files (*star* files) are copied to PIC and synchronized as soon as they are generated. The transference of the files is performed by using *rsync* processes. More details about the data center can be found at reference [Rei09].

## 8.2 La Palma computing and network

| Machine                 | CPU cores | CPU (GHz) | RAM (GB) | Max. proc. 7:00-18:00 UTC | Max. proc. 18:00-7:00 UTC |
|-------------------------|-----------|-----------|----------|---------------------------|---------------------------|
| <i>muxana</i>           | 8         | 2.8       | 8        | 6                         | 2                         |
| <i>muxana2, muxana3</i> | 4         | 3         | 3        | 4                         | 2                         |
| <i>muxana{4-9}</i>      | 8         | 2         | 4        | 8                         | 4                         |
| <i>muxdaq</i>           | 8         | 2.8       | 4        | 8                         | 0                         |
| <i>pc19</i>             | 8         | 2.3       | 3        | 4                         | 0                         |

Table 8.2: *Main characteristics of the computers available for the on-site analysis as of January 2010. Last two columns show the number of maximum simultaneous on-site analysis processes that are allowed at each machine.*

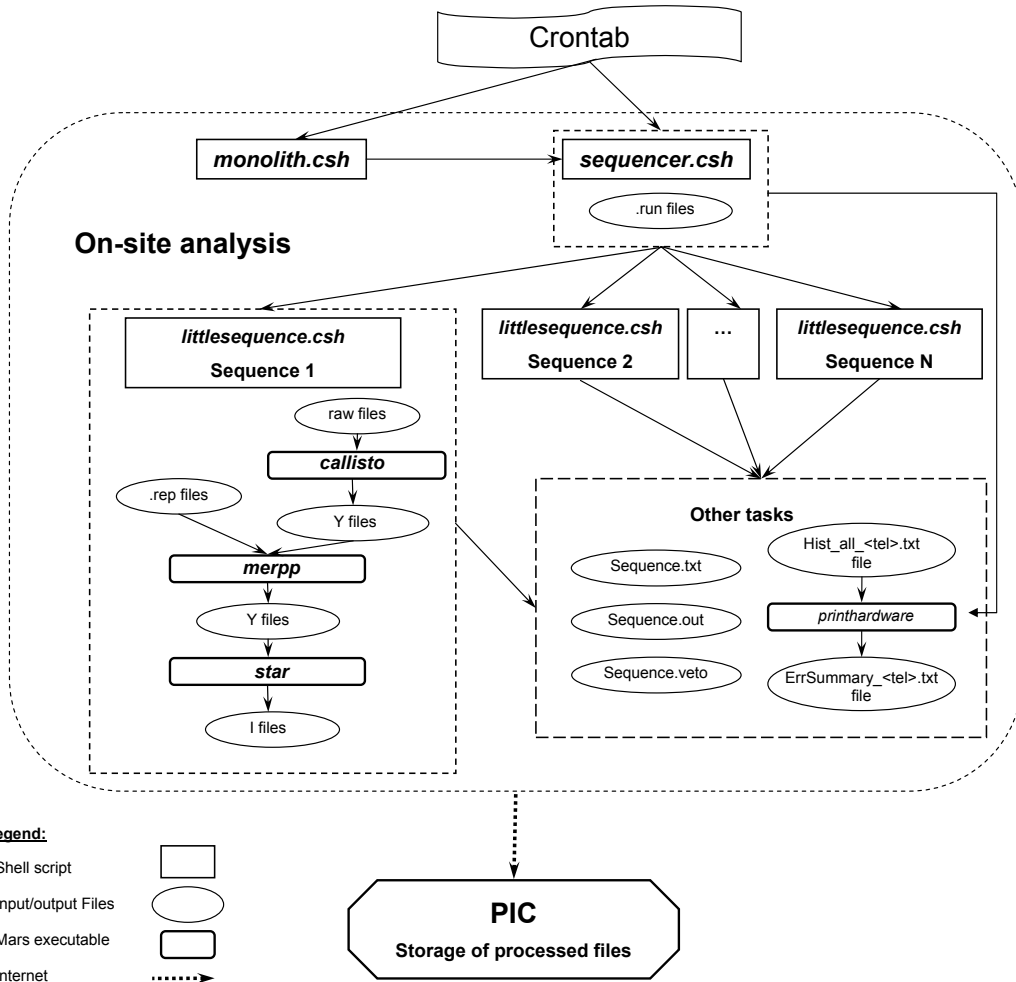


Figure 8.1: *On-site analysis program scheme. The most relevant scripts, executables and input/output files are shown in a schematic view. The products of the on-site analysis are transferred to PIC.*

### 8.3 Program description

The aim of the QOSA software is to perform the first part of the data reduction (calibration, image cleaning and parametrization) of MAGIC data, allowing a prompt transfer to PIC. The QOSA software achieves its objective by a high degree of parallelization of the data reduction and starting to work as soon as the first data files are recorded.

Unless unexpected problems happen during the analysis process, all star files are available around 12:00 UTC in the morning, after the data taking night. These reduced data are available to be downloaded at the MAGIC data center.

In this section, MAGIC-I data processing software will be described. The software for MAGIC-II was developed while this thesis was written, and is rather similar to MAGIC-I one. Its particularities are described in section 8.4.

In the following sections, when a directory on the computing system is mentioned, it is quoted in an abbreviated form, starting with the “\$” character. The detailed directory paths are indicated in Table 8.3.

#### 8.3.1 Program control scripts

The QOSA program is run by the analysis computers described in section 8.2, and belongs to the user *analysis*. The program is located at the directory `$QOSA` in the *muxana* machine. The sub-directories *bin*, *macros* and *awk* contain, respectively, the *csh*, *root* and *AWK* scripts, while the *config* directory contains the configuration details. Reduced data are stored at the corresponding `$star` analysis directory of the night, while calibrated files are moved to the `$cal` directory after they are generated. A schematic view of the most relevant directories is shown in Figure 8.2.

The QOSA program automatic operation is managed through the Linux “cron daemon” at *muxana* using the crontab file from user *analysis*, defined at *muxana* machine. The following two scripts, that are launched in the *muxana* computer, are the responsibles of starting the different tasks of QOSA:

- ***sequencer.csh***: this c-shell script takes care of the sequence creation and of the launching of the *littlesequence.csh* processes responsible of the data reduction. The “cron daemon” only executes *sequencer.csh* to process the data taken the night before, and it works from 9:00 UTC to 23:00 UTC, being launched every 10 minutes.
- ***monolith.csh***: checks if there is remaining data from previous days to be processed. It also controls partially the processing while the data taking is on course. In the case there is data to be processed, this script launches *sequencer.csh* for the corresponding date. The script *monolith.csh* is launched every 15 minutes.

### 8.3 Program description

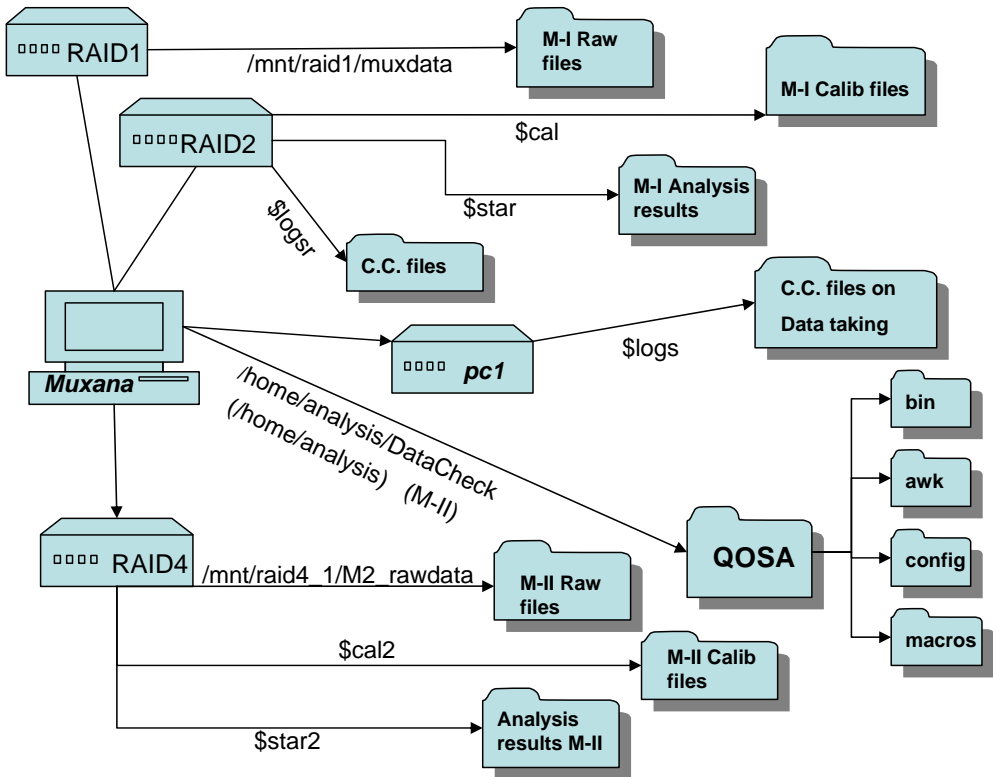


Figure 8.2: *Scheme of directories relevant for the on-site analysis.*

Other auxiliary scripts are:

- ***eraser.csh***: allows to immediately halt all the on-site analysis processes in all the analysis machines and prevents the cron daemon to launch any more on-site analysis processes. Option “stop” halts all processes, while “start” resumes the on-site analysis (the processes will be launched by the cron daemon jobs explained before). This script can be also called by the operators in case it is needed to stop the on-site analysis program. The *osakiller* executable at *operator* home directory halts all processes by calling *eraser.csh*, while *osastarter*, at the same machine, cancels the previous halt order (calling also *eraser.csh*), so the on-site analysis processes can be launched by the “cron daemon” again. The operators might want to stop the on-site analysis in certain situations, as for example, in case the disk access of the QOSA processes is interfering with the data acquisition.
- ***Status2Web.sh***, launched by the “cron daemon” every 10 minutes from 9:00 UTC to 19:00 UTC, performs some auxiliary tasks useful for the on-site analysis administrators. It copies some information to a webpage<sup>1</sup>, so the status of the ongoing processes can be tracked without the need of a *ssh* connection to La Palma computing system. This information is the amount

<sup>1</sup> <http://www.magic.iac.es/operations/datacheck/info/>

## 8.3 Program description

---

of free disk space on the RAID systems, the number of processes running and the list of raw files not yet processed for the last three days.

A schematic view of the QOSA program components is shown in Figure 8.1. All the QOSA program code can be found at the MAGIC CVS repository.

### 8.3.2 Sequencer tasks

The *sequencer.csh* script is normally launched by the “cron daemon” as said before. It can also be manually executed to start the on-site analysis for any datataking night. If no argument is specified, previous night’s data analysis is launched. If one specific night is given as an argument, the program will be launched for the selected night. As an example, the command:

```
$QOSA/bin/sequencer.csh 2010_04_01
```

will launch QOSA for 2010 April the 1st.

The script *sequencer.csh* first creates a list of the runs to be analyzed, using the *AWK* script called “nightsummary.awk” that reads the run summary files (extension *.run*) present at the central control files directory. The output of this script is stored in a file called *NightSummary\_<tel>\_<YYYY>\_<MM>\_<DD>.txt*, present in the analysis directory. For each sub-run the file contains a line with relevant information that will be needed later in the QOSA processes, like the run start time, run stop time, number of events, zenithal angle, etc.

Reading the information summarized at *nightsummary.txt*, *sequencer.csh* creates the sequences to be analyzed. In the on-site analysis context, a sequence contains one data run with all its sub-run files. If the two runs before the data run of the sequence are a pedestal and a calibration runs, then both are included in the sequence. Any run tagged as *test* will be ignored: these are technical runs requested by experts that are not intended to be analyzed in the standard way. Before any further work, the script checks if the sequence has already finished the *callisto* and *star* processes. This is achieved verifying if the first and last *callisto* and *star* files have been correctly created.

Working in a sequence basis, the best degree of parallelization is obtained if the the calibration constants from the pedestal-calibration pair can be shared as starting values for the data runs. If the temperature at the camera center remains constant (within 1 degree) along these sequences, then the calibration parameters are assumed to remain stable enough, and therefore it is possible to share them for all this group of sequences. Any small variation on the calibration parameters is then corrected using the interleaved calibration and pedestal events. For this parallelization, the calibration parameters stored at the file *calib.root* are used, obtained from a *callisto* (option *-c*) process. In case the temperature variation

### 8.3 Program description

---

| Short Name | Full path   |
|------------|---|
| \$logs     | /remote/pc1/home/control/SuperArehucas_CC/logbooks/         |
| \$logsr    | /mnt/raid2/Reports/ccdata                                   |
| \$QOSA     | /home/analysis/DataCheck/QOSA                               |
| \$fin      | /home/analysis/DataCheck/osa_finished                       |
| \$star     | /mnt/raid1/analysis/DataCheck/Data/analysis/<month>/<day>   |
| \$cal      | /mnt/raid1/analysis/CalibRootFiles/<year>_<month>_<day>     |
| \$star2    | /mnt/raid4_3/analysis/QOSA/DataM2/<month>/<day>             |
| \$cal2     | /mnt/raid4_3/analysis/CalibRootFilesM2/<year>_<month>_<day> |
| \$dominoc  | /mnt/raid4_1/calib_coeff/                                   |

Table 8.3: Relevant directories for the QOSA software, and their abbreviated name used in this chapter.

is above 1 degree, then the starting calibration parameters for sequences without pedestal and calibration pair is the output *signal.root* file from the previous callisto process. In this last scenario, one process has to wait until the previous one has finished. In both cases, the best calibration of the data is guaranteed.

A maximum number of processes that can be run in each analysis machine simultaneously was decided, according to the characteristics of each machine, and the disk access capacity, avoiding possible interference with the DAQs of both telescopes during data taking. Table 8.2 shows the maximum number of processes allowed by each machine. The program manages the CPU availability by checking the number of on-site analysis processes already running on each of the computers, and in case there is room for an additional process, it will launch *littlesequence.csh* (see section 8.3.3) for the corresponding sequence, unless a *veto* file is found. A veto file is created during the processing of a sequence if a problem that cannot be solved with the available input card arises. Only three trials (with each adequate input card) are allowed for each callisto and star processes before the veto is created.

After the *littlesequence.csh* process is run, two summary files are created:

- ***hist\_all\_<tel>.txt***. This file contains a summary of all the analysis processes already launched by *littlesequence.csh*, obtained by adding each sequences summary. See *littlesequence.csh* section to see the format description. It is used to build the veto files.
- ***ErrSummary\_<tel>.txt***. This file contains an explanation and possible solution for any problem found during all *littlesequence.csh* processes. This file is used also for the daily check procedure, see Chapter 7.

As a final step, *sequencer.csh* launches the root macro *GetAtimes.C*. This macro performs a task needed for the MAGIC Data Quality Check software (see

## 8.3 Program description

---

Chapter 7). It obtains the arrival times distributions from all *callisto* processes of the night and copies the resulting plots to the data check webpage calibration section<sup>1</sup>.

### 8.3.3 Littlesequence tasks

The purpose of the script *littlesequence.csh* is to execute the first analysis steps on a sequence. It is normally called by *sequencer.csh* for every sequence of the data taking night. It can also be manually executed by specifying the following parameters: the date, analysis directory, the *signal/calib.root* file to use, the sequence to process, and the telescope (MAGIC-I or MAGIC-II) to which correspond these data. An example on how to run *littlesequence.csh* is:

```
littlesequence.csh 2009_07_02 $star calib01007345_M1.root  
1007347 M1
```

#### 8.3.3.1 Calibration

The goal of the calibration is to find the response of the whole light detection and amplification chain. Detailed information can be found in [Gau06] and in previous chapters of this thesis.

The script *littlesequence.csh* will first try to perform the calibration of the sequence using the default configuration. The default configuration for MAGIC-I calibration is set by using the input card *callisto\_MUX.rc*, that can be found at MAGIC CVS at PIC, according to the MARS version used at the moment.

In case the calibration fails, *callisto* returns an error code through the *exit status* variable. Most of the errors are well known and there are dedicated input cards to allow the calibration of the data avoiding the error. Nevertheless, the detected problem, which has commonly a hardware problem origin, remains in the calibrated files. These input cards allow to have the data calibrated, even if the original quality of the recorded data is not optimum. The most common error codes are:

- **Error code 5:** This error happens when too many problematic pixels have been found during the calibration. The input card *callisto\_MUX\_clusped.rc* allows to calibrate data with non optimal pedestal files and when a cluster of bad pixels is found. Basically, it bypasses the error warnings, therefore the resulting calibrated files will inherit the problems reported.
- **Error code 13:** This happens when the pedestals have not been correctly recognized with the chosen extractor. The input card *callisto\_MUX\_pedestal.rc* allows to ignore this error and continue calibrating the data with the mentioned non optimum pedestals.

---

<sup>1</sup><http://www.magic.iac.es/operations/datablock/daqdata>

## 8.3 Program description

---

- **Error code 15:** This happens when the pedestal run has too many events not triggered by the pedestal trigger. The files can still be calibrated by using the input card: *callisto\_MUX\_pedcal.rc*. The data will be calibrated using the triggered pedestals.

Other possible errors may happen during the calibration process<sup>1</sup>, and their possible origin can be investigated by using the MARS executable *printhardware*.

After the calibration is performed, the central control reports are added to the calibrated data. These reports contain, among all the subsystems information, the drive and starguider systems reports. Having this information added, the telescope mispointing can be corrected in later stages. The subsystem report information is added to the calibrated files by the MARS executable *merpp* using the *-u* option.

### 8.3.3.2 Image cleaning and parametrization

The next step of the data reduction is to clean the calibrated shower images of the sequence from the LONS. After the images are cleaned, a parametrization of the images is performed. Both image cleaning and image parameter calculation are done by the MARS executable *star*. The image parametrization will be needed at the final steps of the analysis for the signal/background discrimination and for the energy estimation. These last steps will be performed by the source analyzers.

The script *littlesequence.csh* runs *star* for the sequence with the standard configuration obtained from the input cards *star\_timing.rc* for MAGIC-I. The image is cleaned according to the number of phe (photo-electrons) of each pixel and its neighbours, and also according to the arrival times of the pulses at the pixels. The used configuration is the MARS default one. More details on the used image cleaning can be found in section 6.7.1

The list of image parameters produced is rather long. The Hillas parameters [Hil85] are the best known ones. They are basically statistical moments up to third order of the cleaned light distribution on the camera in phe units. Further description of the image parameters can be found in reference [GM08] and section 6.7.2.

The executable *star* also uses the information from the starguider subsystem to correct the data from the mispointing, when this information is correct. It happens often that for twilight or moon observations the information obtained from *starguider* is not adequate for the mispointing correction. If this happens, *star* gives the output error code “6” and *littlesequence.csh* tries again to run *star* with the input card *star\_nostgcal.rc*, what will create output files without mispointing correction.

---

<sup>1</sup>Their meaning can be found in the MARS class MAnalysisProblem.cc at <http://magic.pic.es/priv/cvs/>

## 8.3 Program description

---

### 8.3.3.3 File copy and verification

After the *star* process has finished, the calibrated files of the sequence are copied to the calibrated files directory `$cal`.

For each one of the processed sequences a set of ASCII text files is generated. All these files are named as *sequence\_<tel>-<runnum>*, and they are distinguished by their extension:

- **.txt**: This file is the sequence itself in the standard MARS format.
- **.out**: This is the log file of the sequence. All output messages from *littlesequence.csh* and the MARS executables launched by it are stored here.
- **.history**: This is a file with a brief summary of the processes run on the sequence. This allows to control how many times and with what configuration input card has a MARS executable process been launched, allowing the creation of the previously described veto files. The files contains information like the type of process, the time when it was executed, the used configuration, and the error code in case that the process failed.
- **.veto**: This file is empty and it has a twofold purpose: First one is to limit the number of consecutive times that a failed process can be again run. The actual configuration only allows three trials before the veto file is created. A sequence with an existing *.veto* file will never be processed by the QOSA automatic scripts. The second use of this file is to prevent *littlesequence.csh* to launch *callisto* while the calibrated files are being transferred to the calibrated files directory.

### 8.3.4 Other tasks

The *star* files are synchronized by *rsync* processes to the MAGIC PIC database as soon as they are generated. Due to the big size of the *callisto* files, they are only transferred once, when all the sequences have been fully processed. In order to mark a day as finished, an empty text file is created at the directory `$fn` at *muxana* machine. When the calibrated files are transferred to PIC, they are automatically deleted from the RAID system. After the raw files are copied to tapes, they are also automatically deleted from the RAID. The transfer and data erasing are tasks under the responsibility of other groups in the collaboration.

Finally, the file with the found errors (*ErrSummary\_tel.txt*) is copied to a folder in the MAGIC webpage at La Palma<sup>1</sup>.

---

<sup>1</sup>[www.magic.iac.es/operations/datacheck/CCDAQCheck/](http://www.magic.iac.es/operations/datacheck/CCDAQCheck/)

### 8.4 MAGIC-II update

The QOSA analysis software has been expanded to reduce MAGIC-II data<sup>1</sup>. This software is mainly the adaptation of the existing software to the second telescope requirements. The obtained calibrated files are stored at directory `$cal2` and the analysis directory where the `star` files are stored is `$star2`.

The calibration of MAGIC-II files is slightly different from the first telescope ones. Raw files have to be first “domino-calibrated”, by using the so called “domino coefficients” to take into account the non linearity and temperature dependence of the domino ring sampler. The files containing these coefficients can be found at `$dominoc` directory. Raw files are domino calibrated using the MARS executable `merpp` with the option `--CalibrateDomino`.

A new script, `merpper.csh`, launched from `littlesequence`, takes care of the two needed `merpp` processes, that will be both done before the calibration with `callisto`. The history file for the sequences of MAGIC-II data have a new meaning for the last field of the file in the case of the `merpp` process: 0 if the process went right, and 1 if it failed. Due to computer power and available disk constrains, only one trial of the `merpp` process is allowed for each sequence, and therefore if it fails the sequence is vetoed.

The calibration configuration input card used for `callisto` is `callisto_domino.rc`. The image cleaning form MAGIC-II data is for the time being a very strict one, and absolute 16/6 phe for core/boundary pixels. Time information is not used for the cleaning. The selected image cleaning is so strict because in the time this thesis was written MAGIC-II data analysis was not yet optimized. The used input card is `star_M2.rc`, found at the program configuration directory, and also in the MAGIC CVS.

### 8.5 Conclusion

The software presented here performs a fast standard data reduction that allows the calibrated and `star` files to be transferred quickly to the MAGIC experiment data center at PIC. The produced files are final and commonly used for the last steps of MAGIC analysis results. To achieve this objective, this software uses the computer cluster at MAGIC site at La Palma to optimize, using a high degree of parallelization at sequence level, the processing of the raw data files.

The data volume has increased considerably since the installation of the first version of the on-site analysis: Major hardware updates like the installation of the MUX FADCs, the use of the sum-trigger, and the incorporation of MAGIC-II have increased dramatically the amount of data stored every night. The actual version of the on-site analysis, QOSA, is the result of the evolution of the original

---

<sup>1</sup>This expansion has been performed by D. Nieto, UCM.

## 8.5 Conclusion

---

code [DO06, De 08, Oya06] that, together with the update of the needed computing and storage capacity, has successfully survived the mentioned hardware changes. The results presented in this chapter have been published as a MAGIC internal document [Oya09b] and at the VIII meeting of the Spanish Astronomy Society [OR08].

# Chapter 9

## Mrk 421 2006 multiwavelength campaigns

### 9.1 Introduction

The AGN Markarian 421 (Mrk 421; R.A.  $11^h04^m27.2^s$ , decl.  $+38^\circ12'32.0''$  [J2000.0]) was the first extragalactic source detected in the TeV energy range, using IACTs [[Pun92](#), [Pet96](#)]. With a redshift of  $z = 0.030$  it is one of the closest known and, together with Mrk 501, the best-studied TeV  $\gamma$ -ray emitting blazar. It is an HBL type BL Lac object (see section [3.2.1.2](#)). It has remained as one of the most active VHE blazars since its detection. So far, flux variations by more than one order of magnitude (e.g. [[Fos08](#)], see Figure [9.1](#)), and occasional flux doubling times as short as 15 min [[Gai96](#), [Aha02b](#), [SWL08](#)] have been observed, indicating very compact emission regions. Variations in the hardness of the TeV  $\gamma$ -ray spectrum during flares were reported by several groups (e.g. [[Kre02](#), [Aha05d](#), [Fos08](#)]). Simultaneous observations in the X-ray and VHE bands have shown strong evidences for correlated flux variability [[Kra01](#), [Bl05](#), [Fos08](#)]. With a long history of observations, Mrk 421 is an ideal candidate for long-term and statistical studies of its emission [[Goe08a](#), [Hsu09](#)]. Figure [9.1](#) shows the lightcurve of this blazar as measured by different instruments since its first detection until 2009, where the high degree of variability of Mrk 421 can be seen.

The HBL Mrk 421 has been detected and studied at all wavelengths of the electromagnetic spectrum from radio waves up to VHE  $\gamma$ -rays. Its SED shows the typical double-peak structure for blazars (see Chapter [3](#)). A way to distinguish between the different emission models (see section [3.4](#)) is to determine the position and the structure of both peaks in the SED, using simultaneous, time-resolved data over a broad energy range obtained in multiwavelength (MWL) observational campaigns. The correlation of the variabilities at keV and TeV energies (or lack of it) during outbursts gives valuable information to understand the source's internal

## 9.2 MAGIC observations and data analysis

---

mechanisms and therefore has been used to refine the blazar emission models. In addition, rapid, sub-hour flaring is interesting as it provides direct constraints on the size of the emission region. These rapid flares also present an observational challenge to multiwavelength studies, as truly simultaneous data must be used in order to develop a reliable characterization of the broadband behavior of these objects.

In this chapter the VHE  $\gamma$ -ray observations of Mrk 421 performed with MAGIC during eight nights in April 2006 and one night in June 2006 will be discussed. These measurements were performed simultaneously to X-ray observations by *Suzaku* [Mit07] and H.E.S.S., as well as *XMM-Newton* [Str01, Mas01] and Whipple in April 28 and 29, respectively. During both nights, particularly long, uninterrupted observations in the VHE energy band of  $\approx 3$  h duration were carried out with MAGIC.

Of particular interest are the observations carried out in April 29, 2006. These observations were performed following an *XMM-Newton*-led target of opportunity (ToO) campaign whose objective was to study simultaneous X-ray and VHE emission from bright blazars during outbursts<sup>1</sup>. The ToO program was first triggered in April 2006 by a major outburst from Mrk 421, detected by regular monitoring of the VHE band by the Whipple telescope. Because of *XMM-Newton* visibility constraints, the coordinated MWL observations (comprising MAGIC, Whipple, *XMM-Newton* and KVA) did not take place until after the maximum of the outburst. The continuation of this ToO program was triggered again in May 2008 by another major outburst from Mrk 421 in the VHE band. In this case, the observations were performed with VERITAS and XMM, but once again captured only the decaying portion of the outburst. As these measurements were taken following the continuation of the ToO same proposal, and seek the same scientific goals, they will be also discussed in this chapter.

An onset of activity in the X-ray band triggered an INTEGRAL-led target-of-opportunity (ToO) campaign, which took place in June 14–25, 2006 for a total of 829 ks [Lic08]. Within this campaign, MAGIC observed Mrk 421 at rather high zenith angles from 43 to 52 degrees in parallel with INTEGRAL on June 14, 2006.

## 9.2 MAGIC observations and data analysis

Data were analyzed following the standard MAGIC analysis procedure (see Chapter 6). The observations presented here are among the first data taken by MAGIC after major hardware upgrades in April 2006 [Goe08b], which required to thoroughly examine the data. The data were taken anyway with the 300 MHz FADCs as the new 2 GHz system was still under commissioning. Despite the hardware

---

<sup>1</sup> “Rapid Flares from TeV Blazars”; P.I.: Prof Wei Cui.

## 9.2 MAGIC observations and data analysis

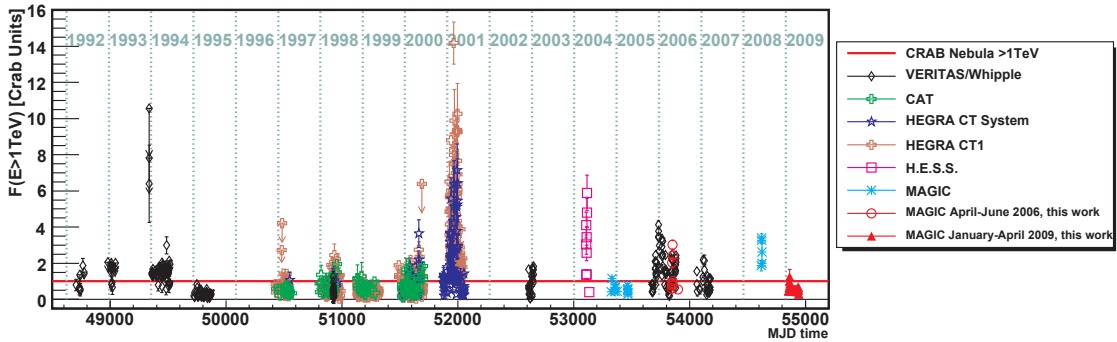


Figure 9.1: *Historical VHE ( $E > 1$  TeV) light curve of Mrk 421 since it's first detection in 1992 [Pun92], as measured by different VHE  $\gamma$ -ray instruments. The red solid line indicates the flux of the Crab Nebula. The red open circles correspond to the measurements described in this chapter. The filled red triangles were obtained during the 2009 MAGIC Mrk 421 campaign, and are described in Chapter 11. The historical data points are taken from the  $\gamma$ -ray light curve archive at DESY: <http://www-zeuthen.desy.de/multi-messenger/GammaRayData/>.*

Table 9.1: *Set of cuts used to estimate the significance of the  $\gamma$ -ray signal.*

| Type      | hadronness       | $\theta^2$               | combined acceptance |
|-----------|------------------|--------------------------|---------------------|
| Detection | $\leq 0.1$ (40%) | $\leq 0.04^\circ$ (64 %) | 26%                 |
| Loose     | dynamical (70%)  | dynamical (70%)          | 48%                 |

changes, the MAGIC subsystems were working as expected with the exception of an unstable trigger behavior for some PMTs, leading to a significant loss of events in one sector of the camera. The loss of events was caused by too late arrival time of events in the FADC window. In order to minimize this effect during the signal extraction, a cubic spline signal extractor (see section 6.6.1) was used, because it is less affected by the problem than other available extractors<sup>1</sup>.

After calibration and signal extraction, noise from night-sky background light was removed from the air-shower images by applying an absolute time image cleaning (see section 6.7.1), requiring a minimum light content of 10 phe for the core pixels of the image and 5 phe for the boundary ones. Since the data were taken with the 300 MHz FADCs, the time information of the pixels was not used for the image cleaning.

The data were filtered by rejecting trivial background events, such as accidental noise triggers, or data taken during adverse atmospheric conditions (see section 6.8.4). The event rate after image cleaning was used as primary run quality indicator. 12.4 hours out of the total 15.0 hours' worth of data survived this quality selection and were used for further analysis.

<sup>1</sup>M. Gaug, private communication.

## 9.2 MAGIC observations and data analysis

---

Table 9.2: *Data sets and observational circumstances.*

| Night      | Observation Window [MJD]  | $t_{\text{eff.}}$ [h] | ZA [ $^{\circ}$ ] |
|------------|---------------------------|-----------------------|-------------------|
| 2006/04/22 | 53847.97679 – 53848.01460 | 0.76                  | 18 – 28           |
| 2006/04/24 | 53849.96428 – 53850.00669 | 0.99                  | 16 – 28           |
| 2006/04/25 | 53850.92813 – 53850.99607 | 1.38                  | 10 – 26           |
| 2006/04/26 | 53851.92862 – 53852.00383 | 1.65                  | 10 – 29           |
| 2006/04/27 | 53852.93474 – 53853.00047 | 1.41                  | 12 – 28           |
| 2006/04/28 | 53853.88173 – 53854.01394 | 2.22                  | 10 – 32           |
| 2006/04/29 | 53854.89514 – 53855.04119 | 2.74                  | 9 – 41            |
| 2006/04/30 | 53855.97283 – 53855.97906 | 0.15                  | 23 – 24           |
| 2006/06/14 | 53900.91979 – 53900.95532 | 0.80                  | 43 – 52           |

$t_{\text{eff.}}$  denotes the effective observation time. ZA gives the zenith angle range of the observations.

The observations were carried out during dark nights, employing the wobble mode (see section 5.8). Image parameters were calculated as described in section 6.7.2. As mentioned before, the data were taken with the 300 MHz FADCs, and therefore no time image parameters were used in the gamma/hadron discrimination. Table 9.1 summarizes the used cuts.

The  $\gamma$ /hadron separation was performed by using the RF method, as described in section 6.8.1. The parameters *size*, *width*, *length*, *size*/ $(\text{width} \times \text{length})$  and *conc* were used to train the algorithm. A cut in the parameter *hadronness* and in the angular parameter  $\theta^2$  (see section 6.9 for details) was performed to extract the events coming from the source, while three *off* regions (at  $90^{\circ}$ ,  $180^{\circ}$  and  $270^{\circ}$  with respect to the source position) were used to determine the background events in the signal region. The *hadronness* used to determine the detection cuts was chosen according to the sensitivity study performed in [Ali09a], due to the lack of Crab Nebula data during the period of observations (and therefore sharing the mentioned hardware instabilities). All significances presented in this chapter were calculated using Eq. 17 of [LM83].

Primary  $\gamma$ -ray energies were reconstructed from the image parameters using the RF method (see section 6.8.2). The arrival directions of the showers were calculated using the DISP method (see section 6.8.3).

For the spectrum calculation, some *loose* cuts were set independently for each energy bin in the spectrum, requiring that the acceptance of MC simulated gamma-rays to be 70% for both *hadronness* and  $\theta^2$  cuts in each energy bin (see 9.1).

In order to estimate the effect caused by the inhomogeneity mentioned above, a simple procedure was applied to the data: The expected number of events, as a function of energy, for the affected sector was estimated as the mean of the number of events in the other five sectors of the camera. (An homogeneous distribution of

### 9.3 Results

---

events through the six sectors is expected for normal conditions.) The difference was computed using the whole data sample in order to have sufficient statistics. A decrease of the differential photon flux of 7% between 250 and 400 GeV and 3% for higher energies for April 2006 data was found. Due to the higher zenith distance and energy threshold, the method was adapted for June 14, 2006 and yielded an increase up to 8% between 450 and 700 GeV and 3% for higher energies. However the above mentioned effect is just an average one, with estimated flux errors of up to 10% for individual nights. The same procedure was applied to a good-quality data set and also to an MC sample. No fake correction was created in these cases.

To mitigate the effect of the inhomogeneity, instead of an (already increased) energy threshold of 250 GeV, higher thresholds of 350 or 450 GeV were applied for some observation nights. With this higher threshold, the estimated systematic error remains within reasonable limits.

For the calculation of the individual light curves, as well as for the overall April 2006 lightcurve the flux between 250 GeV and 350 GeV was extrapolated for the nights with higher threshold. A power-law behavior was assumed in this energy range, with the spectral index determined for the first 3 bins of the whole April data-set (i.e.  $-2.10$ ). The flux normalization for each night was determined at 500 GeV from a fit to the first 3 bins of the spectrum, an energy range which is reliable for all affected nights.

Table 9.2 summarizes the analyzed data sets. The statistical significance of the detection is assessed by applying the detection cuts shown in Table 9.1 for  $\text{size} > 400 \text{ phe}$ . All stated uncertainties are statistical only; the systematic errors are discussed in section 6.12.

## 9.3 Results

### 9.3.1 Results for 2006 April 22 – 30

In April 2006 MAGIC observed Mrk 421 from MJD 53848 to MJD 53856. Two MWL campaigns were carried out during the observations, simultaneously with *Suzaku* [Ush09] and with *XMM-Newton* [Acc09] on MJD 53854 and MJD 53855, respectively. Mrk 421 was also observed by means of the monitoring program of the Whipple 10-m telescope [Hor09], but about 3.5 hours after the MAGIC observations stopped, due to the different longitudes of the two instruments.

### 9.3 Results

---

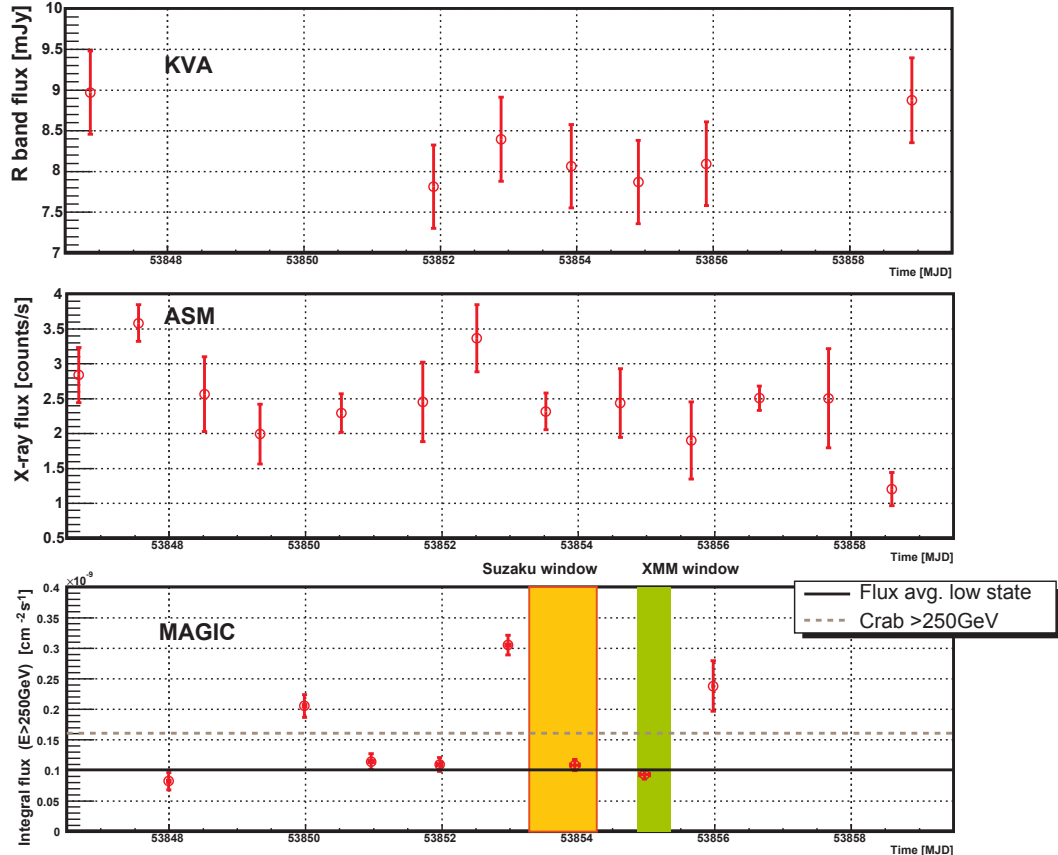


Figure 9.2: Light curve for April 2006 Mrk 421 observations. Upper panel: Light curve of the optical flux ( $R$  band) as measured by the KVA telescope. Middle panel: Day-by-day X-ray counts as observed by the RXTE/ASM (2–10 keV). Lower panel: VHE ( $E > 250$  GeV) light curve as measured by MAGIC, where the data points represent average nightly fluxes. The observation windows of the Suzaku (MJD 53853.28–53854.27) and XMM-Newton (MJD 53854.87–53855.35) MWL campaigns are marked by the yellow and green areas, respectively. A “mean low flux” (solid line) was obtained as an average over all VHE data points below  $1.01 \cdot 10^{-10} \text{ cm}^{-2}\text{s}^{-1}$ . The dashed line gives the Crab nebula flux [Alb08f] for comparison.

### 9.3 Results

---

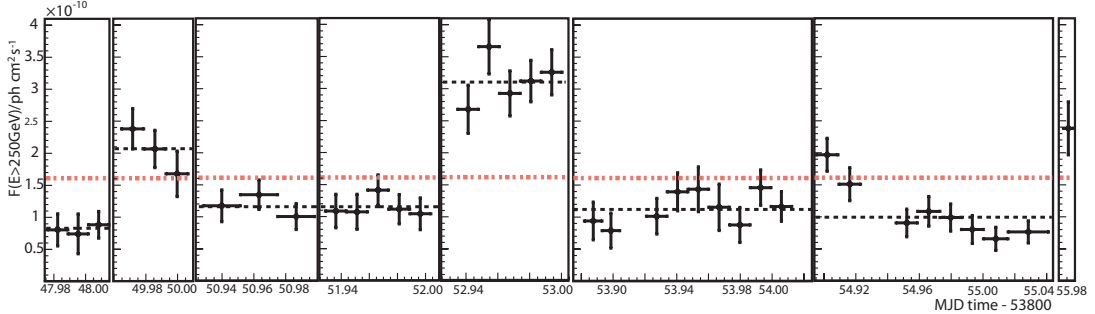


Figure 9.3: *Intra-night VHE ( $E > 250$  GeV) light curve for the Mrk 421 observations in April 2006.* The dot-dashed red line represents the Crab Nebula flux [Alb08f], whereas the individual dashed black lines show the result of a constant fit to the flux bins of the corresponding nights.

A clear  $\gamma$ -ray signal from the source was detected on all 8 observation nights. In total, 2050 excess events were recorded over a background of 836 events, yielding an overall significance of  $45\sigma$ . Mrk 421 exhibited an average flux of  $F_{>250\text{ GeV}} = (1.22 \pm 0.04) \cdot 10^{-10}\text{cm}^{-2}\text{s}^{-1}$ . When compared to earlier observations (see Figure 9.1), these observations indicate a somewhat elevated flux state of Mrk 421. Particularly, apart from a pedestal flux of  $F_{>250\text{ GeV}} = (1.01 \pm 0.04) \cdot 10^{-10}\text{cm}^{-2}\text{s}^{-1}$ , higher flux states were found in the nights of MJD 53850,  $F_{>250\text{ GeV}} = (2.06 \pm 0.19) \cdot 10^{-10}\text{cm}^{-2}\text{s}^{-1}$ , MJD 53853,  $F_{>250\text{ GeV}} = (3.05 \pm 0.16) \cdot 10^{-10}\text{cm}^{-2}\text{s}^{-1}$ , and MJD 53856,  $F_{>250\text{ GeV}} = (2.4 \pm 0.4) \cdot 10^{-10}\text{cm}^{-2}\text{s}^{-1}$  were found (Figure 9.2).

The analysis results on night-by-night basis are summarized in Table 9.5, and include the nightly numbers of excess and background events, significances, average integral fluxes above 250 GeV (where the nights with an energy cut of 350 GeV were extrapolated down to 250 GeV, see section 9.2 for details) and spectral fits with simple power-law functions (PL) of the form:

$$\frac{dF}{dE} = f_0 \cdot (E/E_0)^{-\alpha} \quad (9.1)$$

The obtained differential energy spectra were unfolded using the Tikhonov unfolding technique (see section 6.10.3). Figures 9.4 and 9.5 show the overall differential spectrum for April and individual night spectra, respectively, before and after being de-absorbed with the extragalactic background light model discussed in [FRV08]. In order to estimate the systematic uncertainty due to the analysis, three additional analysis were performed: one using the angular parameter  $\theta^2$  and one *off* region for background signal estimation, and another two using the *alpha* angular parameter, one of them using one *off* region and another one using three *off* regions. Different unfolding procedures were performed for every analysis. An area of systematic uncertainty from the analysis was built with the whole sample

### 9.3 Results

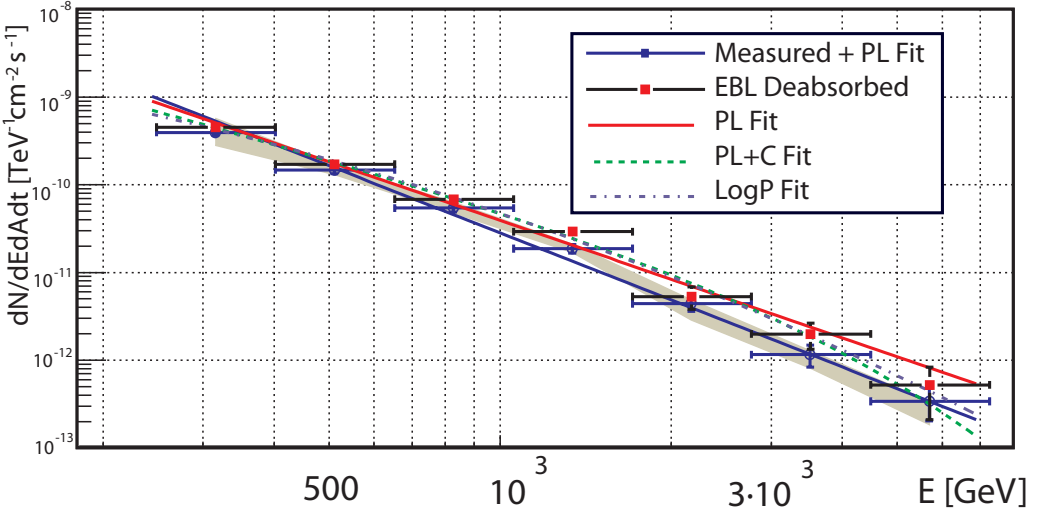


Figure 9.4: Differential energy spectrum for Mkn 421 for April 2006 before (blue open circles) and after correcting for EBL absorption (red solid squares). The measured spectrum was fit to a power law (Eq. 9.1). Power law, log-P (Eq. 9.4) and PL+C (Eq. 9.5) fits were performed to the EBL de-absorbed spectrum (solid red, blue point-dashed and green dashed curves, respectively). Curved fits (log-P and PL+C) describe better the data than simple power law fits, according to a likelihood ratio test. The gray area represents a estimation of the systematics from the different analysis methods (see text for details).

of successfully unfolded spectral points (see for example the gray area in Figure 9.4).

The energy thresholds of the individual observations are also given in Table 9.5. As the analysis threshold is always lower than the applied energy cut, the latter one defines the energy threshold value.

The strong  $\gamma$ -ray signal allowed to infer light curves with a resolution below one hour for all of the observation nights which are shown in Figure 9.3. Most light curves are compatible with a constant flux during the nightly observation time (see Table 9.5 for all constant-fit  $\chi^2_{\text{red}}$  values), while on MJD 53855 a clear intra-night variability is apparent. A fit with a constant function indicates significant flux variability ( $\chi^2_{\text{red}} = 24/7$ ,  $P = 9.7 \cdot 10^{-4}$ ). A flux halving time of  $34 \pm 11$  minutes was calculated according to a simple model consisting in a profile of an exponential plus a constant background:

$$F(t) = f_0 + f_1 \cdot e^{-\tau_{\text{decay}}(t-t_0)} \quad t \leq t_0 \quad (9.2)$$

Note that this interesting observation window has also been covered by *XMM-Newton* observations in the X-ray band (see section 9.4).

### 9.3 Results

---

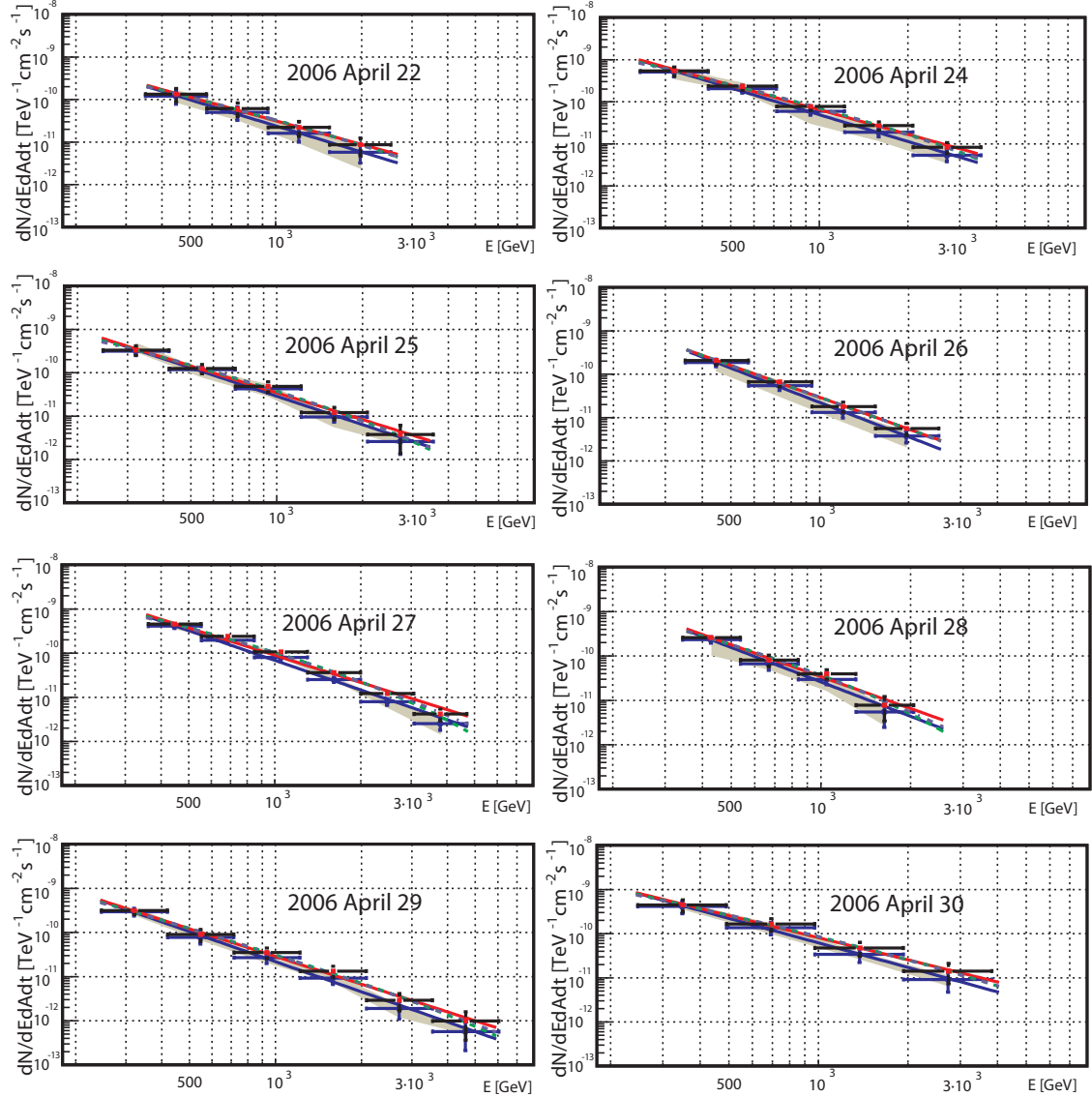


Figure 9.5: Differential energy spectra for Mkn 421 for individual nights in April 2006 before (blue) and after correcting for EBL absorption (red squares). Every individual measured spectrum was fit to a power law (Eq. 9.1). Power law, log- $P$  (Eq. 9.4) and  $PL+C$  (Eq. 9.5) fits were performed to the EBL de-absorbed spectra (solid red, blue point-dashed and green dashed curves, respectively). Only for April 27 curved fits are preferred over simple power law fits, according to a likelihood ratio test. The gray areas represent estimations of the systematics from the different analysis methods (see text for details).

## 9.3 Results

---

### 9.3.1.1 Observations at other wavelengths

The KVA (Kungliga Vetenskaps Akademien, Royal Swedish Academy of Sciences) telescope<sup>1</sup> is located at La Palma (Canary Islands), close to the MAGIC telescopes, and operated by the Tuorla Observatory since Autumn 2003. It is a 35 cm diameter telescope, used for optical R-band auxiliary observations during MAGIC observations. The upper panel of Figure 9.2 shows the optical lightcurve obtained during the MAGIC April 2006 observations. The contribution from the host galaxy and nearby stars ( $F = 8.1 \pm 0.4$  mJy, [Nil07]) has been subtracted from the overall flux.

The RXTE satellite performed observations of the source during all the MAGIC observation nights. The middle panel of Figure 9.2 shows the corresponding flux in the X-ray band, as observed by the All-Sky-Monitor (ASM<sup>2</sup>) on-board the RXTE satellite. The RXTE Proportional Counter Array (PCA) [Jah96] also measured the source every night<sup>3</sup>.

*Suzaku* observed the source from 06:46 UT April 28 (MJD 53853) through April 29 (MJD 53854) 06:30 UT, in the energy range from 0.5 keV to 60 keV. A significant variability was found during these observations, decreasing in each energy band of a factor 2–4 since the beginning to the middle of the observation window, and then starting to increase in the second half of the observations. The source had reached its lowest X-ray flux state and started slowly to increase during the MAGIC observation window (21:10 UT April 28 – 00:20 UT April 29). The VHE flux measured with MAGIC this day is consistent with a constant flux (see Table 9.5 and Figure 9.3).

The observations of *XMM-Newton* were performed during (MJD 53854.8639 – 53855.3488) being the first part of them simultaneous to MAGIC observations for  $\sim 4$  hours. The simultaneous VHE observations continued with Whipple observations during  $\sim 3.5$  hours, about 3.5 hours after the MAGIC observations ended. These observations, that make a rather large sample of X–VHE simultaneous data, will be further discussed in section 9.4.

### 9.3.1.2 Cross-band correlations

In Figure 9.2 a correlation seems apparent between the KVA and MAGIC measured fluxes. The method described in [Hru08, Alb07e] was applied to the set of simultaneous optical (R band) and VHE points in order to quantify this possible correlation. A set of  $10^5$  light curves was simulated based on the Gaussian errors of the data points. For each pair of simulated optical/VHE light curves, the value of Pearson’s  $r$  was calculated, and a probability density function (PDF)

<sup>1</sup><http://tur3.tur.iac.es/>

<sup>2</sup>[http://heasarc.gsfc.nasa.gov/xte\\_weather/](http://heasarc.gsfc.nasa.gov/xte_weather/)

<sup>3</sup>D. Bose, private communication.

### 9.3 Results

---

$f_A(r)$  was built. A second function  $f_B(r)$ , named *auto-correlation* PDF, was built as in the previous case but for the perfectly correlated case. The “perfectly correlated points” were obtained by shifting each measured data point to the closest position on the best fit linear function, while keeping the measured uncertainties. Note that due to the uncertainties of the measurements the Pearson’s r factor will be always  $< 1$  even for the perfectly correlated case. A third function  $f_C(r)$ , named *non-correlation* PDF, was built from uniformly smeared data points. Another function  $f_D(r)$  exists (see e.g. appendix C of [Tay97]), which is an analytical function that also describes the uncorrelated case, without taking into account the uncertainties of the measurements.  $f_D(r)$  is expected to be very similar to  $f_C(r)$ , since the smearing performed to produce this PDF does not increase the randomness of the already randomized seed event. See Figures from 10.4 to 10.9 in Chapter 10 for examples of the various types of PDFs.

A measure of the correlation present between two data samples can be obtained by comparing  $f_A(r)$  (smeared measurement PDF) with  $f_B(r)$  (perfectly correlated PDF) and  $f_C(r)$  (uncorrelated PDF). The PDFs are compared following a robust method based on the Fourier convolution of two empirical PDFs [PGL05]. The probability of a correlation will be noted as  $P_{AB} = P(f_A(r), f_B(r))$ , and the probability of no correlation  $P_{AC} = P(f_A(r), f_C(r))$ . Furthermore, the error of the probabilities can be estimated by comparing the auto-correlation and uncorrelated PDFs  $P_{BC} = P(f_B(r), f_C(r))$ , and additionally comparing  $f_A(r)$  with a PDF  $f_E(r)$  built analogous to  $f_B(r)$ , but translating all the points to the line that crosses the center of gravity of the points that is perpendicular to the best fit line (see [Hru08] for details). It is important to note that this method is not adequate for cases where the best fit functions’ slopes are close to zero or infinity [Hru08].

From the total 8 nights with MAGIC measurements during April 2006 only 5 had KVA simultaneous measurements. Considering the method described above to look for a correlation, a value of Pearson’s r of  $0.55 \pm 0.33$  was found. The probability of agreement between the measured PDF and the fully correlated PDF  $P_{AB}$  is  $0.69 \pm 0.31$ , while the probability that the measurements came as a result of a statistical fluctuation of an entirely uncorrelated physics case is lower,  $P_{AC} 0.36 \pm 0.31$ . The probability for the first scenario to be true and for the second to be false is  $P_{AB}(1 - P_{AC}) = 0.44$ , and the probability for the opposite is  $P_{AC}(1 - P_{AB}) = 0.11$ , which indicates that the correlation scenario is favoured.

Additionally, possible X-ray and VHE correlations were studied for RXTE/ASM data, that were available for every MAGIC observation night. The average count rate was calculated from those RXTE/ASM pointings (dwells) which were taken simultaneously with MAGIC, allowing  $\pm 1$  hour delay with respect to the VHE data. A Pearson’s r  $0.12 \pm 0.31$  was found for the X-ray and VHE correlation. Additionally, the best fit function was found to be almost horizontal what indicates, together with the found r, a lack of correlation. No correlation

### 9.3 Results

---

was found between the KVA and RXTE/ASM fluxes ( $r = 0.05 \pm 0.47$ ) the best fit function being again almost horizontal.

The results of the previously described correlation analysis are summarized in Table 9.7.

#### 9.3.2 Results for 2006 June 14

An onset of activity to  $\approx 2$  times the average quiescent-flux level of Mrk 421 was measured in April 2006 by the RXTE/ASM instrument. It triggered an INTEGRAL ToO campaign from June 14, 2006 to 25 for a total of 829 ks [Lic08]. This  $> 30$  mCrab flux remained until September 2006. During the 9-day campaign, Mrk 421 was targeted by various instruments in the radio, optical, X-ray and VHE wavebands. Results are reported in [Lic08]. On June 14, 2006 MAGIC observed Mrk 421 at rather high zenith angles in parallel with the OMC, JEM-X, and IBIS measurements aboard INTEGRAL. Further VHE coverage was provided by the Whipple 10-m telescope on June 18, 19 and 21, 2006 [Lic08].

The MAGIC observations on June 14, 2006 lasted for 50 minutes. The high zenith angles of 43 to 52 degrees of these observations and the previously mentioned inhomogeneities resulted in an energy threshold of  $E_{\text{thresh.}} = 450$  GeV. In spite of the overall rather difficult observational circumstances [Alb06a], a firm detection on the  $7.5\sigma$  significance level was achieved. The flux level of the source was found to be  $2.6 \pm 0.5 \times 10^{-11}$  for  $E > 450$  GeV, corresponding to 0.4 Crab units.

The corresponding differential energy spectrum is shown in Figure 9.6. Between 450 GeV and 2.2 TeV, it can be described by a simple power-law of the form:

$$\frac{dF}{dE} = (6.7 \pm 1.8) \cdot 10^{-11} \text{TeV}^{-1} \text{cm}^{-2} \text{s}^{-1} \cdot (E/0.5 \text{TeV})^{-2.2 \pm 0.4} \quad (9.3)$$

with a  $\chi^2_{\text{red}} = 0.63/1$  ( $P = 43\%$ ). For comparison the spectral points reported by the Whipple 10-m telescope averaged over the nights of June 18, 19, and 21, 2006 are also shown in the figure. Generally, there might be systematic differences between the Whipple and MAGIC measurements. It could, however, be shown that such inter-instrument systematic effects are rather small and under control, e.g. those between MAGIC and H.E.S.S. [Maz05]. Particularly the Crab nebula spectra measured by Whipple and MAGIC agree quite well [Alb08f]. The Mrk 421 flux measured by the Whipple 10-m telescope four days after the MAGIC observation is substantially higher than the measurements presented here (Figure 9.6), pointing to a clear evolution of the source emission level within the INTEGRAL campaign.

The mentioned INTEGRAL MWL campaign showed several strong flares in the X-ray range, that were not present at lower energies. On the other hand, the

## 9.4 MWL campaign during April 29-30, 2006 and May 7, 2008

---

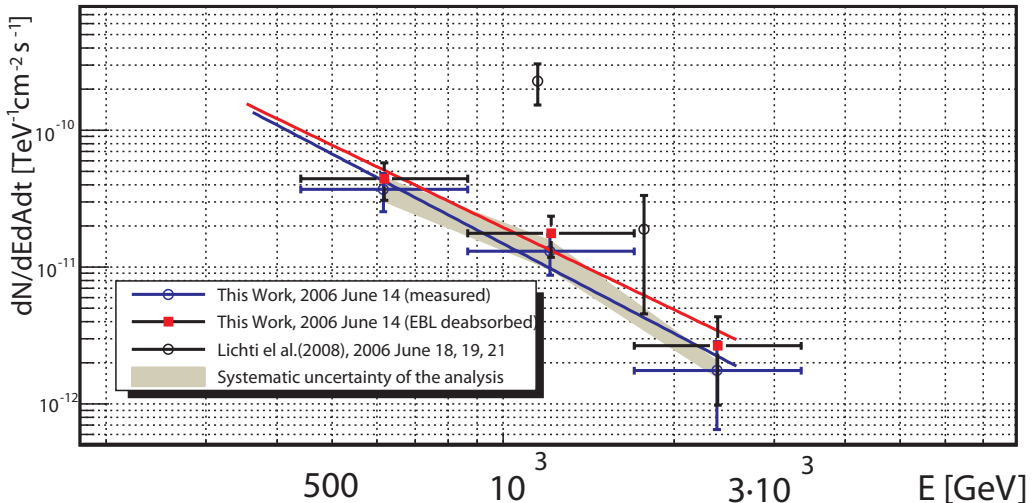


Figure 9.6: *Differential photon spectrum for Mrk 421 for June 14, 2006 as measured (blue open circles) and after EBL de-absorption (red solid squares). A power-law fit to the measured spectrum results in a spectral slope of  $\alpha = -2.2 \pm 0.4$  and in  $\alpha = -2.0 \pm 0.4$  after EBL de-absorption. Also shown are spectral points measured with the Whipple 10-m telescope [Lic08] during June 18-21, 2006.*

TeV observations were too sparse to allow any conclusion regarding correlated flux variabilities between VHE and X-rays [Lic08].

## 9.4 MWL campaign during April 29-30, 2006 and May 7, 2008

The observations performed with MAGIC during April 29, 2006 (described above) were performed in the context of a MWL campaign where also *XMM-Newton* and Whipple participated. The objective of these observations was to obtain truly simultaneous X-ray and TeV flux measurements from Blazars in outburst. The interpretation of the 2006 data sample was performed together with another data sample obtained in similar conditions, after a ToO trigger following the continuation of the same program. In this case, the *XMM-Newton* measurements were carried out simultaneously with VERITAS, and took place in May 7, 2008.

### 9.4.1 XMM-Newton observations

X-ray and UV observations were taken by the XMM-Newton satellite's EPIC-pn (EPN) detector [Str01], covering a spectral range of approximately 0.5 – 10 keV, and the Optical Monitor (OM; [Mas01]), capable of covering the range between 170 and 650 nm (7.3 eV and 1.9 eV). The 2006 and 2008 observations produced

## 9.4 MWL campaign during April 29-30, 2006 and May 7, 2008

---

Table 9.3: *Summary of Mrk 421 XMM-Newton Observations.*

| Obs. Window [MJD]       | Avg. PN Rate [cts s <sup>-2</sup> ] | Avg. OM Rate [cts s <sup>-2</sup> ] |
|-------------------------|-------------------------------------|-------------------------------------|
| 53854.8639 – 53855.3488 | $336.30 \pm 0.09$                   | $13.5 \pm 0.2$                      |
| 54593.0653 – 54593.5653 | $411.31 \pm 0.12$                   | $35.82 \pm 0.03$                    |

EPN exposures of approximately 42 ks and 43 ks, respectively. A total of 15 and 10 exposures were taken with the OM during the 2006 and 2008 observations, respectively, with total exposure times of 32.5 ks and 22.0 ks. For all exposures, the OM was in imaging mode with the UVM2 filter (200 - 300 nm) in place. Table 9.3 summarizes these observations. See [Acc09] for further details.

The X-ray data were fit with a power law modified by interstellar absorption, yielding a value for the photon index of  $\alpha = 2.258 \pm 0.002$  and  $2.153 \pm 0.002$  for the data obtained simultaneously with the 2006 MAGIC and Whipple observations, respectively. For X-ray data taken during the 2008 VERITAS observations, a photon index of  $\alpha = 2.519 \pm 0.010$  was found. The spectrum was unfolded and de-absorbed to derive the intrinsic X-ray spectrum of Mrk 421 [Acc09].

The count rates found for the OM exposures were converted to flux using the standard conversion factor<sup>1</sup> and an average point was determined for each time interval. In addition, using the ultraviolet extinction law from [Car89], the absolute extinction for the UVM2 band was calculated to be  $A(\text{UVM2}) = 0.13$ , allowing for de-reddening of the OM data using a correction factor of 1.13.

### 9.4.2 Whipple observations (2006)

The Whipple 10 m IACT [Kil07] performed 3 hours of observation on April 30, 2006 from 4:37 UT to 8:05 UT (MJD 53855.1924 – 53855.3368). The observations were taken with a source zenithal angle range of  $11^\circ$ – $45^\circ$ , during favorable weather conditions. Details of data reduction can be found in [Acc09]. The obtained energy spectrum was fit using a simple power law  $dN/dE = f_0 \cdot (E/E_0)^{-\alpha}$ , with  $f_0 = 2.6 \pm 0.8 \text{ TeV}^{-1} \text{ cm}^{-2} \text{ s}^{-1}$ ,  $E_0 = 1 \text{ TeV}$  and  $\alpha = 2.2 \pm 0.4$ , yielding a  $\chi^2_{\text{red}} = 2.0/4$  ( $P = 73\%$ ) (Uncertainties are statistical only). The threshold of this analysis is  $\sim 400$  GeV. Figure 9.7 shows the differential spectrum as measured with Whipple, together with the one measured with MAGIC few hours before, and the one measured with VERITAS in the May 7, 2008 campaign.

### 9.4.3 VERITAS observations (2008)

The VERITAS IACTs array observed Mrk 421 for 2.5 hours on May 7, 2008 from 3:59 UT to 6:28 UT (MJD 54593.1660 – 54593.2694). The observations were

<sup>1</sup><http://heasarc.nasa.gov/docs/xmm/sas/USG/node135.html>

## 9.4 MWL campaign during April 29-30, 2006 and May 7, 2008

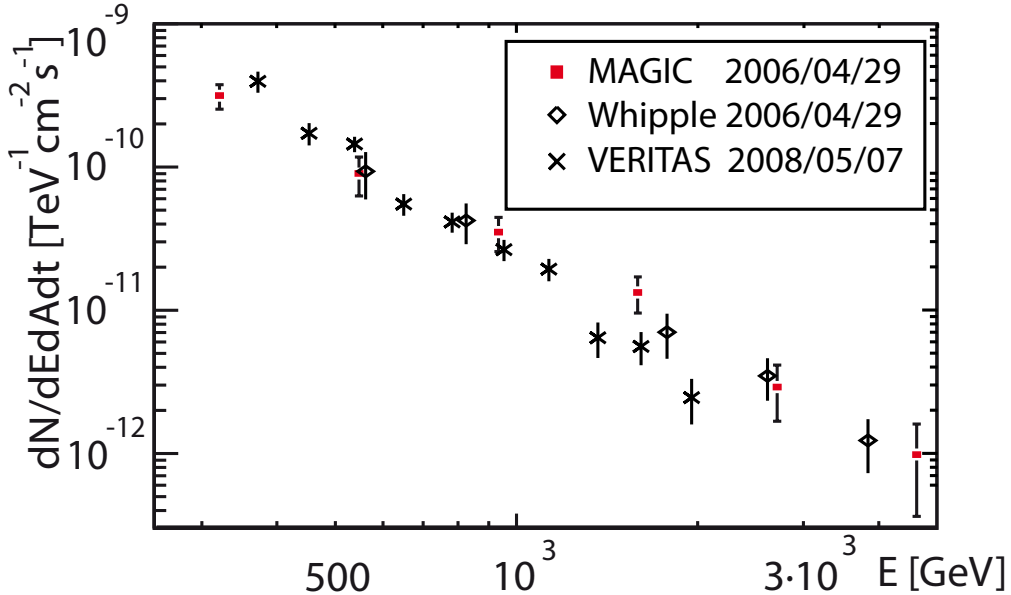


Figure 9.7: *VHE spectra as measured with the VHE  $\gamma$ -ray detectors on the two ToO XMM-Newton campaigns. The data obtained with MAGIC are shown in red squares, Whipple in black diamonds and VERITAS in black crosses. April 29-30, 2006 measurements (MAGIC and Whipple) show a very similar behavior, while April 7, 2008 measurements (VERITAS) show that the source's spectrum was steeper.*

taken with a source zenithal angle range from  $11^\circ$  to  $35^\circ$ . Data quality checks confirmed good weather during the observations. Details of data reduction can be found in [Acc09]. The obtained energy spectrum was fit using a simple power law of the form  $dN/dE = f_0 \cdot (E/E_0)^{-\alpha}$ , with  $f_0 = 2.01 \pm 0.15 \text{ TeV}^{-1} \text{ cm}^{-2} \text{ s}^{-1}$ ,  $E_0 = 1 \text{ TeV}$  and  $\alpha = 2.91 \pm 0.13$ , yielding a  $\chi^2_{\text{red}} = 9.7/8$  ( $P = 29\%$ ) (Uncertainties are statistical only). The threshold of this analysis is  $\sim 275 \text{ GeV}$ .

### 9.4.4 Results of the campaign

#### 9.4.4.1 Spectral energy distribution and modeling

Figure 9.8 shows the broadband SEDs corresponding to the three epochs of VHE observations. It is important to note that within each epoch the multiwavelength data are genuinely simultaneous. The VHE points have been de-absorbed with the extragalactic background light model discussed in [FRV08]. Optical data (R band) obtained from KVA during April 29, 2006 are also shown in the SED, after de-reddening from galactic extinction ( $A(R)=0.041^1$ ).

Clear spectral variability is observed between epochs. Modeling of the SEDs was carried out using a one-zone SSC model [TMG01]. The injected relativistic particles (electrons) follow a smoothed broken power law energy distribution. The

<sup>1</sup>Obtained from NED: <http://nedwww.ipac.caltech.edu/>

## 9.4 MWL campaign during April 29-30, 2006 and May 7, 2008

---

electron distribution extends from  $\gamma_{min}$  to  $\gamma_{max}$ , with an electron number density  $N$ , indexes  $n_1$  and  $n_2$  below and above the break at  $\gamma_{br}$ . The injected relativistic particles are assumed to follow a broken power-law spectrum with normalization factor  $K$ . The tangled magnetic field intensity is  $B$  and the dimension of the emission region is  $R$ , with a Doppler beaming factor  $\delta$ . The parameters for these models are shown in Table 9.4.

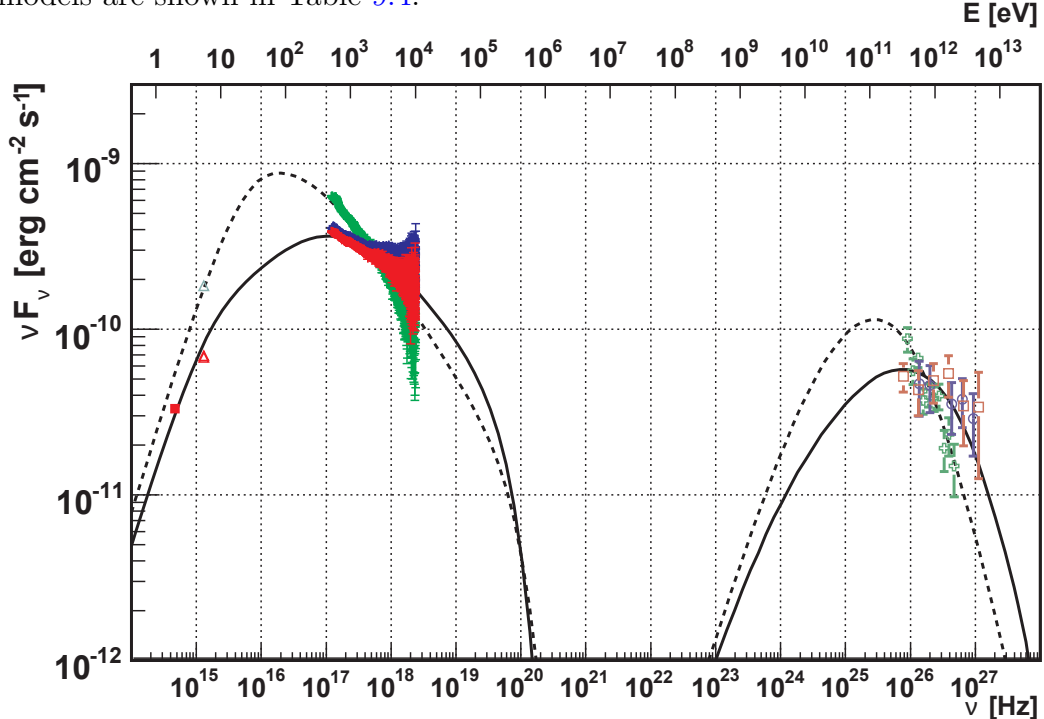


Figure 9.8: Spectral energy distribution with a SSC model for 2006 (solid curve) and 2008 (dashed curve) XMM-Newton MWL campaigns data. The data from KVA, XMM-Newton OM, XMM-Newton EPN, MAGIC, Whipple and VERITAS are shown with filled squares, triangles, filled circles, squares, circles, and crosses, respectively, with data taken during the MAGIC, Whipple and VERITAS observation times shown in red, blue and green.

### 9.4.4.2 Cross-band correlation

The VHE, X-ray and UV light curves are shown in Figure 9.9. The X-ray light curve was binned in 500 seconds time interval, while the bins for the VHE light curves were primarily determined by the standard length of data runs for the respective telescopes. The Whipple data are grouped in 28-minute bins, while the MAGIC and VERITAS data are in 20-minute bins. To provide a direct comparison between the results obtained with different VHE experiments,  $\gamma$ -ray fluxes of Whipple and VERITAS have been extrapolated down to MAGIC's energy

#### 9.4 MWL campaign during April 29-30, 2006 and May 7, 2008

---

Table 9.4: *SED model parameters.*

| Parameter                    | 2006 | 2008 |
|------------------------------|------|------|
| $\gamma_{min}[\cdot 10^3]$   | 11   | 17   |
| $\gamma_{break}[\cdot 10^4]$ | 12   | 4.2  |
| $\gamma_{max}[\cdot 10^5]$   | 2.0  | 2.0  |
| $n_1$                        | 2.0  | 2.0  |
| $n_2$                        | 4.0  | 4.2  |
| $B[\cdot 10^{-3}G]$          | 32   | 60   |
| $K[\cdot 10^3 cm^{-3}]$      | 1.7  | 2.0  |
| $R[\cdot 10^{15}]$           | 5.5  | 9.5  |
| $\delta$                     | 62   | 47   |

The electron distribution extends from  $\gamma_{min}$  to  $\gamma_{max}$ , with a break at  $\gamma_{br}$ , and with spectral indices  $n_1$  and  $n_2$  below and above the break. The electron number density is  $N$ . The broken power-law spectrum has a normalization factor  $K$ . The tangled magnetic field intensity is  $B$  and the dimension of the emission region is  $R$ , with a Doppler beaming factor  $\delta$ .

threshold. A possible systematic error in flux calibration between the MAGIC and VERITAS experiments was estimated to be of the order of 10% with MAGIC systematically measuring a lower flux than VERITAS [Acc09]. The systematic uncertainty in the Whipple and VERITAS flux calibration was found to be on the order of 40% with Whipple systematically measuring a higher flux than VERITAS [Acc09]. These systematic uncertainties are not included in the data error bars nor corrected. MAGIC data made up the most variable portion of the VHE light curve, being inconsistent with a constant flux in the VHE band (see section 9.3.1). Mrk 421 also varied significantly at X-ray energies during the 2006 observation, with the count rate initially decreasing during the course of the MAGIC observation and slowly increasing during the Whipple observation. Though both showed significant variability, the whole X-ray and VHE data sample does not appear to be correlated. Figure 9.10 shows the measured VHE flux and X-ray count rates where the X-ray data were rebinned to match the resolution of the corresponding VHE data. To quantify the correlation and examine the uncertainty in this correlation, the same method as used in section 9.3.1.2 was applied. An average  $r$  value of  $0.02 \pm 0.10$  for the whole X-ray-VHE sample was found, indicating a clear lack of correlation, as suggested by Figure 9.10.

Individual correlation between X-rays and VHE instrument in different epochs were also studied. For the MAGIC and X-ray simultaneous measurements, a correlation for MAGIC observations ( $r = 0.71 \pm 0.11$ ) is apparent. The probability of agreement between the measured PDF and the fully correlated PDF

#### 9.4 MWL campaign during April 29-30, 2006 and May 7, 2008

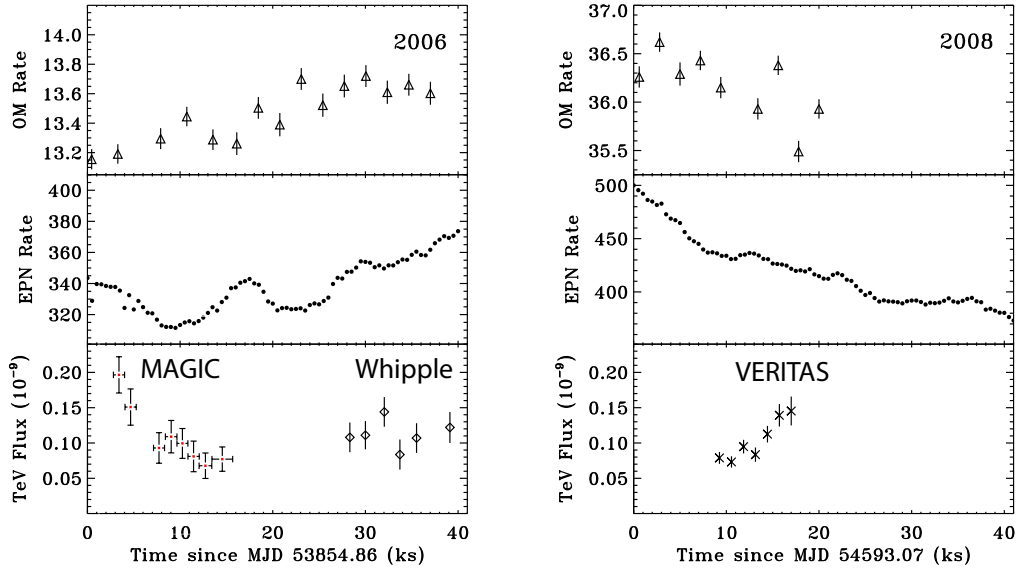


Figure 9.9: *UV, X-ray and VHE light curves for April 29-30, 2006 observations (left) and May 7, 2008 observations (right).* XMM-Newton OM data (200-300 nm) are shown with triangles in units of  $\text{cts s}^{-1}$ . XMM-Newton EPN data (0.5 - 10.0 keV) are shown with filled circles in units of  $\text{cts s}^{-1}$ . Error bars for the EPN data are smaller than the data points. The data from MAGIC, Whipple and VERITAS are shown with red squares, black diamonds, and black crosses, respectively in units of  $\text{photons cm}^{-2} \text{s}^{-2}$  (above 250 GeV). Error bars indicate  $1\sigma$  uncertainties. Note that the EPN and OM scales differ on the 2006 and 2008 panels.

$P_{AB}$  is  $0.38 \pm 0.06$ , while the probability that the measurements came as a result of a statistical fluctuation of an entirely uncorrelated physics case is significantly lower  $P_{AC}$   $0.06 \pm 0.06$ . The probability for the first scenario to be true and for the second to be false is  $P_{AB}(1-P_{AC}) = 0.36$ , and the probability for the opposite is  $P_{AC}(1-P_{AB}) = 0.04$ , which indicates that the correlation scenario is more likely. In the case of Whipple and X-rays observations, a lack of correlation is present with  $r=0.04 \pm 0.34$ . Grouping together the April 29–30, 2006 measurements (MAGIC and Whipple), no correlation could be claimed ( $r = 0.25 \pm 0.14$ ,  $P_{AB}=0.39^{+0.44}_{-0.39}$ ,  $P_{AC}=0.41^{+0.44}_{-0.41}$ ,  $P_{AB}(1-P_{AC})=0.23$  and  $P_{AC}(1-P_{AB})=0.25$ ). The correlation coefficient found for the VERITAS and XMM-Newton 2008 observations is  $-0.82 \pm 0.12$ , with the following probabilities for different correlation scenarios:  $P_{AB}=0.35 \pm 0.02$ ,  $P_{AC}=0.03 \pm 0.02$ ,  $P_{AB}(1-P_{AC})=0.34$  and  $P_{AC}(1-P_{AB})=0.01$ , what indicates that the anti-correlation scenario is more probable than the opposite.

In order compare these results to previous work, the best fit correlation between the X-ray and VHE bands found in [Bi05] is plotted in Figure 9.10 (blue dashed line). To more directly compare these data to [Bi05], the line was scaled to match the Whipple 10m points in Figure 4 (gray dot-dashed line). The overall normalization shift could be a reflection of hysteresis on long timescales.

#### 9.4 MWL campaign during April 29-30, 2006 and May 7, 2008

---

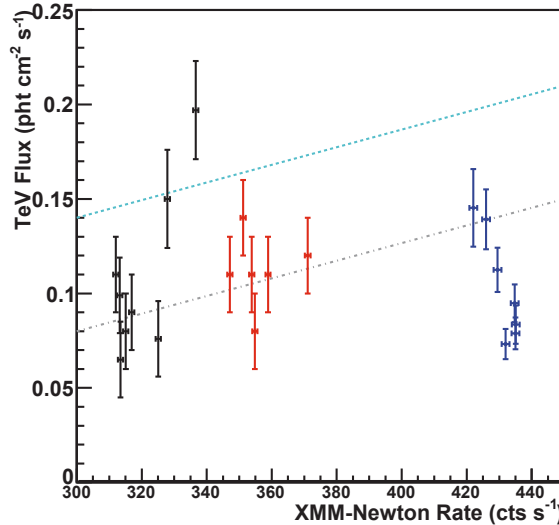


Figure 9.10: *Simultaneous XMM-Newton EPN (0.5 – 10 keV, in units of  $\text{cts s}^{-1}$ ) and VHE data ( $E > 250 \text{ GeV}$ , in units of  $\text{ph} \times 10^{-10} \text{ cm}^{-2} \text{ s}^{-1}$ ) to search for correlation between the two bands. MAGIC data points are drawn in black, Whipple points in red, and VERITAS points blue. The dashed blue line is the X-ray/VHE correlation best fit from [Bl05] converted to the appropriate units. The dot-dashed grey line has the same slope but is scaled to the average of the Whipple results.*

Although the scatter in the VHE points is large, the VERITAS points are systematically below the scaled correlation. This effect is made worse by the fact that the Whipple points are known to be systematically higher than the VERITAS points (by 40%).

It appears to be no correlation between the VHE and UV variations, most notably during the first half of the 2006 observation, where the UV rates increase as the VHE flux decreases. A correlation factor  $r = 0.12 \pm 0.15$  was found using the method described above for the whole sample, with a best fit line almost horizontal. There was no correlation present during individual observation epochs.

The UV rates during both observations appear to roughly follow the trend of the X-ray rates, with a significantly higher rate during the 2008 observation. There is a clear relation between the two bands fluxes in the long term evolution, having a Pearson's  $r$  of  $0.940 \pm 0.001$  (see Figure 9.11). But in the study of the individual 2006 and 2008 data correlation, the behavior changes considerably: the best fit lines show flatter slopes, while it is not possible to clearly identify a correlation:  $r=0.46 \pm 0.08$ ,  $P_{AB} < 0.40$ ,  $P_{AC} < 0.40$ ,  $P_{AB}(1-P_{AC})=0.01$  and  $P_{AC}(1-P_{AB})=0.09$  for 2006 data;  $r=0.57 \pm 0.08$ ,  $P_{AB} < 0.40$ ,  $P_{AC} < 0.40$ ,  $P_{AB}(1-P_{AC})=0.1$  and  $P_{AC}(1-P_{AB})=0.09$  for 2008 data. The apparent unequal behavior when considering short timescales (minutes-hours) and long ones (years), that can be clearly seen in Figure 9.11, suggests different nature on the internal mechanisms governing the behavior of the source.

#### 9.4 MWL campaign during April 29-30, 2006 and May 7, 2008

---

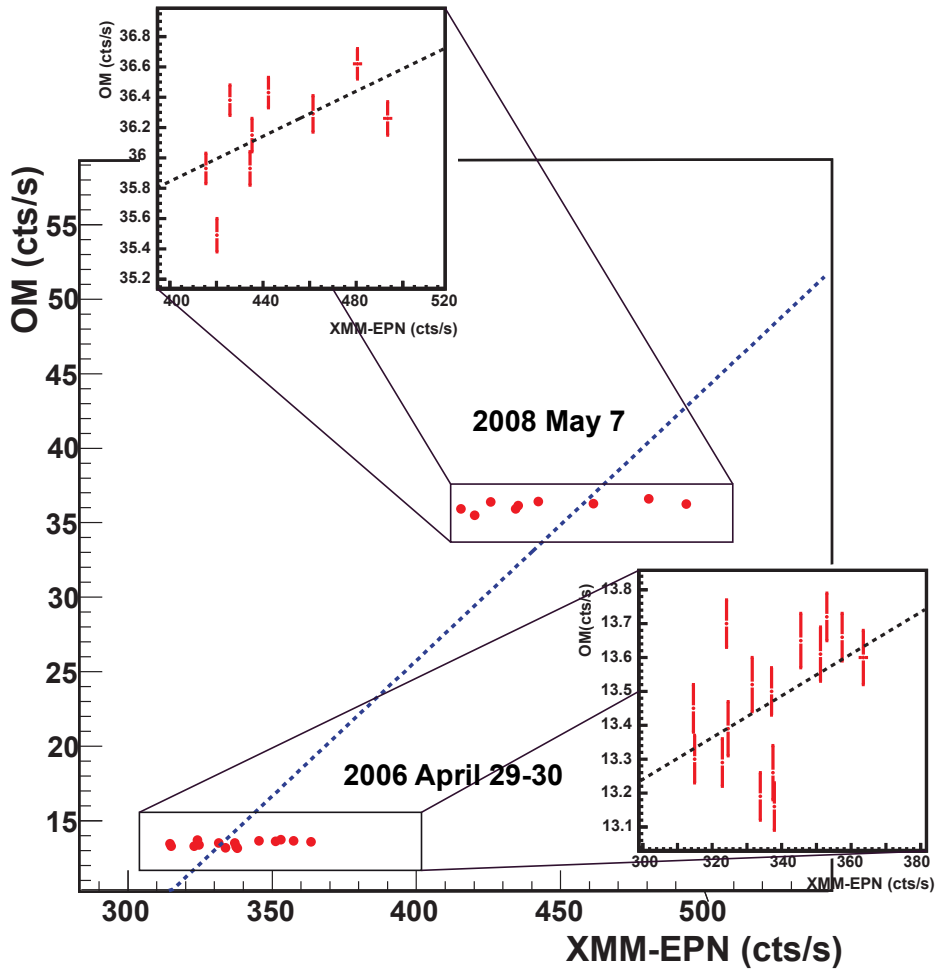


Figure 9.11: Simultaneous XMM-Newton EPN (0.5 – 10 keV, in units of  $\text{cts s}^{-1}$ ) and OM (UVM2 band, in units of  $\text{cts s}^{-1}$ ) measured fluxes, to search for correlation between the two bands. There is a clear relation between both band fluxes in the different epochs. The blue dashed line is the best fit line for the whole sample of 2006 and 2008 data. The fluxes within the different epochs, that are shown zoomed in the small box displays, appear to follow also correlated trends, even if it cannot be confirmed when studying in detail the samples. The slopes of the best fit functions of the 2006 and 2008 data are much flatter than when considering the whole sample together, suggesting different internal mechanisms affecting the short and long timescales.

## 9.5 Comparison with MAGIC published results

---

### 9.4.4.3 Spectral hysteresis

The spectral evolution of the X-ray data was examined in [Acc09] to determine if any hysteresis was present during the observations indicating a dependence of the system on previous states. The data were divided into three energy bands in order to calculate hardness ratios: 0.5–1 keV, 1–3 keV, and 3–10 keV. These bands were chosen such that each band contains a roughly equal number of counts. The hardness ratio was defined for each energy band pair as the fraction of flux between the higher energy band respect to the lower energy one. Figure 9.12 shows the evolution of the hardness ratios versus intensity (in terms of count rates) through the flare seen in the 2006 data (which peaks near 17–18 ks into the observation; see Figure 9.9). Spectral hysteresis is clearly seen during this rapid flare. Clockwise patterns indicate a lag in the response of lower-energy photons with respect to that of higher-energy photons. Similar patterns have been seen previously (e.g., [Bri01]), though counter-clockwise patterns have been observed as well [Cui04]. Different hysteresis patterns indicate a complex mechanism that may differ between outbursts. No rapid flares were observed during the 2008 observation. Examination of the entire 2008 observation did not reveal any overall spectral hysteresis pattern occurring on the order of several hours. Similarly, no overall hysteresis was found when considering the entire 2006 observation [Acc09].

## 9.5 Comparison with MAGIC published results

In parallel to the results presented above, an independent analysis was performed by Stefan Rügamer<sup>1</sup>, using the Mars Cheobs version (see section 6.2). Both analysis were thoroughly compared, and were found to be consistent within uncertainties. In general, the analysis of Stefan Rügamer resulted to be more sensitive, and measured systematically slightly higher fluxes. Figure 9.13 shows a comparison of both April and June observations spectra comparisons. It was decided to use this analysis in the final published results at [Acc09, And09b].

## 9.6 Discussion

### 9.6.1 Spectral shape

A possible curvature in the spectrum was investigated in all April EBL de-absorbed spectra: they were fit to a logarithmic curvature term, corresponding

---

<sup>1</sup>Würzburg University.

## 9.6 Discussion

---

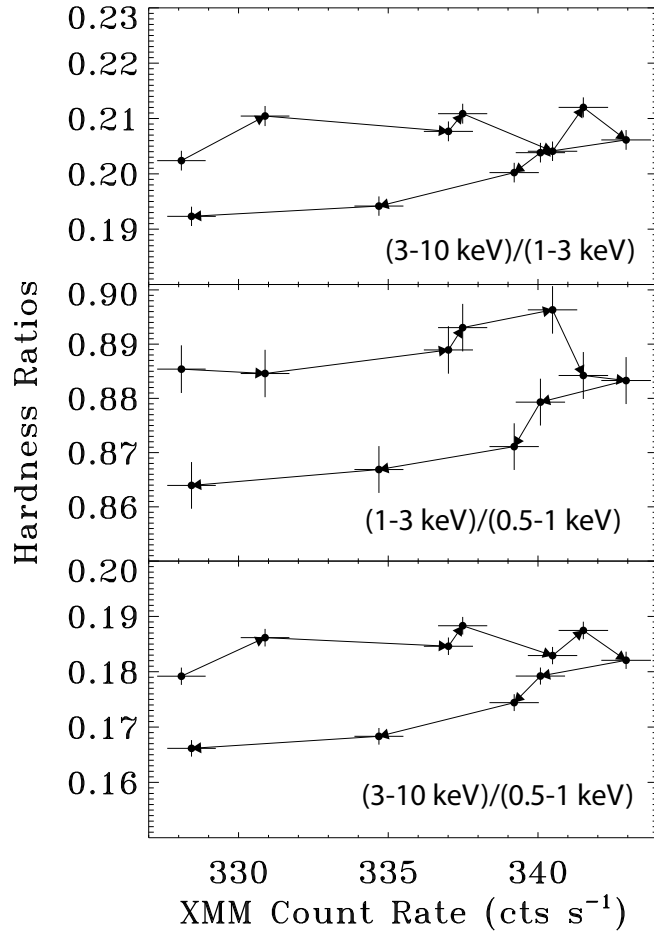


Figure 9.12: *Hardness ratio vs intensity plots to study spectral hysteresis during the increase in activity centered around 17 ks into the 2006 XMM-Newton observation. Three bands are used for this analysis. The upper panel uses  $(3\text{-}10 \text{ keV})/(1\text{-}3 \text{ keV})$  for the hardness ratio, the middle panel uses  $(1\text{-}3 \text{ keV})/(0.5\text{-}1 \text{ keV})$ , and the bottom panel uses  $(3\text{-}10 \text{ keV})/(0.5\text{-}1 \text{ keV})$ . The arrows indicate the progression of time. Clockwise hysteresis is present in all three panels, indicating a lag in the lower energy bands. Adapted from [Acc09].*

## 9.6 Discussion

---

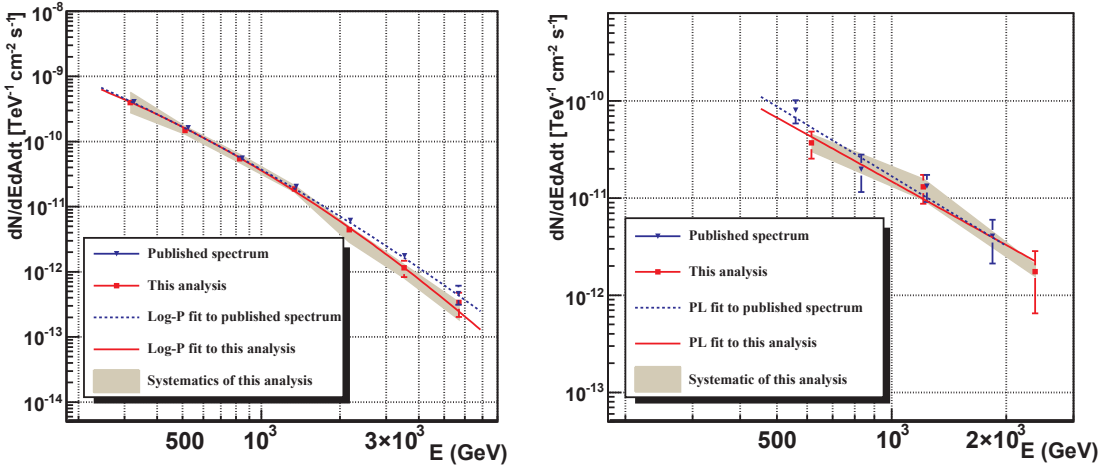


Figure 9.13: Comparison between this work and the parallel independent analysis used in the published results [Acc09, And09b]. The spectral points and fits from this work is in red, the ones shown in publications are in blue. Left: April combined differential spectrum and log-P (eqn. 9.4) fit. Right: June differential spectrum and PL (9.1) fit.

to a parabolic power-law (log-P) in a  $\log(E^2 dF/dE)$  vs.  $\log E$  representation [Mas04], and power-law with exponential cut-off (PL+C) of the form

$$\frac{dF}{dE} = f_0 \cdot (E/E_0)^{-(\alpha + \beta \cdot \log_{10}(E/E_0))} \quad (9.4)$$

and

$$\frac{dF}{dE} = f_0 \cdot (E/E_0)^{-\alpha} \cdot e^{-E/\beta}, \quad (9.5)$$

respectively (See Figure 9.5). A likelihood ratio test (e.g. [MG07]) was applied to all the fits, giving only clear preference towards a log-P or a PL+C compared to a simple power-law for the spectrum of April 27 ( $P > 90\%$ ), the observation with higher statistics of the sample. For the other individual spectra, probabilities  $< 60\%$  were obtained (see Table 9.5 for details). Also the high statistics data sets defined by combining all data from April, all data from the five pedestal and all data from the three high state April nights, clearly showed evidence of a parabolic or cut-off shape of the spectra. The results of the fits and the probability of a likelihood ratio test are given in Table 9.6. For all these nights the data did not allow to prefer between log-P and PL+C models. The fact that all of the high statistics data sets show a curved spectral shape is an indication of this feature being always visible for Mrk 421 and hence source intrinsic.

A shift of the high-energy peak (attributed to Inverse Compton radiation) in the SED towards higher energies with an increasing flux level is expected in leptonic acceleration models. In the VHE domain, such a shift can be traced by spectral hardening. Variations in the hardness of the TeV  $\gamma$ -ray spectrum

## 9.6 Discussion

---

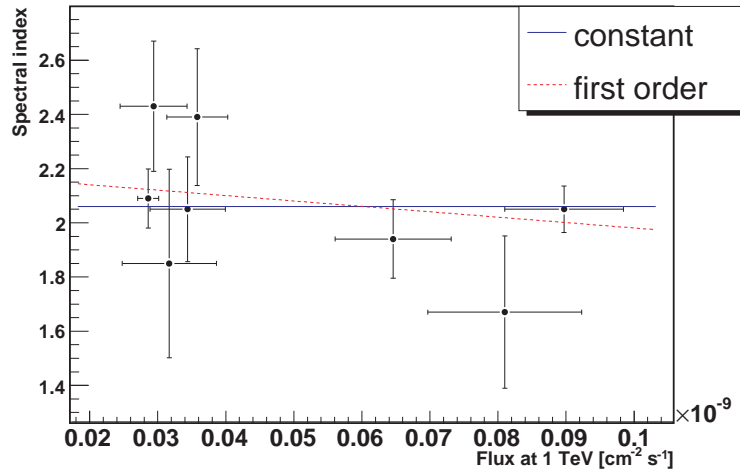


Figure 9.14: *Spectral index vs. flux at 0.5 TeV deduced from a simple power-law fit after EBL de-absorption for Mrk 421 in April 2006. The  $\chi^2_{\text{red}}$  for a constant fit (spectral index uncorrelated with flux level; blue solid line) amounts to  $7.2/8$  ( $P \approx 41\%$ ), while a linear correlation (red dashed line) has a  $\chi^2_{\text{red}} = 6.2/6$ , equal to  $P \approx 41\%$ .*

during flares were reported by several groups e.g. [Kre02, Aha05d, Fos08]. In order to check for a correlation of the spectral hardness with the flux level of the de-absorbed spectrum, these parameters are represented in Figure 9.14 for each April night. It was found that there is not a clear preference between a constant ( $\chi^2_{\text{red}} = 7.2/8$ ,  $P \approx 41\%$ ) or a linear dependence of spectral hardness and flux level ( $\chi^2_{\text{red}} = 6.2/6$ ,  $P \approx 41\%$ ). Although evident flux variations are present in these observations, the overall dynamical range of 4 in flux might be too small to see a significant spectral hardening with increasing flux.

The curved power-laws enable to locate a peak in the de-absorbed spectrum at  $E_{\text{peak}} = E_0 \cdot 10^{(2-\alpha)/(2\beta)}$  for the log-P and at  $E_{\text{peak}} = (2 - \alpha) \cdot \beta$  if  $\alpha < 2$  for the PL+C fit. Additionally, the spectral cut-off is naturally obtained from the PL+C fit as the fit parameter  $\beta$ . The results are shown in Table 9.6. The values of  $E_{\text{peak}}$  as determined using the log-P and the PL+C were compatible with each other for the data sets averaging several nights and showed indications for an increase of the peak energy with rising flux level, as predicted if the VHE radiation were due to SSC mechanisms. Another way of determining the peak position can be achieved by using the apex form of the parabola of the log-P in a logarithmic representation, as performed in [Alb07c]:

$$\log_{10} E^2 \frac{dF}{dE} = \log_{10}(f_0) + \log_{10}(\alpha) \left( \log_{10} \left( \frac{E}{E_{\text{peak}}} \right) \right) \quad (9.6)$$

Figure 9.15 shows the results obtained here together with historical values taken from [Alb07c]. The new data points confirm the previously suggested correlation of peak energy with flux level.

## 9.6 Discussion

---

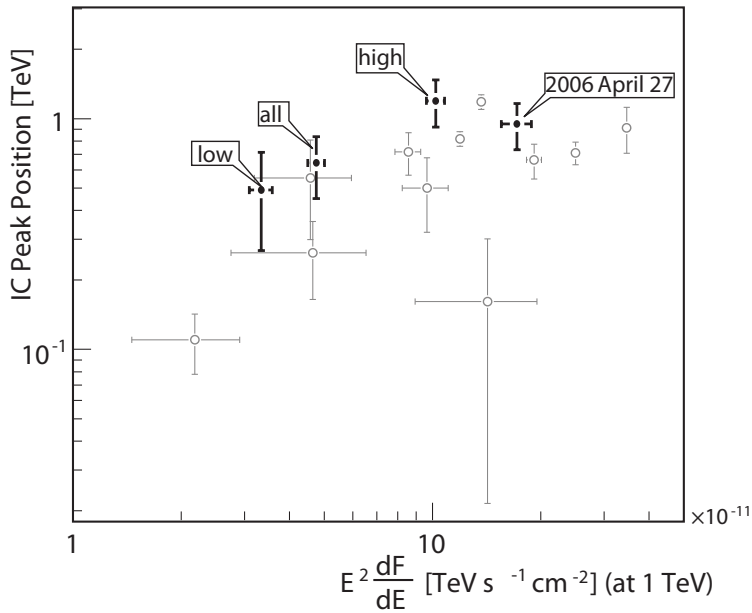


Figure 9.15: Derived peak position using the log-P apex fit (eqn. 9.4) versus flux at 1 TeV for the data sets presented in Table 9.6. Historical data peak positions, taken from ([Alb07c])(in gray), were also determined with the log-P apex fit. The data confirm the indication of a correlation between the two parameters.

Although the peak energy measured on April 27, 2006 exceeds the one of All April Data and Low-State data set, it is, despite having a higher flux, comparable with the one derived for the High-State data set. This discrepancy in terms of the expected behaviour in SSC models can be explained with the different nature of the data sets: The April 27, 2006 data represent a rather particular, 1.4 h long episode of an individual flare event, whereas the High-State data set is an average of three individual flares. Due to the sparse sampling, most probably each of these observations caught different epochs of the individual flare evolutions, during which the spectral shape can change considerably in terms of spectral index and curvature (see e.g. [Kat06]). Hence the two data sets are not necessarily directly comparable.

The observation of a relation between flux (and thus, fluence) and the position of the VHE peak in the SED could be pointing to a relation similar to the one suggested by Lorenzo Amati [Ama02] and observed by [Sak06] for GRBs. The “Amati relation” is an empirical correlation existing between the peak energy of GRBs and the total released energy. Since the TeV  $\gamma$ -ray production is assumed to take place in a relativistic jet, and many of the same radiative processes are involved (on a larger scale, of course) it might be a similar (or related) mechanism at work on a different scale. Some authors have interpreted the Amati relation as caused by internal shock models [Per07, MZ09]. Moreover, shocks caused by

## 9.6 Discussion

---

the collision between different shells of matter moving at different speeds inside blazar jets have been predicted [Apa01]. The similarities of these GRB and blazar jet scenarios, where shocks happen, could explain the similarities in both empirical relations, in agreement with the *universal* first-order relativistic shock acceleration models. A trend towards a relation between flux and spectral index in the TeV energy range has also been noted by [Wag08], studying 17 known TeV blazars. Additionally, a relation was found, but in the X-ray band, between the synchrotron peak flux and position, after a deep spectral analysis of all *Swift* observations of Mrk 421 between April 2006 and July 2006 [Tra10].

The large uncertainties on the derived cut-off energies do not allow to conclude if there is a shift on the cutoff energy with increasing fluxes. All the derived cutoff values are, however, far from the predicted cutoff energies from cosmological energies: The predictions of Kneiske lower-limit model [KD08] indicate that the EBL cut-off for Mrk 421 is expected to be around 13 TeV, while according to the model by Franceschini et al. [FRV08] the cut-off is expected to be around 9 TeV.

In Figure 9.16, “historical” spectra taken between 1998 and 2005 are compared with the pedestal and high state spectrum derived from the observations reported here. It is obvious that the pedestal state spectrum represents one of the lowest flux states ever measured in VHE for Mrk 421, whereas the high state spectrum shows no exceptionally high flux level of this source. Both spectra are harder than historical spectra with comparable flux levels, in particular harder than the VERITAS 2008 spectra shown in this chapter and in [Don09], enabling one of the best measurements of the turnover of the SED in a low flux state. While a previous observation yielded a rather flat spectrum in the VHE regime [Aha02b], a rather clear peak (flat structure in the SED) was measured. The low-state spectrum has a shape similar to the one measured by HEGRA CT1, although at an approximately three times lower flux level. The high-state spectral shape resembles the high-state Whipple spectrum, which in turn has an about three times higher flux. This tendency can also be seen in Figure 9.15, which shows that the peak positions derived with these data are systematically higher than historical measurements for comparable flux levels. Within the SSC framework this difference in flux for comparable spectral shapes can be caused by, e.g., a lower number of electrons with the same energy distribution as in the high-flux case.

### 9.6.2 Correlations between energy bands

During the *XMM-Newton* and VHE observations of Mrk 421, simultaneous multi-wavelength data on sub-hours timescales were obtained. These data are essential for the study of correlations during rapid flares. The variability observed during the 2006 outburst in the simultaneous X-ray and VHE observations should be enough to provide useful information about a correlation, if any, between the two

## 9.6 Discussion

---

energy bands. In addition, the observations from VERITAS in May 7, 2008 during a separate outburst, provide an extended picture for investigating possible correlations between these two bands. Rapid X-ray and VHE flares are often expected to be correlated in one-zone SSC scenarios, as all photons are expected to originate from the same population of electrons. Examination of the observed SEDs can provide additional constraints on model parameters and reveal what factors strongly affect each flare's spectral profile. The observed SEDs (see Figure 9.8) show a clear steeper spectrum for the 2008 observation than for the 2006 observation, particularly at X-ray energies. This is the opposite behavior to previous measurements, where spectral hardening with increased flux (e.g., [Xue06]) was observed. In addition, both peaks in the SED show a slight shift to lower energies during the 2008 observation in opposite to previous ones: the April 2006 MAGIC results presented above, other observations as presented in [Bl05], and SSC model predictions. The SSC model is able to roughly fit the observational data, but for that, relative large Doppler factors are required to be included in the modeling. Other SSC models ([BC02]) have been applied to these data, requiring similarly high values of  $\delta^1$ . The found Doppler factors are larger than those usually attributed to HBLs ( $\sim$ 10-20) but, on the other hand, the emission of Mrk 421 has sometimes been modeled with values of  $\delta > 50$  in SSC context (e.g. [Kon03, Fos08]).

Historically, multiwavelength campaigns have observed correlation between the X-ray and VHE emission in Mrk 421, though the data sets are not comprised entirely of strictly simultaneous multiwavelength data (e.g., [Bl05, Fos08, Alb07c]). Though the dynamical range of the observed variability is not as large as that seen in previous long-term monitoring campaigns, these observations seem to point to short-term variability that shows a different correlation pattern. When studying *XMM-Newton*-VHE simultaneous observation as a whole data set, no obvious correlation is present. On the other hand, the study of the individual observation epochs gave indications of correlation of X-ray and VHE flux during MAGIC observations, no correlation during Whipple observations, and negative correlation during the VERITAS observations. The VHE flux measured by MAGIC showed a significant flux decrease correlated with the X-ray flux, in a similar attitude as in historical measurements. On the other hand, the VERITAS light curve also showed an obvious variability (but with a smaller dynamical range when compared with MAGIC observations), in this case anti-correlated with the X-ray flux. During the Whipple observations, the source showed a low, steady VHE flux, without correlation with X-ray flux. In different time scales, the correlation study performed with the April MAGIC and RXTE/ASM showed no evident X-ray and VHE correlation, in opposite to what was observed in previous MAGIC observations [Alb07c]. The impossibility of finding an overall VHE

---

<sup>1</sup>M. Böttcher, Private Communication.

## 9.6 Discussion

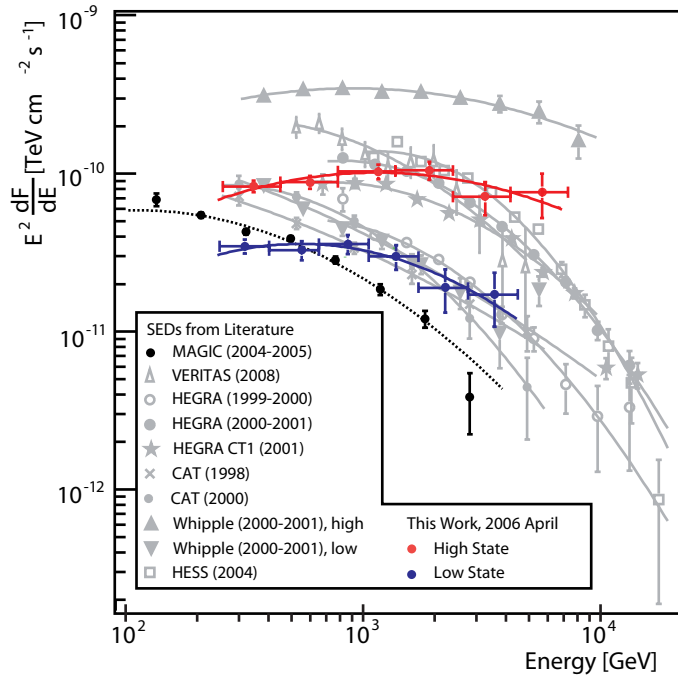


Figure 9.16: *EBL de-absorbed historical spectra of Mrk 421 (see [Alb07c] for references) along with both high (red) a low (blue) states' spectra from the MAGIC 2006 April campaign and the flare spectrum of [Don09]. The solid line is the result of a fit using eqn. 9.4. Note that the historical data were de-absorbed using the model of [PBS05], and this work with [FRV08].*

and X-rays flux correlated behavior suggests the presence of complex scenarios for the VHE photon creation, like ones where X-ray and VHE photons may originate from electrons with different energies, similar to what was deduced during a study of PKS2155-304 [Aha09b]. Other scenarios that could explain the observed variability patterns include the possibility of an inhomogeneous emission region, multiple emission regions, or hadronic origin of the VHE emission. Mrk 421 is clearly behaving very differently in these observations from what is usually reported of the source (e.g., [Bl05]), where the X-ray and VHE variabilities are seen to be strongly correlated. Such peculiarity makes it difficult to generalize the results to other blazars.

In addition, the *XMM-Newton* OM allowed for a detailed search for UV/X-ray or UV/VHE correlations in short timescales, while the KVA observation allowed similar studies in longer timescales. Though previous multiwavelength campaigns on Mrk 421 have obtained optical, X-ray and VHE data, correlations between the X-ray and optical data have either not been studied or were not significant (e.g., [Alb07c, Bl05, Hor09]). The average rate from the *XMM-Newton* PN detector during the April 7, 2008 observation was about 20% higher than the rates measured during the 2006 observation. The count rate more than doubles between the 2006 and 2008 observation. The UV rates also appears to vary in

## 9.7 Summary

---

accordance with the X-ray rate within the individual observations. Calculation of the Pearson's r value for the total UV/X-ray data set yielded a value of  $0.940 \pm 0.001$ , indicating a strong correlation, what provides direct observational evidence for a link between the emission mechanisms at X-ray and UV wavelengths. This correlation comes, however, from the long term evolution. When examining the minute-hour time-scales, the UV/X-ray correlation is not so evident. On the other hand, no correlation was found between the optical R band fluxes and the quasi-simultaneous RXTE/ASM X-ray measurements during the April 2006 campaign.

During the XMM-Newton simultaneous observations, it seems there is an anti-correlated trend between UV and VHE flux, even if the correlation analysis cannot confirm any anti-correlation. On the other hand, some evidences of exactly the opposite trend appear to be present when comparing the day-by-day measurements in the R-band and the VHE measurements performed by MAGIC in April 2006, even if the low statistics of the studied sample do not allow to draw any firm conclusion regarding the correlation.

Hysteresis was observed during one rapid flare in the X-ray data from the 2006 observation. No rapid flares occurred during the 2008 observation. Spectral hysteresis has been commonly observed in blazars, but the phenomenon is not yet understood completely. A simple model is used in [KM99] to produce spectral hysteresis patterns that may be observed during the course of a flare. In this model, the behavior is characterized by the relationship between three timescales associated with the duration of the flare variability  $t_{var}$ , synchrotron  $t_{cool}$  and particle acceleration  $t_{acc}$ . The relationship between these timescales results in four possible cases that are discussed in detail in [KM99]. The clockwise hysteresis found in the X-ray data, indicating a lag at lower energies in the X-ray band, coupled with the essentially symmetric shape of the flare in the X-ray light curve seems to indicate that the case with  $t_{cool} \gg t_{var} \gg t_{acc}$  is most relevant to this observation. The lag in the low energy photons is a result of the inverse relationship between  $t_{cool}$  and the energy of the cooling particles. Although observed clockwise patterns were observed in one of the observations, other patterns have also been observed. This is yet another example of the personality of the source and may indicate physical differences between individual flares and outbursts.

## 9.7 Summary

Data of a sequence of mild flares of the blazar Mrk 421 during one week from April 22 to 30, 2006, peaking at  $\approx 2.0$  Crab units have been presented. The nocturnal observations lasted at least for about one hour to allow for the reconstruction of night-by-night spectra. During three observation nights high fluxes were recorded, in which, however, no variability could be measured. In two of these nights, rather

## 9.7 Summary

---

hard spectral indices were found, but this was also the case for the night with the lowest flux.

During the night of April 29, 2006 with a non particularly high flux of  $\approx 0.65$  Crab units, clear intra-night variability with a flux-doubling time of  $36 \pm 10$  minutes was observed.

A MWL observation was performed together with Whipple and *XMM-Newton*, with the primary focus of studying the rapid flaring activity of blazars on sub-hour timescales in both the X-ray and VHE bands. These observations were studied together with others performed in May 7, 2008, which share similar characteristics. Contrary to historical observations, no clear X-ray and VHE correlation was found when studying the whole data sample, but correlation seems to be present in the MAGIC 2006 observations and anti-correlation during the VERITAS 2008 observations. The data are well described by an SSC one-zone model, but they require relatively large Doppler factors. Contrary to what is expected in SSC models, 2008 data show a shift to lower energies of both SED peaks with higher fluxes compared to 2006 data. This is also opposite to what was observed in the IC peak during the 2006 campaign.

During the INTEGRAL-triggered MWL campaign in June 2006 one night observation of Mrk 421 was performed, complementing the three-night observations conducted by the Whipple 10-m telescope four days later. Taking the MAGIC and Whipple results together, a variability of the flux level of Mrk 421 also during the INTEGRAL observations is evident. The energy coverage of the Whipple telescope spectrum ( $\Delta E \approx 600$  GeV) was not sufficient to assess any spectral evolution by comparing it to the MAGIC spectrum ( $\Delta E \approx 2$  TeV).

## 9.7 Summary

Table 9.5: Analysis results.

| Obs. night | $N_{\text{exc}}$ | $N_{\text{bck}}$ | $S$         | $E_{\text{cut}}$ [GeV] | $F(E > E_{\text{min}})$ | $\chi^2_{\text{red, const}}$ | $f_0$           | $\alpha$        | $\chi^2_{\text{red, PL}}$ | P(logPL) | P(PL+C) |
|------------|------------------|------------------|-------------|------------------------|-------------------------|------------------------------|-----------------|-----------------|---------------------------|----------|---------|
| 2006/04/22 | 79               | 40               | $8.3\sigma$ | 350                    | $0.82 \pm 0.14$         | 0.39/2                       | $0.99 \pm 0.27$ | $2.0 \pm 0.3$   | 0.1/2                     | 12%      | 14%     |
| 2006/04/24 | 267              | 125              | $16\sigma$  | 250                    | $2.06 \pm 0.19$         | 2.2/2                        | $2.1 \pm 0.3$   | $2.11 \pm 0.15$ | 1.0/3                     | 56%      | 59%     |
| 2006/04/25 | 228              | 115              | $14\sigma$  | 250                    | $1.14 \pm 0.13$         | 1.2/2                        | $1.30 \pm 0.15$ | $2.18 \pm 0.15$ | 1.6/3                     | 40%      | 41%     |
| 2006/04/26 | 248              | 107              | $15\sigma$  | 350                    | $1.10 \pm 0.11$         | 1.6/4                        | $1.4 \pm 0.2$   | $2.6 \pm 0.2$   | 0.23/2                    | 0%       | 2%      |
| 2006/04/27 | 545              | 99               | $28\sigma$  | 350                    | $3.05 \pm 0.16$         | 3.4/4                        | $3.2 \pm 0.3$   | $2.23 \pm 0.09$ | 7.7/4                     | 93%      | 96%     |
| 2006/04/28 | 288              | 173              | $15\sigma$  | 350                    | $1.09 \pm 0.09$         | 6.0/8                        | $1.56 \pm 0.07$ | $2.6 \pm 0.3$   | 1.0/2                     | 39%      | 32%     |
| 2006/04/29 | 354              | 164              | $18\sigma$  | 250                    | $0.93 \pm 0.07$         | 24/7                         | $1.05 \pm 0.03$ | $2.27 \pm 0.11$ | 0.9/4                     | 48%      | 43%     |
| 2006/04/30 | 42               | 12               | $6.9\sigma$ | 250                    | $2.4 \pm 0.4$           | —                            | $2.2 \pm 0.4$   | $1.8 \pm 0.3$   | 0.62/1                    | 27%      | 27%     |
| 2006/06/14 | 63               | 30               | $7.5\sigma$ | 450                    | $0.26 \pm 0.05$         | 0.05/1                       | $0.67 \pm 0.18$ | $2.2 \pm 0.4$   | 0.62/1                    | N/A      | N/A     |

Number of excess ( $N_{\text{exc}}$ ) and background ( $N_{\text{bck}}$ ) events, resulting significances  $S$ , lower cuts in event energy, integral fluxes  $F$  above  $E_{\text{min}} = 250$  GeV for the 2006 April data and  $E_{\text{min}} = 450$  GeV for the 2006 June 14 data (in units of  $10^{-10} \text{ cm}^{-2} \text{s}^{-1}$ ), fit quality of a constant-flux fit to the individual observation nights (see Figure 9.3), power-law fit results for the differential energy spectra of  $dN/dE = f_0 \cdot (E/E_0)^{-\alpha}$  with  $E_0 = 0.5$  TeV;  $f_0$  in units of  $10^{-10} \text{ TeV}^{-1} \text{cm}^{-2} \text{s}^{-1}$ , and probability of a likelihood ratio test for log-parabolic power-law fits (log-P, eqn. 9.4) and power-law with an exponential cut-off fits (PL+C, eqn. 9.5).

Table 9.6: Special fit results.

| Data Set              | Used Fit | $E_0$ [TeV] | $f_0$           | $\alpha$        | $\beta$           | $\chi^2_{\text{red, fit}}$ | Likelihood | $E_{\text{peak}}$ [TeV] |
|-----------------------|----------|-------------|-----------------|-----------------|-------------------|----------------------------|------------|-------------------------|
| 2006/04/27            | PL       | 0.5         | $3.7 \pm 0.4$   | $2.05 \pm 0.09$ |                   | 8.2/4                      |            |                         |
|                       | log-P    | 0.5         | $3.7 \pm 0.4$   | $1.69 \pm 0.19$ | $0.5 \pm 0.3$     | 3.3/3                      | 96%        | $1.0 \pm 0.6$           |
|                       | PL+C     | 0.5         | $4.77 \pm 1.1$  | $1.5 \pm 0.4$   | $2.2 \pm 1.7$ TeV | 4.6/3                      | 93%        | $1.0 \pm 0.8$           |
| All April Data        | PL       | 0.5         | $1.83 \pm 0.02$ | $2.22 \pm 0.04$ |                   | 18.7/5                     |            |                         |
|                       | log-P    | 0.5         | $1.94 \pm 0.04$ | $1.85 \pm 0.11$ | $0.62 \pm 0.18$   | 3.3/4                      | 99%        | $0.66 \pm 0.14$         |
|                       | PL+C     | 0.5         | $2.34 \pm 0.20$ | $1.69 \pm 0.16$ | $2.3 \pm 0.7$ TeV | 3.6/4                      | 99%        | $0.7 \pm 0.4$           |
| High State Nights     | PL       | 0.5         | $3.61 \pm 0.06$ | $2.00 \pm 0.05$ |                   | 6.8/4                      |            |                         |
|                       | log-P    | 0.5         | $3.66 \pm 0.08$ | $1.73 \pm 0.13$ | $0.38 \pm 0.17$   | 1.3/3                      | 97%        | $1.1 \pm 0.6$           |
|                       | PL+C     | 0.5         | $4.1 \pm 0.6$   | $1.65 \pm 0.16$ | $4 \pm 2$ TeV     | 1.2/3                      | 97%        | $1.4 \pm 0.7$           |
| Pedestal State Nights | PL       | 0.5         | $1.37 \pm 0.15$ | $2.20 \pm 0.06$ |                   | 4.2/4                      |            |                         |
|                       | log-P    | 0.5         | $1.45 \pm 0.05$ | $1.96 \pm 0.15$ | $0.6 \pm 0.3$     | 0.74/3                     | 92%        | $0.55 \pm 0.16$         |
|                       | PL+C     | 0.5         | $1.8 \pm 0.3$   | $1.7 \pm 0.3$   | $2.1 \pm 1.1$ TeV | 0.58/3                     | 92%        | $\leq 1.1$ TeV          |

Results of log-P and PL+C fits after EBL de-absorption for special data sets.  $f_0$  is given in units of  $10^{-10} \text{ TeV}^{-1} \text{cm}^{-2} \text{s}^{-1}$ ,  $\alpha$  and  $\beta$  are the fit parameters as stated in the text, and ‘‘Likelihood’’ denotes the probability of a likelihood ratio test. The peak energy is  $E_{\text{peak}} = E_0 \cdot 10^{(2-\alpha)/(2\beta)}$  for the log-P and  $E_{\text{peak}} = (2 - \alpha) \cdot \beta$  for the PL+C.

## 9.7 Summary

---

Table 9.7: Results of a correlation test for each data pair.

| Instruments     | Sample               | $r$               | $P_{AB}$               | $P_{AC}$               | $P_{AB}(1-P_{AC})$ | $P_{fAC}(1-P_{AB})$ |
|-----------------|----------------------|-------------------|------------------------|------------------------|--------------------|---------------------|
| KVA-MAGIC       | April 2006           | $0.55 \pm 0.33$   | $0.69 \pm 0.31$        | $0.36 \pm 0.31$        | 0.44               | 0.11                |
| RXTE/ASM-MAGIC  | April 2006           | $0.12 \pm 0.31$   |                        |                        |                    |                     |
| KVA-RXTE/ASM    | April 2006           | $0.05 \pm 0.47$   |                        |                        |                    |                     |
| XMM/EPN-VHE     | XMM-Newton campaigns | $0.02 \pm 0.10$   |                        |                        |                    |                     |
| XMM/EPN-MAGIC   | 29 April, 2006       | $0.71 \pm 0.11$   | $0.38 \pm 0.06$        | $0.06 \pm 0.06$        | 0.36               | 0.36                |
| XMM/EPN-Whipple | 30 April, 2006       | $0.04 \pm 0.34$   |                        |                        |                    |                     |
| XMM/EPN-VHE     | 29–30 April, 2006    | $0.25 \pm 0.14$   | $0.39^{+0.44}_{-0.39}$ | $0.41^{+0.44}_{-0.41}$ | 0.23               | 0.25                |
| XMM/EPN-VERITAS | 7 May, 2008          | $-0.82 \pm 0.12$  | $0.35 \pm 0.02$        | $0.03 \pm 0.02$        | 0.34               | 0.01                |
| XMM/OM-VHE      | XMM-Newton campaigns | $0.12 \pm 0.15$   |                        |                        |                    |                     |
| XMM/OM-MAGIC    | 29 April, 2006       | $-0.50 \pm 0.37$  |                        |                        |                    |                     |
| XMM/OM-Whipple  | 30 April, 2006       | $-0.21 \pm 0.54$  |                        |                        |                    |                     |
| XMM/OM-VERITAS  | 7 May, 2008          | $-0.29 \pm 0.33$  |                        |                        |                    |                     |
| XMM/OM-XMM/EPN  | XMM-Newton campaigns | $0.940 \pm 0.001$ |                        |                        |                    |                     |
| XMM/OM-XMM/EPN  | 29–30 April, 2006    | $0.46 \pm 0.08$   | $<0.40$                | $<0.40$                | 0.01               | 0.09                |
| XMM/OM-XMM/EPN  | 7 May, 2008          | $0.57 \pm 0.08$   | $<0.40$                | $<0.40$                | 0.01               | 0.09                |

Average values of the Pearson's  $r$  obtained for the different data pairs measured in different energy bands, together with the correlation study results when it was possible to perform it:  $P_{AB}$  is the probability of agreement between the measured PDF and the fully correlated PDF,  $P_{AC}$  is the probability for measurements coming from fluctuation of an entirely uncorrelated physics case,  $P_{AB}(1-P_{AC})$  is the probability for the first scenario to be true and for the second to be false, and  $P_{fAC}(1-P_{AB})$  is the probability for the opposite scenario. See the text for further details.

# Chapter 10

## Observations of 1ES 1426+428 during 2008 MWL campaigns

### 10.1 Introduction

The AGN 1ES 1426+428 (R.A.  $14^h 28^m 32.7^s$ , decl.  $+42^\circ 40' 20.6''$  [J2000.0]; also known as H1426+428) was the sixth extragalactic source detected in the TeV energy range. It was detected for the first time by the Whipple telescope [Hor02], and confirmed by the HEGRA [Aha02a] and CAT [Dja02] IACTs. These three independent detections were achieved on a five  $\sigma$ -level significance. Further long term exposures by Whipple and HEGRA in 2002 showed the source in a lower flux state, yielding again only a five  $\sigma$ -level detection [Aha03, FV04]. The reconstructed spectra were well described by a power law, although the lower energy part (300 GeV to 1 TeV), measured by Whipple, was much steeper than the part at higher energies (above 800 GeV) measured by HEGRA.

With a relatively high redshift of  $z = 0.129$ , it's VHE  $\gamma$ -ray radiation is expected to be strongly absorbed by the EBL (see section 2.4). According to up-to-date EBL models [KD08, FRV08], a cutoff in the spectrum of the source is expected around 500–850 GeV energies. The relative large redshift makes this source interesting for EBL studies, as it may help to constrain the EBL models if its spectrum is modeled according to the known properties (e.g., spectral index) of nearby blazars like Mrk 421 and Mrk 501, less affected by the EBL, or by the expected properties from emission models. These kind of studies already gave valuable results when studying other distant blazars (see e.g. [DK05, Col08, MR07]).

1ES 1426+428 is an HBL type BL Lac that is usually classified as an *extreme blazar*. This concept was introduced in [Ghi99] to describe those BL Lac objects whose first peak is sometimes located in the hard X-ray band. Such AGN, which lie at the end of the blazar sequence proposed in [Fos98] (see section 3.5 for

## 10.2 MAGIC observations and data analysis

---

a description), are good candidates for TeV emission since the second peak of their SEDs is supposed to lie at high energies, meaning that they would emit more power in the VHE regime than other types of blazars. 1ES 1426+428 has shown SEDs with low energy bump (attributed to synchrotron emission) peaking occasionally at  $E > 100$  keV [Wol08].

In other campaigns, not described here, MAGIC observed 1ES 1426+428 in 2005 (from March to May) and in 2006 (in June). During the 2005 campaign the observations suffered from bad weather and technical problems, resulting in only 6 h of good quality data. These data show no significant signal, and an upper limit to the integral flux above 190 GeV of 5% of Crab Nebula was derived [Alb08d]. In the second campaign the data quality was quite bad due to inhomogeneities in the detector, similar to those affecting the Mrk 421 2006 data described in Chapter 9. The analysis of the 2006 1ES 1426+428 2006 data is still on-going.

In this chapter, results from a MWL campaign of 1ES 1426+428 performed in May-June 2008 will be presented, including measurements with MAGIC in the VHE band, observations with *Suzaku* and *Swift* satellites in the X-ray band, and observations with the KVA telescope and the *Swift* UVOT in the optical/UV bands.

## 10.2 MAGIC observations and data analysis

MAGIC observed 1ES 1426+428 during 14 nights in 2008, at zenith angles between  $13.5^\circ$  and  $33^\circ$  in *on-off* mode (as described in section 5.8). The first two nights were completely discarded as the observations were performed in *wobble* mode and/or under strong moonlight conditions. A total of 18.8 h. of data survived the quality cuts. Details of the observation are provided in Table 10.1. Additionally 10.8 h of *off* data were found to match the same observation conditions as the *on* data.

These data were taken using the *analogue sum trigger*, briefly described in 5.3, with the aim of reaching a low energy threshold. After a careful look to these data, as well as to a dedicated analysis of Crab Nebula *on* and *off* data samples obtained with similar settings, it was found that it was not possible to perform a standard Hillas analysis with the *sum trigger* events: different data sub-samples showed divergences in the *alpha* distributions and therefore no reliable analysis method was found to calculate possible excess events when considering events that only were triggered by the *analogue sum trigger*. For this reason, it was decided to perform an standard analysis just with those events triggered by the level 1 trigger, thus using a scheme identical to the standard one (described in Chapter 6).

After calibration and signal extraction, noise from night-sky background light was removed from the air-shower images by applying an absolute time image

## 10.2 MAGIC observations and data analysis

---

Table 10.1: *Data sets and observational circumstances.*

| Night      | Observation Window [MJD] | $t_{\text{eff.}}$ [h] | ZA [ $^{\circ}$ ] |
|------------|--------------------------|-----------------------|-------------------|
| 2008/05/21 | 54607.8930 – 54607.9409  | excluded              | 18 – 30           |
| 2008/05/23 | 54609.9758 – 54609.9837  | excluded              | 13                |
| 2008/05/24 | 54610.8991 – 54610.9602  | 0.5                   | 14 – 26           |
| 2008/05/25 | 54611.8969 – 54612.0297  | 1.7                   | 14 – 26           |
| 2008/05/26 | 54612.8983 – 54613.0451  | 2.3                   | 15 – 25           |
| 2008/05/27 | 54613.8964 – 54614.0434  | 2.3                   | 15 – 25           |
| 2008/05/28 | 54614.8963 – 54615.0477  | 2.4                   | 15 – 27           |
| 2008/05/29 | 54615.9023 – 54616.0370  | 1.6                   | 23 – 24           |
| 2008/05/31 | 54617.9878 – 54618.0439  | 1.3                   | 16 – 28           |
| 2008/06/02 | 54619.9007 – 54619.9996  | 1.4                   | 15 – 20           |
| 2008/06/03 | 54620.9828 – 54621.0224  | 0.9                   | 14 – 25           |
| 2008/06/04 | 54621.9467 – 54622.0541  | 2.1                   | 13 – 33           |
| 2008/06/05 | 54622.9308 – 54622.9918  | 1.4                   | 13 – 19           |
| 2008/06/06 | 54623.9668 – 54624.0002  | 0.8                   | 15 – 21           |

$t_{\text{eff.}}$  stands for the effective observation time. ZA gives the zenith angle range of the observations. Data of May 21 were excluded because observations were performed in wobble mode and under strong moonlight. Data of May 23 were excluded as they were taken under strong moon-light conditions.

Table 10.2: *Set of cuts used to estimate the significance of a possible  $\gamma$ -ray signal.*

| hadronness        | alpha                      | combined acceptance |
|-------------------|----------------------------|---------------------|
| $\leq 0.06$ (42%) | $\leq 0.05^{\circ}$ (85 %) | 36%                 |

cleaning (see section 6.7.1), requiring a minimum light content of 6 phe for the core pixels of the image and 3 phe for the boundary ones. Additional time constrains were required:  $\Delta t_{\text{core}} = 4.5$  ns and  $\Delta t_{\text{boundary}} = 1.5$  ns (see 6.7.1 for details). A minimum cut of 150 phe in the parameter *size* was performed.

For the  $\gamma$ /hadron separation, the RF method (described in section 6.8.1) was used. The parameters *size*, *width*, *length*, *size*/*width*  $\times$  *length*, *conc*, *dist*, *M3Long*, *time RMS* and *time gradient* were used to train the *hadronness* parameter. A cut in the parameter *hadronness* and in the angular parameter *alpha* (see section 6.9 for details) was performed for both the *on* and the *off* samples. The analysis cuts were determined from the Crab Nebula data sample mentioned before, that consists of 6.5 h of *on* data and 6.7 h of *off* data. The optimum cuts found are shown in Table 10.2. With these cuts, the sensitivity is 2.0% of the Crab Nebula flux in 50 h of observation.

Data affected by bad atmospheric conditions like high humidity and cloudiness were excluded, as well as those showing fluctuating event rates. In total, 18.8 h of *on* data and 10.8 h of *off* data survived these quality cuts. The threshold of the analysis, defined as the peak of the energy distribution of the MC events after all

## 10.2 MAGIC observations and data analysis

---

Table 10.3: *Analysis results for individual data sets.*

| Night      | Excess | Background | scale | Significance |
|------------|--------|------------|-------|--------------|
| 2008/05/24 | -8±10  | 100±4      | 0.05  | -0.77        |
| 2008/05/25 | 13±20  | 310±8      | 0.16  | 0.67         |
| 2008/05/26 | 17±25  | 486±11     | 0.24  | 0.69         |
| 2008/05/27 | 29±25  | 497±11     | 0.25  | 1.2          |
| 2008/05/28 | -26±25 | 520±11     | 0.26  | -1.0         |
| 2008/05/29 | 38±18  | 247±7      | 0.12  | 2.2          |
| 2008/05/31 | 42±20  | 306±8      | 0.15  | 2.1          |
| 2008/06/02 | 8±17   | 231±6      | 0.12  | 0.47         |
| 2008/06/03 | 8±17   | 224±6      | 0.11  | 0.50         |
| 2008/06/04 | 1±19   | 306±8      | 0.15  | 0.04         |
| 2008/06/05 | 18±13  | 141±5      | 0.07  | 1.4          |
| 2008/06/06 | -2±14  | 167±5      | 0.08  | -0.18        |
| Total      | 140±80 | 3530±52    | 1.8   | 1.8          |

*Number of excess events, scaled number of background events in the signal region, scaled factor applied to the number of off events, and statistical significance of the excess according to formula 17 of [LM83].*

cuts, was found to be 170 GeV.

The analysis did not revealed any significant VHE signal coming from 1ES 1426+428, neither using the whole data set nor considering night by night observations (see Table 10.3). Also the search for a signal in different energy bins did not yield a significant excess. Integral upper limits to the source's emission were calculated in terms of the number of excess events within a 95% confidence level, using the method of Rolke et al. ([Rol05]), as described in section 6.11. A systematic error of 30% for energy estimation and effective area calculation was assumed. The number of the excess events was converted into flux upper limits assuming a photon index of -3, which represents the average slope value for this source compared to historical detections (-3.55 in [Hor02], -3.5 in [Pet02], and -2.6 in [Aha02a]). For comparison, other spectral indices of -2.5, -3.5 and -4.0 were considered for the flux upper limit calculation. Integral upper limits above different energy values were also determined, as shown in Table 10.4. The obtained flux upper limits above the energy threshold are on the level of 2–3% of the Crab Nebula flux.

Additionally, 95% confidence level differential upper limits to the flux emission were derived. In the same way as done for integral upper limits, four different spectral indices were assumed for this calculation. These differential upper limits were corrected from the EBL absorption according to the model by Franceschini et al. [FRV08]. The derived differential upper limits in 4 energy bins are summarized in Table 10.5.

## 10.2 MAGIC observations and data analysis

---

Table 10.4: *Integral upper limits.*

| $E_{\text{th}}$ [GeV] | $\alpha = -2.5$ | $\alpha = -3.0$ | $\alpha = -3.5$ | $\alpha = -4.0$ |
|-----------------------|-----------------|-----------------|-----------------|-----------------|
| 100                   | 40 (7)          | 50 (9)          | 61 (11)         | 72 (13)         |
| 130                   | 19 (5)          | 23 (6)          | 26 (7)          | 29 (7)          |
| <b>170</b>            | <b>5.5 (2)</b>  | <b>6.5 (2)</b>  | <b>7.1 (3)</b>  | <b>7.7 (3)</b>  |
| 200                   | 4.8 (2)         | 5.2 (3)         | 5.6 (3)         | 5.9 (3)         |
| 250                   | 3.1 (2)         | 3.2 (2)         | 3.5 (2)         | 3.7 (2)         |
| 320                   | 2.4 (2)         | 2.5 (2)         | 2.6 (2)         | 2.8 (2)         |
| 400                   | 2.3 (3)         | 2.4 (3)         | 2.5 (3)         | 2.6 (3)         |
| 500                   | 2.8 (5)         | 2.8 (5)         | 2.9 (5)         | 2.9 (5)         |
| 630                   | 3.2 (8)         | 3.2 (8)         | 3.3 (8)         | 3.4 (8)         |
| 800                   | 2.5 (9)         | 2.0 (8)         | 2.1 (8)         | 2.1 (8)         |
| 1000                  | 1.4 (8)         | 1.5 (8)         | 1.5 (8)         | 1.5 (8)         |

95% confidence level integral upper limits in units of  $10^{-12}\text{cm}^{-2}\text{s}^{-1}$  as a function of the assumed spectral index  $\alpha$  and the energy threshold. The numbers inside parenthesis indicate the equivalent upper limit in percentage of the Crab Nebula flux. The upper limits corresponding to the analysis energy threshold appear remarked in bold text.

Table 10.5: *Differential upper limits.*

| $\alpha$ | [170–315] | [315–545] | [545–1000] | [1000–3000] |
|----------|-----------|-----------|------------|-------------|
| -2.5     | 3.0 (3)   | 1.0 (4)   | 0.35 (5)   | 0.072 (7)   |
| -3.0     | 3.3 (3)   | 1.1 (4)   | 0.38 (5)   | 0.083 (7)   |
| -3.5     | 3.7 (3)   | 1.2 (4)   | 0.41 (5)   | 0.097 (7)   |
| -4.0     | 4.3 (3)   | 1.4 (4)   | 0.46 (5)   | 0.012 (7)   |
| -2.5     | 4.5 (4)   | 2.4 (9)   | 1.7 (20)   | 0.85 (85)   |
| -3.0     | 4.7 (4)   | 2.5 (8)   | 1.7 (20)   | 0.92 (75)   |
| -3.5     | 5.1 (4)   | 2.7 (8)   | 1.8 (20)   | 1.0 (70)    |
| -4.0     | 5.8 (4)   | 2.9 (8)   | 1.9 (20)   | 1.1 (70)    |

95% confidence level differential flux upper limits in units of  $10^{-11}\text{cm}^2\text{s}^{-1}\text{TeV}^{-1}$  for a power-law  $\gamma$ -ray spectrum with spectral index  $\alpha$  in energy ranges in units of GeV. The numbers inside parenthesis indicate the equivalent upper limit in percentage of the Crab Nebula flux. First four rows correspond to the measured flux upper limits, the remaining four rows are the EBL de-absorbed flux upper limits.

## 10.3 Observations at other wavelengths

### 10.3.1 X-ray observations

*Swift* observed 1ES 1426+428 with short snapshots of 1-2 ks each from May 28 to June 10, overlapping with MAGIC observations when possible. All *Swift* observations were performed using all three on-board instruments: the X-ray telescope (XRT, [Bur05]), the UV and optical telescope (UVOT, [Rom05]) and the Burst Alert Telescope (BAT, [Bar05]). In this work the XRT data from 0.2 to 10 keV will be used together with the UVOT data (see next section). The details of the *Swift* data analysis are provided in [Leo09, Ale10]. Figure 10.2 shows the X-ray light curve measured by the XRT detector.

The joint Japanese-US satellite *Suzaku* ([Mit07]) carries four X-ray telescopes sensitive in the 0.3–12 keV band, with CCD cameras in the focal plane, together with a non-imaging instrument sensitive in the 10–600 keV band, composed by a Si-PIN photo-diodes detector (probing the 10–60 keV band) and a GSO scintillator detector (sensitive above 30 keV). Observations of 1ES 1426+428 were carried out between June 5 to June 8 for a total time of 100 ks. *Suzaku* data analysis was performed in a similar way as described in [Tag08]. The source was clearly detected by *Suzaku*.

### 10.3.2 Optical and UV observations

Optical and UV light curves were obtained from the UVOT detector on-board *Swift*, performing measurements in each of the UVW3, UVM2, UVW1, U, V and B (see Figure 10.2) bands. Additionally, The KVA telescope performed R band observations during a 3 month period during 2008, including the epoch when MAGIC observations were performed.

The contribution of the host galaxy in the R band was taken from [Nil03], for the B band we followed the results reported in [Hyy07], while the contribution in the other filter regions were extrapolated from those in the R and B bands through a power law emission model.

In Figure 10.1 the optical light curve in the R band, obtained during MAGIC observation period is shown. The contribution from the host galaxy (taken from [Nil03]) has been subtracted. Note that the optical flux increased by 20% during the MWL campaign.

### 10.3 Observations at other wavelengths

---

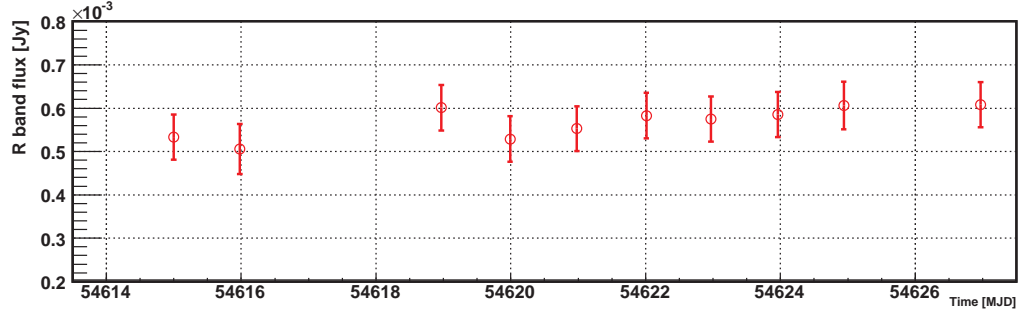


Figure 10.1: *Light curve of the optical flux of 1ES 1426+428 in the R band as measured by the KVA telescope. The contribution of the host galaxy has been subtracted.*

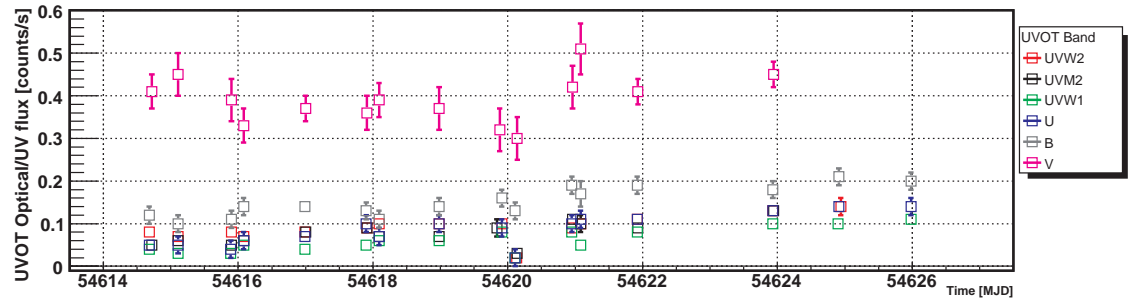


Figure 10.2: *Light curve of 1ES 1426+428 in the optical-UV flux in different bands as measured by Swift UVOT detector.*

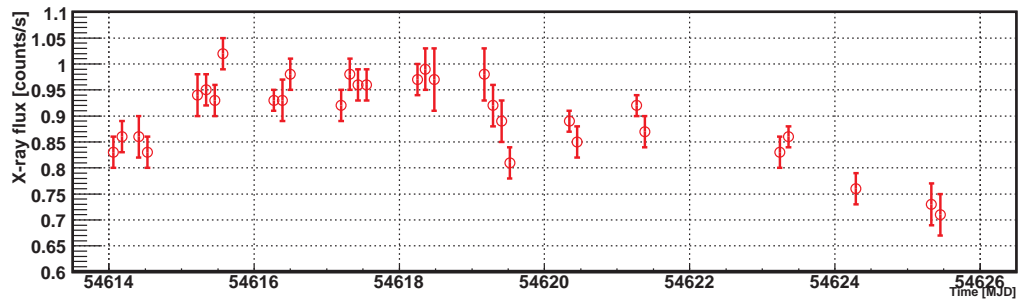


Figure 10.3: *Light curve of 1ES 1426+428 in the X-rays (0.2–10 keV) as measured by Swift XRT detector.*

## 10.4 Cross-band correlation

The correlation between the X-ray flux measured by *swift*-XRT and the optical and UV flux measured by the *swift*-UVOT in different energy bands was calculated as it was done in section 9.3.1.2. For the correlation analysis, XRT-UVOT data pairs having a time difference higher than 5 h were excluded, considering the ones inside this time window as simultaneous. For each XRT-UVOT band measurement a set of  $10^5$  light curves was simulated based on the Gaussian errors of the data points. For each pair of simulated light curves, the value of Pearson's r was calculated. A histogram of these possible r values was generated, giving the average values shown in Table 10.7. Furthermore, the probability of full correlated, total uncorrelated, probability for the first scenario to be true and for the second to be false, and the opposite are given in the same table. No correlation was found to be present between the XRT fluxes and B and V bands, as it can be seen clearly in Figures 10.4 and 10.5. Left panels of Figures 10.6, 10.7, 10.8 and 10.9 show indications of a correlation between the fluxes in the X-ray band and the flux in the U, UVW1, UVM2, UVW2 bands. The correlation factors are shown in Table 10.7. For the U, UVW1, UVM2, UVW2 bands, the value of Pearson's r is  $\sim 0.4$ , but taking into account the uncertainties, only in the U band, and specially in the UVW1 band, the correlated scenario is significantly more likely than the non correlated one (see the PDFs of the different scenarios in the right panels of Figures 10.6 and 10.7).

## 10.4 Cross-band correlation

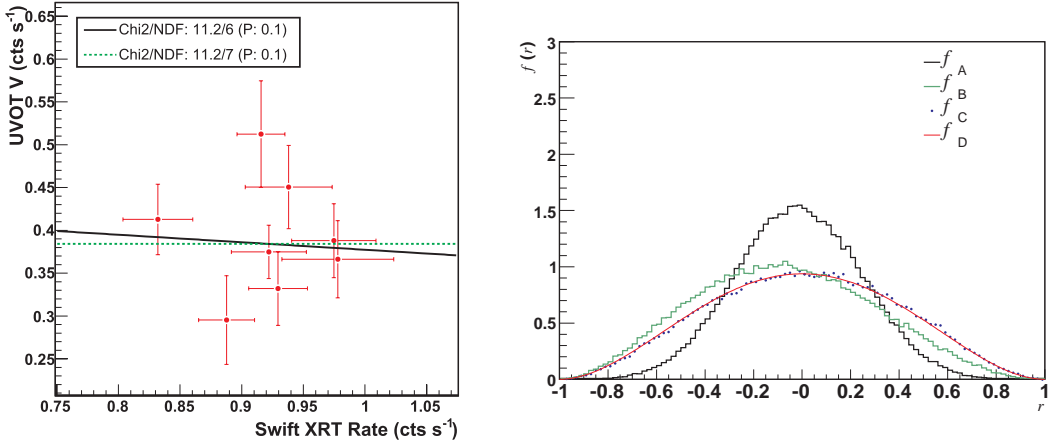


Figure 10.4: Left:  $V$  band flux (Swift UVOT) versus  $X$ -ray flux (Swift XRT) correlation plot, showing the best fit function (black line) and constant fit (dot-dashed green line). Right: Correlation coefficient distributions from Monte Carlo simulations:  $f_A$  for data,  $f_B$  for perfectly correlated case,  $f_C$  of uncorrelated case, and  $f_D$  for an analytical solution in the uncorrelated case.

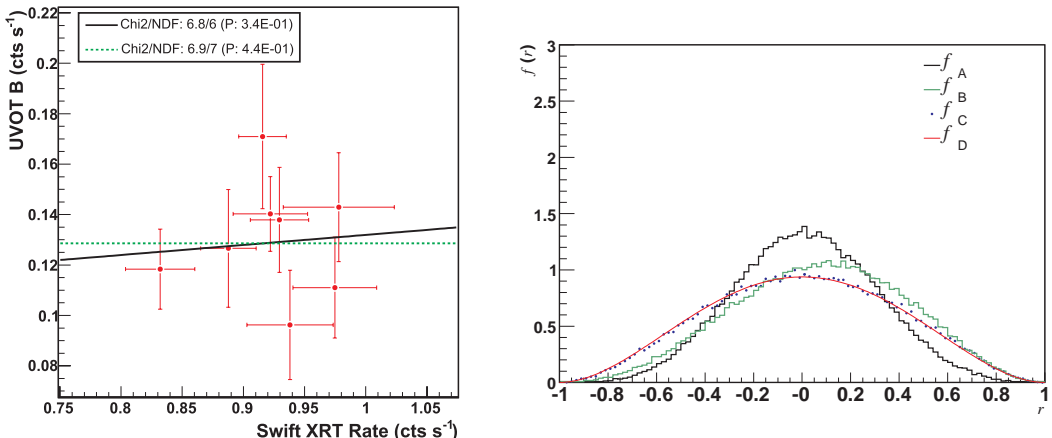


Figure 10.5: Left:  $B$  band flux (Swift UVOT) versus  $X$ -ray flux (Swift XRT) correlation plot, showing the best fit function (black solid line) and constant fit (dot-dashed green line). Right: Correlation coefficient distributions from Monte Carlo, the notation is the same as before.

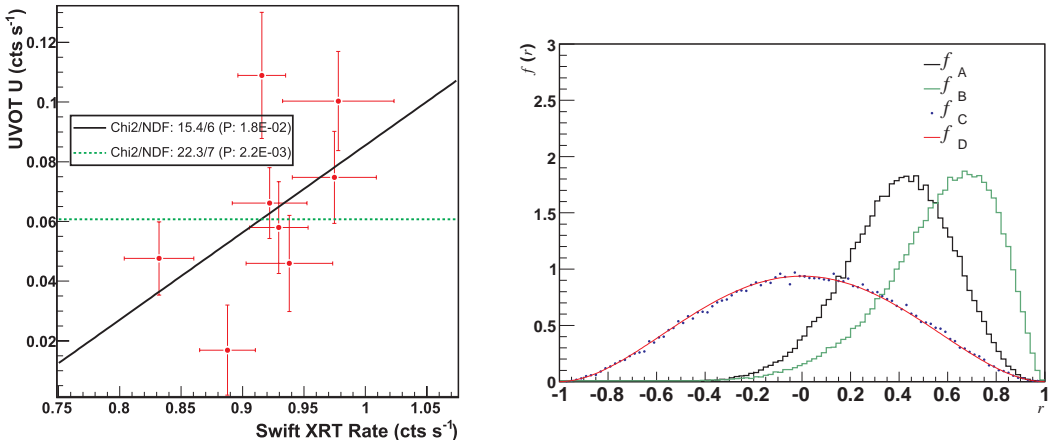


Figure 10.6: Left:  $U$  band flux (Swift UVOT) versus  $X$ -ray flux (Swift XRT) correlation plot, showing the best fit function (black solid line) and constant fit (dot-dashed green line). Right: Correlation coefficient distributions from Monte Carlo simulations, the notation is the same as before.

## 10.4 Cross-band correlation

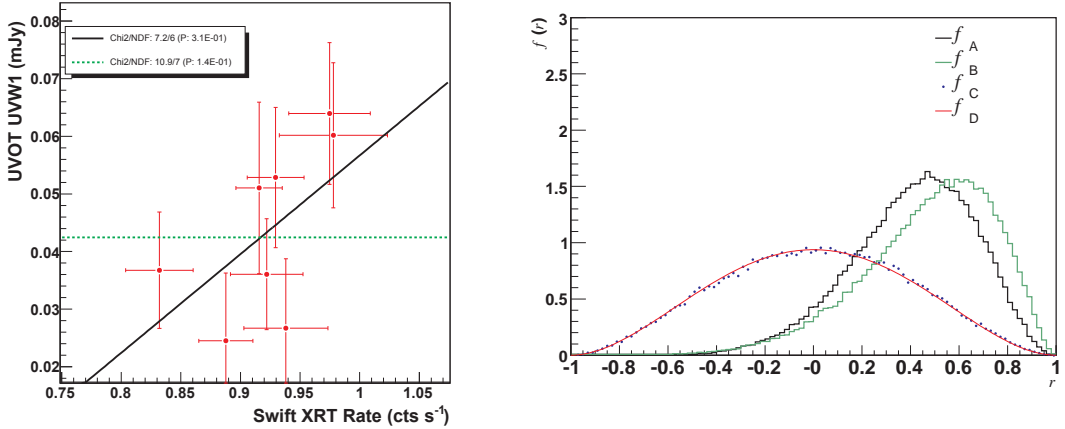


Figure 10.7: *Left:* UVOT UVW1 band flux (Swift UVOT) versus X-ray flux (Swift XRT) correlation plot, showing the best fit function (black solid line) and constant fit (dot-dashed green line). *Right:* Correlation coefficient distributions from Monte Carlo simulations, the notation is the same as before.

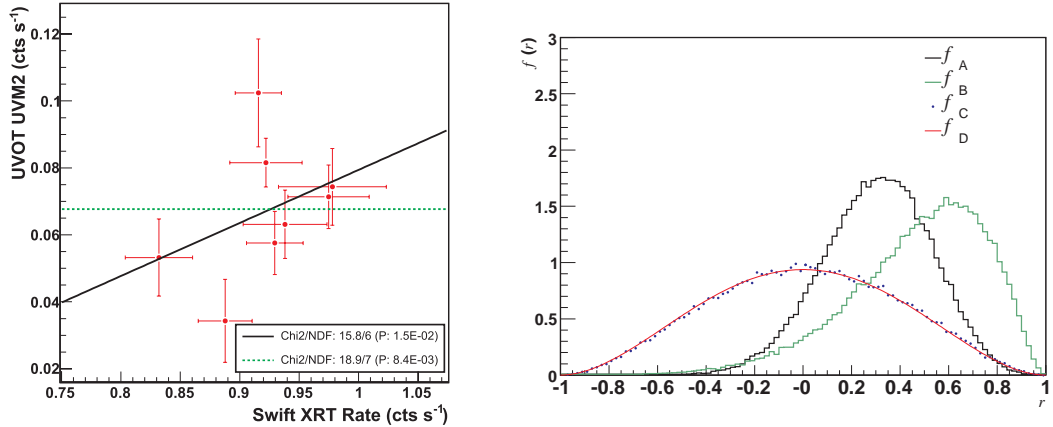


Figure 10.8: *Left:* UVOT UVM2 band flux (Swift UVOT) versus X-ray flux (Swift XRT) correlation plot, showing the best fit function (black solid line) and constant fit (dot-dashed green line). *Right:* Correlation coefficient distributions from Monte Carlo simulations, the notation is the same as before.

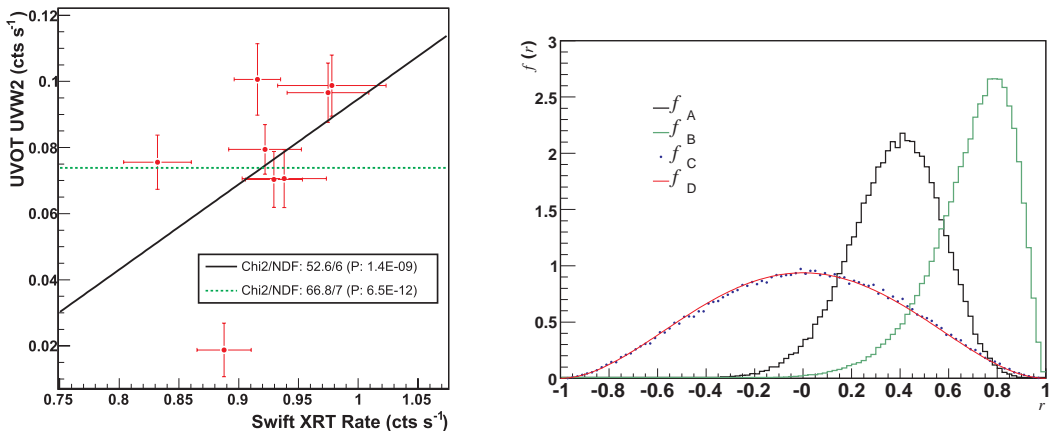


Figure 10.9: *Left:* UVOT UVW2 band flux (Swift UVOT) versus X-ray flux (Swift XRT) correlation plot, showing the best fit function (black solid line) and constant fit (dot-dashed green line). *Right:* Correlation coefficient distributions from Monte Carlo simulations, the notation is the same as before.

## 10.5 Spectral energy distribution and modeling

Figure 10.10 shows the broadband SEDs corresponding to the MWL observations of 1ES 1426+428. The optical and UV fluxes have been corrected from Galactic extinction<sup>1</sup>. The spectrum from *Suzaku* was obtained from June 5 to June 8 and therefore it is only simultaneous to a fraction of the data. The HE flux as measured by *Fermi*-LAT, reported in the *Fermi*-LAT First Source Catalog (1FGL) [The10] was added to the SED<sup>2</sup>. Note that the measurements from *Fermi*-LAT were performed a few months after MAGIC measurements (from August 4, 2008 to July 4, 2009). The red and blue arrows report the measured MAGIC upper limits, obtained assuming a  $-3$  photon index, are shown with and without EBL absorption, respectively. The flux upper limit is significantly changed after the de-absorption, as expected by the relative high redshift ( $z=0.129$ ) of the source. For comparison, historical MWL data are shown, including those data from Whipple [Hor02]. It is clear that the source was in a lower state than in historical measurements.

The SED was modeled by a one-zone SSC model [TMG01], see section 9.4.4.1 for a description. The observed SED can be described with rather typical parameters from HBLs. The parameters for the model are shown in Table 10.6. It has to be noted that the upper limits do not allow to constrain the SED model as well as if the source would have been detected.

## 10.6 Discussion

MAGIC observed 1ES 1426+428 during a low state of activity of the source in the VHE band. No significant flux was detected from the source. Flux upper limits on the level of a few percent of the Crab Nebula flux were derived. If the source would have shown a flux at a level comparable to the one it showed during 1999-2000 as reported by the HEGRA collaboration [Aha02a], corresponding to  $\sim 10\%$  of the Crab Nebula flux, the source should have been detected by MAGIC with a  $5\sigma$  level after just 2 h of observations. The observations of the source by Whipple and HEGRA in 2002 revealed that the source was in a lower state, corresponding to  $\sim 4\%$  of the Crab Nebula flux [Aha03, FV04]. Even with the 2002 flux, MAGIC should have detected the source in a  $5\sigma$  level after  $\sim 12$  h of observation. The upper limit to the flux reported in this work,  $\simeq 2.5\%$  of the flux of the Crab Nebula for a 95% confidence level, is clearly lower than the mentioned historical measurements.

In contrast to the low flux observed in VHE, 1ES 1426+428 showed an intermediate state in the X-ray fluxes, with a hard spectrum with a flux  $F = 4 \times 10^{-11}$  erg

---

<sup>1</sup>Using the extinction coefficients found in <http://nedwww.ipac.caltech.edu/>

<sup>2</sup>Data obtained from <http://fermi.gsfc.nasa.gov/ssc>

## 10.6 Discussion

---

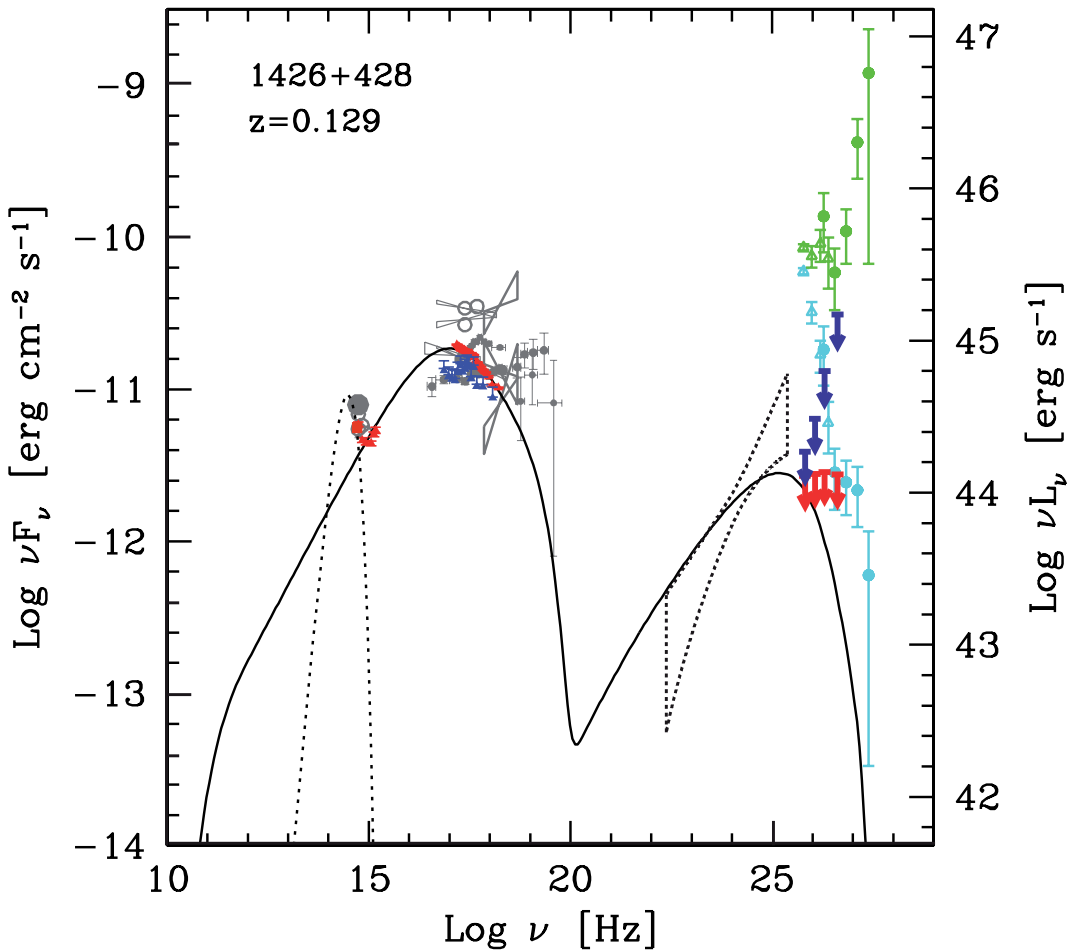


Figure 10.10: Spectral energy distribution with a one-zone SSC model [TMG01] for the 2008 1ES 1426+428 MWL campaign (solid curve). The data from KVA are shown in red filled square, the Swift UVOT data are shown in red triangles. The average Suzaku spectrum is represented in red and the Swift XRT spectrum is represented by the blue dots. The “butterfly” mark represents the  $1-\sigma$  uncertainty area after 11 months of Fermi-LAT measurements [The10] (not simultaneous to MAGIC measurements). The red and blue arrows report the measured MAGIC upper limits with and without EBL absorption, respectively. Pale blue and green points are the historical Whipple data [Hor02], with and without EBL absorption. Other gray markers are historical measurements in the X-ray and optical-UV energy bands. The optical-UV data are not corrected for the emission of the host galaxy, which is described with a black body law, represented by the dotted curve.

## 10.6 Discussion

---

Table 10.6: *SED model parameters.*

| Parameter                     | 2006 |
|-------------------------------|------|
| $\gamma_{min} [\cdot 10^2]$   | 1.0  |
| $\gamma_{break} [\cdot 10^4]$ | 1.0  |
| $\gamma_{max} [\cdot 10^5]$   | 10   |
| $n_1$                         | 2.0  |
| $n_2$                         | 4.0  |
| $B [\cdot 10^{-3} G]$         | 180  |
| $K [\cdot 10^3 cm^{-3}]$      | 2.8  |
| $R [\cdot 10^{15}]$           | 5.9  |
| $\delta$                      | 25   |

$\text{cm}^{-2} \text{s}^{-1}$  and a photon index  $\alpha > 2$ , thus indicating a synchrotron peak well below 1 keV. The X-ray flux is comparable to historical measurements, but the slope is quite different from the one observed during previous observations. The historical X-ray data taken during the VHE outburst showed a hardening of the spectrum with photon index  $< 2$ , with the synchrotron peak at higher energies, up to 100 keV. The comparison of the VHE and X-ray states with historical data suggests a relation between the VHE activity and the hardening of the X-ray spectrum and the corresponding shift of the synchrotron peak to higher energies. This in turn seems to suggest that the VHE emission may be related to the slope of the injected electron distribution. Since the X-ray spectrum is in average flat (slope  $\sim 2$ , see [Leo09, Ale10]) a minimal change to the electron distribution could produce a dramatic change in the synchrotron peak location. Further multiwavelength observations could reveal the physical quantities (e.g. the slope or energy break of the injected electrons distribution) that govern this interplay among X-ray and VHE spectral properties.

A possible correlation between the X-ray and optical/UV fluxes from *Swift* was investigated. A correlation between these bands is expected, since it is understood that X-ray and optical/UV photons originate in the same synchrotron mechanism. These measurements were not truly simultaneous but inside a 5 hour time window. No correlation was found to be present between the XRT and UVOT B and V bands measurements, while indications of a relation between the fluxes in X-rays and the flux in the U, UVW1, UVM2, UVW2 bands seemed to be present. When studying more carefully these data, only for the U and UVW1 bands the correlated scenario is significantly more likely than the non correlated one. In order to further investigate the correlation between these bands, additional true simultaneous measurements, covering a wider dynamical range of source's emission would be required.

## 10.7 Summary

MAGIC observed 1ES 1426+428 during a low state in the VHE band. Upper limits of the order of 2.5% of the Crab Nebula flux were derived for  $F > 170$  GeV. The corresponding X-ray spectrum is hard, indicating that the synchrotron peak is located at energies lower than 1 keV. The data are well described by a one-zone SSC model. The comparison of VHE and X-ray states with historical data points to a correlation of the VHE activity with the hardening of the X-ray spectrum and the corresponding shift of the synchrotron peak to higher energies. Hints of correlation between X-ray and UV emission were found.

A preliminary version of these results was presented at the 2009 ICRC [[Leo09](#)], and a publication is in preparation with the results presented in this chapter [[Ale10](#)].

## 10.7 Summary

---

Table 10.7: Results of a correlation test for each XRT-UVOT data pair.

| Data Pair | $r$              | $P(f_A, f_B)$   | $P(f_A, f_C)$          | $P(f_A, f_B)(1-P(f_A, f_C))$ | $P(f_A, f_C)(1-P(f_A, f_B))$ |
|-----------|------------------|-----------------|------------------------|------------------------------|------------------------------|
| XRT-UVW2  | $0.37 \pm 0.19$  | $0.18 \pm 0.09$ | $0.38 \pm 0.09$        | 0.11                         | 0.31                         |
| XRT-UVM2  | $0.30 \pm 0.22$  | $0.56 \pm 0.37$ | $0.49 \pm 0.37$        | 0.29                         | 0.21                         |
| XRT-UVW1  | $0.41 \pm 0.25$  | $0.80 \pm 0.41$ | $0.37^{+0.41}_{-0.37}$ | 0.50                         | 0.07                         |
| XRT-U     | $0.39 \pm 0.22$  | $0.52 \pm 0.21$ | $0.37 \pm 0.21$        | 0.32                         | 0.18                         |
| XRT-B     | $0.01 \pm 0.28$  | N/A             | N/A                    | N/A                          | N/A                          |
| XRT-V     | $-0.01 \pm 0.25$ | N/A             | N/A                    | N/A                          | N/A                          |

Average values of the Pearson's  $r$  obtained for the different data pairs measured by XRT and UVOT, together with the correlation study results:  $P(f_A, f_B)$  is the probability of agreement between the measured PDF and the fully correlated PDF,  $P(f_A, f_C)$  is the probability for measurements coming from fluctuation of an entirely uncorrelated physics case,  $P(f_A, f_B)(1-P(f_A, f_C))$  is the probability for the first scenario to be true and for the second to be false, and  $P(f_A, f_C)(1-P(f_A, f_B))$  is the probability for the opposite scenario.

# Chapter 11

## Observations of Mrk 421 and Mrk 501 during 2009

### 11.1 Introduction

HBL type AGN have been observed extensively during years in most of the energy bands. Despite of previous intense observations, the nature of the emission mechanisms of these AGN still exhibits many uncertainties. The LAT instrument on-board the *Fermi* Gamma-ray Space Telescope observatory [The10], operating since August 2008 enables a continuous sensitive monitoring in the HE band, from 0.1 to 100 GeV (even going up to 400 GeV for the brightest sources), a region poorly sampled before *Fermi* came into operation. The possibility of observing simultaneously with MAGIC and *Fermi*, that can reach energies below 100 GeV, allows to sample for the first time, without any gap, the SED of blazars from 0.1 to several TeV. Due to the high sensitivity of both instruments, it is possible to obtain high statistics of simultaneous data of bright VHE blazars, even if they are in low state.

In the context of observing in detail bright blazars with MAGIC, a sample of three well known, nearby and bright blazars was selected: Mrk 421 [Pun92] ( $z=0.030$ ), Mrk 501 [Qui96] ( $z=0.034$ ) and 1ES 1959+650 [Nis99] ( $z=0.047$ ). MAGIC–*Fermi* LAT observations were carried out together with a strong MWL coverage in the radio, optical, UV and X-ray bands. In this chapter, a MAGIC data analysis performed for the first two sources, Mrk 421 and Mrk 501, will be described. The analysis of 1ES 1959+650, not performed by the author of this thesis<sup>1</sup>, was still not finished when this thesis was written, and will not be discussed here.

An overview of the AGN Mrk 421 is provided in Chapter 9.

---

<sup>1</sup>The analysis was being performed by Diego Tescaro (IFAE).

## 11.2 MAGIC observations and data analysis

---

The AGN Markarian 501 (Mrk 501; R.A.  $16^h53^m52.2^s$ , decl.  $+39^\circ45'37.0''$  [J2000.0]) is an HBL type BL Lac object. Its VHE emission was discovered in 1996 [Qui96], becoming the second extragalactic source to be detected in the TeV energy range, using IACTs. With a redshift of  $z = 0.034$  it is one of the closest known and, along with Mrk 421, the best-studied TeV  $\gamma$ -ray emitting blazar. The source shows a very high degree of variability, keeping a reasonably high flux even in quiescent states (which is, however, lower than the quiescent flux of Mrk 421). In 1997 the source showed a high state of activity (see Figure 11.1), showing fluxes of the order of 10 times those of the Crab Nebula at the same energies. During this state, the source's emission was detected in energies as high as  $\sim 20$  TeV [Aha01b]. Simultaneous X-ray observations of the source revealed a high state of the source, showing an extremely hard spectrum, peaking at  $\sim 100$  keV, what represents a shift of the peak position two order of magnitudes higher compared to previous observations [Cat97, Pia98, Tav01], therefore indicating a clear correlation between the  $\gamma$ -ray and X-ray states. The following years the source showed a low emission of the order of 20–30% the Crab Nebula flux. Correlation between X-rays and VHE rays was found during a MWL campaign in 2004 [Gli06]. In the previous study, the correlation between X-ray and  $\gamma$ -ray emissions appears to be stronger when the source is brighter.

MAGIC observed Mrk 501 in 2005 May–July, when the source showed strong flux variation, with flux doubling times as short as a few minutes [Alb07e]. It observed again this source in 2006, when the source exhibited a low flux of about 20% of the Crab Nebula flux, without a significant variability [And09c]. Further observations were performed in 2008, when it also showed a low flux of the order of 20% of the Crab Nebula flux, but significant X-ray and VHE flux variabilities were found [Kra09].

## 11.2 MAGIC observations and data analysis

The observations were carried out in the first half of 2009, during dark nights, employing the *wobble* mode (see section 5.8). The data were analyzed following the standard MAGIC analysis procedure (see Chapter 6). Only observational dark nights, with a correct performance of the detector were considered for the analysis (see Tables 11.2 and 11.3).

After calibration and signal extraction, noise from night-sky background light was removed from the air-shower images by applying an absolute time image cleaning (see section 6.7.1), requiring a minimum light content of 6 phe for the core pixels of the image and 3 phe for the boundary ones. Additional time constrains were required:  $\Delta t_{core} = 4.5$  ns and  $\Delta t_{boundary} = 1.5$  ns (see 6.7.1 for details). Image parameters were calculated as described in section 6.7.2. A minimum cut of 100 phe in the parameter *size* was applied to the data.

## 11.2 MAGIC observations and data analysis

---

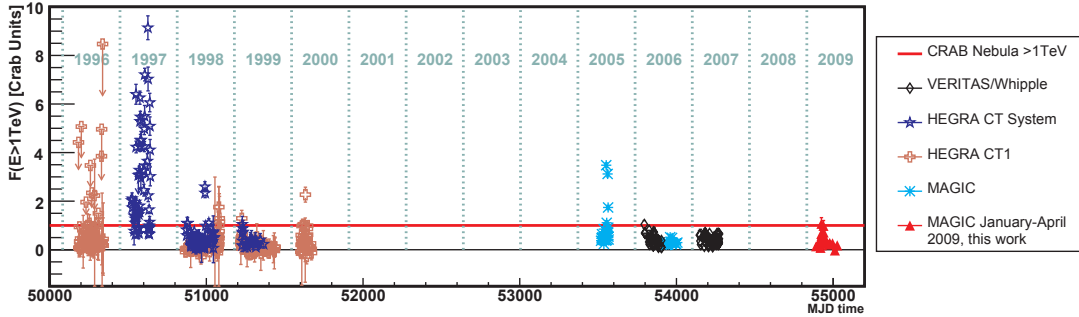


Figure 11.1: *Historical VHE ( $E > 1$  TeV) light curve of Mrk 501 since it's first detection in 1996 [Qui96], as measured by different VHE  $\gamma$ -ray instruments. The red solid line indicates the flux of the Crab Nebula. The filled red triangles, obtained during 2009 by MAGIC are result of the analysis described in this chapter. The historical data points are from the  $\gamma$ -ray LC archive at DESY: <http://www-zeuthen.desy.de/multi-messenger/GammaRayData/>*

Data were filtered by rejecting trivial background events, such as accidental noise triggers, or data taken during adverse atmospheric conditions (see section 6.8.4). The event rate after image cleaning was used as primary sub-run quality indicator. Additionally, the mean values of the discrimination thresholds, cloudiness and humidity parameters were used to further filter the bad quality sub-runs. A total of 28.6 h of data survived the quality selection and were used for further analysis in the case of Mrk 421, and 15.6 h for Mrk 501.

Table 11.1: *Set of cuts used for Mrk 421 and Mrk 501 analysis.*

| Type      | <i>hadronness</i> | <i>alpha</i>            | combined acceptance |
|-----------|-------------------|-------------------------|---------------------|
| Detection | $\leq 0.05$ (41%) | $\leq 7.5^\circ$ (87 %) | 36%                 |
| Loose     | dynamical (90%)   | dynamical (80%)         | 72%                 |

For the  $\gamma$ /hadron separation, a RF regression method was used, as described in section 6.8.1. The parameters *size*, *width*, *length*, *size*/*(width × length)*, *conc*, *dist*, *M3Long*, *time RMS* and *time gradient* were used to train the algorithm. Cuts in the parameter *hadronness* and in the angular parameter *alpha* (see section 6.9 for details) were performed for both the *on* and the *off* samples. For the significance calculation, the *off* sample was obtained from three *off* regions (at  $90^\circ$ ,  $180^\circ$  and  $270^\circ$  with respect to the source position in the camera). The analysis detection cuts were determined by optimizing the sensitivity from the Crab Nebula data sample described in section 6.3. With these cuts the sensitivity of MAGIC is such that would detect a Crab-like source, that exhibits a 1.7% Crab Nebula flux, with a  $5\sigma$  confidence level after 50 h of observation. For the spectrum

## 11.2 MAGIC observations and data analysis

---

Table 11.2: *Mrk 421 data sets and observational circumstances.*

| Night        | Observation Window [MJD] | $t_{\text{eff.}}$ [h] | ZA [ $^{\circ}$ ] | $\sigma$  |
|--------------|--------------------------|-----------------------|-------------------|-----------|
| 2009/01/22   | 54853.0745 – 54853.1563  | 1.1                   | 10 – 31           | 13        |
| 2009/01/24   | 54855.0670 – 54855.1527  | 1.7                   | 10 – 31           | 19        |
| 2009/01/26   | 54857.0628 – 54857.1168  | 1.0                   | 17 – 30           | 15        |
| 2009/01/28   | 54859.0567 – 54859.1458  | 1.9                   | 9 – 30            | 17        |
| 2009/01/30   | 54861.0527 – 54861.0527  | 0.4                   | 26 – 30           | 11        |
| 2009/02/01   | 54863.0587 – 54863.0689  | 0.2                   | 25 – 28           | 7.7       |
| 2009/02/03   | 54865.0752 – 54865.1638  | 2.0                   | 9 – 21            | 21        |
| 2009/02/25   | 54886.9743 – 54887.0708  | 1.1                   | 10 – 31           | 16        |
| 2009/03/01   | 54890.9118 – 54890.9967  | 1.4                   | 11 – 23           | 16        |
| 2009/03/17   | 54906.9295 – 54907.0130  | 1.5                   | 10 – 29           | 21        |
| 2009/03/19   | 54908.9878 – 54909.0137  | 0.6                   | 10 – 14           | 12        |
| 2009/03/21   | 54910.9317 – 54911.0024  | 1.6                   | 10 – 26           | 15        |
| 2009/03/23   | 54912.9110 – 54912.9967  | 1.9                   | 10 – 30           | 16        |
| 2009/03/29   | 54918.9259 – 54918.9824  | 1.5                   | 10 – 23           | 9.9       |
| 2009/03/31   | 54920.8880 – 54920.9925  | 2.2                   | 10 – 31           | 17        |
| 2009/04/15   | 54936.8532 – 54937.0614  | 1.5                   | 17 – 36           | 21        |
| 2009/04/17   | 54937.8602 – 54938.0547  | 1.6                   | 17 – 35           | 18        |
| 2009/04/19   | 54939.8611 – 54940.0494  | 0.9                   | 22 – 35           | 10        |
| 2009/04/21   | 54941.8638 – 54942.0444  | 1.7                   | 16 – 35           | 15        |
| 2009/04/22   | 54942.8631 – 54942.8717  | 0.2                   | 20 – 22           | 4.5       |
| 2009/04/23   | 54943.9667 – 54944.0375  | 1.3                   | 15 – 34           | 17        |
| 2009/04/24   | 54944.8641 – 54945.0380  | 1.7                   | 16 – 36           | 15        |
| <b>total</b> | –                        | <b>28.6</b>           | –                 | <b>70</b> |

$t_{\text{eff.}}$  denotes the effective observation time. ZA gives the zenith angle range of the observations, and  $\sigma$  the measured statistical significance according to the detection cuts.

calculation, some *loose* cuts were set independently for each energy bin, as shown in Table 11.1. In order to be less affected by systematic effects at lower energies, where the overlap with *Fermi* LAT measurements occur, only one *off* region was used for the differential and light curve calculation. All significances presented in this chapter were calculated using Eq. 17 of [LM83].

The primary  $\gamma$ -ray energies were reconstructed from the image parameters using the RF method (see section 6.8.2). The arrival directions of the showers, used for the  $\theta^2$  crosscheck analysis (see below) was reconstructed with the disp RF method (see section 6.8.3.2).

Tables 11.2 and 11.3 summarize the analyzed data sets. The statistical significance of the detection is assessed by applying the detection cuts shown at Table 11.1 for  $\text{size} > 450$  phe, using three *off* regions.

The obtained differential energy spectra were unfolded using the Tikhonov technique (see section 6.10.3). In order to estimate the systematic uncertainty due to the analysis, three additional analysis were performed: one using the angular parameter *alpha* and three *off* region for background signal estimation,

## 11.2 MAGIC observations and data analysis

---

Table 11.3: *Mrk 501 Data sets and observational circumstances.*

| Night        | Observation Window [MJD] | $t_{\text{eff.}}$ [h] | ZA [ $^{\circ}$ ] | $\sigma$  |
|--------------|--------------------------|-----------------------|-------------------|-----------|
| 2009/03/01   | 54891.2371 – 54891.2786  | 0.9                   | 14 – 24           | 3.4       |
| 2009/03/23   | 54913.2555 – 54913.2148  | 1.3                   | 15 – 29           | 9.9       |
| 2009/03/29   | 54919.2264 – 54919.2550  | 0.6                   | 11 – 12           | 2.4       |
| 2009/03/31   | 54921.2409 – 54921.2552  | 0.3                   | 12 – 14           | 2.8       |
| 2009/04/02   | 54923.1336 – 54923.2505  | 1.3                   | 12 – 29           | 8.2       |
| 2009/04/03   | 54924.2354 – 54924.2526  | 0.3                   | 12 – 15           | 7.5       |
| 2009/04/04   | 54925.1279 – 54925.2474  | 0.4                   | 13 – 29           | 9.3       |
| 2009/04/05   | 54926.1560 – 54926.2495  | 0.2                   | 13 – 21           | 5.4       |
| 2009/04/17   | 54938.2118 – 54938.2356  | 0.5                   | 14 – 19           | 7.6       |
| 2009/04/18   | 54939.2133 – 54939.2357  | 0.5                   | 14 – 20           | 8.8       |
| 2009/04/19   | 54940.1362 – 54940.2364  | 1.9                   | 12 – 21           | 9.7       |
| 2009/04/25   | 54946.0088 – 54946.2283  | 0.9                   | 21 – 46           | 6.8       |
| 2009/04/27   | 54948.2203 – 54948.2326  | 0.2                   | 22 – 25           | 2.8       |
| 2009/05/26   | 54977.0475 – 54977.1198  | 1.6                   | 11 – 17           | 11.0      |
| 2009/05/27   | 54978.0270 – 54978.1177  | 0.6                   | 11 – 18           | 2.8       |
| 2009/06/02   | 54984.0779 – 54984.0969  | 0.2                   | 12 – 16           | 1.6       |
| 2009/06/14   | 54995.9278 – 54996.0488  | 1.8                   | 11 – 31           | 7.7       |
| 2009/06/29   | 55011.0448 – 55011.0790  | 0.6                   | 11 – 40           | 4.4       |
| 2009/07/14   | 55025.9051 – 55026.0538  | 1.3                   | 11 – 35           | 7.0       |
| <b>total</b> | –                        | <b>15.6</b>           | –                 | <b>29</b> |

$t_{\text{eff.}}$  denotes the effective observation time. ZA gives the zenith angle range of the observations, and  $\sigma$  the measured statistical significance according to the detection cuts.

and another two using the  $\theta^2$  angular parameter, one using one *off* region and another using three *off* regions. For each analysis, different unfolding procedures were performed. With the whole sample of successfully unfolded spectral points, an area of systematic uncertainty was built: The minimum and maximum flux values of each spectral point obtained from the different analysis was used to build the area (see the example the gray area in Figures 11.3 and 11.5, where the larger systematics from the analysis are at the lowest and highest energies).

The energy threshold of the analysis, defined as the maximum of the energy distribution of the accepted MC events, corresponds to 110 GeV for the used loose cuts.

All stated uncertainties on this chapter are statistical only. The systematic errors are discussed in section 6.12.

The analysis results of both sources presented here were compared with an independent analysis performed by Diego Tescaro, yielding results consistent inside the uncertainties.

## 11.3 Results

During the observations of both sources, intense MWL campaigns took place<sup>1</sup>. In total, 19 instruments participated in the campaigns, that lasted from January 20, 2009 to June 1, 2009 in the case of Mrk 421, and from March 17, 2009 to July 31, 2009 in the case of Mrk 501. The instruments that participated are described in Table 11.6.

### 11.3.1 Mrk 421

A clear  $\gamma$ -ray signal from the source was detected for all the observation nights. In total, 4085 excess events were recorded over a background of 523 events, yielding an overall significance of  $70\sigma$ .

Figure 11.2 shows the day-by-day lightcurve of Mrk 421 in the optical R-band, as measured by the KVA telescope, the X-ray flux (2–10 keV) as measured by the RXTE/ASM, and the VHE integral flux above 200 GeV. The contribution from the host galaxy and nearby stars in the R-band ( $F = 8.1 \pm 0.4$  mJy, [Nil07]) has been subtracted from the optical lightcurve. The average VHE flux exhibited by the source is  $F_{>200\text{ GeV}} = (1.27 \pm 0.03) \cdot 10^{-10} \text{ cm}^{-2}\text{s}^{-1}$ , what is about 65% of the Crab Nebula flux in those energies. When compared to earlier observations, these results indicate that the source was in the pedestal state. On the other hand, the source exhibited variability, as a constant fit to the lightcurve yielded an unacceptable  $\chi^2_{red}$  of 120/21. During MJD 54863 the source exhibited a flux comparable to 130% of the one of the Crab Nebula at those energies, but only 0.2 h of data are available this night. The source was not showing the same degree of variability as it did during the 2006 MWL campaigns, discussed in Chapter 9.

Figure 11.3 shows the overall differential spectrum, before and after being de-absorbed with the extragalactic background light model discussed in [FRV08]. A spectral fit with PL function (Eq. 9.1) was performed, yielding an unfavourable value of the  $\chi^2_{red}$  of 47.4/7 ( $P=5 \cdot 10^{-8}$ ). A possible curvature in the spectrum was investigated in both measured and EBL de-absorbed spectra: they were fit to log-P (Eq. 9.4) and PL+C (Eq. 9.5) functions. A likelihood ratio test (e.g. [MG07]) was applied to all the fits, giving a clear preference towards a log-P or a PL+C compared to a simple power-law ( $P=99\%$ ). The results of the fits and the probability of a likelihood ratio test are given in Table 11.4. For these data the PL+C model is favoured over the log-P one.

## 11.3 Results

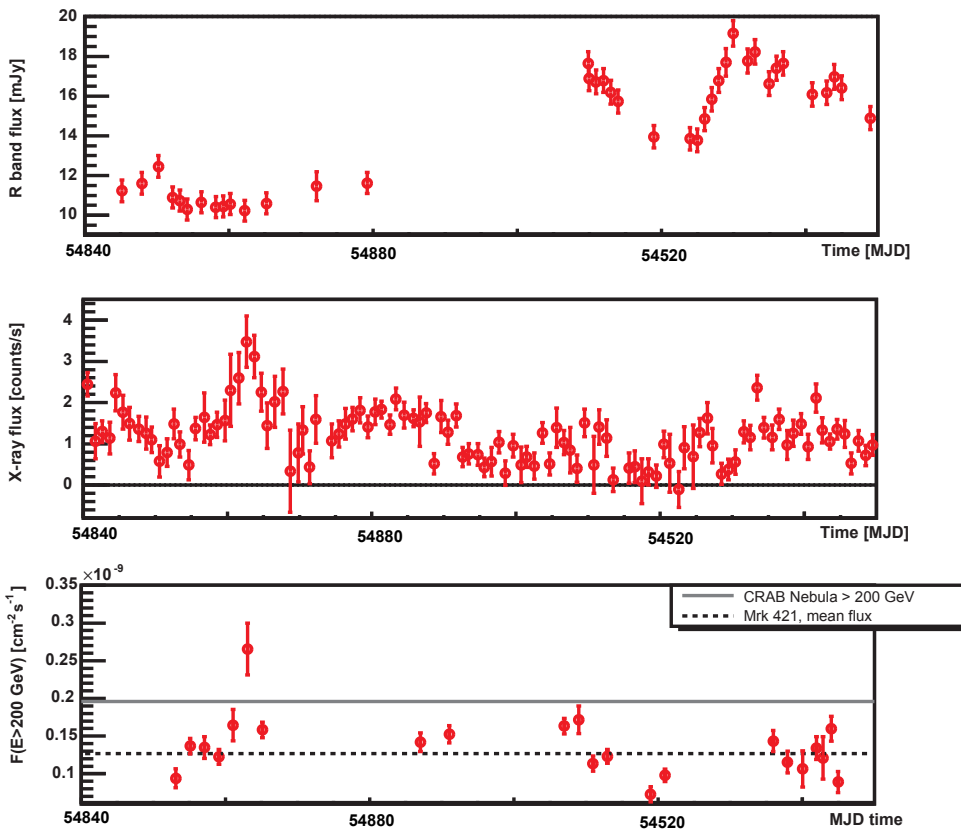


Figure 11.2: *Light curves during 2009 Mrk 421 MWL observations. Upper panel: Light curve of the optical flux as measured by the KVA telescope, where the host galaxy contribution has been subtracted. Middle panel: Day-by-day X-ray counts as observed by the RXTE/ASM. Lower panel: VHE ( $E > 200 \text{ GeV}$ ) light curve as measured by MAGIC, where the data points represent average nightly fluxes. A “mean flux” of  $1.27 \cdot 10^{-10} \text{ cm}^{-2}\text{s}^{-1}$  (black dashed line) was found as an average over all VHE data points. The gray solid line gives the Crab Nebula flux [Alb08f] for comparison.*

### 11.3.2 Mrk 501

A clear  $\gamma$ -ray signal from the source was detected for most of the observation nights. For the nights with shorter observation time, only 2-3  $\sigma$ -level detections were possible. In total, 899 excess events were recorded over a background of 425 events, yielding an overall significance of 29  $\sigma$ .

Figure 11.4 shows the day-by-day lightcurve of Mrk 501 in the optical R-band as measured by the KVA telescope, the X-ray flux (2–10 keV) as measured by the RXTE/ASM, and the VHE integral flux above 200 GeV. In the same

<sup>1</sup>Further details of the campaigns, coordinated by David Paneque, can be found in [http://www.slac.stanford.edu/~dpaneque/MW\\_Mrk421\\_2009/0bs.html](http://www.slac.stanford.edu/~dpaneque/MW_Mrk421_2009/0bs.html) for Mrk 421, and in [http://www.slac.stanford.edu/~dpaneque/MW\\_Mrk501\\_2009/0bs.html](http://www.slac.stanford.edu/~dpaneque/MW_Mrk501_2009/0bs.html) for Mrk 501.

### 11.3 Results

---

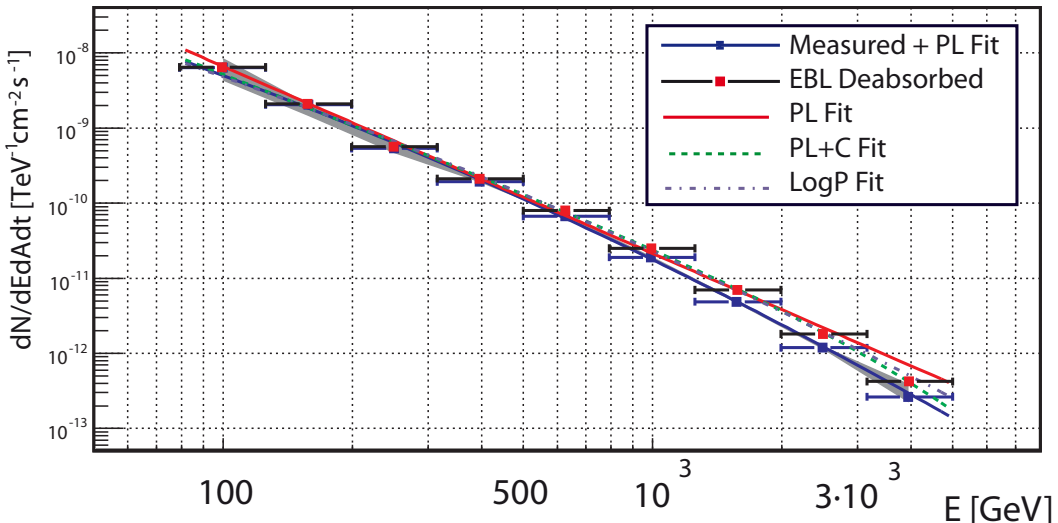


Figure 11.3: Differential energy spectrum for Mrk 421 during the 2009 MWL campaign before (blue) and after (red) correcting for EBL absorption. The measured spectrum was fit to a power law (Eq. 9.1), log-P (Eq. 9.4) and PL+C (Eq. 9.5) fits were performed to the EBL de-absorbed spectrum (solid red, blue dot-dashed and green dashed curves, respectively). Curved fits (log-P and PL+C) describe better the data than simple power law fits, according to a likelihood ratio test. The gray area represents an estimation of the systematics from the different analysis methods (see text for details).

way as done before with Mrk 421, the contribution from the host galaxy and nearby stars of Mrk 501 in the R-band ( $F = 12.0 \pm 0.3$  mJy, [Nil07]) has been subtracted from the optical lightcurve. Mrk 501 exhibited an average flux of  $F_{>200\text{ GeV}} = (5.2 \pm 0.2) \cdot 10^{-11} \text{ cm}^{-2}\text{s}^{-1}$ , what is about the 25% of the Crab Nebula flux in those energies, and substantially below the Mrk 421 flux level. When compared to earlier observations (see Figure 11.1), these observations indicate a low flux state of the source. The source exhibited a clear variability, as a constant fit to the lightcurve yielded an unacceptable  $\chi^2_{\text{red}}$  of 94/28. Despite of the source's variability, the source's flux did not exceed the Crab Nebula flux (for  $E > 200$  GeV) during any of the nights, showing a similar state of activity as in the 2006 observations performed by MAGIC [And09c], and a behavior clearly different to the one seen in the MAGIC measurements in 2005, when the flux state reached up to 3.5 times the Crab Nebula flux level [Alb07e].

Figure 11.5 shows the overall differential spectrum of Mrk 501 as measured by MAGIC, before and after being de-absorbed with the extragalactic background light model discussed in [FRV08]. The spectra were fit to a PL function (Eq. 9.1), yielding value of the  $\chi^2_{\text{red}}$  of 6.3/7 ( $P=0.5$ ). A possible curvature in the spectrum was investigated in both measured and EBL de-absorbed spectra: they were fit to log-P (Eq. 9.4) and PL+C (Eq. 9.5) functions. A likelihood ratio test was applied to all the fits, giving a preference towards a PL+C and a log-P compared

## 11.3 Results

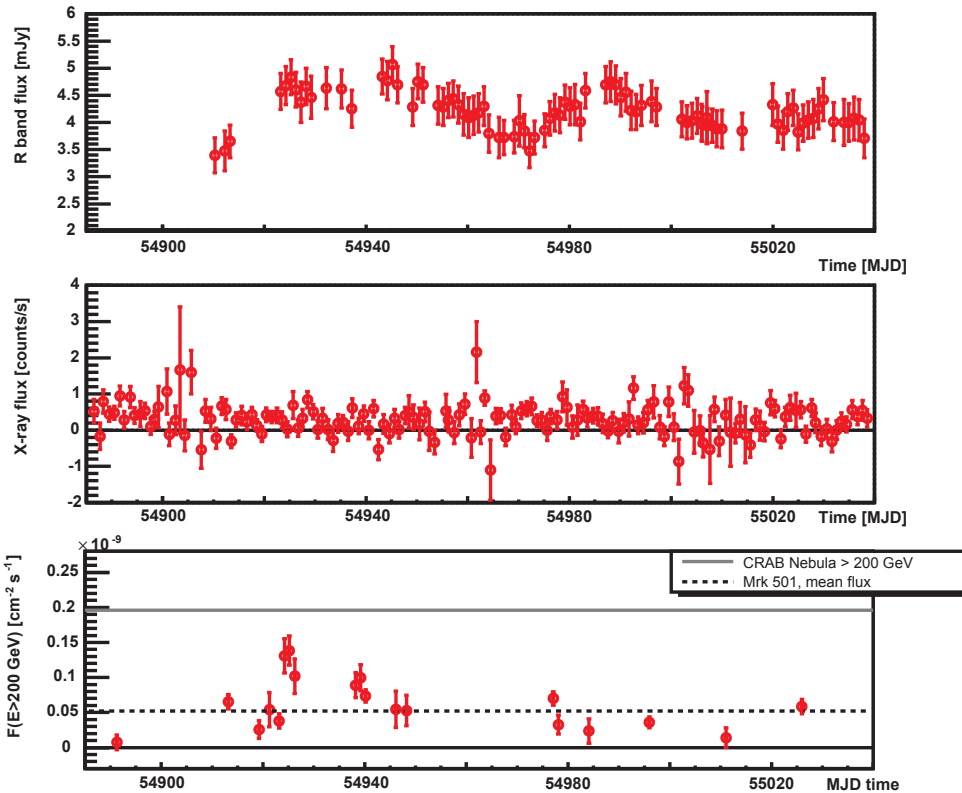


Figure 11.4: *Light curve of Mrk 501 during the 2009 MWL observations. Upper panel: Light curve of the optical flux as measured by the KVA telescope, where the host galaxy contribution has been subtracted. Middle panel: Day-by-day X-ray counts as observed by the RXTE/ASM. Lower panel: VHE ( $E > 200 \text{ GeV}$ ) light curve as measured by MAGIC, where the data points represent average nightly fluxes. A “mean flux” of  $0.52 \cdot 10^{-10} \text{ cm}^{-2} \text{s}^{-1}$  (black dashed line) was obtained as an average over all VHE data points. The gray solid line gives the Crab Nebula flux [Alb08f] for comparison.*

to a simple power-law ( $P > 90\%$ ) in the measured spectrum, and also towards the PL+C in the de-absorbed spectrum. There are also indications towards a preference of a log-P fit in the de-absorbed spectrum, but, however, no so strong: the likelihood ratio test gave a 83% probability of preference of this fit over a PL. The results of the fits and the probability of a likelihood ratio test are given in Table 11.5. The previous tests suggest that the spectrum is curved, the PL+C model being favoured over the other ones.

### 11.3.3 Cross-band correlations

In Figure 11.2 a certain correlation seems apparent between the X-ray and VHE fluxes of Mrk 421. In order to quantify this possible correlation, those RXTE/ASM measurements simultaneous to MAGIC observations were selected. This was

### 11.3 Results

---

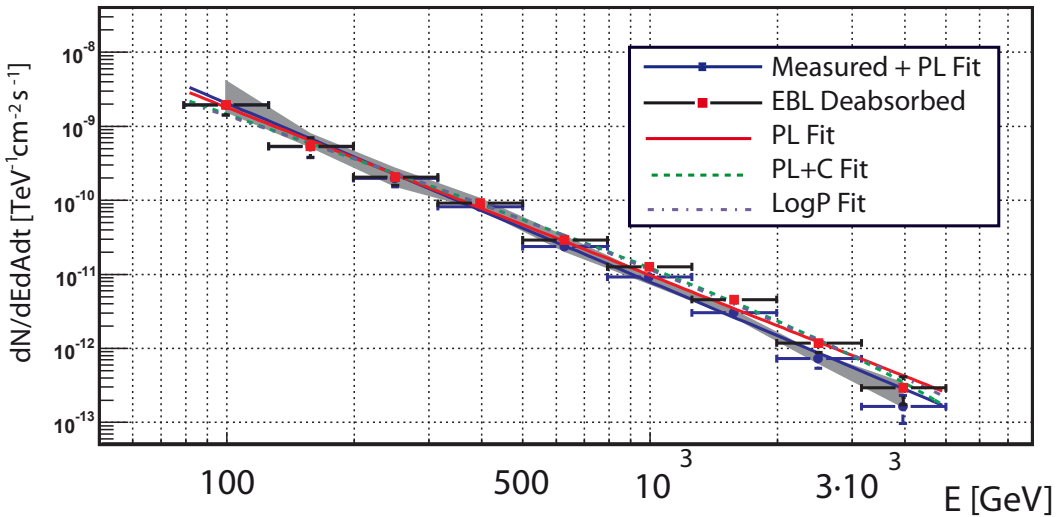


Figure 11.5: Differential energy spectrum for Mrk 501 during the 2009 MWL campaign before (blue) and after (red) correcting for EBL absorption. Measured spectrum was fit to a PL (Eq. 9.1), log-P (Eq. 9.4) and PL+C (Eq. 9.5) fits were performed to the EBL de-absorbed spectrum (solid red, blue dot-dashed and green dashed curves, respectively). Curved fits (log-P and PL+C) describe better the data than simple power law fits, according to a likelihood ratio test. The gray area represents a estimation of the systematics from the different analysis methods (see text for details).

achieved selecting those pointings (dwells in RXTE terminology) inside a  $\pm 0.1$  day time window common to MAGIC measurements, averaging the resulting counts. Nevertheless it came out that due to the low flux state of the source, the distribution of resulting fluxes was largely governed by the uncertainties, being the magnitudes smaller than the corresponding uncertainties. Therefore, no correlation study was performed. An even worse case happened with the measurements of Mrk 501, where even the day-by-day X-ray lightcurve is largely governed by the uncertainties, as can be seen from the middle panel of Figure 11.4.

For both sources the optical and VHE fluxes do not seem to be correlated during their respective campaigns. To more carefully investigate any possible correlation, a similar study as those in Chapters 9 and 10 was performed. No correlation seems to be present for Mrk 421, with a Pearson's r coefficient of  $0.07 \pm 0.14$ . The comparison of the measured PDF with the full correlated and uncorrelated PDFs did not give valuable information in this case, the uncertainties being too large. In the case of Mrk 501, a Pearson's r of  $0.36 \pm 0.23$  was obtained. Again, the comparison of the PDFs yield too large uncertainties, and therefore no conclusion can be drawn from their comparison.

## 11.4 Discussion

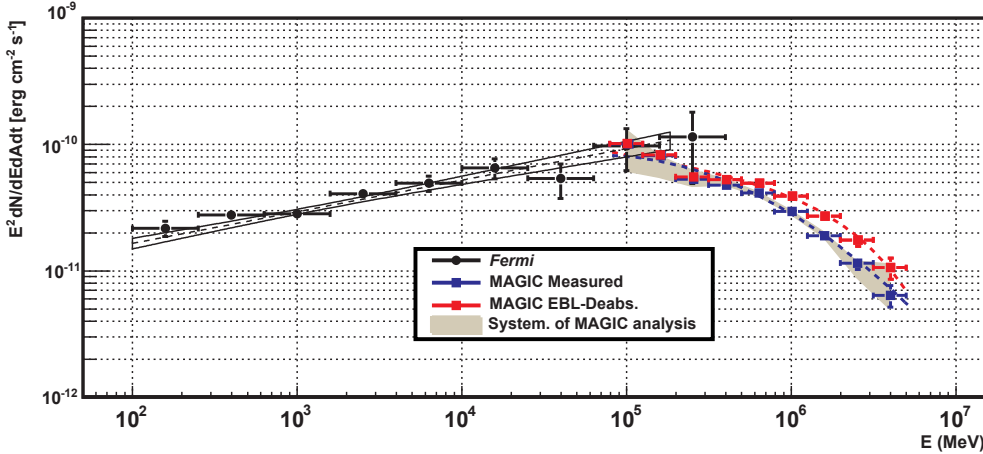


Figure 11.6: Differential energy spectrum in the (0.1–5000) GeV energy range for Mrk 421 during the 2009 MWL campaign. HE data from *Fermi LAT* [?], simultaneous to those from MAGIC, are shown in black, being the area inside the gray lines the  $1-\sigma$  uncertainty contour area. The Fermi spectrum can be described by a pure power law with photon index  $1.79 \pm 0.02$  [Pan09]. The MAGIC data are shown before (blue) and after (red) correcting for EBL absorption. The MAGIC spectrum was fit to a PL+C (Eq. 9.1). It is important to remark that both instruments have overlapping points in the 80–400 GeV region.

## 11.4 Discussion

MAGIC observed the blazars Mrk 421 y Mrk 501 during low states of the sources in the VHE band. The low energy threshold of MAGIC allowed to perform simultaneous measurements with those carried out with the *Fermi LAT* detector. The overlap region around  $\sim 100$  GeV had been *terra incognita* before the observations allowed by these two instruments.

Figure 11.6 shows the higher energy region of the SED of Mrk 421, as measured by both instruments, from 0.1 GeV to 5000 GeV. The data from *Fermi LAT* and MAGIC match in their overlap energies (80–400) GeV, indicating the presence of a maximum of the SED in this area. Moreover, log-P fits (Eq. 9.4) of the MAGIC spectrum allowed to estimate the peak position to be located around 50–100 GeV (see Table 11.4 for details).

In order to compare the spectrum of Mrk 421 with previous observations, Figure 11.7 shows the EBL-deabsorbed spectrum of Mrk 421 during this MWL campaign, together with the spectra taken between 1998 and 2008, including the pedestal and high state spectrum of 2006 MWL campaign shown in Chapter 9. The spectrum reported here represents, together with the one measured with MAGIC during 2004–2005, one of the lowest flux states ever measured in VHE for Mrk 421. These two spectra show a similar behavior, being the one presented here a slightly harder one. Note the different behavior of the 2006 low state data sample, that indicates a harder spectral shape for a comparable flux level. As explained in section 10.6, evidences of an increase of the GeV-TeV peak energy

## 11.4 Discussion

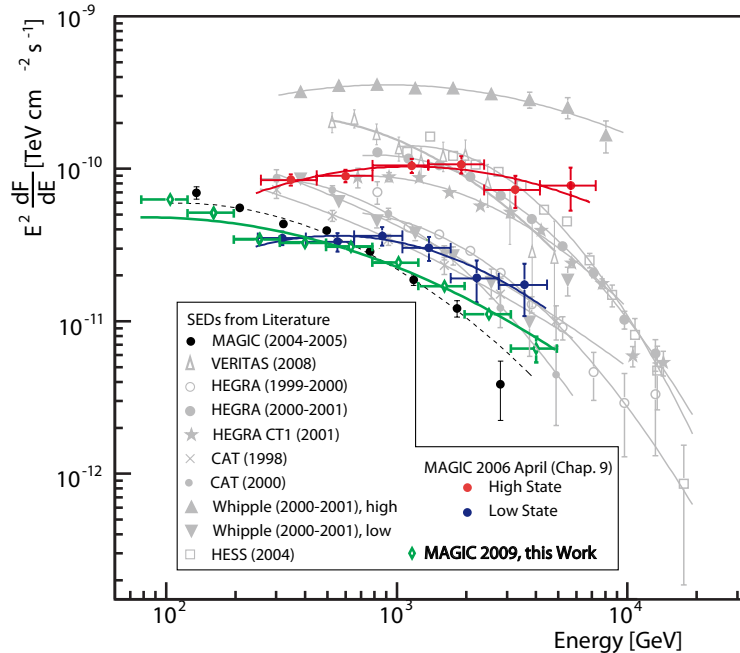


Figure 11.7: *EBL de-absorbed historical spectra and log-P fits of Mrk 421 (see [Alb07c] for references) along with the 2009 MWL campaign spectrum (green). The high (red) and low (blue) state spectra from the MAGIC 2006 April campaign described in Chapter 9 and the flare spectrum of [Don09] are also shown. The green solid line is the result of a fit using eqn. 9.5. Note that the historical data were de-absorbed using the model of [PBS05], while for this work [FRV08] was used.*

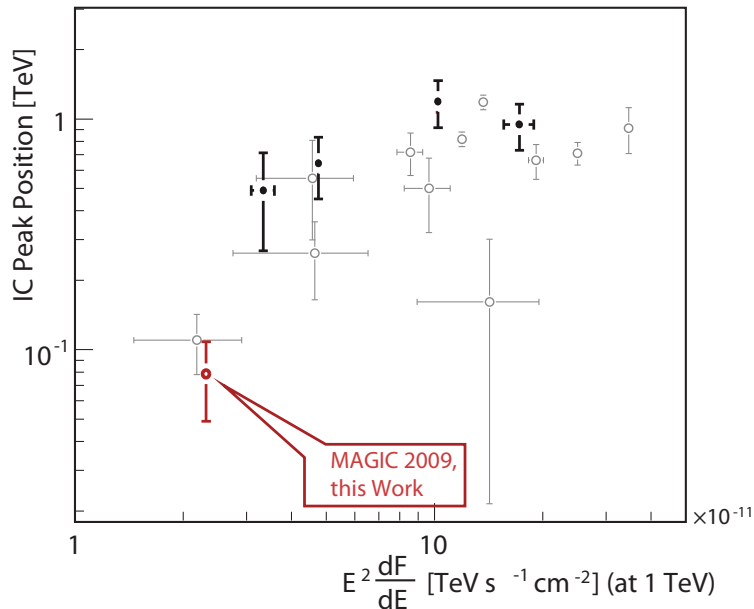


Figure 11.8: Derived peak position of Mrk 421 in different epochs using the log-P fit (eqn. 9.4) versus flux at 1 TeV. 2009 data peak is shown in red, 2006 MAGIC results from Chapter 9 are shown in solid black circles, and historical data peak positions, taken from ([Alb07c]), are shown in gray.

## 11.4 Discussion

---

in the SED of this source with rising flux level have been found, what is also predicted if the VHE radiation is due to SSC mechanisms. The observed peak of the data presented in this Chapter supports this scheme, as can be seen in Figure 11.6.

Figure 11.9 shows the higher energy region of the SED of Mrk 501, as measured by *Fermi* LAT and MAGIC. The *Fermi* LAT data were obtained from the 5.5 month measurements reported by the *Fermi* LAT collaboration [Feg09], containing measurements from MJD 54682 to MJD 54842, and from the *Fermi* LAT 1FGL [The10], obtained by expanding the previous observations up to MJD 55016, covering a 11 month interval. The measurements from [Feg09] were carried out a few months before the MAGIC ones, but a fraction of the measurements on the 1FGL are partially simultaneous to those from MAGIC, that were performed from MJD 54981 to MJD 55025. The data from Fermi LAT and MAGIC match well in their overlapping energies (around 100 GeV), and additionally indicate that a maximum in the SED should not be far from those energies. The curved fits of the MAGIC data allow to estimate the position of this SED maximum. Table 11.5 shows the derived peak position for different fits. Even if the peak position cannot be determined with a high accuracy, these results indicate that it should be located at energies between 40 and 400 GeV. As mentioned before, it is a theoretically expected behavior for HBLs to exhibit a maximum in this region. The results presented here are a clear confirmation of this prediction.

Figure 11.10 shows the measured spectrum of Mrk 501 during the MWL campaign analyzed here, together with the VHE spectra taken between 1997 and 2006. The spectrum reported here represents a low flux state of the source. The 2009 spectrum is flatter than the one measured by MAGIC in 2006, and resembles a similar spectral shape, but with a lower flux, similar to the low and medium states measured in 2005. Within the SSC framework this difference in flux for comparable spectral shapes can be caused by, e.g., a lower number of electrons with the same energy distribution as in the high-flux case.

Figure 11.11 shows the broadband SEDs of Mrk 421 using the measurements from the whole sample of instruments of the 2009 MWL campaign (specified in Table 11.6). This SED was presented in the 2009 Fermi Symposium [Pan09], where the VHE data points are taken from the analysis performed by Diego Tescaro mentioned before. The SED shown in this Figure constitutes the most complete SED ever determined for Mrk 421. A preliminary modeling of this detailed SED was performed in [Pan09], being well described by one-zone SSC models. The reduced data from the different instruments during the MWL campaign was not yet in the final state when this thesis was written. In the following months the broad-band spectra of both Mrk 421 and Mrk 501 from these MWL campaigns will be made public (publications are in preparation).

Historically, multiwavelength campaigns have observed correlation between the X-ray and VHE emission in both Mrk 421 (e.g., [Bl05]) and Mrk 501 (e.g.,

## 11.5 Summary

---

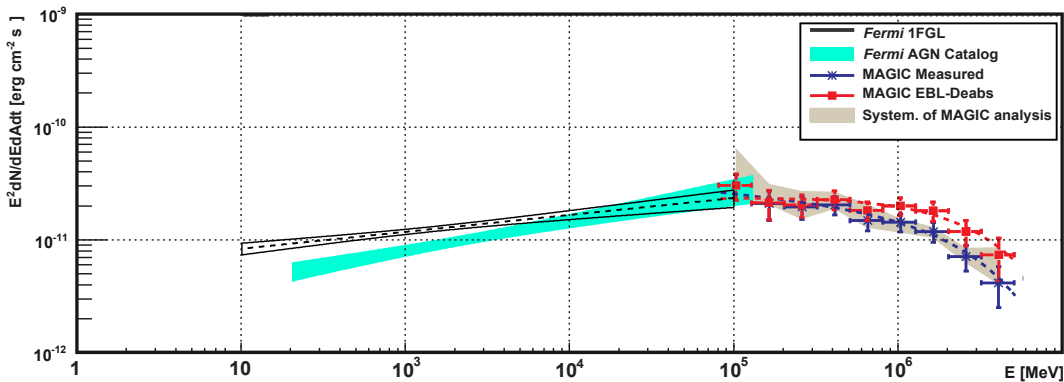


Figure 11.9: *Differential energy spectrum in the (0.1-5000) GeV energy range for Mrk 501 in 2009. The HE data from Fermi LAT is from the Fermi AGN catalog, obtained in a 5.5 month interval, from MJD 54682 to MJD 54842 (pale blue area) and from the 1FGL, obtained expanding the previous observation another 5.5 months, to a total from MJD 54682 to MJD 55016 (black dashed lines and area). Both Fermi areas denote the 1- $\sigma$  uncertainty region. MAGIC data, partially simultaneous to 1FGL measurements (from MJD 54981 to MJD 55016) is shown before (blue) and after (red) correcting for EBL absorption. MAGIC spectrum was fit to a PL+C (Eq. 9.5). Both instruments have a small overlapping region around 100 GeV region.*

[Alb07e]). The low state of the source in the X-ray band did not allow to perform a correlation study with the RXTE/ASM data. On the other hand, no evidences of correlation between VHE and optical fluxes were found.

## 11.5 Summary

MAGIC VHE measurements from two bright blazars, Mrk 421 and Mrk 501 have been presented in this chapter. These measurements were performed in the context of intense MWL campaigns carried out in the first half of 2009. During the observations both sources exhibited low flux states. Clear intra-night variability was found for both sources, but Mrk 421 only exhibited a flux level higher than one Crab unit (for  $E > 200$  GeV) for one night, and Mrk 501 never exceeded the Crab Nebula flux (for  $E > 200$  GeV).

The MWL campaign results presented here have allowed to study in detail the complete HE to VHE spectrum of two of the brightest known TeV blazars. Despite of the low state that these sources were exhibiting during the campaign, a gap-less SED over an energy region that covers almost 6 orders of magnitude has been provided. The peak positions of both blazars was determined to be around 100 GeV for these observations, giving further evidences of a relation of the peak position with the flux state of these sources.

## 11.5 Summary

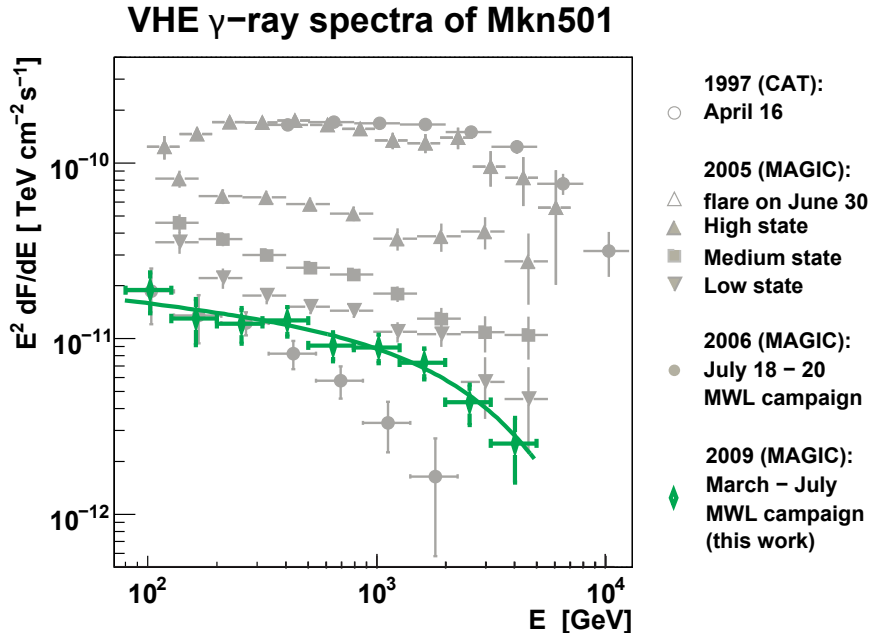


Figure 11.10: Measured historical spectra of Mrk 501 (see [And09c] for references) along with the 2009 MWL campaign spectrum (green). The green solid line is the result of a fit using eqn. 9.5.

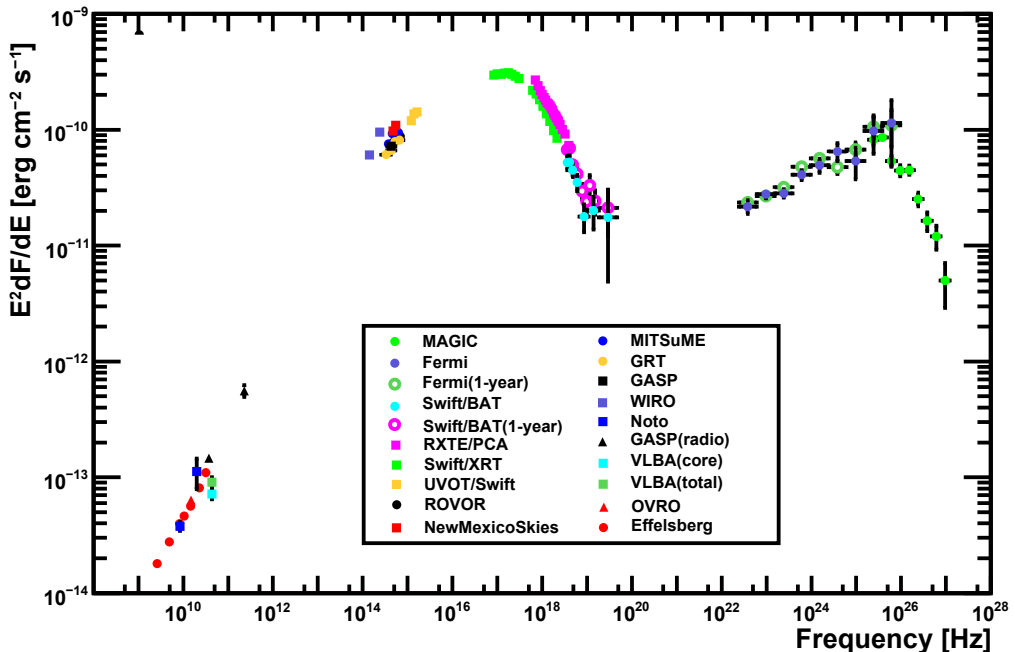


Figure 11.11: SED of Mrk 421 averaged over the 2009 MWL campaign, from [Pan09]. The flux from the host galaxy and nearby stars was subtracted, and optical and X-ray measurements were corrected from galactic extinction. The MAGIC data points, from the analysis performed by Diego Tescaro (compatible to the results of this thesis), were de-absorbed with the extragalactic background light model discussed in [FRV08].

## 11.5 Summary

---

Table 11.4: Mrk 421 fit results.

| Used Fit         | $E_0$ [TeV] | $f_0$             | $\alpha$        | $\beta$           | $\chi^2_{\text{red,fit}}$ | Likelihood | $E_{\text{peak}}$ [TeV] |
|------------------|-------------|-------------------|-----------------|-------------------|---------------------------|------------|-------------------------|
| PL, measured     | 1.0         | $0.163 \pm 0.004$ | $2.64 \pm 0.02$ |                   | 47.4/7                    |            |                         |
| PL+C, measured   | 0.3         | $4.45 \pm 0.17$   | $2.32 \pm 0.06$ | $2.5 \pm 0.5$ TeV | 10.5/6                    | 99%        | N/A                     |
| log-P, measured  | 0.3         | $4.10 \pm 0.12$   | $2.44 \pm 0.05$ | $0.33 \pm 0.07$   | 13.9/6                    | 99%        | $0.06 \pm 0.02$         |
| PL, EBL-deabs    | 1.0         | $0.214 \pm 0.005$ | $2.49 \pm 0.02$ |                   | 39.9/7                    |            |                         |
| PL+C, EBL-deabs  | 0.3         | $4.75 \pm 0.17$   | $2.20 \pm 0.07$ | $2.9 \pm 0.7$ TeV | 12.1/6                    | 99%        | N/A                     |
| log-P, EBL-deabs | 0.3         | $4.41 \pm 0.12$   | $2.31 \pm 0.05$ | $0.28 \pm 0.07$   | 17.4/6                    | 99%        | $0.08 \pm 0.03$         |

Table 11.5: Mrk 501 fit results.

| Used Fit         | $E_0$ [TeV] | $f_0$             | $\alpha$        | $\beta$           | $\chi^2_{\text{red,fit}}$ | Likelihood | $E_{\text{peak}}$ [TeV] |
|------------------|-------------|-------------------|-----------------|-------------------|---------------------------|------------|-------------------------|
| PL, measured     | 1.0         | $0.069 \pm 0.008$ | $2.46 \pm 0.06$ |                   | 6.3/7                     |            |                         |
| PL+C, measured   | 0.3         | $1.58 \pm 0.18$   | $2.13 \pm 0.16$ | $3.2 \pm 1.6$ TeV | 2.0/6                     | 95%        | N/A                     |
| log-P, measured  | 0.3         | $1.49 \pm 0.16$   | $2.23 \pm 0.14$ | $0.26 \pm 0.16$   | 3.4/6                     | 90%        | $0.11 \pm 0.09$         |
| PL, EBL-deabs    | 1.0         | $0.097 \pm 0.012$ | $2.27 \pm 0.06$ |                   | 6.4/7                     |            |                         |
| PL+C, EBL-deabs  | 0.3         | $1.73 \pm 0.20$   | $1.97 \pm 0.16$ | $3.5 \pm 1.9$ TeV | 2.8/6                     | 93%        | <0.70                   |
| log-P, EBL-deabs | 0.3         | $1.61 \pm 0.17$   | $2.07 \pm 0.15$ | $0.27 \pm 0.16$   | 4.4/6                     | 83%        | $0.21 \pm 0.17$         |

Results of log-P and PL+C fits before and after EBL de-absorption.  $f_0$  is given in units of  $10^{-10} \text{TeV}^{-1} \text{cm}^{-2} \text{s}^{-1}$ ,  $\alpha$  and  $\beta$  are the fit parameters as stated in the text, and ‘‘Likelihood’’ denotes the probability of a likelihood ratio test of the fit vs the PL fit. The peak energy is  $E_{\text{peak}} = E_0 \cdot 10^{(2-\alpha)/(2\beta)}$  for the log-P and  $E_{\text{peak}} = (2-\alpha) \cdot \beta$ , if  $\alpha < 2$  for the PL+C fits (otherwise no peak energy is calculated).

## 11.5 Summary

---

Table 11.6: Instruments that participated in the MWL campaigns.

| Energy band        | Instrument | Home webpage  |
|--------------------|------------|---|
| Radio              | Effelsberg | <a href="http://www.mpifr.de/english/radiotelescope/index.html">http://www.mpifr.de/english/radiotelescope/index.html</a>       |
|                    | GASP       | <a href="http://www.to.astro.it/blazars/webt/">http://www.to.astro.it/blazars/webt/</a>   |
|                    | Medicina   | <a href="http://www.med.ira.inaf.it/index_EN.htm">http://www.med.ira.inaf.it/index_EN.htm</a>                                   |
|                    | Metsahovi  | <a href="http://www.metsahovi.fi/en/">http://www.metsahovi.fi/en/</a>   |
|                    | Noto       | <a href="http://www.noto.ira.inaf.it/">http://www.noto.ira.inaf.it/</a>   |
|                    | RATAN-600  | <a href="http://w0.sao.ru/ratan/">http://w0.sao.ru/ratan/</a>   |
|                    | VLBA       | <a href="http://www.vlba.nrao.edu/">http://www.vlba.nrao.edu/</a>   |
|                    | OVRO       | <a href="http://www.ovro.caltech.edu/">http://www.ovro.caltech.edu/</a>   |
|                    | GASP(KVA)  | <a href="http://www.to.astro.it/blazars/webt/">http://www.to.astro.it/blazars/webt/</a>   |
|                    | MITsuME    | <a href="http://www.hp.phys.titech.ac.jp/mitsume/index.html">http://www.hp.phys.titech.ac.jp/mitsume/index.html</a>             |
| X-rays             | Swift-UVOT | <a href="http://heasarc.gsfc.nasa.gov/docs/swift/swiftsc.html">http://heasarc.gsfc.nasa.gov/docs/swift/swiftsc.html</a>         |
|                    | RXTE       | <a href="http://heasarc.gsfc.nasa.gov/docs/xte/rxte.html">http://heasarc.gsfc.nasa.gov/docs/xte/rxte.html</a>                   |
|                    | Swift-XRT  | <a href="http://heasarc.gsfc.nasa.gov/docs/swift/swiftsc.html">http://heasarc.gsfc.nasa.gov/docs/swift/swiftsc.html</a>         |
|                    | Swift-BAT  | <a href="http://heasarc.gsfc.nasa.gov/docs/swift/swiftsc.html">http://heasarc.gsfc.nasa.gov/docs/swift/swiftsc.html</a>         |
|                    | WIRO       | <a href="http://physics.uwy.edu/~chip/wiro/wiro.html">http://physics.uwy.edu/~chip/wiro/wiro.html</a>                           |
| HE $\gamma$ -rays  | Fermi      | <a href="http://www-glast.stanford.edu/index.html">http://www-glast.stanford.edu/index.html</a>                                 |
|                    | MAGIC      | <a href="http://wwwmagic.mppmu.mpg.de/">http://wwwmagic.mppmu.mpg.de/</a>   |
|                    | VERITAS    | <a href="http://veritas.sao.arizona.edu/">http://veritas.sao.arizona.edu/</a>   |
| VHE $\gamma$ -rays | Whipple    | <a href="http://veritas.sao.arizona.edu/content/blogsection/6/40/">http://veritas.sao.arizona.edu/content/blogsection/6/40/</a> |

# Chapter 12

## Concluding Remarks

The work presented in this thesis can be divided in two parts, one being related to software development and maintenance, and the other to VHE sources analysis and interpretation. Regarding the first part, details of the MAGIC data quality check and on-site analysis programs, developed and maintained during several years by a team composed by the author and other UCM MAGIC group members, have been provided. For the second part, detailed multiwavelength studies of VHE blazars have been performed, expanding the actual knowledge of this kind of objects.

### 12.1 Software work

One of the goals of the MAGIC-I telescope design was to lower the energy threshold of the previous generation of IACTs, improving at the same time the detection sensitivity. A second telescope was added to the MAGIC experiment in 2009, designed to work in stereoscopic mode together with the first MAGIC telescope, and expecting to lower the accessible energy while improving the detector sensitivity. In order to reach a low energy threshold, the detection of faint air showers is needed, requiring a high trigger rate of the order of 300 Hz. In the case of the analogue sum trigger observations, the mentioned rate is doubled. Therefore a large data stream must be recorded and analyzed.

The MAGIC experiment is composed by a complex set of subsystems. In order to optimize the efficiency of MAGIC telescopes, it is important that all these systems are monitored in a daily basis. The MAGICDC software presented in this work inspects if any subsystem failure happened during the data taking night, allowing a fast reaction to hardware malfunctions. The MAGICDC program has kept growing since its installation in January 2004 [De 08], increasing the number of subsystems to check. During these years, MAGICDC has allowed to quickly

## 12.2 Analysis of blazars

---

detect many of the hardware problems that MAGIC had, and thus reduce the time required to solve them.

To manage and reduce the high data volume produced by the MAGIC telescopes, an on-site data reduction system was developed and installed in the computing cluster at MAGIC site. The QOSA software performs a fast but complete data reduction, allowing calibrated and image parameter files to be quickly transferred to the MAGIC Collaboration data-center at PIC. The produced files are used for the final steps of MAGIC analysis results. To be able to quickly reduce the large data volumes stored with MAGIC, the MAGICDC code has been developed in a way that the processing of the files is performed with a high degree of parallelization. The data volume has increased considerably since the installation of the first version of the on-site analysis [DO06, De 08, Oya06]: major hardware updates like the installation of the MUX FADCs, the use of the sum-trigger, and the incorporation of MAGIC-II have increased dramatically the amount of data stored every night. The actual version of QOSA presented in this work is the result of the evolution of the original code that, together with the update of the needed computing and storage capacity, has successfully adapted to cope with the mentioned hardware changes.

## 12.2 Analysis of blazars

Since measurements of the EGRET experiment discovered blazars as sources of high energy  $\gamma$ -rays, the search for emission of VHE radiation from these sources has been a major goal for ground-based  $\gamma$ -ray astronomy. The first discovery of a blazar emitting at VHE energies (Mrk 421) was performed with the Whipple telescope in 1992 [Pun92]. At the moment this thesis was written, 38 extragalactic sources had been established as VHE emitters, including 30 blazars. After the first 11 months of measurements of *Fermi* LAT, the noteworthy amount of 689 sources has been identified as HE blazars [The10], (compared to those 66 identified as blazars from EGRET results after four years of observations [Har99]). Many of the *Fermi* extragalactic sources are considered promising candidates for ground-based VHE observations.

The known VHE blazars are rather nearby sources because VHE photons are strongly attenuated by interaction with the EBL light, still poorly modeled. The EBL restricts the accessible region to relatively nearby sources, or to those relatively distant sources in high states of emission, as happened with the MAGIC observations of 3C 279 [Col08]. Most of the VHE blazars are of the HBL type subclass of BL Lac objects. Other blazars types (LBL and FSRQ) have been detected by IACTs even if they are not so bright in the VHE region.

## 12.2 Analysis of blazars

---

The SED of blazars is characterized by a “two bumps” structure, the higher energy one being located in the VHE region. The SED features from blazars are usually interpreted by two families of models: leptonic models [MGC92, Kra04, BC02, TMG98] that assume that the observed  $\gamma$ -ray emission is due to the inverse Compton emission from the accelerated electrons scattering photons, either previously produced in the synchrotron processes (SSC models) or ambient photons (EC models), and those hadronic models [MB92, Bed93, MP01, Aha00] that explain that the VHE radiation originated from proton (or other nuclei) initiated cascades.

This thesis adds information to the still limited current knowledge of VHE blazars, discussing the results from four MWL campaigns that included MAGIC-I telescope measurements. The campaigns consisted of the observation of Mrk 421 in April and June 2006, the observation of 1ES 1426+428 in May-June 2008, and the observation of both Mrk 421 and Mrk 501 in the first half of 2009.

In April and June 2006, MAGIC observed the HBL Mrk 421 during 9 nights, with some simultaneous X-ray/soft  $\gamma$ -ray observations with *XMM-Newton*, *Suzaku* and INTEGRAL satellites, UV observation with the OM of the *XMM-Newton* satellite, and optical observation with the KVA telescope. Additionally, quasi-simultaneous observation were performed with the Whipple telescope in the VHE band. Even if the source was not in a particularly high state, a clear signal from the source was detected for every observation night.

A sequence of mild flares was detected during the week from April 22 to 30, 2006, showing the maximum during April 27, with a flux of  $\approx 2.0$  Crab units. During three observation nights high fluxes were recorded, in which, however, no variability could be measured. Rather hard spectral indices were found in these nights. Indication of spectral evolution with increasing fluxes were observed, as expected by SSC models. Mrk 421 was behaving quite differently during these observations compared to previous observations, allowing to determine the VHE peak positions even in the lower flux states. The derived peak positions were found to be systematically higher than historical measurements for comparable flux levels, what was interpreted, within the SSC framework, as caused by a different number of electrons with the same energy distribution. During the night of April 29, 2006, with a non particularly high flux of  $\approx 0.65$  Crab units, clear intra-night variability with a flux-doubling time of  $36 \pm 10$  minutes was observed.

The MWL observation performed together with Whipple and *XMM-Newton* in April 29–30, 2006 were studied in parallel with others performed in May 7, 2008 which share similar characteristics, and were obtained in the same observation program. Contrary to historical observations, no clear X-ray and VHE correlation was found when studying the sample composed of MAGIC, Whipple and VERITAS data simultaneous to *XMM-Newton* measurements, but a correlation seems to be present in the MAGIC 2006 observations and an anti-correlation

## 12.2 Analysis of blazars

---

during the VERITAS 2008 observations. SSC one-zone models were able to correctly describe the data of both campaigns, but requiring relative large Doppler factors ( $\delta \geq 45$ ). Contrary to what is expected in SSC models, having the source a higher flux in 2008 than in 2006, it's both SED peaks are located at lower energies than in 2006.

During the INTEGRAL-triggered MWL campaign in June 2006 one night observation of Mrk 421 was performed, complementing the three-night observations conducted by the Whipple telescope four days later. Taking the MAGIC and Whipple results together, a variability of Mrk 421 also during the INTEGRAL observations is evident. The energy coverage of the Whipple telescope spectrum ( $\Delta E \approx 600$  GeV) was not sufficient to assess any spectral evolution by comparing it to the MAGIC spectrum ( $\Delta E \approx 2$  TeV).

MAGIC observed 1ES1426+428 in 2008, during a low state of emission in the VHE band. Upper limits of the order of 2.5% of the Crab Nebula flux were derived, indicating that the source was in a much lower state than during historical measurements (4–10% Crab Nebula flux). Simultaneous X-ray and Optical/UV observation were performed with *Suzaku*, *Swift* and KVA. The corresponding X-ray spectrum is hard, with  $\alpha > 2$ , indicating that the synchrotron peak is located at energies lower than 1 keV. The comparison of VHE and X-ray measured state with historical data points to a correlation of the VHE activity with the hardening of the X-ray spectrum and the corresponding shift of the synchrotron peak to higher energies. Some indication of correlation between the X-rays and U and UVW1 band were found in these data.

During the first half of 2009, MAGIC VHE measurements were made for both Mrk 421 and Mrk 501 blazars. These measurements were performed in the context of intense MWL campaigns, including simultaneous measurements with the *Fermi* LAT detector. A clear night-by-night variability was found for both sources. Mrk 421 only exhibited a flux level higher than the Crab Nebula (for  $E > 200$  GeV, up to 130% Crab Nebula Flux) for one night, and Mrk 501 never exceeded the Crab Nebula flux (for  $E > 200$  GeV, up to 65% of the Crab Nebula Flux). These results allowed to study the spectral features of two of the brightest TeV blazars in a gap-less region in the SED of these sources of almost 6 orders of magnitude. The higher energy peak positions were determined to be around 100 GeV, giving further evidences of a relation of the peak position with the flux state.

Summarizing, in this thesis, simultaneous MWL observations of known blazars were performed. These MWL observation are important to understand and to be able to distinguish between different emission mechanisms. For example, in SSC models a strong correlation between X-ray and VHE emission is expected, as well as a correlation between the optical/UV emission and the X-ray one. During historical measurements, mostly conducted in high states of the sources, a clear X-ray and VHE correlation was detected [Bł05, Alb07e]. In the correlation studies

### 12.3 Outlook

---

performed in this thesis, where the fluxes of the sources were not particularly high, it was not possible to determine a general rule regarding to the correlations, and thus giving further indications of the complex systems that blazars are. On the other hand, the new measurements of Mrk 421 and Mrk 501, performed together with MAGIC and *Fermi* allowed to fill a gap existing in the energies around 1–100 GeV for these well known blazars, allowing to measure their higher energy bump position in the SED even in the source’s low states.

Despite the new information about blazars exposed in this thesis, these AGN are still far from being understood. In general, the origin of the  $\gamma$ -ray photons coming from AGN is not clear. The different behaviors regarding the X-ray and VHE flux correlations, the changes in the fluxes and in the spectral shapes indicate that complex mechanisms operate in the AGN, with the possibility that both leptonic and hadronic complex processes are happening simultaneously. It is also not clear how do jets form, and what mechanisms cause them to become active when they go into flaring states.

## 12.3 Outlook

Both the on-site analysis and the data quality check software experienced upgrades while this thesis was being written. The data quality check software competences were assumed by the Croatian Consortium of MAGIC since the beginning of 2010. The process of finishing the installation of the remaining items of the MAGIC-II data check extension, consisting mainly in the subsystems check, was being carried out at the moment this thesis was written. Additionally, it was planned to develop some checks of the stereo performance of the MAGIC system.

Regarding the quick on-site analysis software, the UCM MAGIC group recently installed the MAGIC-II and stereo extensions of the program. Thanks to these extensions, reduced the data of both MAGIC telescopes were transferred regularly to PIC. At the moment this thesis was written there were plans to install another process in QOSA, that would perform a  $\gamma$ /hadron separation and energy estimation of the data, allowing to automatically calculate the significance of the detected excess events from the observed sources.

Continuous observations of bright blazars are important to determine the SEDs in different flux states because source activity states cannot be predicted in advance. By increasing the number of observations of these sources, it might be possible to build general rules to apply during the different states of activity. In that sense, *Fermi* is a very useful tool, but further coordinated simultaneous observations from the radio to the VHE bands can expand the existing wide-range SEDs. Additionally, true simultaneous observations of sources during intense flaring states, as performed in [Alb07e], will allow to study very short term

## 12.3 Outlook

---

variability, that may provide information of both internal processes happening in these sources as well as cosmological (EBL) and fundamental physics implications (for example quantum gravity studies [MJ08]).

In particular, the following aspects may contribute in the future to expand the existing knowledge of blazars:

- In the short term, further observations from the *Fermi* satellite, expanding the 1FGL results, together with the IACT projects upgrades (second phases of MAGIC and HESS, with improved sensitivity and lower energy thresholds), will provide complete spectra from MeV to TeV energies, as it was done with the 2009 campaign in this thesis for Mrk 421 and Mrk 501, for more blazars and in different states of activity. The new projects will certainly increase the number of known  $\gamma$ -ray blazars. For example, the mentioned second phases of MAGIC and H.E.S.S. are expected to discover about 100 sources among the blazar objects. The *Fermi* satellite has already detected more than 600 blazars after 11 months of observations, mainly LBLs and FSRQs. Such a number of objects may allow to perform systematic studies to find answers about the fundamental physics of blazars. It is expected that a fraction of the new *Fermi* blazars will be also good candidates to be VHE emitters. Sensitive measurements on this energy range may make possible to distinguish between emission of hadronic or leptonic origin, because in the former case, the spectrum may have a characteristic bump around 100 MeV and a power law for the higher energy range, arising from the decay of the neutral pions. If sources of hadronic origin are identified, it will be the first clear evidence of extra-galactic sites of cosmic-ray acceleration. In addition,  $\gamma$ -ray emission should be accompanied by neutrinos in the case of hadronic origin. Such sources can be interesting targets for projects like IceCube. Discovery of hadronic origin sources can therefore provide an important guideline for a new “high-energy neutrino astronomy”.
- The *Fermi* LAT detector covers the whole sky in 3 hours thanks to its large field of view. Hence, it is continuously observing sources in the  $\gamma$ -ray range. The long term light curves, together with the monitoring campaigns of bright blazars in the VHE and X-ray bands will allow to conduct periodic studies of the emissions. Discovery of periodicities in the light curves may give us new insight into the jet and black-hole system (e.g., precession of the jet, binary black-hole system, etc.).
- Finally, the Cherenkov Telescope Array (CTA) and the Advanced Gamma Imaging System (AGIS) projects are expected to greatly improve both the sensitivity and energy range of ground detectors. Both CTA and AGIS will be able to perform detailed studies in a broad energy range, with a factor

### 12.3 Outlook

---

10 improved sensitivities with respect to actual IACTs, reaching to the 1 milliCrab level. With these sensitivities it will be possible to investigate in detail short term variability of blazars, and to enable more detailed studies of the EBL features, hence allowing to better reproduce the intrinsic spectra of the extragalactic sources. In the X-ray band, the launch of the Monitor of All-sky X-ray Image (MAXI) [Mat09] in 2009 July 16, will soon allow sensitive monitoring of blazars in the 0.5 to 30 KeV energy band. Additionally, the International X-ray Observatory (IXO) and the Extended Roentgen Survey with an Imaging Telescope Array (eROSITA) will provide further X-ray coverage when they come into operation.

As a conclusion, the near future will be a very promising era for the study of VHE  $\gamma$ -ray extragalactic sources. In short and medium timescales it is expected that the actual population of known TeV blazars will be expanded and that more detailed studies of the already known ones will be performed, perhaps allowing to unravel the mystery that has surrounded these sources since their discovery.

# Appendix A

## Data quality check plots

The whole sample of plots produced by the data quality check is shown in this appendix. For simplicity, only MAGIC-I plots will be shown, being analogous those of MAGIC-II . See Chapter 7 for a full description of the MAGICDC software.

### A.1 Subsystems data check

See section 7.3.2 for further details.

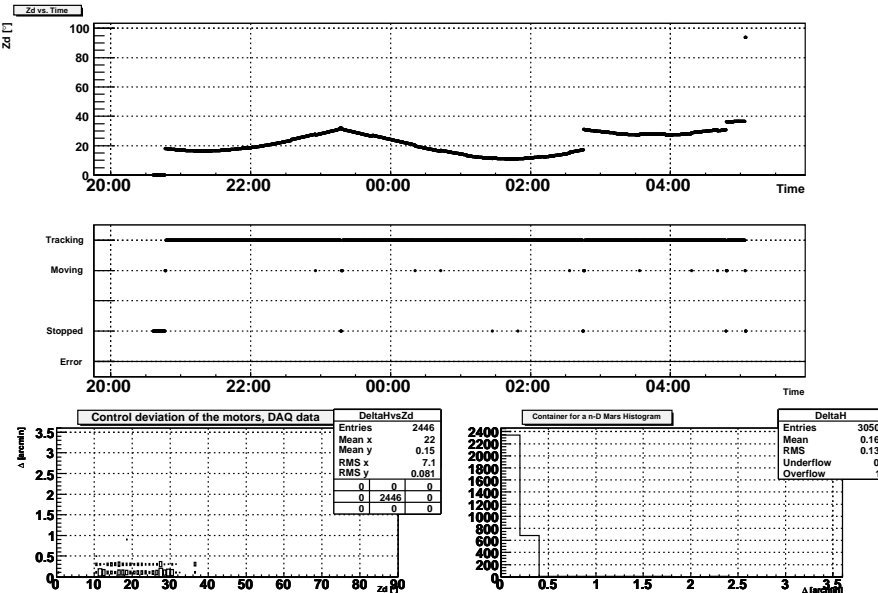


Figure A.1: *Drive system report plots. From top to bottom: the zenith angle of the telescope pointing position versus time; the status reported by the system versus time; and the control deviation of the motors (during data taking) versus the zenith angle of pointing position (on the left). The distribution of the control deviation in units of arc-minutes of the motors is shown on the lower right panel).*

## A.1 Subsystems data check

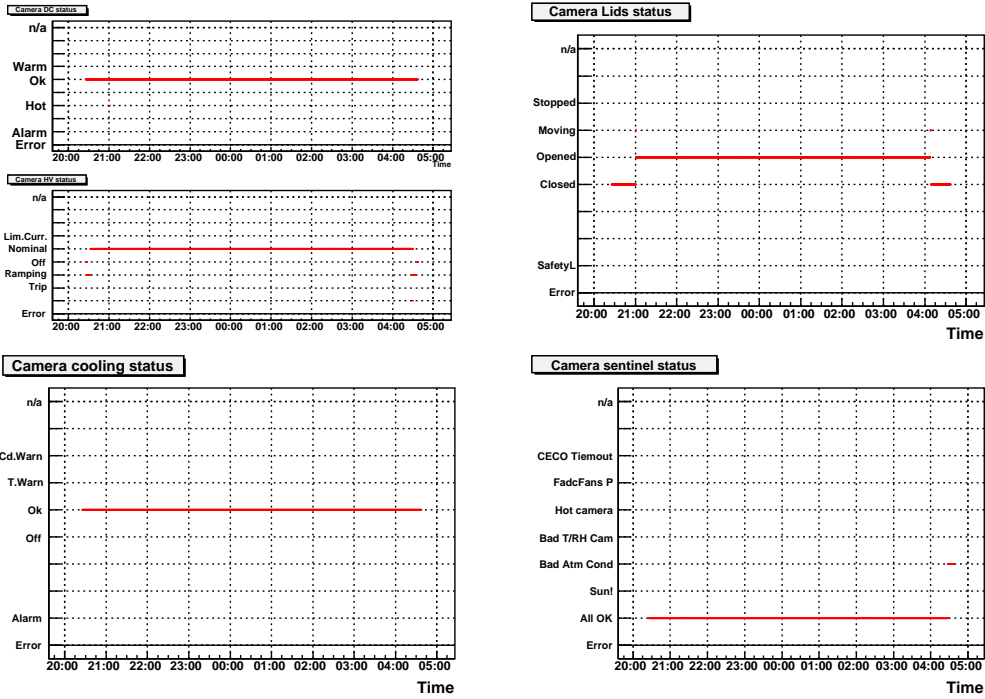


Figure A.2: Camera status report plots. Top left: PMT high voltages and DCs. Top right: camera lids. Bottom left: cooling system. Bottom right: camera sentinel.

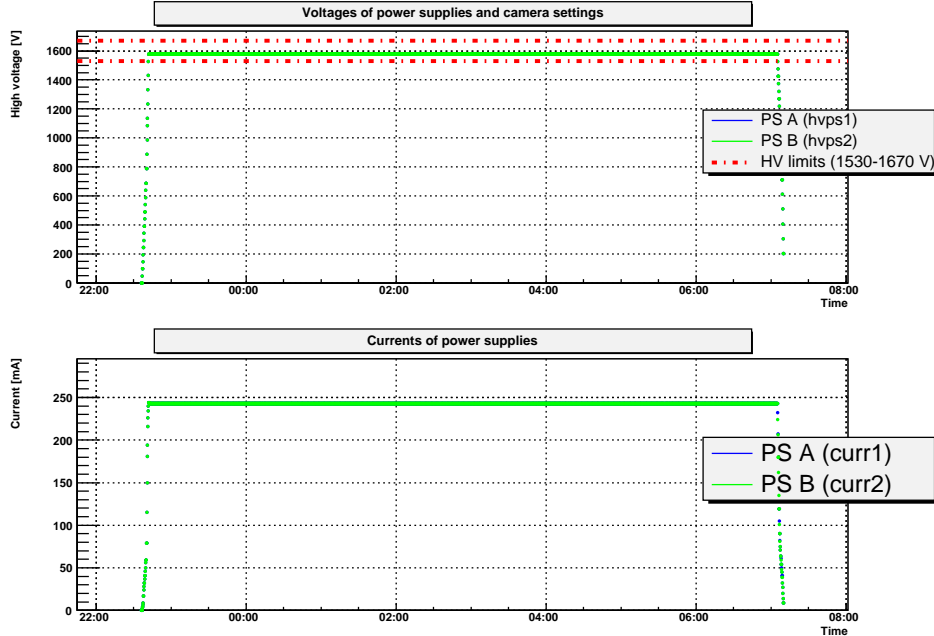


Figure A.3: Power supplies report plots. High voltage and direct current from the power supplies (A, in blue and B, in green). The red-dotted lines are the corresponding limit values for the current HV settings.

## A.1 Subsystems data check

---

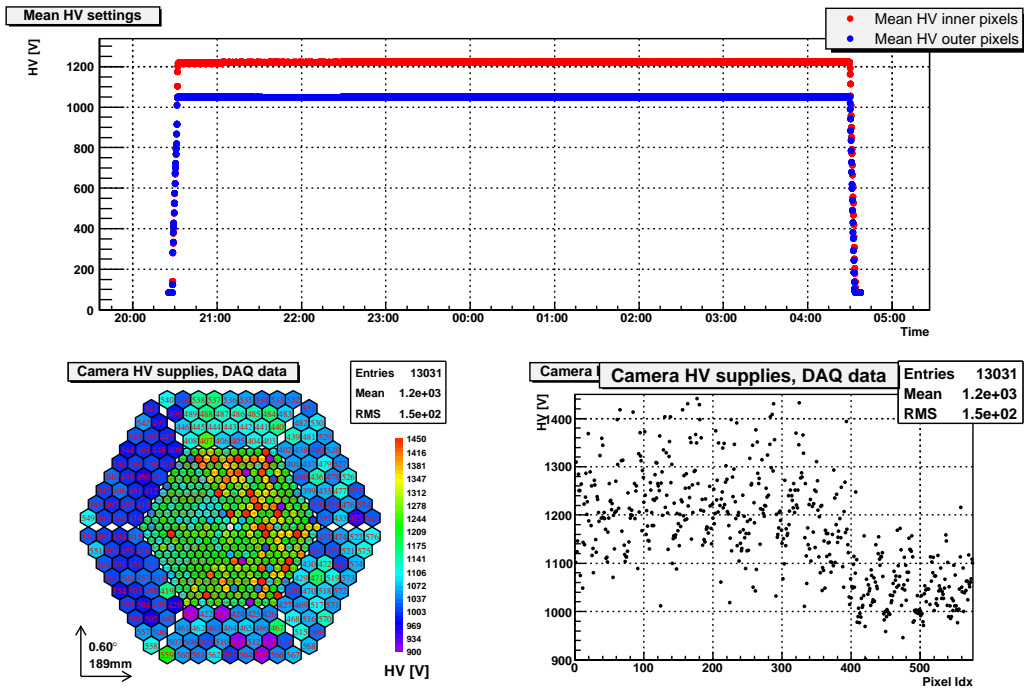


Figure A.4: *HV settings report plots. Mean high voltage settings for the whole camera versus time (top) and time average per pixel (bottom).*

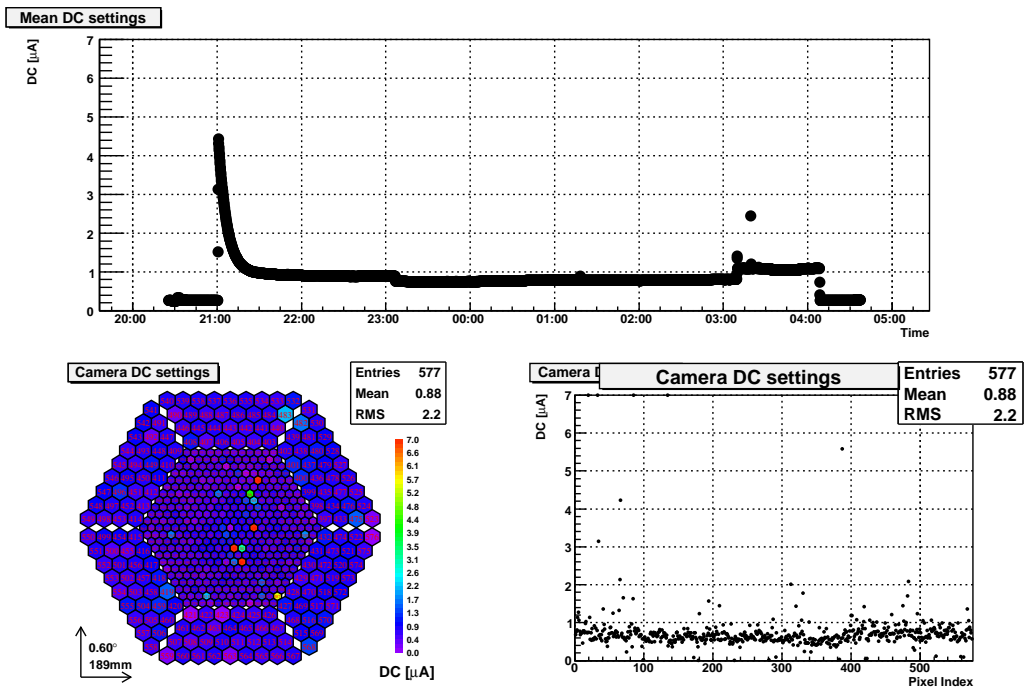


Figure A.5: *DC report plots. Mean direct current settings for the whole camera versus time (top) and time average per pixel (bottom).*

## A.1 Subsystems data check

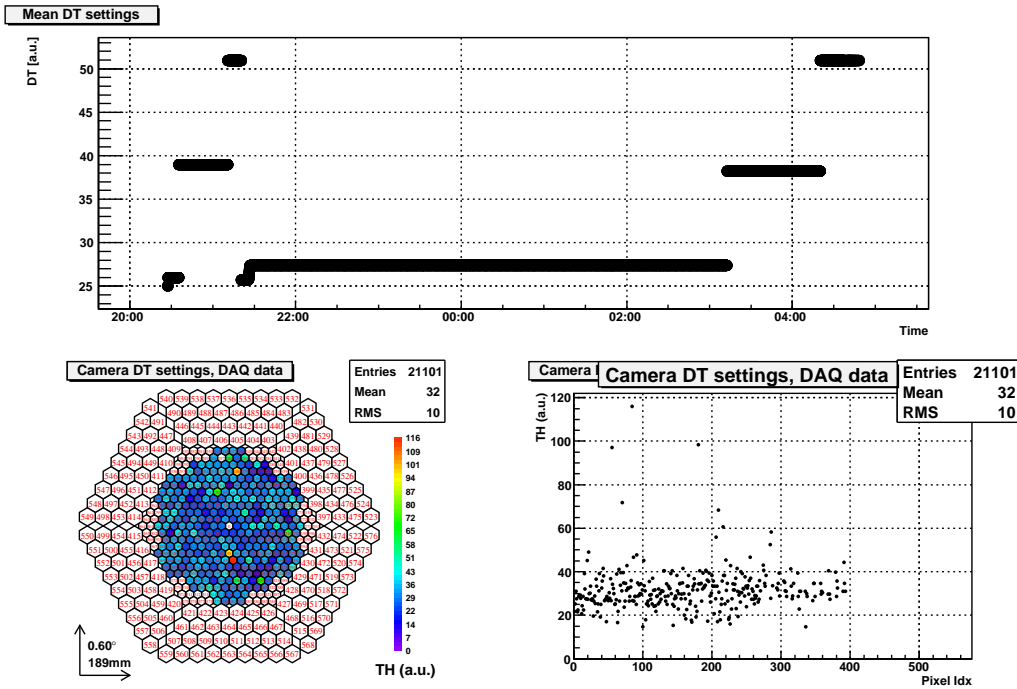


Figure A.6: *DT settings report plots. Mean threshold settings for the whole camera versus time (top) and time average per pixel (bottom).*

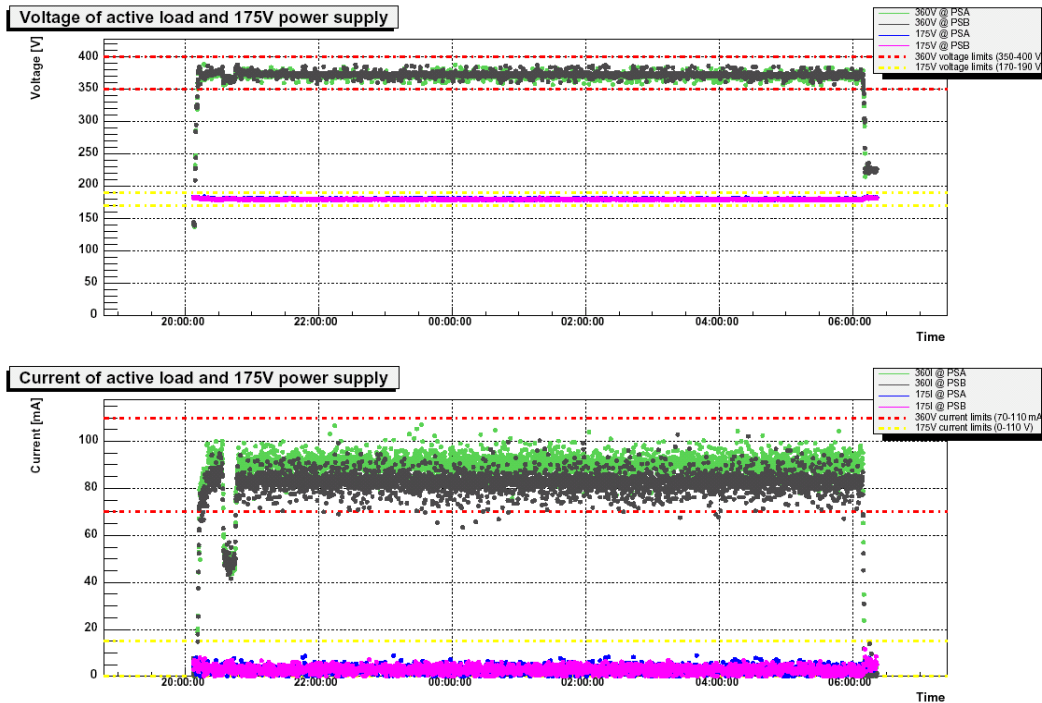


Figure A.7: *Active loads report plots. High voltage and direct current applied to 360 V active loads (A (green) and B (grey)), and independent power supply of 175 V (A (blue) and B (pink)). The red-dotted and yellow-dotted lines correspond to the limits to the applied fixed voltages.*

## A.1 Subsystems data check

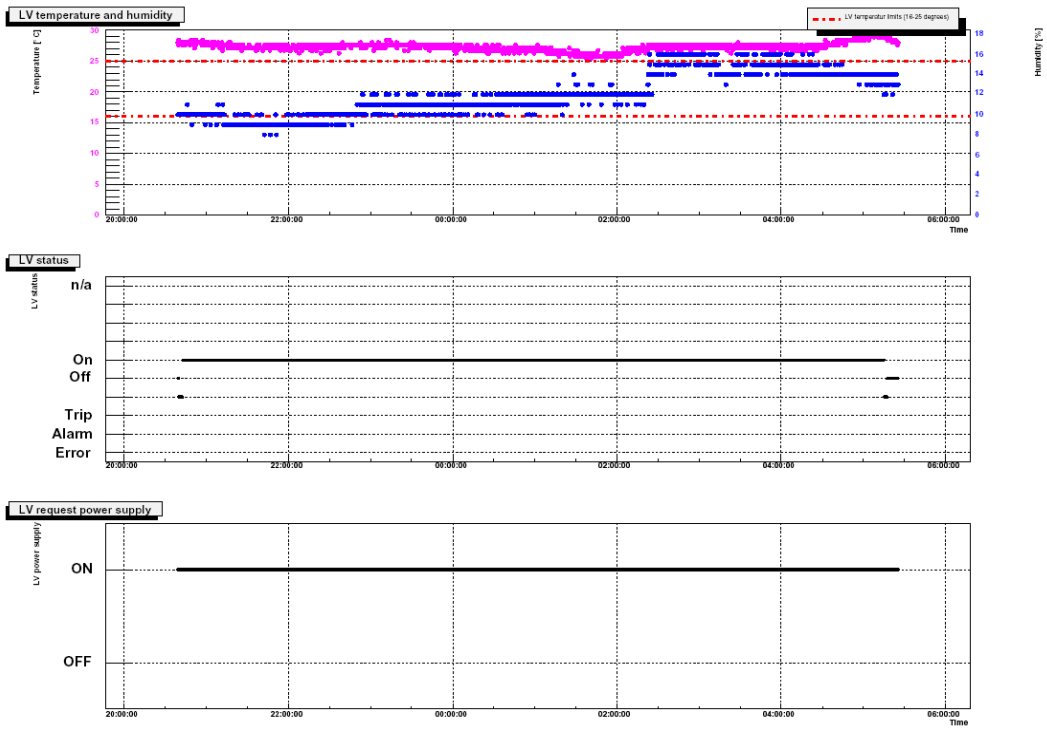


Figure A.8: Low voltage report plots. From top to bottom: Temperature and humidity in the LV box versus time, the status report of the LV system, and the status of the LV power supply.

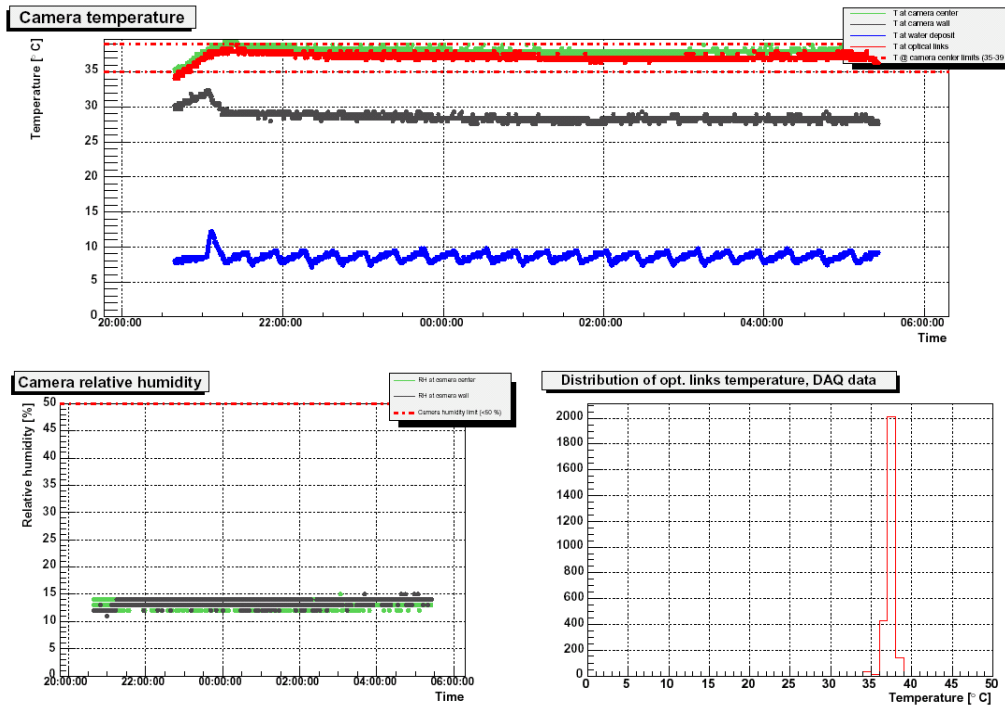


Figure A.9: Cooling system report plots. Top display: temperature versus time of the camera center (green), wall (grey), water deposit (blue) and optical links (red). Bottom left: humidity of the camera at its center (green) and walls (grey). Bottom right: distribution of the optical links temperature during the data taking.

## A.1 Subsystems data check

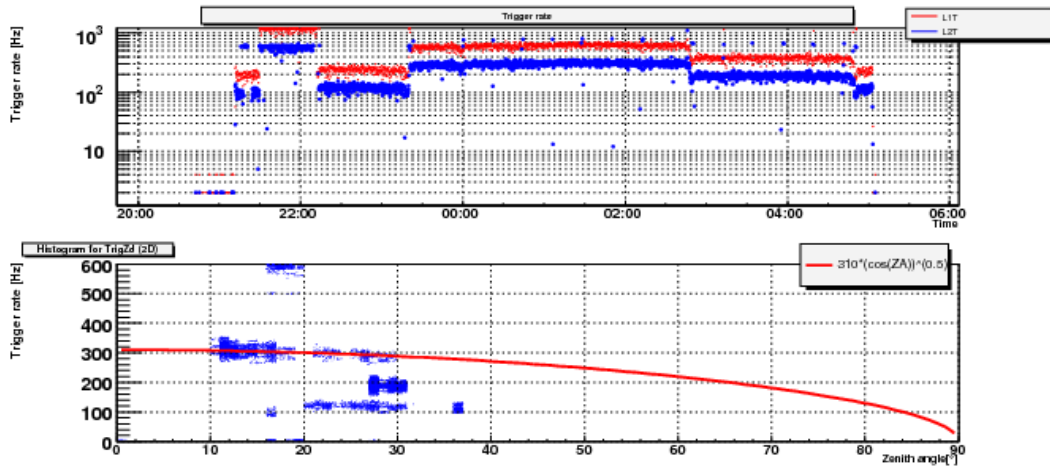


Figure A.10: *L1T* and *L2T* report plots. *Top*: *L1T* (red) and *L2T* (blue) rate (Hz) versus time. *Bottom*: *L2T* rate (Hz) versus pointing zenith angle (deg) during data taking. The red line corresponds to the expected *L2T* rate (interlaced events included) for the different zenith angles.

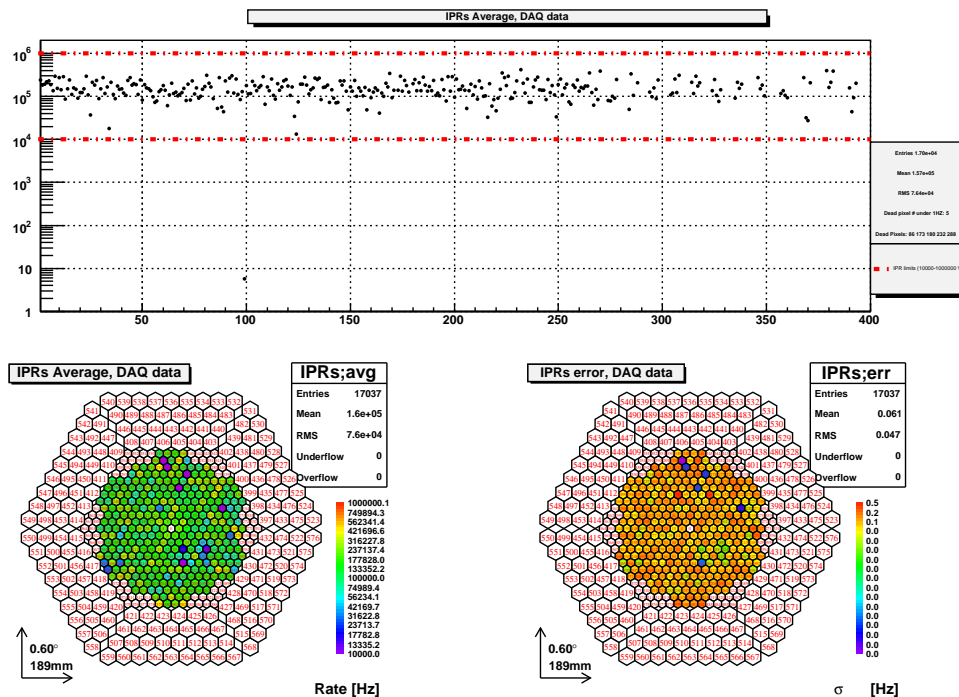


Figure A.11: *IPR* report plots. *Top*: time average of the *IPR* (Hz) versus pixel number. Red dashed lines show the limits of acceptable values of the *IPR*. The legend shows the number of the dead pixels, that are not plotted in the graph. *Bottom*: (left) time average of the *IPR* (Hz) in camera display and (right) time RMS of the *IPR* (Hz) shown as camera display.

## A.1 Subsystems data check

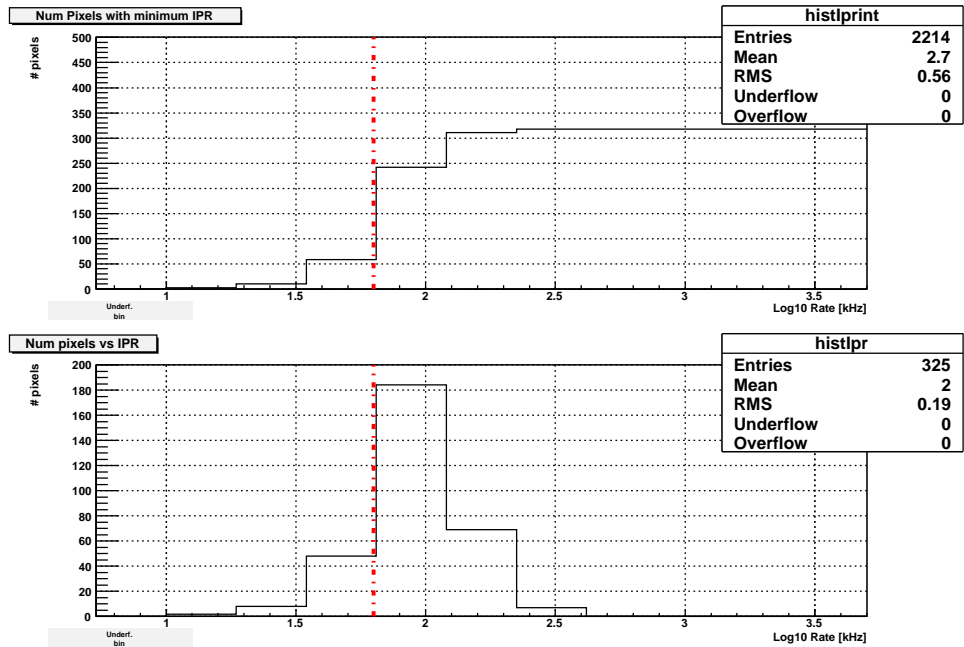


Figure A.12: More IPR report plots. Top: Number of pixels showing a minimum IPR (kHz). Bottom: Number of pixels with a certain IPR (kHz). Red dotted line marks the 60 kHz limit.

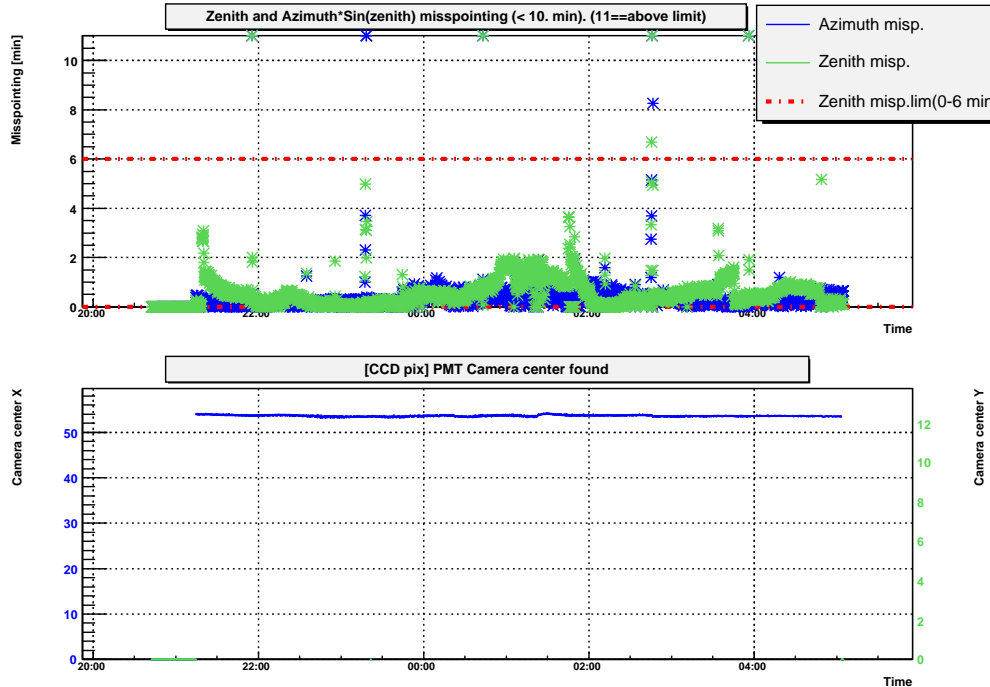


Figure A.13: Starguider report plots. Top: Absolute value of the zenith and azimuth mispointing (arc-min.) versus time. Bottom: The X and Y position in the CCD camera of the PMT camera center versus time. The red-dotted line corresponds to a mispointing within 1 camera pixel.

## A.1 Subsystems data check

---

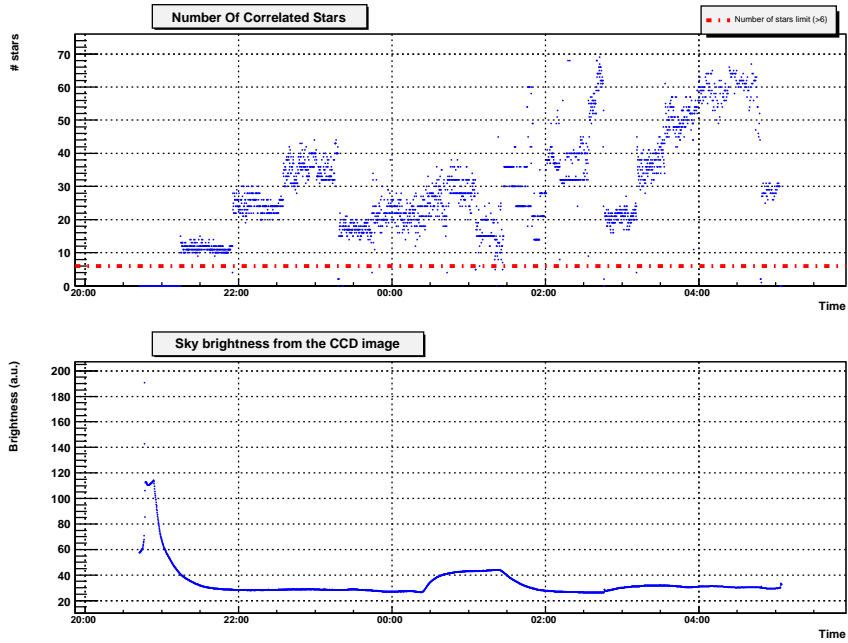


Figure A.14: *Star guider report plots. Top: Evolution of number of stars correctly identified at the catalog. Bottom: Sky brightness (in arbitrary units) from the CCD image versus time. The red-dotted line corresponds to the minimum number of correlated stars found by the star guider system which is needed to compute a good mispointing estimate.*

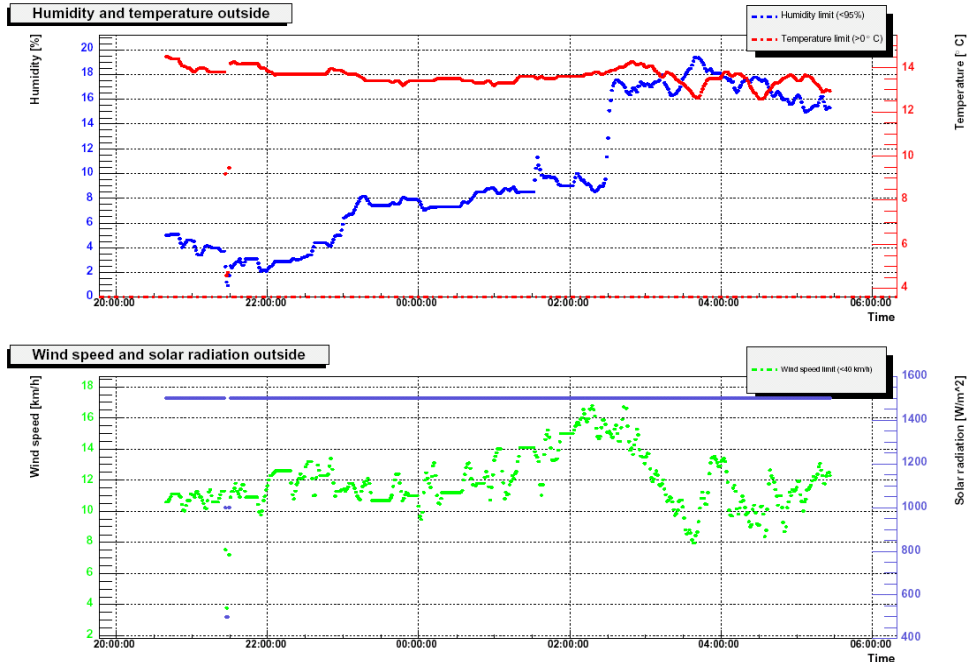


Figure A.15: *Weather station report plots. On top: Humidity (blue) and temperature (red) outside versus time. On bottom: Wind speed (green) and solar radiation (violet) (not working in this example) versus time. The dotted lines correspond to upper limits for a safe telescope operation. Above these values it is advisable to park the telescope.*

## A.1 Subsystems data check

---

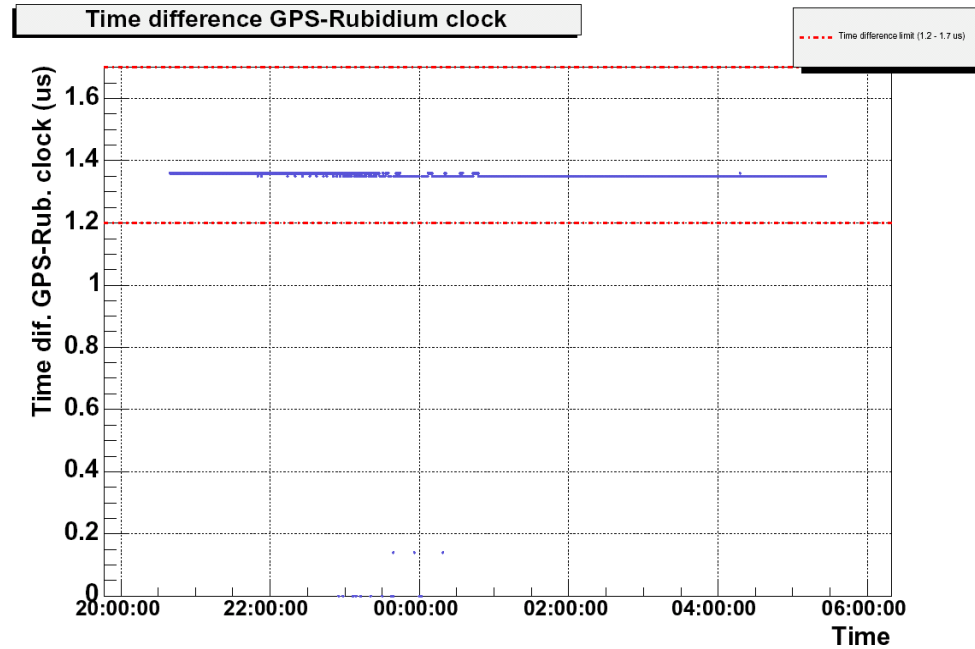


Figure A.16: Time report plot. Time difference ( $\mu\text{s}$ ) between GPS and rubidium clock. The red-dotted lines are upper and lower limits.

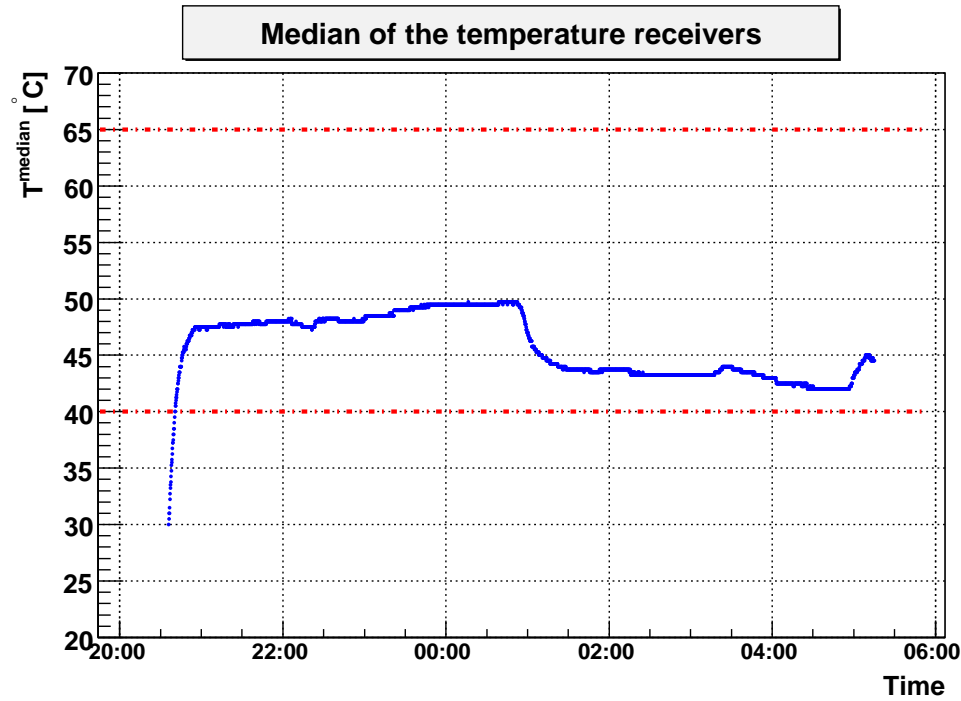


Figure A.17: Receiver temperature evolution along the night. The red dashed lines represent the safety limits.

## A.1 Subsystems data check

---

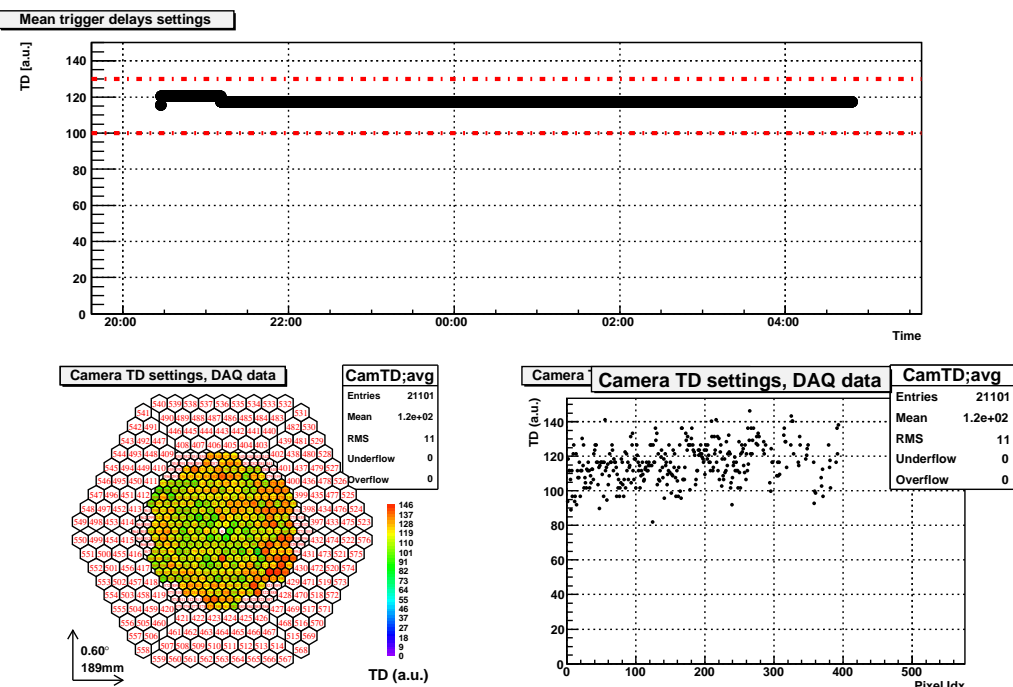


Figure A.18: *Trigger delays.* Top: Mean trigger delay evolution along the night. The correct region where the mean delay should be is defined by the red dashed lines. Bottom: Mean trigger delays of individual pixels for the whole data taking night.

## A.2 Data acquisition system quality check

---

### A.2 Data acquisition system quality check

See section 7.3.3 for further details.

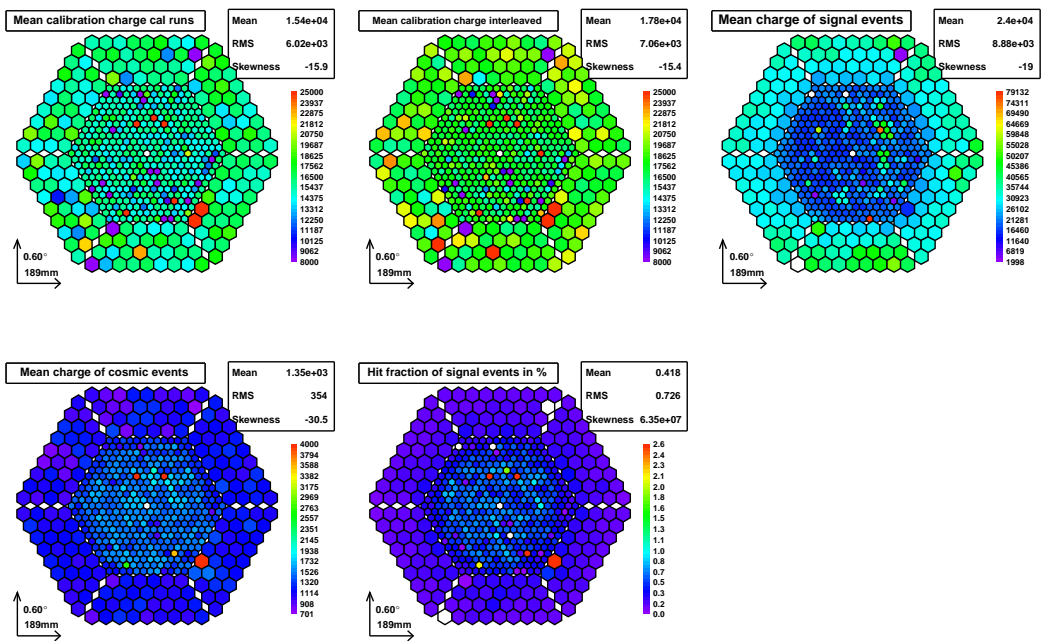


Figure A.19: Top left: Mean charge from calibration events from calibration runs. Top middle: Mean charge the interleaved calibration events from data runs. Top right: cosmic signal events. Bottom left: The mean charge from cosmic events. For these events, all pixels are taken into account when a cosmics trigger occurred. Bottom middle: The hit fraction of cosmic signal events with respect to all cosmic events.

## A.2 Data acquisition system quality check

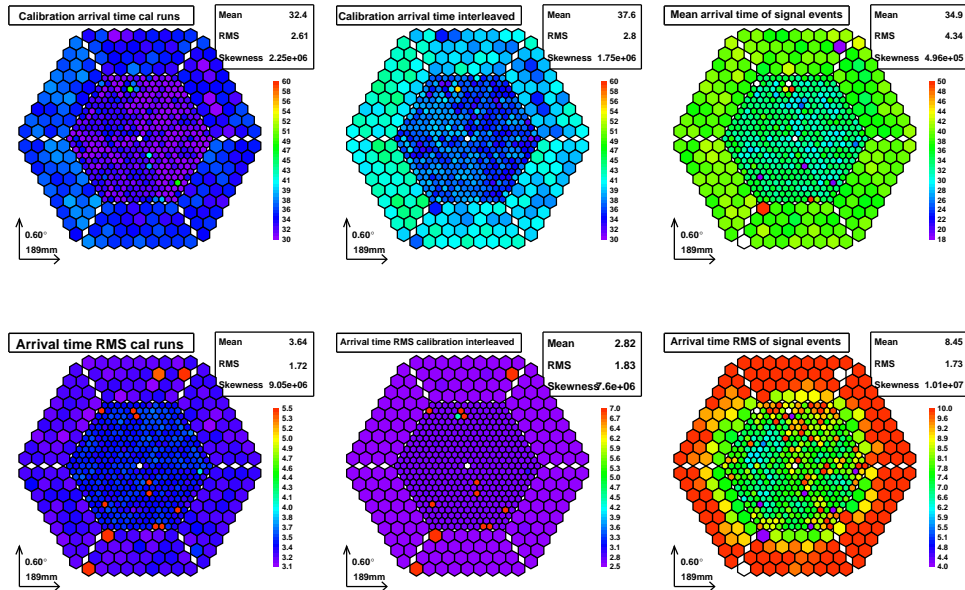


Figure A.20: Top left: Mean arrival time from calibration events of calibration runs. Top center: Mean arrival time from calibration interleaved events. Top right cosmic signal events. Bottom left: The arrival time RMS from events of calibration runs. Bottom center: Arrival time RMS from calibration interleaved events. Bottom left: Arrival time RMS from cosmic signal events.

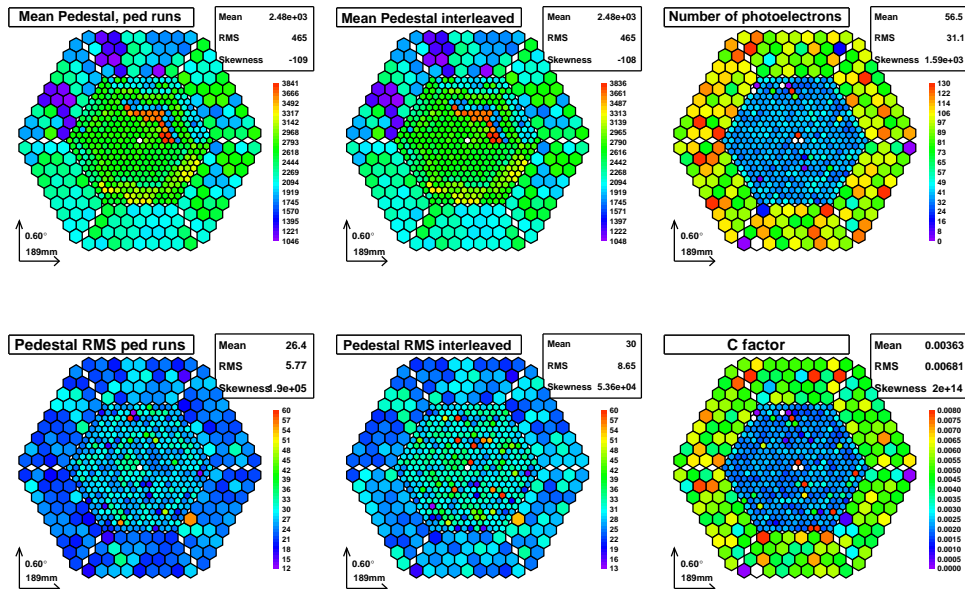


Figure A.21: Top left: Mean pedestal from events of pedestal runs. Top center: Mean pedestal from interleaved events. Top right: Number of photo electrons from interleaved calibration events . Bottom left and center: Pedestal RMS from events of pedestal and data runs. Bottom left: Mean conversion factor from FADC counts to photo-electrons.

## A.2 Data acquisition system quality check

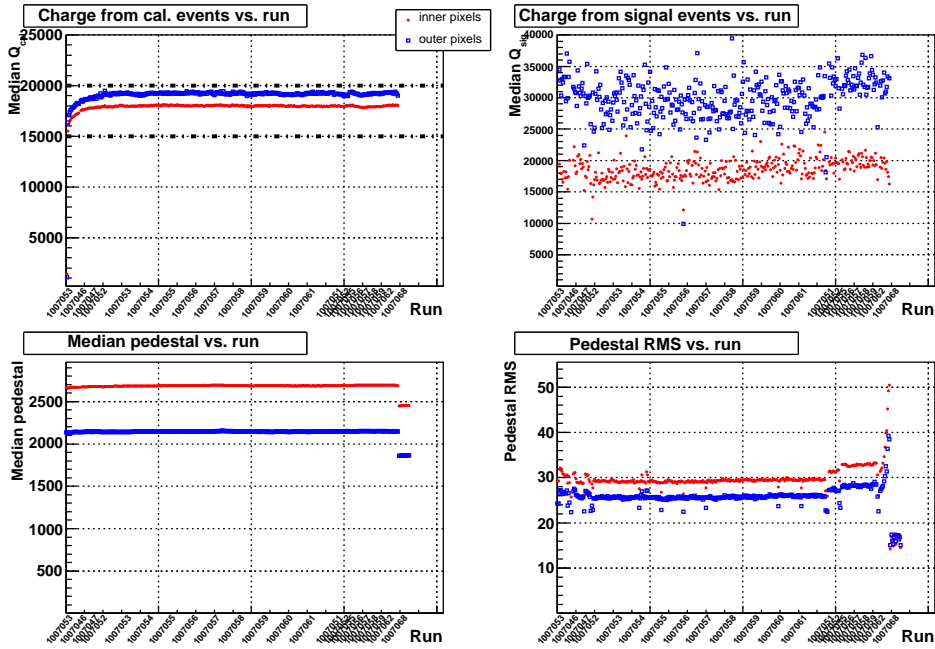


Figure A.22: Top: Evolution of the median charge for calibration (left) and cosmic signal events (right) versus run number, for both inner and outer pixels. Bottom: Average pedestal and its RMS for inner and outer pixels.

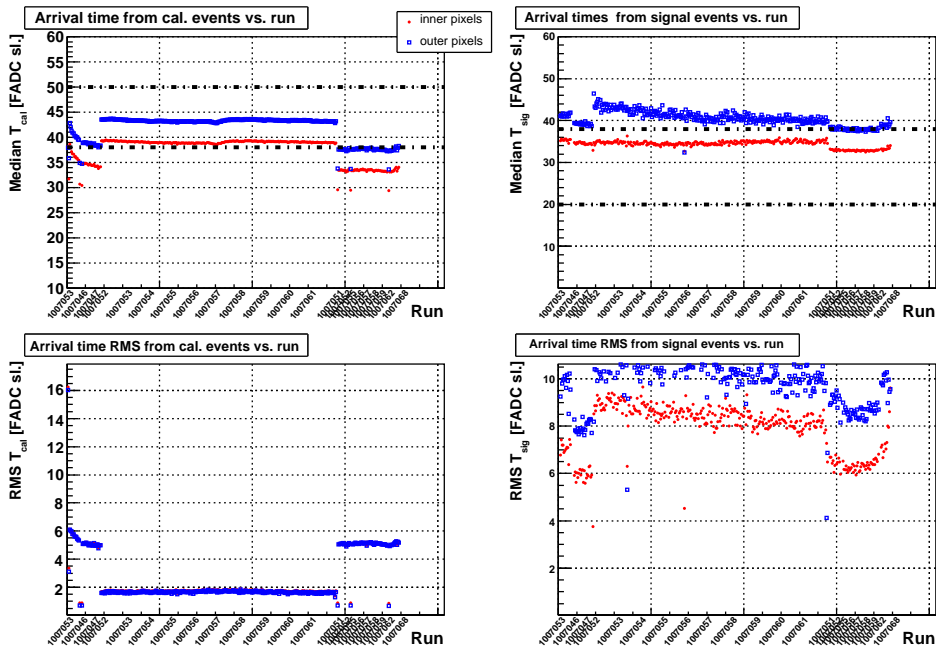


Figure A.23: Top: evolution of the arrival times for calibration (left) and cosmic signal events (right), for both inner and outer pixels. Bottom: RMS of the arrival times for calibration (left) and cosmic signal events (right), for both inner and outer pixels.

## A.2 Data acquisition system quality check

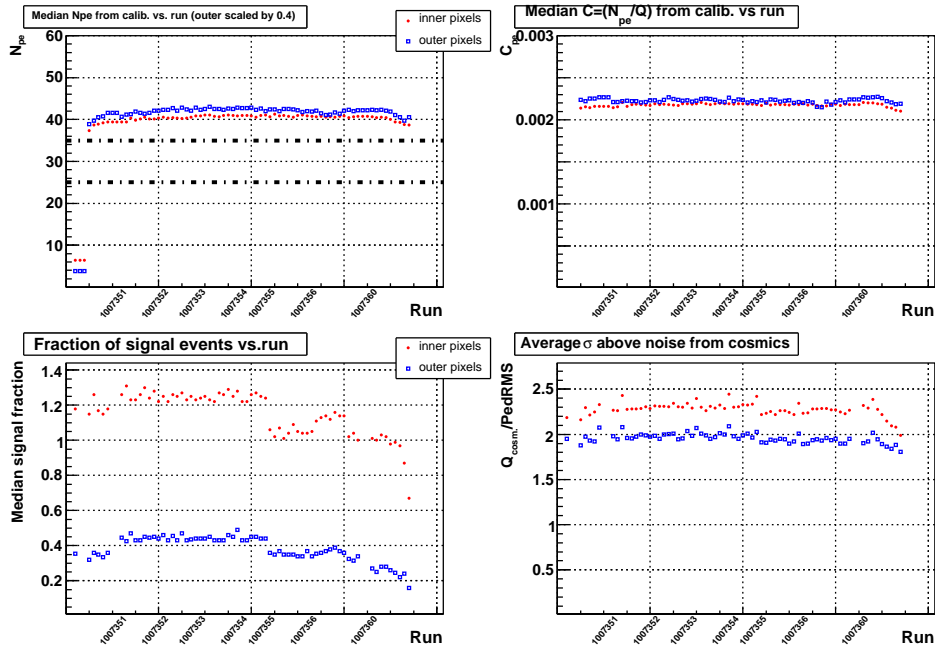


Figure A.24: Top left: Evolution plot of the  $N_{pe}$  along the night for interleaved calibration events. outer pixels numbers have been scaled a 0.4 factor. Top right: median conversion factor from FADC counts to photo electrons from interleaved calibration events for inner and outer pixels. Bottom left: hit fraction of cosmic signal events. Bottom right: averaged ratio of charge in cosmic events to the pedestal RMS.

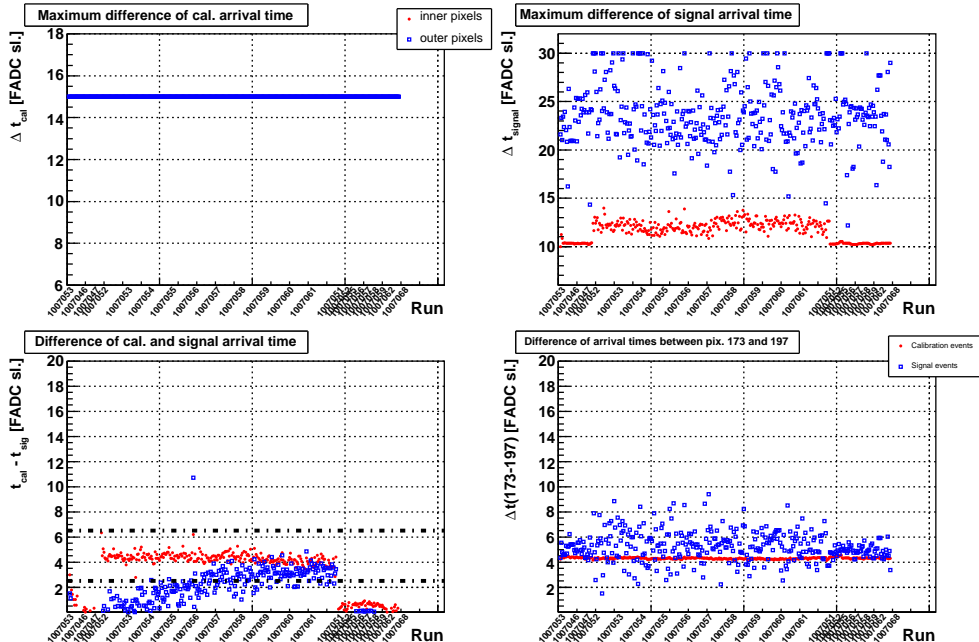


Figure A.25: Top left: maximum arrival times difference between pixels for calibration events. Top right: Maximum arrival time differences between two pixels for cosmic signal events. Bottom left: average arrival time difference between calibration and cosmic signal events. Bottom right: Arrival time difference between pixels 173 and 197, for calibration and cosmic signal events.

## A.2 Data acquisition system quality check

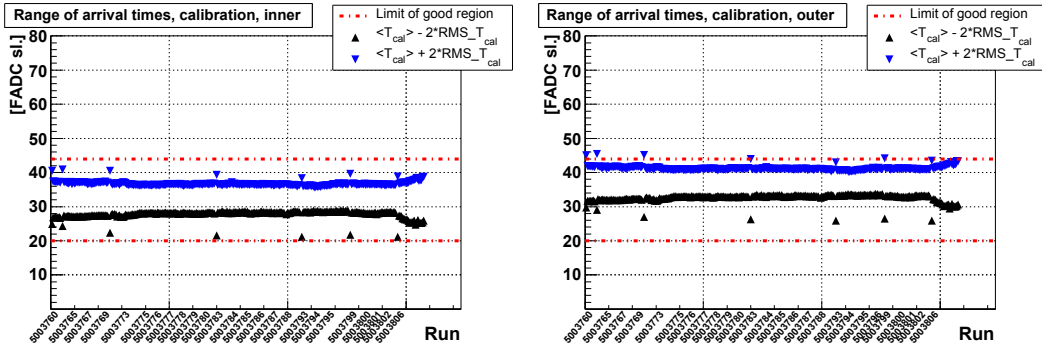


Figure A.26: *Evolution of quality check test for arrival times of calibration pulses along the night.*

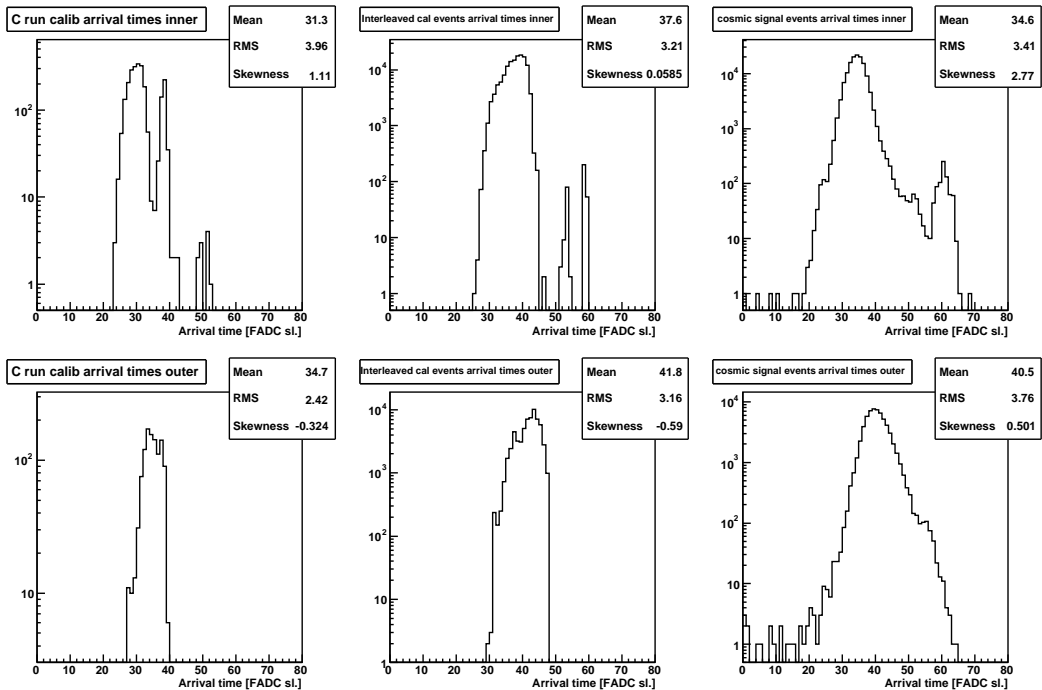


Figure A.27: *Top, from left to right: Arrival time distribution of calibration pulses from calibration runs, calibration pulses from data runs and cosmic signal arrival times, for inner pixels. Bottom: same arrival distributions for outer pixels.*

### A.3 Calibration data quality check

---

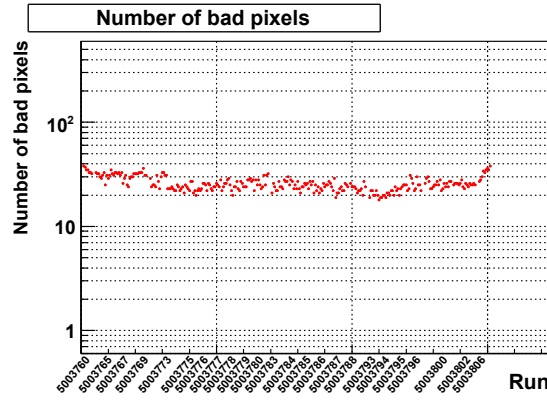


Figure A.28: *Evolution of number of bad pixels over the data taking night.*

## A.3 Calibration data quality check

See section 7.3.4 for further details.

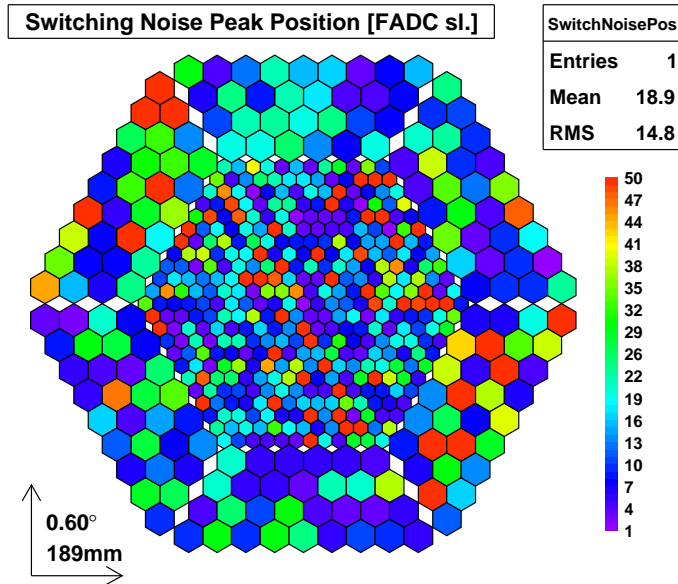


Figure A.29: *Camera display containing each pixel's switching noise peak position in units of FADS slice.*

### A.3 Calibration data quality check

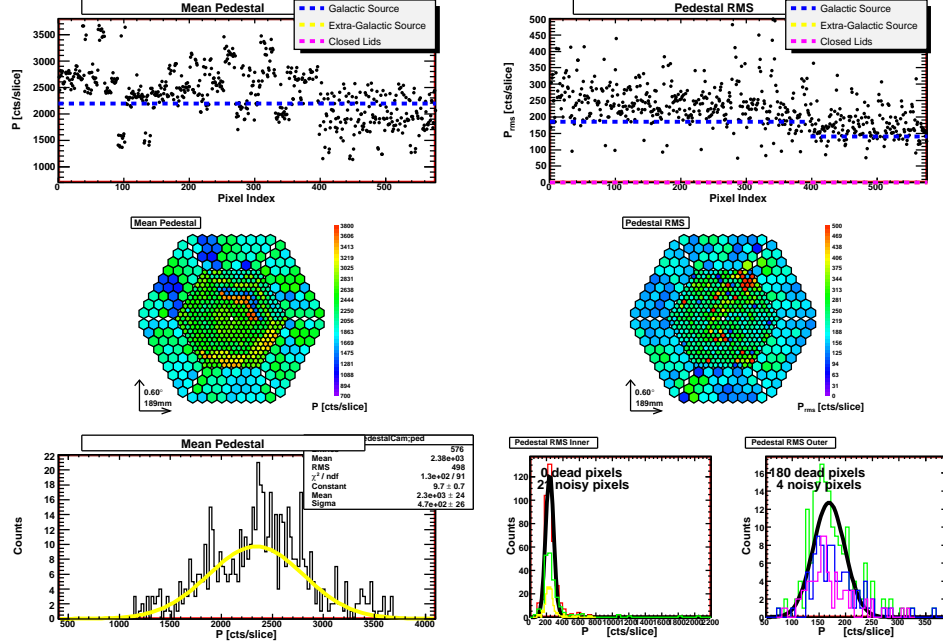


Figure A.30: *Pedestal mean and RMS (from pedestal run).* From top to bottom: pedestal mean (left) and RMS (right) versus pixel index viewed as a profile and camera display views, and the mean and RMS distributions together with the Gaussian fits. The reference lines correspond to the typical pedestal values obtained pointing to galactic (blue) or extragalactic (yellow) sources and with closed lids (pink).

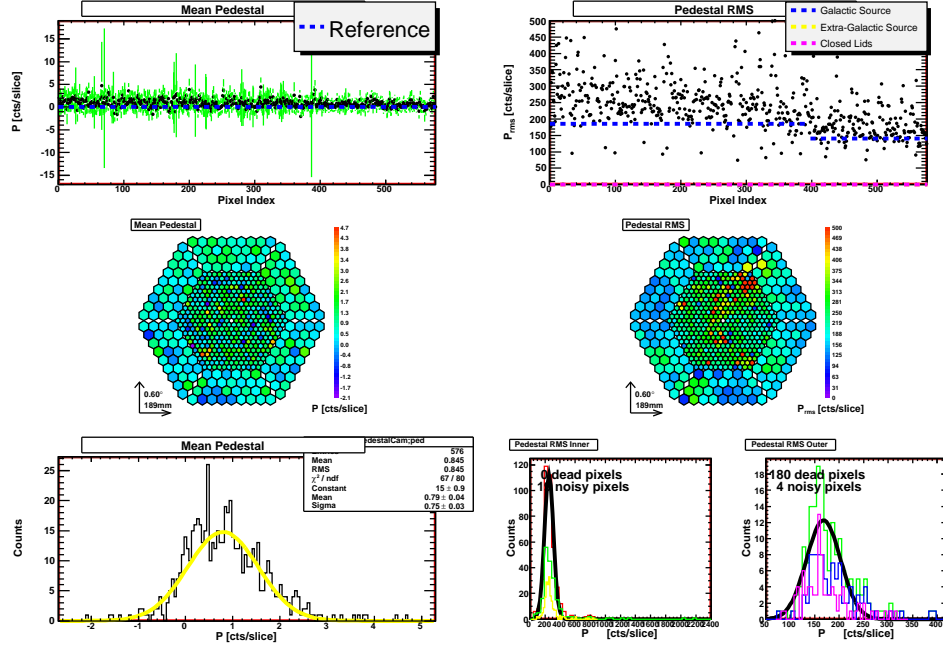


Figure A.31: *Pedestal Mean and RMS (from calibration extracted run).* From top to bottom: pedestal mean (left) and RMS (right) versus pixel index in profile and camera display views, and the mean and RMS distributions together with the gaussian fits. The reference lines correspond to the pedestal values when pointing to galactic (blue) and extragalactic (yellow) sources and with closed lids (pink).

### A.3 Calibration data quality check

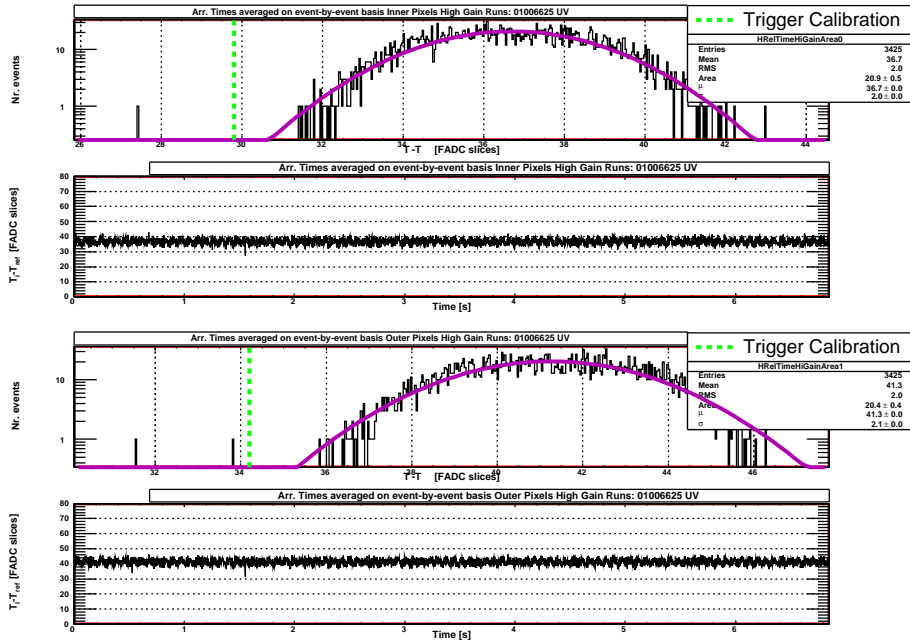


Figure A.32: Mean arrival time (FADC slice). From top to bottom: mean arrival time distribution for inner pixels (first 2 plots) and outer pixels (last 2 plots). The second and fourth plot show this arrival time parameter versus time (sec) during the calibration run, which lasts a few seconds, for both inner and outer pixels.

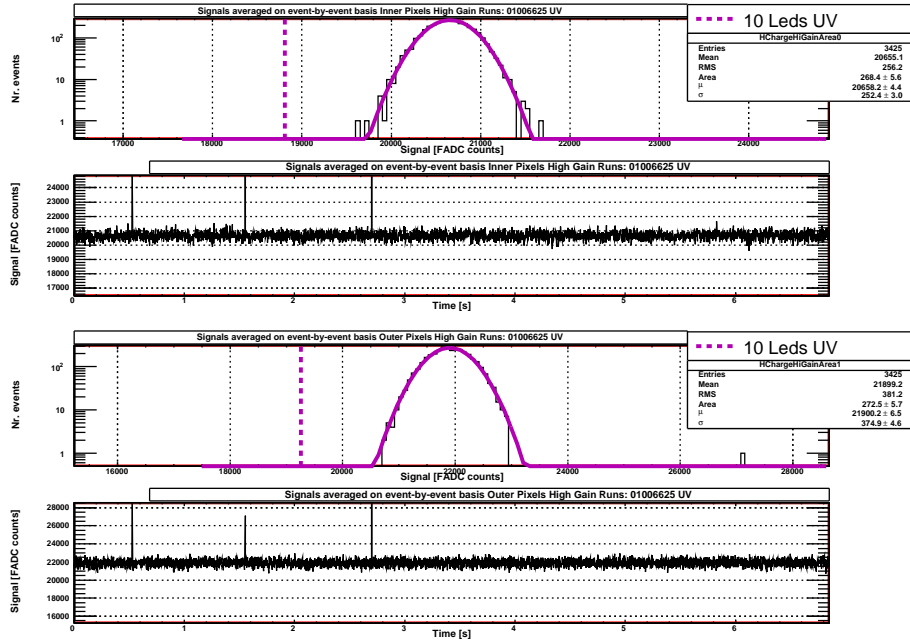


Figure A.33: Calibration signal charge (FADC counts). From top to bottom: mean calibration signal charge (FADC counts) distribution for inner (first 2 plots) and outer pixels (last 2 plots). The second and fourth plot show this mean charge versus time (sec) during the calibration run for both inner and outer pixels. The reference lines correspond to the expected light for the specific calibration script.

### A.3 Calibration data quality check

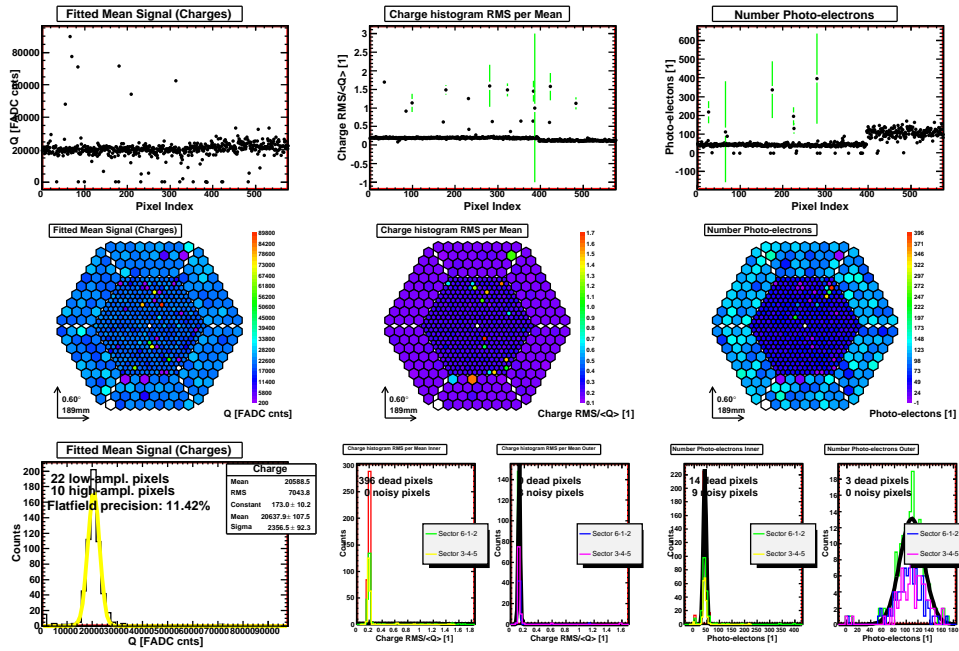


Figure A.34: Fitted charge (FADC counts) and Npe. From top to bottom: the average versus pixel index as profile and camera display, and the distribution for the following variables: fitted mean charge and RMS, and the Npe.

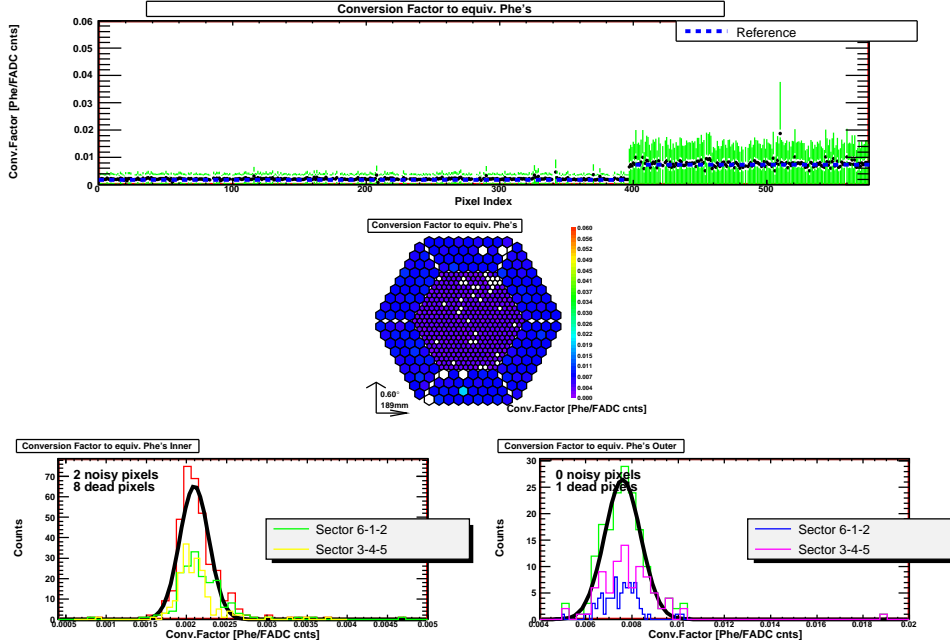


Figure A.35: Conversion factors from FADC counts to Npe. From top to bottom: the average value versus pixel index as profile and as a camera display, and the distribution for the number of the conversion factor.

### A.3 Calibration data quality check

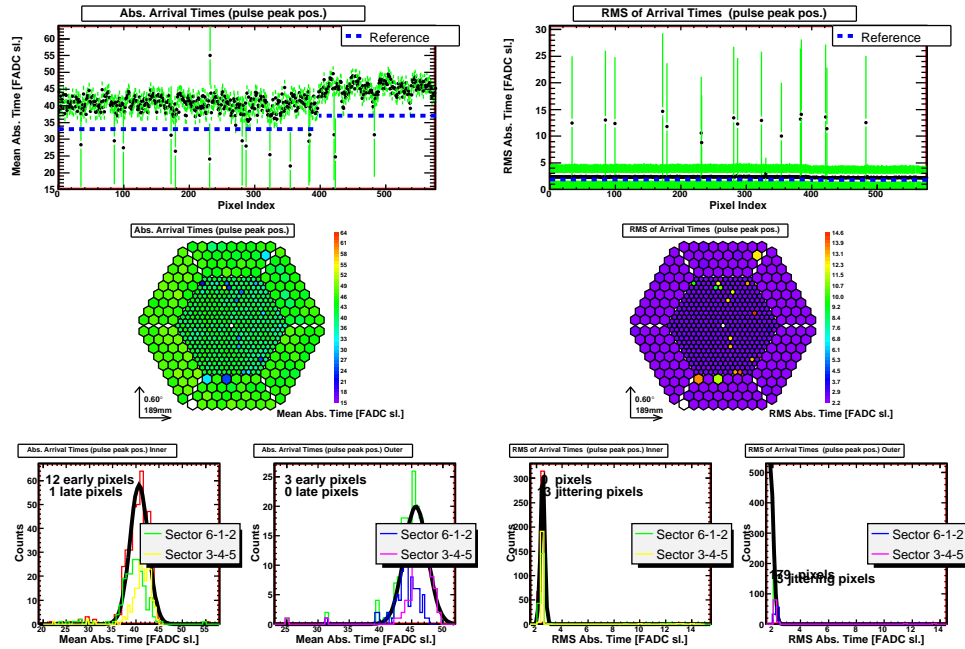


Figure A.36: *Arrival times (FADC slice)*. From top to bottom: Mean and RMS of arrival FADC slice in profile and camera display and their distributions (for inner and outer pixels).

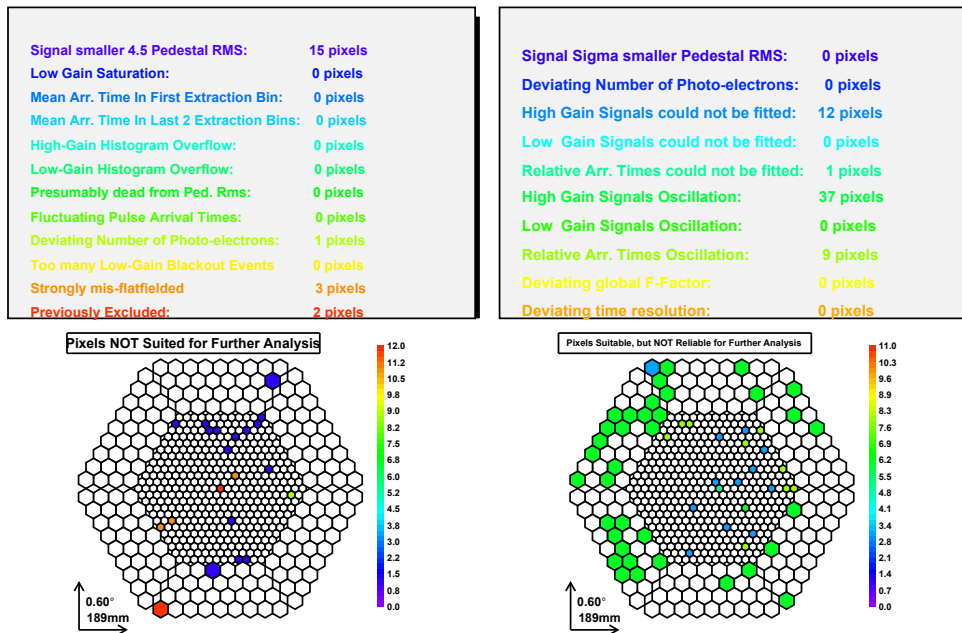


Figure A.37: *Faulty pixels*. Legend with information about the calibrated defective pixels and a camera display showing the corresponding pixels, with colors indicating the kind of defect. On the left the “non suited pixels” and on the right the “non reliable” pixels.

### A.3 Calibration data quality check

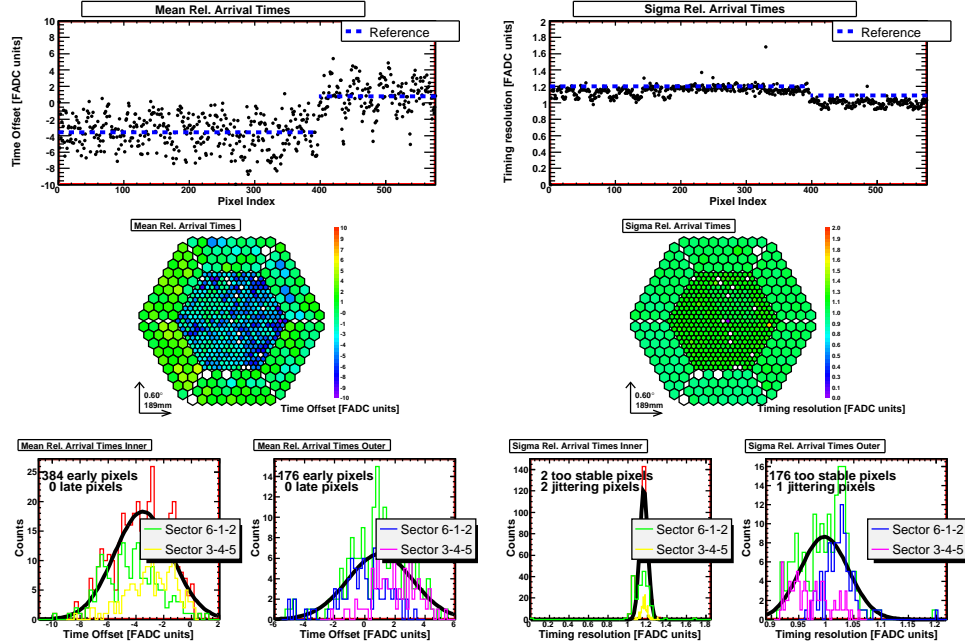


Figure A.38: *Relative arrival time (FADC slice)*. From top to bottom: mean and RMS of relative arrival FADC slice in profile and camera display and their distributions (for inner and outer pixels).

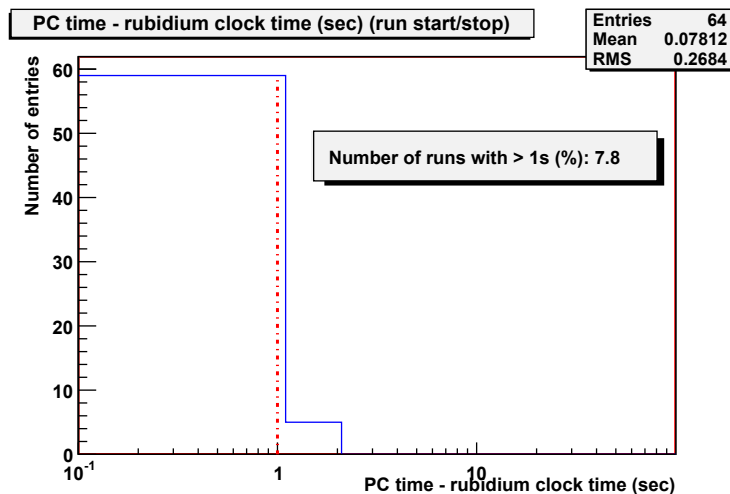


Figure A.39: *Distribution of the time difference between the PC and the rubidium clock. The red dashed reference line is 1 second of time difference.*

### A.3 Calibration data quality check

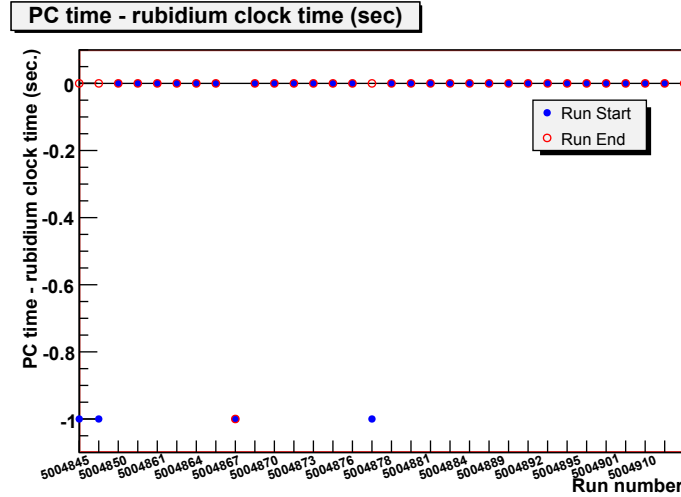


Figure A.40: *Evolution plot of the time difference between the PC and the rubidium clock. Two values of the time difference are obtained per each pedestal run, one at the start and another at the end of the run.*

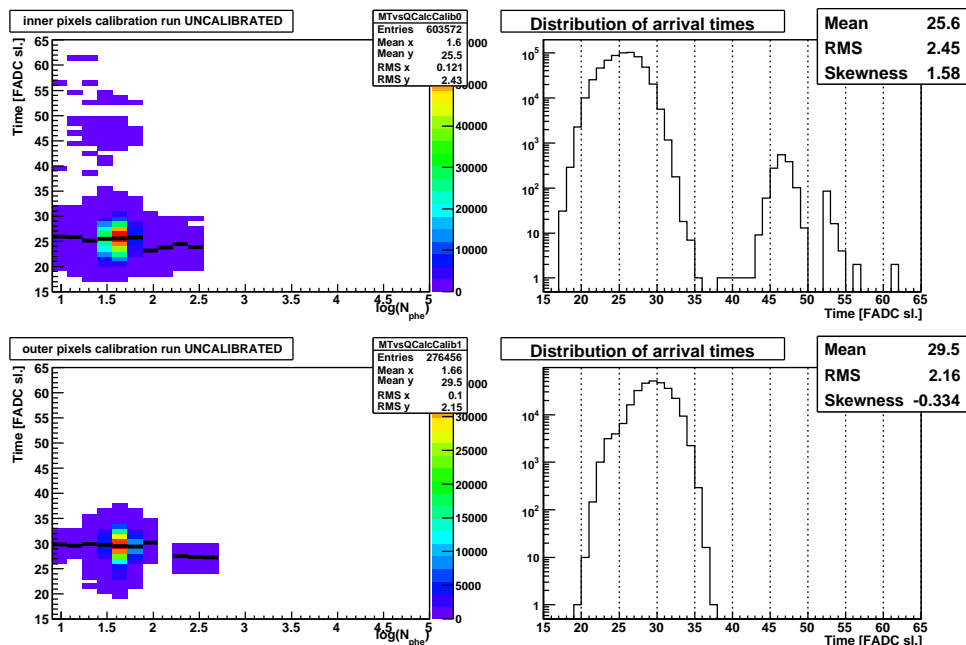


Figure A.41: *Size dependant and overall distributions of calibration pulses, for calibration runs, from both inner and outer pixels.*

### A.3 Calibration data quality check

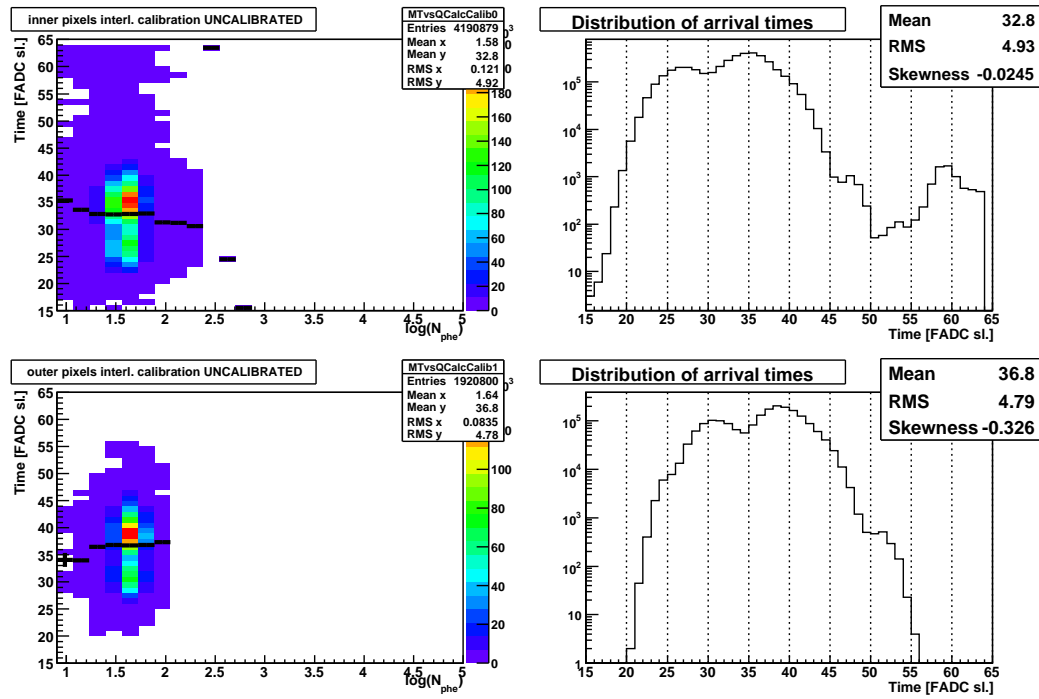


Figure A.42: *Size dependant and overall distributions of interleaved calibration pulses, from data runs, for both inner and outer pixels.*

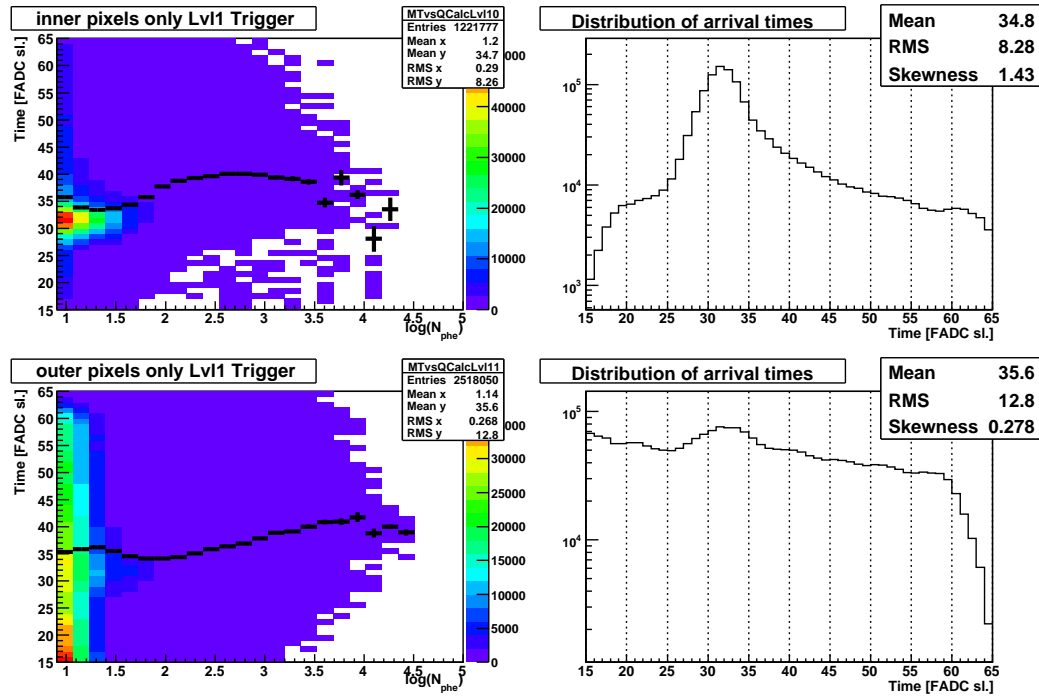


Figure A.43: *Size dependant and overall distributions of level 1 trigger events for both inner and outer pixels.*

### A.3 Calibration data quality check

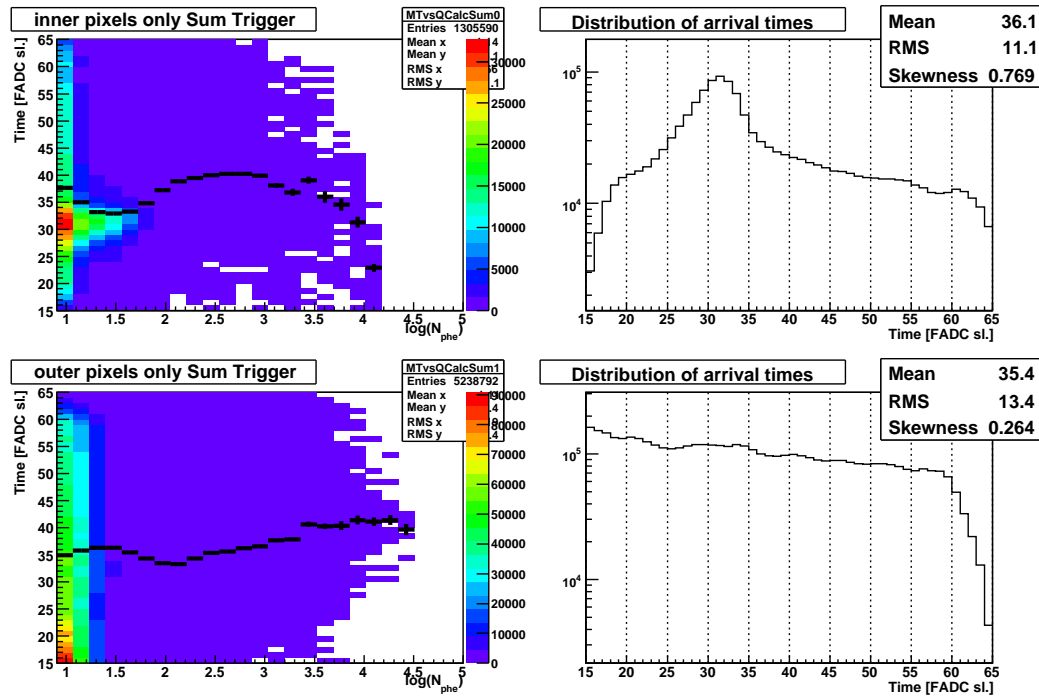


Figure A.44: *Size dependant and overall distributions of sum trigger events for both inner and outer pixels.*

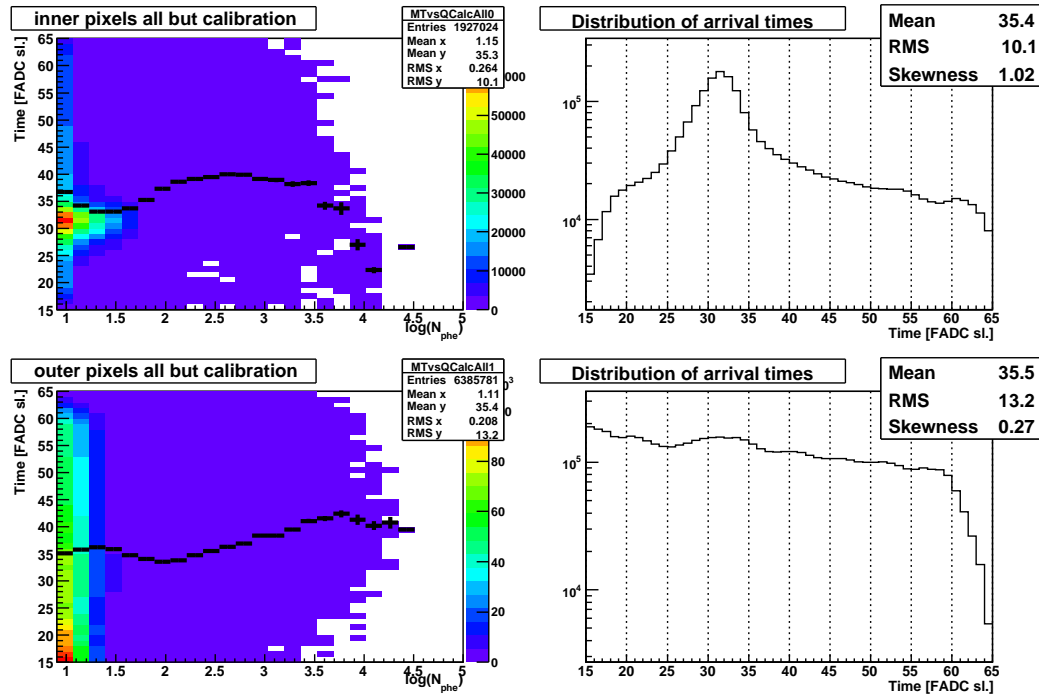


Figure A.45: *Size dependant and overall distributions of all events except calibration ones, for both inner and outer pixels.*

## A.4 Hillas parameter plots

---

### A.4 Hillas parameter plots

See section 7.3.5 for further details.

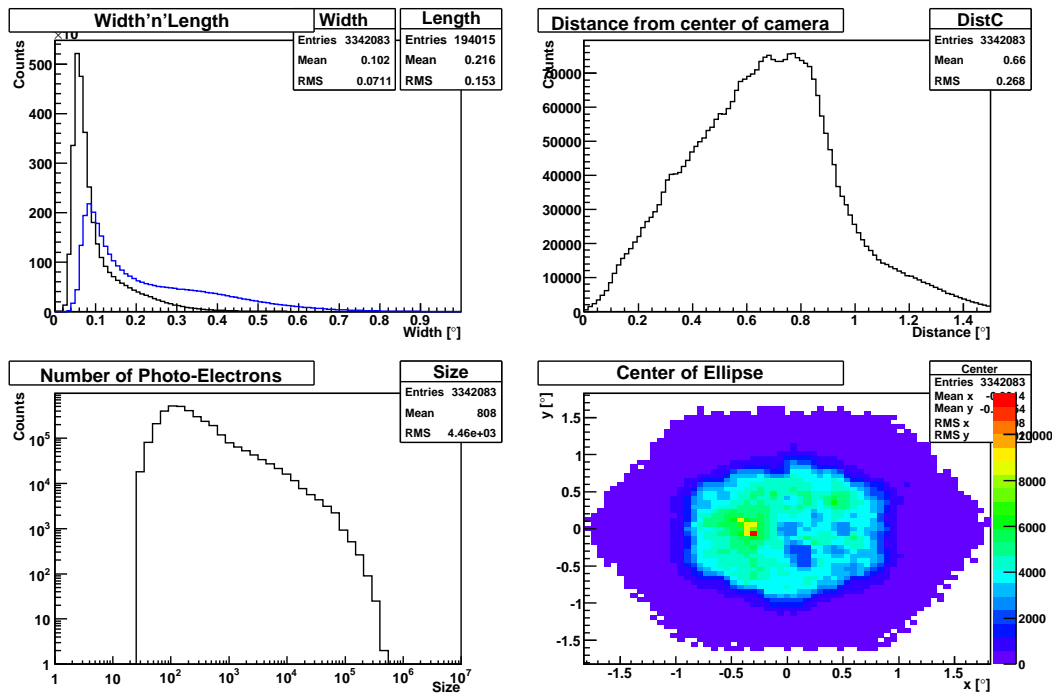


Figure A.46: *Hillas parameters*. Top left: length and width (deg), defined as the second moments of the image. Top right: distance from the center of the ellipse to camera center (deg). Bottom left: Size, defined as total number of photo-electrons after the image cleaning. Bottom right: CoG of the center of the ellipse (deg).

## A.4 Hillas parameter plots

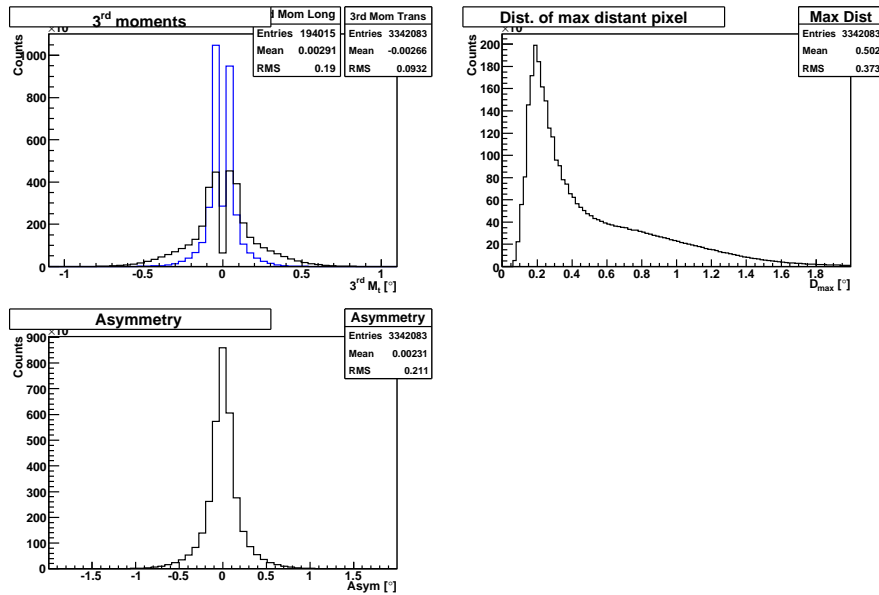


Figure A.47: Extended image parameters. Top left: Longitudinal and transverse third moments of the image (deg). Top right: distance from most distant used pixel to camera center (deg). Bottom left: Distance from the pixel with more number of photo-electrons to center, projected onto major axis, (deg).

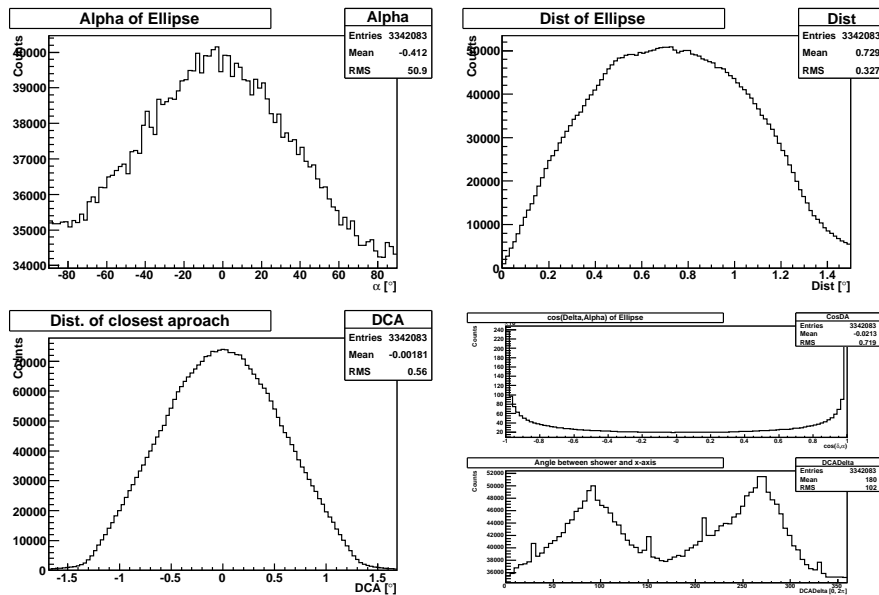


Figure A.48: Source-dependent image parameters. Top left: angle between major axis and the line source-to-center. Top right: distance from the source position in the camera to the center of Hillas ellipse. Bottom left: Distance to closest approach. Bottom right: cosine of angle between  $d$  and  $a$ , where  $d$  is the vector from the source position to the center of the ellipse  $a$  is a vector along the main axis of the ellipse, defined with positive  $x$ -component and angle of the shower axis with respect to the  $x$ -axis.

## A.4 Hillas parameter plots

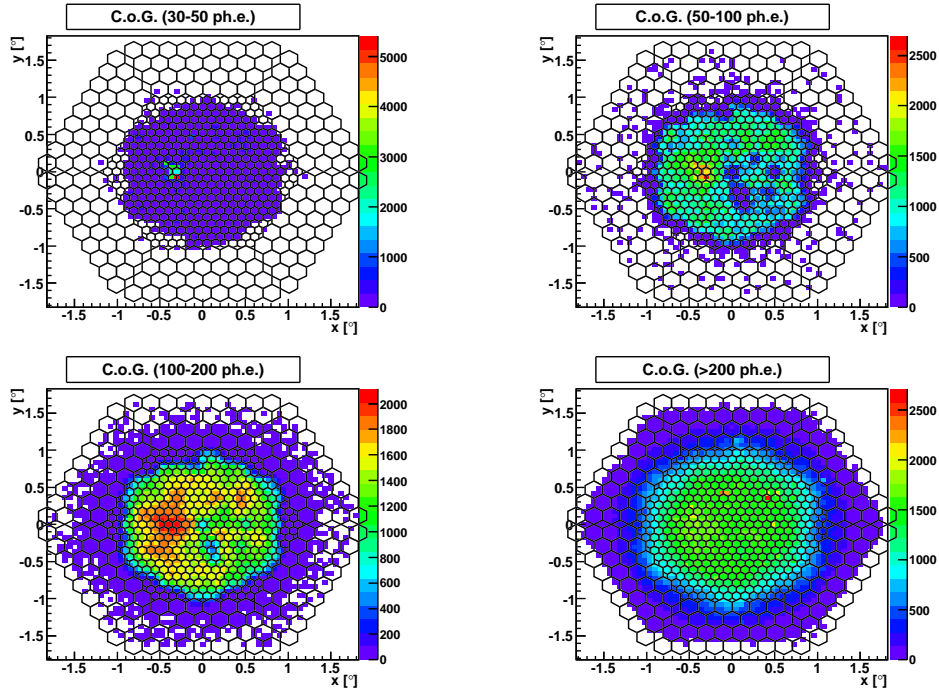


Figure A.49: Homogeneity plots. Center of gravity of the cleaned image (deg) for different size bins.

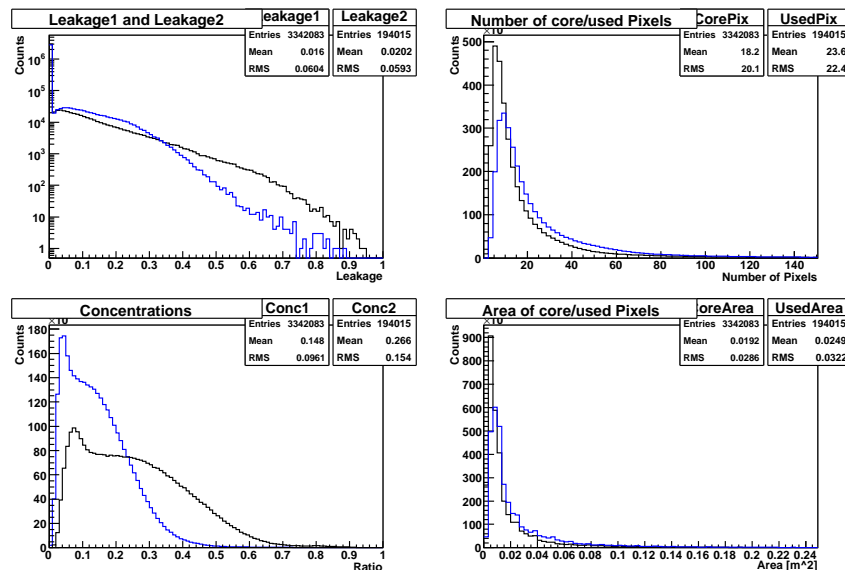


Figure A.50: More image parameters. Top left: Leakage1, defined as measured number of photo-electrons in outermost ring of pixels over total size of the image, and leakage2, identically defined but for the 2 outer rings. Top right: Number of pixels which survived the image cleaning and number of core pixels. Bottom left: Concentration ratio 1, defined as the number of photo-electrons of the highest pixel over the size of the image, and Concentration ratio 2, defined identically but for the two highest pixels. Bottom right: Area of pixels which survived the image cleaning and area of core pixels, both in m<sup>2</sup>.

## A.4 Hillas parameter plots

---

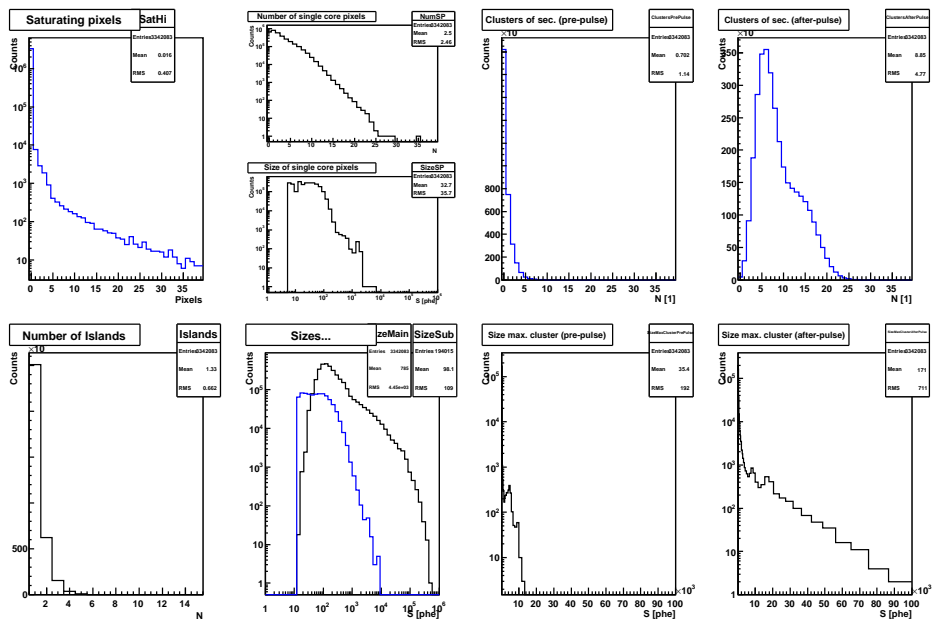


Figure A.51: *Image parameters.* Top, from left to right: number of pixels with saturating gains, number of single core pixels and their size, number of clusters from secondaries pre-pulse, number of clusters from secondaries after-pulse. Bottom, from left to right: number of islands found, sizes of primary and secondary islands in photo-electrons, size of maximum cluster from secondaries pre-pulse in photo-electrons and size of maximum cluster from secondaries after-pulse in photo-electrons.

# Appendix B

## Example of a sequence

Next lines show an example of a sequence, similar to those used in the data quality check and on-site analysis softwares.

```
# Sequence number (identifier)
Sequence: 5004672.5004672
# Observation Period (used to get the path-names)
Period: 87
# Date of sunrise of the observation night
Night: 2010-01-18
# Start time of the sequence (first data run)
Start: 2010-01-18 02:17:15
# Project name of data-runs of sequence
Project: Mrk421-W0.40+000
# Source name of all runs of sequence
Source: Mrk421-W0.40+000
# Wobble mode:
Wobble: 0
Telescope: 1
# List of all calibration runs of this sequence
CalRuns: 5004671.001
# List of pedestal runs belonging to the calibration runs of this sequence
PedRuns: 5004670.001
# List of all data runs belonging to this sequence
DatRuns: 5004672.001 5004672.002 5004672.003 5004672.004 5004672.005
```

# Appendix C

## List of acronyms and abbreviations

### C.1 Acronyms used in the dissertation

**1FGL** Fermi-LAT first source catalog

**4NN** Four Next Neighbour

**AGN** Active Galactic Nucleus/Nuclei

**AMC** Active Mirror Control

**ASM** All Sky Monitor

**ADC** Analog to Digital Converter

**BLR** Broad Line Region

**CC** Central Control

**CCD** Charge-Coupled Device

**CIB** Cosmic Infrared Background

**CMB** Cosmic Microwave Background

**COB** Cosmic Optical Background

**CR** Cosmic Ray

**CSS** Compact Steep Spectrum

**DAQ** Data Acquisition

---

## C.1 Acronyms used in the dissertation

---

**DM** Dark Matter

**dSphs** dwarf Spheroidal galaxies

**DT** Discrimination Threshold

**EAS** Extensive Air Shower

**EBL** Extragalactic Background Light

**EC** External Compton

**EHE** Extremely High Energy, above 30 PeV

**EM** Electromagnetic

**FADC** Flash Analog to Digital Converter

**FoV** Field of View

**FR-I** Fanaroff-Riley type I radio galaxy

**FR-II** Fanaroff-Riley type II radio galaxy

**FSRQ** Flat Spectrum Radio Quasar

**GBM** *Fermi* Gamma-ray Burst Monitor

**GC** Galactic Center

**GPS** GHz Peaked Source

**GRB** Gamma-Ray Burst

**HBL** High-frequency BL Lac

**HE** High Energy, 30 MeV - 30 GeV

**IACT** Imaging Atmospheric Cherenkov Telescopes

**IBL** Intermediate-frequency BL Lac

**IC** Inverse Compton

**ISM** InterStellar Medium

**KVA** *Kungliga Vetenskaps Akademien* telescope

**L1** First Level trigger

## C.1 Acronyms used in the dissertation

---

**LAT** *Fermi* Large Area Telescope

**LBL** Low-frequency BL Lac

**log-P** log-parabolic Power-law function

**LE** Low Energy, below 30 MeV

**LONS** Light of Night Sky background

**LV** Low Voltage

**MAGICDC** Magic Data Check software

**MARS** MAGIC Standard Analysis Software

**MBH** Massive Black Hole

**MWL** Multiwavelength

**MC** Monte Carlo

**NLR** Narrow Line Region

**Npe** Number of photo-electron

**PCA** Proportional Counter Array

**PDF** Probability Density Function

**PIC** Port d'Informació Científica

**PL** simple Power Law function

**PL+C** Power-Law with exponential Cut-off function

**PMT** PhotoMulTipler

**PSF** Point Spread Function

**PWN** Pulsar Wind Nebula

**QE** Quantum Efficiency

**QOSA** Quick On-Site Analysis software

**RF** Random Forest regression method

**RIC** Radio Intermediate Quasar

---

## C.2 Acronyms used in the bibliography

---

**SED** Spectral Energy Distribution

**SNR** SuperNova Remnant

**SSC** Synchrotron self-Compton

**SSRQ** Steep Spectrum Radio Quasar

**SUM** analogue SUM trigger

**SUSY** Super-Symmetric

**ToO** Target of Opportunity

**UHE** Very High Energy, 30 TeV - 30 PeV

**UV** UltraViolet

**VCSEL** Vertical Cavity Surface Emitting Laser

**VHE** Very High Energy, 30 GeV - 30 TeV

**z** redshift

**ZD** Zenith Distance

## C.2 Acronyms used in the bibliography

**A&A** Astronomy and Astrophysics

**Adv. Sp. Res.** Advances in Space Research

**AIP Conf. Proc.** AIP Conference Proceedings

**Astrop. Phys.** Astroparticle Physics

**ApJ** The Astrophysical Journal

**ApJS** The Astrophysical Journal Supplement Series

**MAGIC-TDAS** MAGIC internal documentation: Technical, Data Acquisition and Software notes

**MNRAS** Monthly Notices of the Royal Astronomical Society

**NewA** New Astronomy

## C.2 Acronyms used in the bibliography

---

**NewAR** New Astronomy Reviews

**NIM A** Nuclear Instruments and Methods A

**Nucl. Phys. Proc. Suppl.** Nuclear Physics B Proceedings Supplements

**PASJ** Publications of the Astronomical Society of Japan

**Phys. Let. B** Physics Letters B

**Sp. Sc. Rev.** Space Science Reviews

# References

- [AA96] Atoyan, A.M. and Aharonian, F. On the mechanisms of gamma radiation in the Crab Nebula. *MNRAS*, 278:525–541, 1996. Cited on page [22](#).
- [AAB06] Aharonian F., Akhperjanian A.G., and Bazer-Bachi A.R., et al. A low level of extragalactic background light as revealed by  $\gamma$ -rays from blazars. *Nature*, 440:1018–1021, 2006. Cited on page [17](#).
- [AB03] Aharonian, F. and Bogovalov, S.V. Exploring physics of rotation powered pulsars with sub-10 GeV imaging atmospheric Cherenkov telescopes. *NewA*, 8:85–103, 2003. Cited on page [22](#).
- [Abd09a] Abdo, A.A., et al. Fermi LAT Observations of LS I +61°303: First Detection of an Orbital Modulation in GeV Gamma Rays. *ApJ*, 701:L123–L128, 2009. Cited on page [26](#).
- [Abd09b] Abdo, A.A., et al. The First Fermi Large Area Telescope Catalog of Gamma-ray Pulsars. *ApJS*, Accepted for publication, 2009. Cited on page [30](#).
- [Abr04] Abraham, J., et al. Properties and performance of the prototype instrument for the Pierre Auger Observatory. *NIM A*, 523:50–95, 2004. Cited on page [6](#).
- [Abr07] Abraham, J., et al. Correlation of the Highest-Energy Cosmic Rays with Nearby Extragalactic Objects. *Science*, 318:938, 2007. Cited on page [6](#).
- [Abr09] Abraham, J., et al. Astrophysical Sources of Cosmic Rays and Related Measurements with the Pierre Auger Observatory. *Proceedings of the 31st International Cosmic Ray Conference, Lódź, Poland*, 2009. Cited on page [6](#).
- [Acc08] Acciari, V.A., et al. VERITAS Observations of the  $\gamma$ -Ray Binary LS I +61 303. *ApJ*, 679:1427–1432, 2008. Cited on page [26](#).

## REFERENCES

---

- [Acc09] Acciari, V.A., et al. Simultaneous Multiwavelength Observations of Markarian 421 During Outburst. *ApJ*, 703:169–178, 2009. Cited on pages [141](#), [150](#), [151](#), [153](#), [157](#), [158](#), and [159](#).
- [Ace09] Acero, F., et al. Detection of Gamma Rays from a Starburst Galaxy. *Science*, 326:1080, 2009. Cited on page [27](#).
- [Ach06] Achterberg, A., et al. On the selection of AGN neutrino source candidates for a source stacking analysis with neutrino telescopes. *Astrop. Phys.*, 26:282–300, 2006. Cited on page [38](#).
- [AD04] Atoyan, A. and Dermer, C.D. TeV Emission from the Galactic Center Black Hole Plerion. *ApJ*, 617:L123–L126, 2004. Cited on page [24](#).
- [AH98] Aharonian, F. and Heinzelmann, G. The HEGRA Experiment - Status and Recent Results. *Nucl. Phys. Proc. Suppl.*, 60B:193–198, 1998. Cited on page [31](#).
- [Aha00] Aharonian, F. Tev gamma rays from BL Lac objects due to synchrotron radiation of extremely high energy protons. *NewA*, 5:377–395, 2000. Cited on pages [46](#) and [203](#).
- [Aha01a] Aharonian, F. TeV blazars and cosmic infrared background radiation. *27th International Cosmic Ray Conference. Hamburg, Germany. Under the auspices of the IUPAP. Edited by R. Schlickeiser*, page 250, 2001. Cited on page [17](#).
- [Aha01b] Aharonian, F., et al. Reanalysis of the high energy cutoff of the 1997 Mkn 501 TeV energy spectrum. *A&A*, 366:62–67, 2001. Cited on page [185](#).
- [Aha02a] Aharonian, F., et al. TeV gamma rays from the blazar H 1426+428 and the diffuse extragalactic background radiation. *A&A*, 384:L23–L26, 2002. Cited on pages [169](#), [172](#), and [179](#).
- [Aha02b] Aharonian, F., et al. Variations of the TeV energy spectrum at different flux levels of Mkn 421 observed with the HEGRA system of Cherenkov telescopes. *A&A*, 393:89–99, 2002. Cited on pages [137](#) and [162](#).
- [Aha03] Aharonian, F., et al. Observations of H1426+428 with HEGRA. Observations in 2002 and reanalysis of 1999&2000 data. *A&A*, 403:523–528, 2003. Cited on pages [169](#) and [179](#).
- [Aha04a] Aharonian, F. *Very High Energy Cosmic Gamma Radiation*. World Scientific, 2004. Cited on pages [6](#) and [9](#).

## REFERENCES

---

- [Aha04b] Aharonian, F., et al. The Crab Nebula and Pulsar between 500 GeV and 80 TeV: Observations with the HEGRA Stereoscopic Air Cerenkov Telescopes. *ApJ*, 614:897–913, 2004. Cited on page [22](#).
- [Aha04c] Aharonian, F., et al. Very high energy gamma rays from the direction of Sagittarius A\*. *A&A*, 425:L13–L17, 2004. Cited on page [23](#).
- [Aha05a] Aharonian, F., et al. Discovery of the Binary Pulsar PSR B1259-63 in Very-High-Energy Gamma Rays around Periastron with H.E.S.S. *A&A*, 442:1–10, 2005. Cited on page [25](#).
- [Aha05b] Aharonian, F., et al. Discovery of Very High Energy Gamma Rays Associated with an X-ray Binary. *Science*, 309:746–749, 2005. Cited on page [25](#).
- [Aha05c] Aharonian, F., et al. Very high energy gamma rays from the composite SNR G 0.9+0.1. *A&A*, 432:L25–L29, 2005. Cited on page [23](#).
- [Aha05d] Aharonian, F., et al (H.E.S.S. Collab.). Observations of Mkn 421 in 2004 with HESS at large zenith angles. *A&A*, 437:95–99, 2005. Cited on pages [137](#) and [160](#).
- [Aha06a] Aharonian, F., et al. A detailed spectral and morphological study of the gamma-ray supernova remnant RX J1713.7-3946 with HESS. *A&A*, 449:223–242, 2006. Cited on page [23](#).
- [Aha06b] Aharonian, F., et al. Discovery of very-high-energy  $\gamma$ -rays from the Galactic Centre ridge. *Nature*, 439:695–698, 2006. Cited on page [26](#).
- [Aha08] Aharonian, F., et al. Observations of the Sagittarius dwarf galaxy by the HESS experiment and search for a dark matter signal. *Astrop. Phys.*, 29:55–62, 2008. Cited on page [27](#).
- [Aha09a] Aharonian, F., et al. H.E.S.S. upper limit on the very high energy gamma-ray emission from the globular cluster 47 Tucanae. *A&A*, Accepted for publication, 2009. Cited on page [28](#).
- [Aha09b] Aharonian, F., et al. Simultaneous Observations of PKS 2155-304 with HESS, Fermi, RXTE, and Atom: Spectral Energy Distributions and Variability in a Low State. *ApJ*, 696:150–155, 2009. Cited on page [164](#).
- [Alb06a] Albert, J., et al. Observation of Gamma Rays from the Galactic Center with the MAGIC Telescope. *ApJ*, 638:L101–104, 2006. Cited on pages [24](#), [25](#), and [148](#).

## REFERENCES

---

- [Alb06b] Albert, J., et al. Variable Very-High-Energy Gamma-Ray Emission from the Microquasar LS I +61 303. *Science*, 312:1771–1773, 2006. Cited on pages [25](#) and [26](#).
- [Alb07a] Albert, J., et al. Discovery of VHE Gamma Radiation from IC 443 with the MAGIC Telescope. *ApJ*, 664:L87–L90, 2007. Cited on pages [23](#) and [24](#).
- [Alb07b] Albert, J., et al. MAGIC upper limits on high energy emission from GRBs. *ApJ*, 667:358–366, 2007. Cited on page [21](#).
- [Alb07c] Albert, J., et al. Observations of Mkn 421 with the MAGIC Telescope. *ApJ*, 663:125–138, 2007. Cited on pages [43](#), [160](#), [161](#), [163](#), [164](#), and [195](#).
- [Alb07d] Albert, J., et al. Unfolding of differential energy spectra in the MAGIC experiment. *NIM A*, 494:494–506, 2007. Cited on page [94](#).
- [Alb07e] Albert, J., et al. Variable Very High Energy  $\gamma$ -Ray Emission from Markarian 501. *ApJ*, 669:862–883, 2007. Cited on pages [146](#), [185](#), [191](#), [197](#), [204](#), and [205](#).
- [Alb07f] Albert, J., et al. Very High Energy Gamma-ray Radiation from the Stellar-mass Black Hole Cygnus X-1. *ApJ*, 665:L51, 2007. Cited on page [25](#).
- [Alb08a] Albert, J., et al. FADC Signal reconstruction for the MAGIC telescope. *NIM A*, 594:407–419, 2008. Cited on page [118](#).
- [Alb08b] Albert, J., et al. Implementation of the Random Forest Method for the Imaging Atmospheric Cherenkov Telescope MAGIC. *NIM A*, 588:424–432, 2008. Cited on page [80](#).
- [Alb08c] Albert, J., et al. Signal Reconstruction for the MAGIC Telescope. *NIM A*, 594:407–419, 2008. Cited on page [73](#).
- [Alb08d] Albert, J., et al. Systematic search for VHE gamma-ray emission from X-ray bright high-frequency BL Lac objects. *ApJ*, 681:944–953, 2008. Cited on page [170](#).
- [Alb08e] Albert, J., et al. Upper limit for gamma-ray emission above 140 GeV from the dwarf spheroidal galaxy Draco. *ApJ*, 679:428–431, 2008. Cited on page [27](#).
- [Alb08f] Albert, J., et al. VHE  $\gamma$ -Ray Observation of the Crab Nebula and its Pulsar with the MAGIC Telescope. *ApJ*, 674:1037–1055, 2008. Cited on pages [69](#), [71](#), [79](#), [97](#), [142](#), [143](#), [148](#), [190](#), and [192](#).

## REFERENCES

---

- [Alb09] Albert, J., et al. Periodic very high energy gamma-ray emission from LS I +61 303 observed with the MAGIC telescope. *ApJ*, 693:303–310, 2009. Cited on page [26](#).
- [Ale10] Aleksić, J. et al. Multiwavelength observation of the blazar 1ES1426+428 in May-June 2008. *In preparation*, 2010. Cited on pages [174](#), [181](#), and [182](#).
- [Ali08] Aliu, E., et al. Observation of Pulsed  $\gamma$ -Rays Above 25 GeV from the Crab Pulsar with MAGIC. *Science*, 322:1221, 2008. Cited on pages [23](#), [60](#), [66](#), and [71](#).
- [Ali09a] Aliu, E. et al. Improving the performance of the single-dish Cherenkov telescope MAGIC through the use of signal timing. *Astrop. Phys.*, 30:293–305, 2009. Cited on pages [76](#), [77](#), and [140](#).
- [Ali09b] Aliu, E., et al. Magic upper limits on the VHE gamma-ray emission from the satellite galaxy Willman 1. *ApJ*, 697:1299–1304, 2009. Cited on page [27](#).
- [Ama02] Amati, L., et al. Intrinsic spectra and energetics of BeppoSAX Gamma-Ray Bursts with known redshifts. *A&A*, 390:81, 2002. Cited on pages [21](#) and [161](#).
- [Ame99] Amenomori, M., et al. Observation of Multi-TeV Gamma Rays from the Crab Nebula using the Tibet Air Shower Array. *ApJ*, 525:L93–L96, 1999. Cited on page [31](#).
- [AN05] Aharonian, F. and Neronov, A. High-energy Gamma Rays from the Massive Black Hole in the Galactic Center. *ApJ*, 619:306–313, 2005. Cited on page [23](#).
- [And06] Anderhub, H., et al. Search for VHE Gamma-ray Emission from the Globular Cluster M13 with the MAGIC Telescope. *ApJ*, 702:266–269, 2006. Cited on page [28](#).
- [And09a] Anderhub H., et al. Correlated X-ray and Very High Energy emission in the gamma-ray binary LS I +61 303. *ApJ*, 706:L27–L30, 2009. Cited on page [26](#).
- [And09b] Anderhub, H., et al. Magic TeV Gamma-Ray Observations of Markarian 421 during Multiwavelength Campaigns in 2006. *Submitted to A&A*, 2009. Cited on pages [157](#) and [159](#).

## REFERENCES

---

- [And09c] Anderhub, H., et al. Simultaneous Multiwavelength observation of Mkn 501 in a low state in 2006. *ApJ*, 705:1624–1631, 2009. Cited on pages 185, 191, and 198.
- [And10] Anderhub, H., et al. MAGIC Gamma-Ray Observation of the Perseus Galaxy Cluster. *ApJ*, 710:634–647, 2010. Cited on page 28.
- [Ant93] Antonucci, R. Unified models for active galactic nuclei and quasars. *Annual Review of Astronomy and Astrophysics*, 31:437–521, 1993. Cited on page 36.
- [Apa01] Apada, M., et al. Internal shocks in the jets of radio-loud blazars. *MNRAS*, 325:1559–1570, 2001. Cited on page 162.
- [Arq02] Arqueros, F., et al. Very high-energy gamma-ray observations of the Crab nebula and other potential sources with the GRAAL experiment. *Astrop. Phys.*, 17:293–318, 2002. Cited on page 31.
- [AS79] Arons, J. and Scharlemann, E.T. Pair formation above pulsar polar caps - Structure of the low altitude acceleration zone. *ApJ*, 231:854–879, 1979. Cited on page 23.
- [Atk00] Atkins, R., et al. Evidence for TeV Emission from GRB 970417a. *ApJ*, 533:L119, 2000. Cited on page 21.
- [Atw09] Atwood, W., et al. The Large Area Telescope on the Fermi Gamma-ray Space Telescope Mission. *ApJ*, 697:1071–1102, 2009. Cited on page 30.
- [BA00] Bogovalov, R.K. and Aharonian, F. Very-high-energy gamma radiation associated with the unshocked wind of the Crab pulsar. *MNRAS*, 313:504–514, 2000. Cited on page 22.
- [Bar05] Barthelmy, S.D., et al. The Swift Ultra-Violet/Optical Telescope. *Sp. Sc. Rev.*, 120:143–164, 2005. Cited on page 174.
- [BB03] Bednarek, W. and Bartosik, M. Gamma-rays from the pulsar wind nebulae. *A&A*, 405:689–702, 2003. Cited on page 22.
- [BC02] Boettcher, M. and Chiang, J. X-Ray Spectral Variability Signatures of Flares in BL Lacertae Objects. *ApJ*, 581:127–142, 2002. Cited on pages 44, 163, and 203.
- [BD09] Bretz, T. and Dorner, D. MARS: The Cherenkov observatory edition. *AIP Conf. Proc.*, 1085:664–669, 2009. Cited on page 69.

## REFERENCES

---

- [Bed93] Bednarek, W. On the gamma-ray emission from 3C 279. *ApJ*, 402:L29–L32, 1993. Cited on pages [46](#) and [203](#).
- [BGB07] Blasi, P., Gabici, S., and Brunetti, G. Gamma Rays from Clusters of Galaxies. *International Journal of Modern Physics A*, 22:681–706, 2007. Cited on page [27](#).
- [Bie02] Biermann, P.L., et al. Single and binary Black Holes and their active environment. *Proceedings of the 7eme Colloquium Cosmologie, ‘High Energy Astrophysics from and for Space’, Paris, June*, 2002. Cited on page [38](#).
- [Big75] Bignami, G.F., et al. The COS-B experiment for gamma-ray astronomy. *Space Science Instrumentation*, 1:245–268, 1975. Cited on page [28](#).
- [Bł05] Błażejowski, M., et al. A Multiwavelength View of the TeV Blazar Markarian 421: Correlated Variability, Flaring, and Spectral Evolution. *ApJ*, 630:130–141, 2005. Cited on pages [45](#), [137](#), [154](#), [155](#), [163](#), [164](#), [196](#), and [204](#).
- [Bos06] Bosch-Ramon, V., et al. The radio to TeV orbital variability of the microquasar LS I +61 303. *A&A*, 459:L25–L28, 2006. Cited on page [25](#).
- [Bou08] Bouvier, A., et al. GRB080825C: Fermi-LAT observations. *GRB Coordinates Network*, 8183:1, 2008. Cited on pages [21](#) and [30](#).
- [Bre01] Breiman, L. Random Forests. *Machine Learning*, 45:5–32, 2001. Cited on page [80](#).
- [Bri01] Brinkmann, W., et al. XMM-Newton observations of Markarian 421. *A&A*, 365:L161–L167, 2001. Cited on page [157](#).
- [BRW71] Browning R., Ramsden D., and Wright P. Np 0532-Pulsed gamma rays above 50 MeV. *Nature*, 232:99, 1971. Cited on page [28](#).
- [BS07] Bednarek, W. and Sitarek, J. High-energy  $\gamma$ -rays from globular clusters. *MNRAS*, 377:920–930, 2007. Cited on page [28](#).
- [Bur05] Burrows, D.N., et al. The Swift X-Ray Telescope. *Sp. Sc. Rev.*, 120:165–195, 2005. Cited on page [174](#).
- [BW03] Bretz, T. and Wagner, R.M. The MAGIC Analysis and Reconstruction Software. *Proceedings of the 28th International Cosmic Ray Conference, Tsukuba, japan*, 5:2947–2950, 2003. Cited on page [69](#).

## REFERENCES

---

- [Car89] Cardelli, J. A., et al. The relationship between infrared, optical, and ultraviolet extinction. *ApJ*, 345:245–256, 1989. Cited on page [150](#).
- [Car09] Carmona, E., et al. A Flexible High Demand Storage System for MAGIC-I and MAGIC-II using GFS. *Proceedings of the 31st International Cosmic Ray Conference, Lódź, Poland*, 2009. Cited on page [126](#).
- [Cat97] Catanese, M., et al. Detection of Gamma Rays with  $E > 100$  MeV from BL Lacertae. *ApJ*, 480:562, 1997. Cited on page [185](#).
- [CCM99] Claspy, W.P., Collins II, G.W., and Martin, J.C. A Reinterpretation of Historical References to the Supernova of A.D. 1054. *Publications of the Astronomical Society of the Pacific*, 111:871–880, 1999. Cited on page [71](#).
- [CGK68] Clark, G.W., Garmire, G.P., and Kraushaar, W.L. Observation of High-Energy Cosmic Gamma Rays. *ApJ*, 153:L202, 1968. Cited on page [28](#).
- [CGS09] Cortina, J., Goebel, F., and Schweizer, T. Technical Performance of the MAGIC Telescopes. *Proceedings of the 31st International Cosmic Ray Conference, Lódź, Poland*, 2009. Cited on pages [64](#), [65](#), and [66](#).
- [CHR86] Cheng, K.S., Ho, C., and Ruderman, M. Energetic radiation from rapidly spinning pulsars. i - Outer magnetosphere gaps. ii - VELA and Crab. *ApJ*, 300:500–539, 1986. Cited on page [23](#).
- [CO06] Cortina, J. and Oya, I. Dailycheck Manual. *MAGIC-TDAS*, 06-02, 2006. Cited on page [121](#).
- [Coa06] Coarasa, J.A. Online PC Farms for MAGIC-II and Data Transfer. *MAGIC Collaboration Meeting, Tenerife*, 2006. Cited on page [126](#).
- [Col97] CASA-MIA Collab. A High Statistics Search for Ultra-High Energy Gamma-Ray Emission from Cygnus X-3 and Hercules X-1. *Phys.Rev.*, D55:1714–1731, 1997. Cited on page [31](#).
- [Col03] The Milagro Collaboration. Observation of TeV Gamma Rays from the Crab Nebula with Milagro Using a New Background Rejection Technique. *ApJ*, 595:803–811, 2003. Cited on page [31](#).
- [Col08] The MAGIC Collaboration. Very high energy gamma rays from a distant quasar: How transparent is the Universe? *Science*, 320:23–33, 2008. Cited on pages [16](#), [17](#), [18](#), [45](#), [169](#), and [202](#).

## REFERENCES

---

- [Cos97] Costa, E., et al. Discovery of an X-ray afterglow associated with the big  $\gamma$ -ray burst of 28 February 1997. *Nature*, 387:783–785, 1997. Cited on page [19](#).
- [Cui04] Cui, W. X-Ray Flaring Activity of Markarian 421. *ApJ*, 605:662–669, 2004. Cited on page [157](#).
- [Dau97] Daum, A., et al (HEGRA Collab.). First results on the performance of the HEGRA IACT array. *Astrop. Phys.*, 8:1–11, 1997. Cited on page [67](#).
- [De 08] De los Reyes, R. *Search for gamma-ray emission from pulsars with the MAGIC telescope: sensitivity studies, data check and data analysis*. PhD thesis, Universidad Complutense de Madrid, 2008. Cited on pages [98](#), [104](#), [122](#), [136](#), [201](#), and [202](#).
- [Del09] Delgado, C. The background model of CELESTINA. *MAGIC-TDAS*, 09–04, 2009. Cited on page [91](#).
- [dH92] de Jager, O.C. and Harding, A.K. The expected high-energy to ultra-high-energy gamma-ray spectrum of the Crab Nebula. *ApJ*, 396:161–172, 1992. Cited on page [21](#).
- [Dja02] Djannati-Ataï, A. Detection of the BL Lac object 1ES 1426+428 in the Very High Energy gamma-ray band by the CAT Telescope from 1998-2000. *A&A*, 391:L25–L28, 2002. Cited on page [169](#).
- [DK05] Dwek, E. and Krennrich, F. Simultaneous Constraints on the Spectrum of the Extragalactic Background Light and the Intrinsic TeV Spectra of Markarian 421, Markarian 501, and H1426+428. *ApJ*, 618:657–674, 2005. Cited on pages [15](#) and [169](#).
- [DO06] De los Reyes, R. and Oya, I. Magic data check and on-site analysis program. *MAGIC-TDAS*, 06-11, 2006. Cited on pages [136](#) and [202](#).
- [Dom05] Domingo-Santamaría, E., et al. The DISP analysis method for point-like or extended gamma source searches/studies with the MAGIC Telescope. *Proceedings of the 29h International Cosmic Ray Conference, Pune, India*, 5:363–366, 2005. Cited on page [85](#).
- [Don09] Donnarumma, I., et al. The June 2008 flare of Markarian 421 from optical to TeV energies. *ApJ*, 691:L13–L19, 2009. Cited on pages [162](#), [164](#), and [195](#).

## REFERENCES

---

- [DR07] Di Sciascio, G. and Rossi, E. Measurement of the angular resolution of the ARGO-YBJ detector. *in Proc. 30th Int. Cosmic Ray Conf. Merida, Mexico*, 2007. Cited on page [31](#).
- [dR09] de Naurois, M. and Rolland, M. A high performance likelihood reconstruction of gamma-rays for Imaging Atmospheric Cherenkov Telescopes. *Astrop. Phys.*, 32:231–252, 2009. Cited on page [80](#).
- [DS93] Dermer C.D. and Schlickeiser R. Model for the High-Energy Emission from Blazars. *ApJ*, 416:458, 1993. Cited on page [45](#).
- [Dur83] Dury, L.O’C. An introduction to the theory of diffusive shock acceleration of energetic particles in tenuous plasmas. *Rep. Prog. Phys.*, 46:973–1027, 1983. Cited on page [23](#).
- [Feg09] Fegan, S.J., et al. Fermi observations of TeV-selected AGN. *ApJ*, 707:1310–1333, 2009. Cited on page [196](#).
- [Fic75] Fichtel, C.E. et al. High-energy gamma-ray results from the second small astronomy satellite. *ApJ*, 198:163–182, 1975. Cited on page [28](#).
- [Fli06] Flix Molina, J. *Observation of gamma-rays from the galactic center with the MAGIC telescope Indirect searches of supersymmetric dark matter*. PhD thesis, Universitat Autònoma de Barcelona, 2006. Cited on page [104](#).
- [FMB93] Falcke, H., Mannheim, K., and Biermann, P.L. The Galactic Center radio jet. *A&A*, 278:L1–L4, 1993. Cited on page [24](#).
- [FMB95] Falcke, H., Malkan, M.A., and Biermann, P.L. The jet-disk symbiosis. II. Interpreting the radio/uv correlations in quasars. *A&A*, 298:375, 1995. Cited on page [39](#).
- [Fom94] Fomin, V.P., et al. New methods of atmospheric Cherenkov imaging for gamma-ray astronomy i. The false source method. *Astrop. Phys.*, 2:137–150, 1994. Cited on page [85](#).
- [For99] Fortson, L.F., et al. Composition Results at the Knee from CASA-BLANCA. *Proceedings of the 26th International Cosmic Ray Conference. August 17-25, 1999. Salt Lake City, Utah, USA. Under the auspices of the IUPAP*, 3:125, 1999. Cited on page [31](#).
- [Fos98] Fossati, G., et al. A unifying view of the spectral energy distributions of blazars. *MNRAS*, 299:433–448, 1998. Cited on pages [46](#) and [169](#).

## REFERENCES

---

- [Fos08] Fossati, G., et al. Multiwavelength Observations of Markarian 421 in 2001 March: An Unprecedented View on the X-Ray/TeV Correlated Variability. *ApJ*, 667:906–925, 2008. Cited on pages [137](#), [160](#), and [163](#).
- [FR74] Fanaroff, J.M. and Riley, J.M. The morphology of extragalactic radio sources of high and low luminosity. *MNRAS*, 167:31–36, 1974. Cited on page [39](#).
- [FRV08] Franceschini, A., Rodighiero, G, and Vaccari A. Extragalactic optical-infrared background radiation, its time evolution and the cosmic photon-photon opacity. *A&A*, 487:837–852, 2008. Cited on pages [16](#), [143](#), [151](#), [162](#), [164](#), [169](#), [172](#), [189](#), [191](#), [195](#), and [198](#).
- [FV04] Falcone, A.D. and VERITAS collab. X-ray and TeV observations of the extreme BL Lac AGN H1426+428 during 2002. *NewAR*, 48:415–417, 2004. Cited on pages [169](#) and [179](#).
- [Gai90] Gaisser, T.K. *Cosmic Rays and Particle Physics*. Cambridge University Press., 1990. Cited on pages [50](#) and [51](#).
- [Gai96] Gaidos, J.A., et al. Extremely rapid bursts of TeV photons from the active galaxy Markarian 421. *Nature*, 383:319–320, 1996. Cited on page [137](#).
- [Gar06] Garczarczyk, M. *First Observations of the GRB Prompt and Early Afterglow Emission Phase at 100 GeV Energy Regime with the 17 Diameter MAGIC Imaging Atmospheric Cherenkov Telescope*. PhD thesis, Universitt Rostock, 2006. Cited on page [61](#).
- [Gau06] Gaug, M. *Calibration of the MAGIC telescope and observation of gamma-ray bursts*. PhD thesis, Universitat Autonoma de Barcelona, 2006. Cited on pages [66](#), [75](#), [115](#), [119](#), and [132](#).
- [GB05] Gaug, M. and Bartko, H., et al. Calibration of the MAGIC Telescope. *Proceedings of the 25th International Cosmic Ray Conference, Durban*, 00:101–106, 2005. Cited on page [75](#).
- [Ghi98] Ghisellini, G., et al. A theoretical unifying scheme for gamma-ray bright blazars. *MNRAS*, 301:451–468, 1998. Cited on page [46](#).
- [Ghi99] Ghisellini, G. Extreme blazars. *Astrop.Phys.*, 11:11–18, 1999. Cited on page [169](#).
- [Gli06] Gliozi, M., et al. Long-Term X-Ray and TeV Variability of Mrk 501. *ApJ*, 646:61–75, 2006. Cited on page [185](#).

## REFERENCES

---

- [GM08] Gaug M. and Moralejo, A. A handbook of the standard MAGIC analysis chain. 2008. Cited on page [133](#).
- [Goe04] Goebel, F. Users guide and reference manual for the Data Acquisition and the FADC system of the MAGIC telescope. *MAGIC-TDAS*, 04-01, 2004. Cited on page [109](#).
- [Goe08a] Goebel, F., et al. Long term monitoring of bright TeV Blazars with the MAGIC telescope. *Proceedings of the 30th International Cosmic Ray Conference, Merida, Mexico*, 3:1025–1028, 2008. Cited on page [137](#).
- [Goe08b] Goebel, F., et al. Upgrade of the MAGIC Telescope with a Multiplexed Fiber-Optic 2GSamples/s FADC Data Acquisition System system. *Proceedings of the 30th International Cosmic Ray Conference, Merida, Mexico*, 3:1481–1484, 2008. Cited on page [138](#).
- [Gui09] Guillemot, L., et al. Discovery of a population of gamma-ray milisecond pulsars by Fermi. *Proceedings 44th Rencontres de Moriond 7 February Italy*, 2009. Cited on page [28](#).
- [Hal86] Halley, E. A Discourse of the Rule of the Decrease of the Height of the Mercury in the Barometer, according as Places are elevated above the Surface of the Earth, with an Attempt to discover the true Reason of the Rising and Falling of the Mercury, upon change of Weather. *Philos. Trans. R. Soc. London*, 16:104–116, 1686. Cited on page [56](#).
- [Hal03] Hal, T.A., et al. Search for TeV Emissions from Pulsars in Binary Systems. *ApJ*, 583:853–860, 2003. Cited on page [28](#).
- [Han02] Hanna, D.S., et al. The STACEE-32 Ground Based Gamma-Ray Detector. *NIM A*, 491:126, 2002. Cited on page [31](#).
- [Har99] Hartman, R.C., et al. The Third EGRET Catalog of High-Energy Gamma-Ray Sources. *ApJS*, 123:79–202, 1999. Cited on page [202](#).
- [He09] HESS Collaboration: Aharonian, F. and et al. Discovery of very high energy gamma-ray emission from Centaurus A with H.E.S.S. *ApJ*, 695:L40–L44, 2009. Cited on page [40](#).
- [Hes12] Hess, V.F. Observations of the penetrating radiation on seven balloon flights. *Physik Z.*, 13:1084, 1912. Cited on page [5](#).
- [Hil85] Hillas, A.M. Cherenkov Images of EAS produced by primary gamma rays and by nuclei. *Proceedings of the 19th International Cosmic Ray Conference, La Jolla*, 3:445, 1985. Cited on pages [77](#), [121](#), and [133](#).

## REFERENCES

---

- [HKC98] Heck, D., Knapp, J., and Capdevielle, J.N., et al. CORSIKA: a Monte Carlo code to simulate extensive air showers. 1998. Cited on page 71.
- [Hor02] Horan, D., et al. (Whipple Collab.). Detection of the BL Lacertae Object H1426+428 at TeV Gamma-Ray Energies. *ApJ*, 571:753–762, 2002. Cited on pages 169, 172, 179, and 180.
- [Hor09] Horan, D., et al. (Whipple Collab.). Multiwavelength Observations of Markarian 421 in 2005-2006. *ApJ*, 695:596–618, 2009. Cited on pages 141 and 164.
- [Hru08] Hrupec, D. *Extragalactic sources of rapidly variable high energy gamma radiation*. PhD thesis, University of Zagreb, 2008. Cited on pages 146 and 147.
- [Hsu09] Hsu, C.-C., et al. Monitoring of bright blazars with MAGIC telescope. *Proceedings of the 31st International Cosmic Ray Conference, Lódź, Poland*, 2009. Cited on page 137.
- [Hyv07] Hyvönen, T., et al. The stellar content of low redshift BL Lacertae host galaxies from multicolour imaging. *A&A*, 476:723–734, 2007. Cited on page 174.
- [Ito02] Itoh, C., et al. Detection of diffuse TeV gamma-ray emission from the neaby starburst galaxy NGC 253. *A&A*, 396:L1–L4, 2002. Cited on page 27.
- [Jah96] Jahoda, K., et al. In-orbit performance and calibration of the Rossi X-ray Timing Explorer (RXTE) Proportional Counter Array (PCA). *Proc. SPIE*, 2808:59–70, 1996. Cited on page 146.
- [Kab07] Kabuki, S., et al. CANGAROO III Search for Gamma Rays from Centaurus A and the  $\omega$  Centauri Region. *ApJ*, 668:968–973, 2007. Cited on page 28.
- [Kat06] Katarzyński, K., et al. Stochastic particle acceleration and synchrotron self-compton radiation in tev blazars. *A&A*, 453:47–56, 2006. Cited on page 161.
- [KBMH04] Kneiske, T.M., Bretz, T., Mannheim, K., and Hartmann, D.H. Implications of cosmological gamma-ray absorption. ii. Modification of gamma-ray spectra. *A&A*, 413:807–815, 2004. Cited on page 17.
- [KC84a] Kennel, C.F. and Coroniti, F.V. Confinement of the Crab pulsar’s wind by its supernova remnant. *ApJ*, 283:694–709, 1984. Cited on page 21.

## REFERENCES

---

- [KC84b] Kennel, C.F. and Coroniti, F.V. Magnetohydrodynamic model of Crab nebula radiation. *ApJ*, 283:710–730, 1984. Cited on page 21.
- [KD08] Kneiske, T.M. and Dole, H. A strict lower-limit EBL: Applications on gamma-ray absorption. *Proceedings of AIP conf.*, 1085:620–623, 2008. Cited on pages 15, 16, 17, 162, and 169.
- [Kel89] Kellermann, et al. VLA observations of objects in the Palomar Bright Quasar Survey. *AJ*, 98:1195–1207, 1989. Cited on page 39.
- [KGTe06] Katarzyński, K., Ghisellini G., Tavecchio F., and et al. Hard TeV spectra of blazars and the constraints to the infrared intergalactic background. *MNRAS*, 368:L52–L56, 2006. Cited on page 18.
- [Kil07] Kildea, J. et al. The Whipple Observatory 10 m gamma-ray telescope, 1997 2006. *Astrop. Phys.*, 28:182–195, 2007. Cited on page 150.
- [KM99] Kirk, J.G. and Mastichiadis A. Variability patterns of synchrotron and inverse Compton emission in blazars. *Astrop. Phys.*, 11:45–48, 1999. Cited on pages 44 and 165.
- [KMH02] Kneiske, T.M., Mannheim, K., and Hartmann, D.H. Implications of cosmological gamma-ray absorption. i. Evolution of the metagalactic radiation field. *A&A*, 368:1–11, 2002. Cited on pages 16 and 17.
- [Kon03] Konopelko, A., et al. Modeling the TeV Gamma-Ray Spectra of Two Low-Redshift Active Galactic Nuclei: Markarian 501 and Markarian 421. *ApJ*, 597:851–959, 2003. Cited on page 163.
- [Kos04] Kosack, K., et al. TeV Gamma-Ray Observations of the Galactic Center. *ApJ*, 608:L97–L100, 2004. Cited on page 23.
- [Kra01] Krawczynski, H., et al. Simultaneous X-Ray and TeV Gamma-Ray Observation of the TeV Blazar Markarian 421 during 2000 February and May. *ApJ*, 559:187–195, 2001. Cited on pages 45 and 137.
- [Kra04] Krawczynski, H., et al. Multiwavelength Observations of Strong Flares from the TeV Blazar 1ES 1959+650. *ApJ*, 601:151–164, 2004. Cited on pages 43, 44, and 203.
- [Kra09] Kranich, D., et al. Multiwavelength Observations of Mrk 501 in 2008. *Proceedings of the 31st International Cosmic Ray Conference, Lódź, Poland*, 2009. Cited on page 185.
- [Kre02] Krennrich, F., et al. Discovery of spectral variability of markarian 421 at tev energies. *ApJ*, 575:L9–L13, 2002. Cited on pages 137 and 160.

## REFERENCES

---

- [KSO73] Klebesadel, R., Strong, I., and Olson, R. Observations of gamma-ray bursts of cosmic origin. *ApJ*, 182:L85, 1973. Cited on page [19](#).
- [LeB03] LeBohec, S., et al. Search for a WIMP Annihilation Signature in the Core of the Globular Cluster M15. *Proceedings 28th International Cosmic Ray Conference. July 31-August 7, Trukuba, Japan*, 2003. Cited on page [28](#).
- [Leo09] Leonardo, E., Bose, D., Mankuzhiyil, N., Oya, I., et al. Multiwavelength observation of the blazar 1ES1426+428 in May-June 2008. *Proceedings of the 31st International Cosmic Ray Conference, Lódź, Poland*, 2009. Cited on pages [174](#), [181](#), and [182](#).
- [Lic08] Lichti, G.G. et al. INTEGRAL observations of the blazar Mrk 421 in outburst. Results of a multi-wavelength campaign. *A&A*, 486:721–734, 2008. Cited on pages [138](#), [148](#), and [149](#).
- [Lie05] Liebing, P. Documentation of the DAQ/CC data quality program. *MAGIC internal documentation*, 2005. Cited on page [109](#).
- [LM83] Li, T.-P. and Ma, Y.-Q. Analysis methods for results in gamma-ray astronomy. *ApJ*, 272:317–324, 1983. Cited on pages [87](#), [88](#), [140](#), [172](#), and [187](#).
- [Lon92] Longair, M.S. *High Energy Astrophysics, vol 1*. Cambridge University Press., 1992. Cited on page [6](#).
- [Maj05] Majumdar, P., et al. Monte Carlo simulation for the MAGIC telescope. *Proceedings of the 29th International Cosmic Ray Conference, Pune, India*, 5:203, 2005. Cited on page [72](#).
- [Mar05] Marleu, P. Intermediate Energy Observations with CACTUS. *Proc. of Cherenkov 2005, Paris, France*, 2005. Cited on page [31](#).
- [Mas01] Mason, K.O., et al. The XMM-Newton optical/UV monitor telescope. *A&A*, 365:L36–L44, 2001. Cited on pages [138](#) and [149](#).
- [Mas04] Massaro, E., et al.. Log-parabolic spectra and particle acceleration in the BL Lac object Mkn 421: Spectral analysis of the complete BeppoSAX wide band X-ray data set. *A&A*, 413:489–503, 2004. Cited on pages [94](#) and [159](#).
- [Mat09] Matsuoka, M., et al. The MAXI Mission on the ISS: Science and Instruments for Monitoring All-Sky X-Ray Images. *Publications of the Astronomical Society of Japan*, 61:999–1010, 2009. Cited on page [207](#).

## REFERENCES

---

- [May39] Mayall, N.U. The Crab Nebula, a Probable Supernova. *Astronomical Society of the Pacific Leaflets*, 3:145, 1939. Cited on page [71](#).
- [Maz05] Mazin, D., et al. Concept of a Global Network of Cherenkov Telescopes (GNCT) and first joint observations of H.E.S.S. and MAGIC. *Proceedings of the 29th International Cosmic Ray Conference, Pune, India*, 4:331–334, 2005. Cited on page [148](#).
- [Maz08] Mazin, D. Constraints on Extragalactic Background Light from Cherenkov telescopes: status and perspectives for the next 5 years. *Proceedings of the Conference "Science with the New Generation of High Energy Gamma-Ray Experiments*, 2008. Cited on page [18](#).
- [MB92] Mannheim K. and Biermann P.L. Gamma-ray flaring of 3C 279 - A proton-initiated cascade in the jet? *A&A*, 253:L21–L24, 1992. Cited on pages [46](#) and [203](#).
- [Mes06] Meszárós, P. Gamma-ray Bursts. *Rept. Prog. Phys.*, 69:2259–2322, 2006. Cited on page [20](#).
- [MG07] Mazin, D. and Goebel, F. Break in the Very High Energy Spectrum of PG 1553+113: New Upper Limit on Its Redshift?. *ApJ*, 655:L13–L16, 2007. Cited on pages [159](#) and [189](#).
- [MGC92] Maraschi, L., Ghisellini, G., and Celotti, A. A jet model for the gamma-ray emitting blazar 3C 279. *ApJ*, 397:L5–L9, 1992. Cited on pages [44](#) and [203](#).
- [Mit07] Mitsuda, K., et al. Suzaku Observations of the Local and Distant Hot ISM. *PASJ*, 59:141–150, 2007. Cited on pages [138](#) and [174](#).
- [MJ08] MAGIC Collaboration and J. Ellis, et al. Probing quantum gravity using photons from a flare of the active galactic nucleus Markarian 501 observed by the MAGIC telescope. *Phys. Lett. B*, 668:253–257, 2008. Cited on page [206](#).
- [MKU01] Meier, D.L., Koide, S., and Uchida, Y. Magnetohydrodynamic Production of Relativistic Jets. *Science*, 291:84–92, 2001. Cited on page [44](#).
- [ML97] Mirzoyan, R. and Lorenz, E. On the Calibration Accuracy of Light Sensors in Atmospheric Cherenkov, Fluorescence and Neutrino Experiments. *Proceedings of the 25th International Cosmic Ray Conference, Durban*, VII:265–268, 1997. Cited on page [75](#).

## REFERENCES

---

- [MO10] Mirabal, N. and Oya, I. Correlating Fermi gamma-ray sources with ultra-high energy cosmic rays. *Accepted in MNRAS*, 2010. Cited on page [6](#).
- [MP01] Mücke, A and Protheroe R.J. A proton synchrotron blazar model for flaring in Markarian 501. *Astrop. Phys.*, 15:121–136, 2001. Cited on pages [46](#) and [203](#).
- [MP07] Meucci, M. and Paoletti, R., et al. The trigger system of the magic telescope: on-line selection strategies for cherenkov telescopes. *IEEE Trans. Nucl. Sci*, 54, no 2, is. 1–2:404–409, 2007. Cited on pages [60](#) and [64](#).
- [MR07] Mazin, D. and Raue, M. New limits on the density of the extragalactic background light in the optical to the far infrared from the spectra of all known TeV blazars. *A&A*, 471:439–452, 2007. Cited on pages [17](#) and [169](#).
- [MT81] Maraschi, L. and Treves, A. A model for LS I 61° 303. *MNRAS*, 194:1–5, 1981. Cited on page [26](#).
- [MZ09] Maxham, A. and Zhang, B. Modeling Gamma-Ray Burst X-Ray Flares Within the Internal Shock Model. *ApJ*, 707:1623–1633, 2009. Cited on page [161](#).
- [ND09] Nieto, D. and Doro, M. Calculation of flux upper limits for a general spectrum. *Private communication*, 2009. Cited on page [96](#).
- [Nil03] Nilsson, K., et al. R-band imaging of the host galaxies of RGB BL Lacertae objects. *A&A*, 400:95–118, 2003. Cited on page [174](#).
- [Nil07] Nilsson, K., et al. Host galaxy subtraction of TeV candidate BL Lacertae objects. *A&A*, 475:199–207, 2007. Cited on pages [146](#), [189](#), and [191](#).
- [Nis99] Nishiyama, T. Detection of a new TeV gamma-ray source of BL Lac object 1ES 1959+650. *Proceedings of the 26th International Cosmic Ray Conference, Salt Lake City, Utah, USA.*, page 370, 1999. Cited on page [184](#).
- [NVT08] Nieppola, E., Valtaoja, E., and Tornikoski, M., et al. Blazar sequence – an artefact of Doppler boosting. *A&A*, 488:867–872, 2008. Cited on page [47](#).

## REFERENCES

---

- [OBS91] O'Dea, C.P., Baum, S.A., and Stanghellini, C. What are the gigahertz peaked-spectrum radio sources? *ApJ*, 380:66–77, 1991. Cited on page [39](#).
- [OR08] Oya, I. and R. de los Reyes, et al. Data check and onsite analysis of the magic telescope. *VIII meeting of the Spanish Astronomy Society, Santander, Spain*, 2008. Cited on pages [123](#) and [136](#).
- [Ost89] Osterbrock, D.E. *Astrophysics of Gaseous Nebulae and Active Galactic Nuclei*. University Science Books, 1989. Cited on page [36](#).
- [Oya06] Oya, I. Master's thesis, Universidad Complutense de Madrid, 2006. Cited on pages [116](#), [117](#), [136](#), and [202](#).
- [Oya09a] Oya, I., De los Reyes,R, et al. Magic Data Check Program. *MAGIC-TDAS*, 09-02, 2009. Cited on pages [114](#) and [123](#).
- [Oya09b] Oya, I., Nieto, D., et al. Magic On-Site Analysis Program. *MAGIC-TDAS*, 09-03, 2009. Cited on page [136](#).
- [Pad07] Padovani, P. The blazar sequence: validity and predictions. *Ap&SS.*, 309:63–71, 2007. Cited on page [46](#).
- [Pan04] Paneque D., et al. A method to enhance the sensititvity of phototmultipliers for air Cherenkov telescopes by applying a lacquer that scatters light. *NIM A*, 518:619–621, 2004. Cited on page [62](#).
- [Pan09] Paneque, D., et al. Study of the Classical TeV blazar Mrk421 with Fermi. *2009 Fermi Symposium, 2–5 November, Washington*, 2009. Cited on pages [194](#), [196](#), and [198](#).
- [PBS05] Primack J.R., Bullock J.S., and Somerville R.S. Observational Gamma-ray Cosmology. *HIGH ENERGY GAMMA-RAY ASTRONOMY: 2nd International Symposium on High Energy Gamma-Ray Astronomy. AIP Conference Proceedings*, 745:1752–1754, 2005. Cited on pages [16](#), [17](#), [164](#), and [195](#).
- [Per07] Perry, M., et al. The exceptionally extended flaring activity in the X-ray afterglow of GRB 050730 observed with Swift and XMM-Newton. *A&A*, 471:83–92, 2007. Cited on page [161](#).
- [Pet96] Petry, D., et al. Detection of VHE  $\gamma$ -rays from MKN 421 with the HEGRA Cherenkov Telescopes. *A&A*, 311:L13–L16, 1996. Cited on page [137](#).

## REFERENCES

---

- [Pet97] Peterson, B.M. *An Introduction to Active Galactic Nuclei*. Cambridge University Press, 1997. Cited on pages [36](#) and [41](#).
- [Pet02] Petry, D., et al. The TeV Spectrum of H1426+428. *ApJ*, 580:104–109, 2002. Cited on page [172](#).
- [PGL05] Poe, G., Giraud, D., and Loomis, J. Computational Methods for Measuring the Difference of Empirical Distributions. *American Journal of Agricultural Economics*, 87:353–365, 2005. Cited on page [147](#).
- [PGS08] Primack J.R., Gilmore R.C, and Somerville R.S. Diffuse Extragalactic Background Radiation. *HIGH ENERGY GAMMA-RAY ASTRONOMY: Proceedings of the 4th International Meeting on High Energy Gamma-Ray Astronomy*, 1085:71–82, 2008. Cited on page [16](#).
- [Pia98] Pian, E., et al. BeppoSAX Observations of Unprecedented Synchrotron Activity in the BL Lacertae Object Markarian 501. *ApJ*, 492:L17, 1998. Cited on page [185](#).
- [Poi03] Poirier, J., et al. Search for sub-TeV gamma rays in coincidence with gamma ray bursts. *Physical Review D*, 67:Issue 4, 2003. Cited on page [21](#).
- [Pun92] Punch, N., et al. Detection of TeV photons from the active galaxy Markarian 421. *Nature*, 358:477–478, 1992. Cited on pages [137](#), [139](#), [184](#), and [202](#).
- [Qui96] Quinn, J., et al. Detection of Gamma Rays with  $E > 300$  GeV from Markarian 501. *ApJ*, 456:L83–L86, 1996. Cited on pages [184](#), [185](#), and [186](#).
- [Rei09] Reichardt, I., et al. The MAGIC data center. *Proceedings of the 31st International Cosmic Ray Conference, Lódź, Poland*, 2009. Cited on pages [68](#), [125](#), and [126](#).
- [RG41] Rossi, B. and Greisen, K. Cosmic Ray Theory. *Reviews of Modern Physics*, 13:240–309, 1941. Cited on page [50](#).
- [RG74] Rees, M.J. and Gunn, J.E. The origin of the magnetic field and relativistic particles in the Crab Nebula. *MNRAS*, 167:1–12, 1974. Cited on page [21](#).
- [Rol05] Rolke, W.A., et al. Limits and confidence intervals in the presence of nuisance parameters. *NIM A*, 551:493–503, 2005. Cited on pages [96](#) and [172](#).

## REFERENCES

---

- [Rom05] Roming, P.W., et al. The Swift Ultra-Violet/Optical Telescope. *Sp. Sc. Rev.*, 120:95–142, 2005. Cited on page [174](#).
- [RS76] Ruderman, M.A. and Sutherland, P.G. Theory of pulsars - Polar caps, sparks, and coherent microwave radiation. *ApJ*, 196:51–72, 1976. Cited on page [23](#).
- [RW93] Ramana Murthy, P.V. and Wolfendale, A.V. *Gamma-Ray Astronomy*. Cambridge University Press., 1993. Cited on pages [6](#) and [13](#).
- [Sak06] Sakamoto, T., et al. Confirmation of the  $E_{peak}^{src}$ - $E_{iso}$  (Amati) Relation from the X-Ray Flash XRF 050416A Observed by the Swift Burst Alert Telescope. *ApJ*, 636:L73–L76, 2006. Cited on page [161](#).
- [Sch01] Schönfelder, V. (ed.). *The Universe in Gamma Rays*. Springer, 2001. Cited on page [29](#).
- [Sey43] Seyfert, C.K. Nuclear Emission in Spiral Nebulae. *ApJ*, 97:28–40, 1943. Cited on page [34](#).
- [SMS06] Stecker, F.W., Malkan, M.A, and Scully, S.T. Intergalactic Photon Spectra from the Far-IR to the UV Lyman Limit for  $0 < z < 6$  and the Optical Depth of the Universe to High-Energy Gamma Rays. *ApJ*, 648:774–783, 2006. Cited on pages [16](#) and [17](#).
- [Som94] Sommer, M., et al. High Energy Gamma Rays from the Intense 1993 January 31 Gamma-Ray Burst. *ApJ*, 422:L63, 1994. Cited on pages [20](#) and [21](#).
- [SS09] Saito, T.Y. and Sitarek, F. Improvement of the  $\theta^2$  analysis by using the Random Forest method in the DISP estimation. *MAGIC-TDAS*, 09–01, 2009. Cited on page [85](#).
- [Ste75] Stecker, F.W. in *Origin of Cosmic Rays (Osborne, J.L., and Wolfendale, A.W., eds)*. Reidel, Dordrecht, Holland., page 267, 1975. Cited on page [8](#).
- [Str01] Strüder, L., et al. The European Photon Imaging Camera on XMM-Newton: The pn-CCD camera. *A&A*, 365:L18–L26, 2001. Cited on pages [138](#) and [149](#).
- [SWL08] Schweizer, T., Wagner, R., and Lorenz, Eckart. A Statistical study of Sub-Hour Flares of the VHE Gamma-Ray Emission of Markarian 421 During a High Flux State in 2001. *AIP Conference Proceedings*, 1085:455–458, 2008. Cited on page [137](#).

## REFERENCES

---

- [Tag08] Tagliaferri, G., et al. Simultaneous Multiwavelength Observations of the Blazar 1ES 1959+650 at a Low TeV Flux. *ApJ*, 679:1029–1039, 2008. Cited on page [174](#).
- [Tav01] Tavecchio, F., et al. Theoretical Implications from the Spectral Evolution of Markarian 501 Observed with BeppoSAX. *ApJ*, 554:725–733, 2001. Cited on page [185](#).
- [Tay97] Taylor, J.R. *An Introduction to Error Analysis*. University Science Books, 1997. Cited on page [147](#).
- [The09a] The VERITAS Collaboration. A connection between star formation activity and cosmic rays in the starburst galaxy M82. *Nature online*, November 1, 2009. Cited on page [27](#).
- [The09b] The VERITAS Collaboration, The VLBA 43 GHz M87 Monitoring Team, The H.E.S.S. Collaboration, The MAGIC Collaboration. Radio Imaging of the Very-High-Energy gamma-Ray Emission Region in the Central Engine of a Radio Galaxy. *Science*, 325:444–448, 2009. Cited on page [18](#).
- [The10] The Fermi-LAT Collaboration. The Fermi Large Area Telescope First Source Catalog. *Submitted to ApJS*, 2010. Cited on pages [179](#), [180](#), [184](#), [196](#), and [202](#).
- [Tho08] Thomson, D.J., et al. Gamma ray astrophysics: the EGRET results. *Rep. Prog. Phys.*, 71, 2008. Cited on page [29](#).
- [TMG98] Tavecchio, F., Maraschi, L., and Ghisellini, G. Constraints on the Physical Parameters of TeV Blazars. *ApJ*, 509:608–619, 1998. Cited on pages [44](#) and [203](#).
- [TMG01] Tavecchio, F., Maraschi, L., and Ghisellini, G. Theoretical Implications from the Spectral Evolution of Markarian 501 Observed with BeppoSAX. *ApJ*, 554:725–733, 2001. Cited on pages [151](#), [179](#), and [180](#).
- [Tra10] Tramacere, A. The Large Flares of Mrk 421 in 2006: signature of electron acceleration and energetic budget of the jet. *Proceedings of The Extreme sky: Sampling the Universe above 10 keV*, 2010. Cited on page [162](#).
- [Tsu04] Tsuchiya, K., et al. Detection of Sub-TeV Gamma Rays from the Galactic Center Direction by CANGAROO-II. *ApJ*, 606:L115–L118, 2004. Cited on page [23](#).

## REFERENCES

---

- [Tt10] The Fermi LAT collaboration and the Fermi Pulsar Timing Consortium: A.A Abdo, et al. Fermi Large Area Telescope Observation of the Crab Pulsar and Nebula. *ApJ*, 708:1254–1267, 2010. Cited on page [23](#).
- [UP95] Urry, C.M. and Padovani, P. Unified Schemes for Radio Sources. *Publications of the Astronomical Society of the Pacific*, 107:803, 1995. Cited on pages [18](#), [19](#), [36](#), and [37](#).
- [Ush09] Ushio, M., et al. Suzaku Wide Band Analysis of the X-Ray Variability of TeV Blazar Mrk 421 in 2006. *ApJ*, 699:1964–1972, 2009. Cited on page [141](#).
- [Wag06] Wagner, R.M. *Measurement of VHE  $\gamma$ -ray emission from four blazars using the MAGIC telescope and a comparative blazar study*. PhD thesis, Technische Universitt Mnchen, 2006. Cited on page [57](#).
- [Wag08] Wagner, R. Synoptic studies of 17 blazars detected in very high-energy  $\gamma$ -rays. *MNRAS*, 385:119–135, 2008. Cited on page [162](#).
- [Wee89] Weekes, T.C., et al. Observation of TeV gamma rays from the Crab nebula using the atmospheric Cerenkov imaging technique. *ApJ*, 342:379–395, 1989. Cited on pages [22](#) and [71](#).
- [Wee03] Weekes, T. *Very High Energy Gamma-Ray Astronomy*. Institute of Physics Publishing. Bristol and Philadelphia., 2003. Cited on page [6](#).
- [Wee08] Weekes, T. Tev Gamma-ray Astronomy: The Story So Far. *Proc. of the 4th Heidelberg International Symposium on High Energy Gamma-Ray Astronomy*, 2008. Cited on page [32](#).
- [Wol08] Wolter, A., et al. The Hard Synchrotron X-ray Spectrum of the TeV BL Lac 1ES 1426+428. *ASP Conference Series*, 386:302, 2008. Cited on page [170](#).
- [Woo08] Wood, M., et al. A Search for Dark Matter Annihilation with the Whipple 10 m Telescope. *ApJ*, 678:594–605, 2008. Cited on page [27](#).
- [Xue06] Xue, Q., et al. X-Ray Spectral Variability of TeV Blazars during Rapid Flares. *ApJ*, 647:194–200, 2006. Cited on page [163](#).
- [Yao06] Yao, W.-M., et al. Review of particle physics. *Journal of Physics G*, 33:1–1232, 2006. Cited on page [55](#).
- [ZMH08] Zanin, R., Moralejo, A., and Hsu, C.C. Online Analysis. *MAGIC-TDAS*, 08-01, 2008. Cited on page [125](#).